Dielectron analysis in $p-p$ collisions at 3.5 GeV with the $HADES$ spectrometer: ω-meson line shape and a new electronics readout for the Multi-wire Drift Chambers

Dissertation
zur Erlangung des Doktorgrades
der Naturwissenschaften

vorgelegt beim Fachbereich Physik
der Johann Wolfgang Goethe-Universität
in Frankfurt am Main

von
Attilio Tarantola Peloni
aus Como, Italien

Frankfurt 2010
(D 30)

vom Fachbereich Physik der
Johann Wolfgang Goethe-Universität als Dissertation angenommen.

Dekan: Prof. Dr. D. Rischke
Gutachter: Prof. Dr. H. Ströbele, Prof. Dr. J. Stroth
Datum der Disputation: 16.12.2010

Kurzfassung

HADES (High Acceptance Di-Electron Spectrometer) ist ein hochauflösendes Dielektronenspektrometer, das am Schwerionen-Synchroton (SIS-18) an der Gesellschaft für Schwerionenforschung (GSI) in Darmstadt aufgebaut wurde.

Die primäre physikalische Motivation des Experiments ist die Messung von e^+e^- Paare im invarianten Massenbereich bis 1 GeV/c^2, sowohl in pion- und protoninduzierten Reaktionen, als auch in Schwerionenkollisionen.

Schwerpunkt des HADES-Physik Programms ist die Erforschung von in-Medium Eigenschaften der leichten Vektormesonen $\rho(770)$, $\omega(783)$ and $\phi(1020)$. Dileptonen sind "penetrating probes", die das Studium der Eigenschaften von Hadronen in Kernmaterie möglich machen. Allerdings ist die Messung dieser Dileptonenpaare schwierig, da sie selten sind und einen sehr grossen kombinatorischen Untergrund haben.

Vor Kurzem wurde HADES mit neuen Detektoren und neuer Elektronik aufgerüstet, um bei höheren Intensitäten und Reaktionen schwererer Kerne messen zu können.

Das breite physikalische Programm von HADES wird in den nächsten Jahren noch am SIS-18 statt finden, und dann am geplanten bevorstehenden international Facility for Antiproton and Ion Research (FAIR) Beschleuniger fortgesetzt werden. In diesem Zusammenhang sind die in der vorliegenden Arbeit vorgestellten physikalischen Ergebnisse wichtige Voraussetzungen für die Untersuchung der "in-Medium" Vektormesonen Eigenschaften in p + A und A+A Kollisionen.

Diese Arbeit besteht aus fünf Teilen. Das erste Kapitel beschreibt die zugrunde liegende physikalische Motivation und gibt eine Übersicht der bisherigen physikalischen Ergebnisse. Im Rahmen des zweiten Kapitels werden das HADES Spektrometer und die Subdetektoren beschrieben. Das dritte Kapitel behandelt die Frage der Identifikation der Leptonen und beschreibt die Rekonstruktion der Spektren der Elektronenpaare in p + p Kollisionen.

Hier werden zwei Reaktionen charakterisiert: der inklusive ($pp \to X\omega$) und der exklusive ($pp \to pp\omega$) Produktionsmechanismus der Dileptonen. In den erhaltenen Spektren werden die entsprechenden Wirkungsquerschnitte mit den jeweiligen statistischen und systematischen Fehlern dargestellt. Ein Vergleich

mit theoretischen Modellen ist enthalten. Die Schlussfolgerungen werden im vierten Kapitel gegeben.

Der letzte Teil dieser Arbeit fokussiert auf das HADES "Upgrade" Programm, dessen Ziel unter anderem das Erreichen einer zuverlässigen und schnellen Datenerfassung der Multi-wire Drift Chambers (MDCs) ist. Das fünfte Kapitel präsentiert meinen Beitrag zu diesem erfolgreichen Projekt während der drei Jahre meiner Anwesenheit an der GSI.

Abstract

The HADES (High Acceptance DiElectron Spectrometer) is an experimental apparatus installed at the heavy-ion synchrotron SIS-18 at GSI, Darmstadt.

The main physics motivation of the HADES experiment is the measurement of e^+e^- pairs in the invariant-mass range up to 1 GeV/c^2 in heavy-ion collisions as well as in pion and proton-induced reactions.

The HADES physics program is focused on in-medium properties of the light vector mesons $\rho(770)$, $\omega(783)$ and $\phi(1020)$, which decay with a small branching ratio into dileptons. Dileptons are penetrating probes which allow to study the in-medium properties of hadrons. However, in heavy-ion collisions, the measurement of such lepton pairs is difficult because they are rare and have a very large combinatorial background.

Recently, HADES has been upgraded with new detectors and new electronics in order to handle higher intensity beams and reactions with heavy nuclei up to Au.

HADES will continue for a few more years its rich physics program at its current place at SIS-18 and then move to the upcoming international Facility for Antiproton and Ion Research (FAIR) accelerator complex. In this context the physics results presented in this work are important prerequisites for the investigation of in-medium vector meson properties in p + A and A+A collisions.

This work consists of five chapters. The first chapter introduces the physics motivation and a review of recent physics results. In the second chapter, the HADES spectrometer is described and its sub-detectors are presented. Chapter three deals with the issue of lepton identification and the reconstruction of the dielectron spectra in p + p collisions is presented. Here, two reactions are characterized: inclusive and exclusive dilepton production reactions. From the spectra obtained, the corresponding cross sections are presented with the respective statistical and systematical errors. A comparison with theoretical models is included as well. Conclusions are given in chapter four.

The final part of this work is dedicated to the HADES upgrade, whose goal is among others the achievement of a reliable and fast data acquisition of the Multiwire Drift Chambers (MDCs). Chapter five presents my contribution to this successful project during the three years of my stay at GSI.

Contents

Chapter 1

Physics Motivation

One of the main questions in nuclear physics research is the understanding of the behavior of hadrons and their constituents in vacuum, as well as under the extreme conditions when embedded into hot and dense matter.

The decay of light vector mesons (ρ, ω and ϕ) into lepton pairs (e^+e^- or $\mu^+\,\mu^-$) offers an ideal probe for those investigations. Electromagnetic decays of vector mesons are the best tool for studying strongly interacting matter, since they are not distorted by strong interactions. The life-time of the vector mesons is comparable with the life-time of the fireball produced in a nucleus-nucleus collision and can provide information about it.

The High Acceptance Di-Electron Spectrometer (HADES) at GSI[1] has been built to investigate the electromagnetic structure and the in-medium modifications of hadrons via the analysis of leptonic decays of light vector mesons.

1.1 Theoretical Introduction: Quantum Chromo Dynamics

Quantum Chromo Dynamics (QCD) is a relativistic field theory, formulated in close analogy to Quantum Electro Dynamics (QED). QED is a gauge theory of massive fermionic matter fields interacting with massless bosonic gauge fields (the photons). QCD is the gauge theory of the strong force, and it describes the interaction of color-charged particles via the exchange of bosons (the gluons), in analogy to the photons in QED. Gluons are massless, but unlike photons, the gluon field is self-interacting, since the gluons carry a non-zero color charge. This allows gluons not only to split into virtual quark-antiquark pairs, but also to split in pairs of gluons. This leads to an important difference from

[1] GSI Helmholtzzentrum für Schwerionenforschung, Darmstadt, Germany.

the electromagnetic interaction: the coupling strength of the strong interaction α_s increases with increasing distance of two quarks. With increasing momentum transfer α_s decreases leading to quasi-free quarks and gluons. This is known as "asymptotic freedom" [4].

In QCD, quarks and gluons are the important degrees of freedom. Quarks come in six flavors: "up", "down", "strange", "charm", "bottom", and "top" [12]. Nambu (1960) and Greenberg (1964) suggested that the quarks as well as gluons also have to carry color[2] as an additional quantum number.

The dynamics of the strong interaction is described by the lagrangian density, which is expressed as:

$$\mathcal{L}_{QCD} = \bar{\psi}(i\gamma^{\mu}\mathbf{D}_{\mu} - \mathbf{M})\psi - \frac{1}{4}\mathbf{G}^{i}_{\mu\nu}\mathbf{G}^{i\mu\nu} \tag{1.1}$$

where ψ are the Dirac Spinors[3] and include the flavor and color quantum numbers. $\mathbf{M} = diag(m_u, m_d, m_s, m_c, m_t, m_b)$ denotes the quark masses of a given flavor. $\mathbf{D}_{\mu} = \partial_{\mu} + ig\frac{\lambda^i}{2}\mathbf{A}^i_{\mu}$ is the covariant derivative, λ^i the Gell-Mann matrices and $\mathbf{A}^i$ the gauge fields with color index $(i = 1, ..., 8)$. $\gamma^{\mu}(\mu = 0, 1, 2, 3)$ are the Dirac matrices and $\mathbf{G}^{i\mu\nu}$ is the gluon tensor:

$$\mathbf{G}^{i}_{\mu\nu} = \partial_{\mu}\mathbf{A}^i_{\nu} - \partial_{\nu}\mathbf{A}^i_{\mu} + igf_{ijk}\mathbf{A}^j_{\mu}\mathbf{A}^k_{\nu} \tag{1.2}$$

which describes the gluon self-interaction. $g = \sqrt{4\pi\alpha_s}$ is related to the strong coupling constant α_s, which increases with space-time distance or equivalently decreases with the momentum transfer squared Q^2 of a given strong process. f_{ijk} is the structure constant of the SU(3) group [12].

Due to quantum fluctuations, the vacuum itself behaves like a polarizable medium[4]. In addition to virtual quark-antiquark pairs, which screen a color charge and thus would make the QCD vacuum diamagnetic, the selfinteraction of gluons induces a color magnetization of the vacuum and makes it paramagnetic. This effect actually overcomes the diamagnetic contribution from

[2]The idea of the color charge arises experimentally from the existence of baryons with three quarks of identical flavor, *e.g.* the Δ^{++} consists of three u quarks. The Pauli principle requires an extra quantum number to allow this quark configuration. Since any two fermions must not occupy the same state but must at least differ in one quantum number, an additional quantum number has been introduced: the color quantum number.

[3]They indicate spin 1/2 quark fields.

[4]In QED the photon can create virtual electron-positron pairs, causing partial screening of the charge of a test particle. This means that the dielectric constant ϵ_0 of the QED vacuum is $\epsilon_0 > 1$, but due to Lorentz invariance $\epsilon_0\mu_0 = 1$, where μ_0 is the magnetic permeability of the vacuum and must hold $\mu_0 < 1$. This means that the QED vacuum behaves as a diamagnetic medium.

quark-antiquark pairs such that $\mu_0^c > 1$. Therefore must hold $\epsilon_0^c < 1$: so that the color-electric interaction between charged objects becomes stronger as their separation grows (infrared slavery)[5]. As the distance between quarks $r \to 0$, ϵ_0^c and $\mu_0^c \to 1$, the interaction becomes weaker. Equivalently with increasing momentum transfer the coupling decreases leading to quasi-free quarks and gluons.

The behavior of α_s is well confirmed by many experiments [1]. These indicate that quarks inside the nucleon behave as point like, non-interacting particles. It follows that the strong fine structure constant $\alpha_s = g_s^2/4\pi$ has a strong Q^2 dependence of the four-momentum transferred in the given strong process and changes according to the approximated formula:

$$\alpha_s(Q^2) = \frac{12\pi}{(33 - 2N_f) \cdot ln(Q^2/\Lambda_{QCD}^2)} \qquad \text{and} \qquad Q^2 \gg \Lambda_{QCD}^2 \tag{1.3}$$

where $\Lambda_{QCD} \simeq 200MeV$ is the fundamental QCD scale parameter and it stands for the scale at which the coupling constant is fixed by an experiment and $N_f = 6$ is the number of flavors in the Standard Model.

The above Equ. 1.3 suggests that α_s gets smaller with growing Q^2. For sufficiently large four-momenta transferred, this means that QCD can be treated using perturbation theory. Moreover, in the limit $Q^2 \to \infty$, the interaction between particles are weak and the non-interaction between color particles is reached.

At small momentum transfer, a perturbative treatment can no longer be justified and no analytical solution of the QCD equations can be derived. In this regime the relevant degrees of freedom change. At large distances the degrees of freedom are colorless objects made of two (mesons) or three (baryons) confined quarks/anti-quarks.

In order to study the evolution of the system, phenomenological or numerical methods have to be used with an approximate shape of the QCD potential. These phenomenological models can describe the other important properties which characterize the QCD, namely the confinement: it is generally believed that the increase of the coupling constant for low values of Q^2 is responsible for the fact that isolated quarks and gluons have not been observed and are permanently confined in hadronic system.

1.1.1 QCD Symmetries: Chiral Symmetry

The main motivation to study properties of vector mesons comes from the chiral symmetry: an approximate symmetry of QCD. The lagrangian is invariant

[5]This is the reason why the QCD vacuum is called antiscreening medium.

under local $SU(3)$ gauge transformations, *i.e.* it is invariant under rotations in color space.

The lagrangian exhibits also a global symmetry $U(1)$ that corresponds to the baryon number conservation. In the limit of vanishing quark masses (which for momentum transfers of $Q \simeq 1\ GeV/c$ is a good approximation for the light quarks u and d), massless fermions with spin 1/2 have helicity or chirality, which is defined as the projection of their spin to the direction of their motion. Such fermions can only be left-handed or right-handed.

The lagrangian in the massless limits shows another symmetry under global axial and vector transformation in $SU(3)$ flavor space, namely "chiral symmetry" [5]. Defining the right and left-handed components of fermion fields with:

$$\psi_{R,L} = \frac{1}{2}(1 \pm \gamma_5)\psi \tag{1.4}$$

the chiral symmetry is represented by the following transformations:

$$SU(3)_R : \psi_R \rightarrow R\psi_R = exp(i\theta_R^a \frac{\lambda_a}{2})\ \psi_R \quad \text{and} \quad \psi_L \rightarrow \psi_L \tag{1.5}$$

$$SU(3)_L : \psi_L \rightarrow L\psi_L = exp(i\theta_L^a \frac{\lambda_a}{2})\ \psi_L \quad \text{and} \quad \psi_R \rightarrow \psi_R \tag{1.6}$$

Where θ_R and θ_L are the vectors of eight arbitrary real constants and λ_a is the eight-vector component of the Gell-Mann matrices. These relations transform the right(left) fermion fields into right(left) fermion fields. The symmetry conserves the projection of the spin on the momentum direction of a quark.

The $SU(3)_R \otimes SU(3)_L$ symmetry can be converted into axial and vector transformations in $SU(3)$ flavor space:

$$\psi \rightarrow exp(i\theta_A^a \frac{\lambda_a}{2})\ \psi \tag{1.7}$$

$$\psi \rightarrow exp(i\theta_V^a \frac{\lambda_a}{2})\ \psi \tag{1.8}$$

It is known that this symmetry is **spontaneously broken** in nature because the symmetry does not manifest itself with parity multiplets in the hadron spectra [5, 6]. The observation of the mass splitting of chiral partners implies a spontaneous breaking of chiral symmetry due to a non-vanishing vacuum expectation value of the quark condensate $< \bar{q}q > \neq 0$. While the vector current ($j_V = j_L + j_R$) is still conserved, the axial-vector symmetry ($j_V = j_L - j_R$) is

spontaneously broken.

The symmetry of the lagrangian would lead to a symmetry of the particle states. Since the chiral symmetry relates positive and negative parity states, they are expected to appear as degenerate particles. In reality this is not the case. In many low-lying states of the meson spectrum, the mass splitting between positive (negative) parity ground states and first excited states of negative (positive) parity are about 500 MeV/c^2; *i.e.* the ρ and its chiral partner a_1 mesons have a mass difference of $\backsimeq$ 550 MeV/c^2 ($m_\rho = 776\ MeV/c^2$ and $m_{a_1} = 1230\ MeV/c^2$ [2]).

A restoration of chiral symmetry should happen in a deconfined state, when the masses of quarks approach zero. A partial restoration could already start at the conditions of hot and dense medium. The tool to experimentally achieve such conditions of high temperature and density are relativistic heavy ion collisions.

Observing this non-perturbative property of QCD, called chiral symmetry restoration, is one of the most interesting challenges in nuclear physics.

The non-vanishing mass of the pseudoscalar mesons is explained by the **explicit breaking** of the chiral symmetry, which is due to the finite quark masses. In the limit of massless quarks ($m_u = m_d = 0$) the pions would be massless but their non-zero mass is generated by breaking explicitly the symmetry.

1.1.2 In-Medium Quark Condensate

A phase with a broken symmetry can be characterized by order parameters at the hadronic level and at the fundamental quark level: the pion-decay constant $f_\pi \approx 92\ MeV$ and the quark condensate $< 0|\bar{q}q|0 >$. These two parameters are related by the Gell-Mann-Oakes-Renner relation [7]:

$$f_\pi^2 M_\pi^2 \approx -\bar{m_q} < 0|\bar{q}q|0 > \approx -2\bar{m_q} < 0|\bar{u}u|0 > \approx -2\bar{m_q} < 0|\bar{d}d|0 > \qquad (1.9)$$

Here $\bar{m_q}$ denotes an averaged quark mass ($0.5(m_u + m_d) \approx 6\ MeV/c^2$). In [7, 8] it is shown that a condition to observe spontaneous symmetry breaking would be the existence of a non-vanishing scalar quark condensate in the QCD vacuum. Derivation of Equ. 1.9 assumes the Partial Conservation of the Axial-vector Current (PCAC) and it connects the parameters of the spontaneous and the explicit chiral symmetry breaking ($< 0|\bar{q}q|0 >$ and m_u, m_d) with the corresponding pion structure constants (f_π).

A value of $f_\pi \approx 92\ MeV$, from pion decay measurements, leads to a vacuum expectation value of $< 0|\bar{q}q|0 > \backsimeq$-$(240\ MeV)^3 \simeq$ -1.6 fm^{-3} [51]. This value is large compared to the normal nuclear density ($\sim 0.17\ fm^{-3}$), indicating a strong

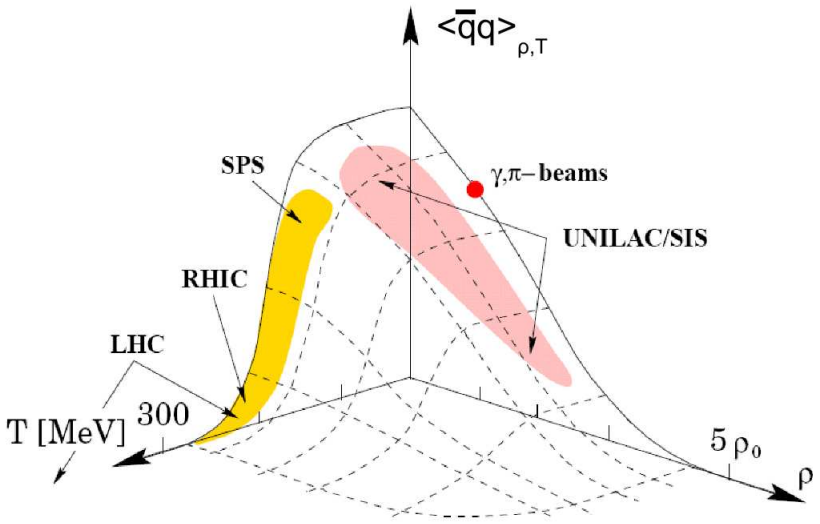

Figure 1.1: The expectation value of the quark condensate described by Nambu-Jona-Lasinio model [3, 9]. The region accessible by different accelerator facilities are colored. The normal nuclear density is denoted ρ_0. The picture has been adapted from [55].

dynamical breaking of chiral symmetry. The expectation value of the quark condensate, as function of density and temperature, is model-dependent and it is described for instance by the Nambu-Jona-Lasinio model [3, 9]. In Fig. 1.1, the behavior of the $< 0|\bar{q}q|0 >$ as a function of density is approximately linear and on the order of 25% at nuclear density matter ($\rho_0 \simeq 0.17\ nucleon/fm^{-3}$). Heavy ion collisions (beam energy $\simeq$ 1-2 GeV) can produce 2-3 ρ_0. The decrease of $< 0|\bar{q}q|0 >$ with temperature happens suddenly, close to the critical temperature, indicating that ultra-relativistic heavy ion collisions are ideal to study the behavior of $< 0|\bar{q}q|0 >$ at high T.

A link between quantities, which can be measured and the decrease of $< 0|\bar{q}q|0 >$ with increasing density and temperature was suggested by Brown and Rho [10]. Brown and Rho proposed that the vector meson masses are proper observables: important effects are dropping hadron masses (BR-scaling), preceding the phase transition towards a restoration of chiral symmetry. The universal BR-scaling in [10] predicts a dropping of the ρ-meson and the ω-meson masses by $15 - 20\%$ at already normal nuclear matter densities:

$$\frac{<\bar{q}q>_\rho}{<\bar{q}q>_0} = \left(\frac{f_\pi^*}{f_\pi}\right)^3 \quad \text{and} \quad \frac{f_\pi^*}{f_\pi} = \frac{m_\sigma^*}{m_\sigma} = \frac{m_N^*}{m_N} = \frac{m_\rho^*}{m_\rho} = \frac{m_\omega^*}{m_\omega} \tag{1.10}$$

where f_π^* is the in-medium pion decay constant.

1.2 Composition of the Dielectron Spectrum: the Cocktail

An electron pair is an electron-positron pair which results from the decay of a massive virtual photon. At low beam energy (*i.e.* from 1 to 4 GeV), the sources of dielectrons can be divided into two categories: **hadron decays** and **bremsstrahlung**. In the present work, the hadrons of interest are: π, η, ω, ρ, ϕ and Δ. These three categories contribute to the measured spectrum. The composition of this spectrum is called the "cocktail".

1.2.1 Hadron Properties

The hadron decays are divided into two sub-categories: **two-body** and **Dalitz (three body)** decays.

1.2.1.1 Two-Body Decays

The lightest vector mesons are $\rho(770)$, $\omega(782)$ and $\phi(1020)$. Their main properties are reported in Table 1.1. These resonances are produced via the quark pair creation $u\bar{u}$ and $d\bar{d}$. Since u and d quarks have almost identical masses, the $u\bar{u}$ and $d\bar{d}$ are approximately degenerate states. The ρ meson is a vector-isovector meson[6]. It is of particular interest, since its lifetime is short compared to the other mesons ($\tau_\rho = 1.3\ fm/c$) and also short compared to the typical fireball time scale ($\sim 10\ fm/c$) at SIS energies.

The ω and ϕ are neutral vector-isoscalar mesons. The ρ^0, and ω mesons are mixed states of the $u\bar{u}$ and $d\bar{d}$ combinations.

Meson	J^P	I	Mass [MeV/c^2]	Width [MeV/c^2]	Lifetime [fm/c]	e^+e^- BR
ρ	1^-	1	775	152	1.3	$4.4 \cdot 10^{-5}$
ω	1^-	0	782	8.43	23.4	$7.2 \cdot 10^{-5}$
ϕ	1^-	0	1019	4.43	44.4	$3.1 \cdot 10^{-4}$

Table 1.1: Main properties of the lightest vector mesons [2].

[6]Therefore it has 3 charge states (ρ^+, ρ^-, ρ^0).

The ϕ meson has a width $\Gamma = 4.4\ MeV$, hence its lifetime is long compared to the lighter ρ meson.

The ρ meson and the ω meson differ by G parity: because of this and recalling the G parity of the π meson (-1), the ρ meson decays strongly predominantly into 2 π-mesons ($\sim 100\%$) and it is a broad resonance.

The same G parity argument applies to the ω meson, which decays strongly mainly into 3 π-mesons ($\sim 89\%$) and because of phase-space limitations, it is much narrower than the ρ meson.

The ϕ meson is a $s\bar{s}$ state and has its dominant strong decay into $K\bar{K}$ ($\sim 83\%$). It is a narrow state since it is close to the $K\bar{K}$ threshold.

In the HADES energy regime, three particles decay via an electromagnetic two-body decay: ρ, ω, $\phi \rightarrow e^+e^-$. From these mesons, the spectral functions are expected to change under certain conditions.

The decay of vector mesons into lepton pairs is an important phenomenon: it converts a strongly interacting resonance into a lepton pair, which interacts only weakly with matter. It is a rare phenomenon, with a Branching Ratio (BR) of the order of 10^{-5} for the low-mass vector mesons, but this phenomenon is not so rare as to preclude experimental observation.

The lifetime of vector mesons is about 10^{-22}s to 10^{-24}s, typical of the strong interaction. These resonances are interpreted as quark-antiquark states. A vector meson is converted into a photon which materializes into a lepton pair. Photons and vector mesons have the same quantum numbers, in particular they must have total angular momentum $J = 1$ and negative parity. Fig 1.2 shows this process. For any vector meson V, with mass m_v, neglecting the electron mass, the decay width into e^+e^- pair can be written as [50]:

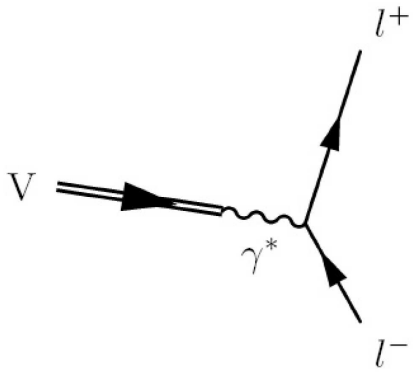

Figure 1.2: A neutral vector meson decays into a lepton pair.

$$\Gamma(V \rightarrow e^+e^-) = \frac{4\pi\alpha^2}{3g_v^2} m_v \tag{1.11}$$

The coupling constants g_v of the vector mesons into photons can be obtained from the measured dielectron decay widths of the vector mesons. According to Equ. 1.11 the ratios of Γ for the ρ, ω and ϕ mesons are proportional to m_v/g_v^2.

1.2.1.2 Dalitz (three body) Decays

At masses $\lesssim 1\ GeV/c^2$ many hadrons undergo three-body Dalitz decays:

- $\pi^0 \longrightarrow e^+e^-\gamma$
- $\eta' \longrightarrow l^+l^-\gamma$
- $\eta \longrightarrow l^+l^-\gamma$
- $\omega \longrightarrow \pi^0 l^+l^-$
- $\Delta \longrightarrow Ne^+e^-$

Unlike the direct meson decays (two-body decays), which produce recognizable peaks in the invariant-mass spectrum, the Dalitz decays produce continuous mass distributions and this makes it difficult to disentangle their individual contributions to the "cocktail".

The Feynman diagrams in Fig. 1.3, 1.4 and 1.5, show the ω vector meson decay and the pseudoscalar meson (π^0,η) decays.

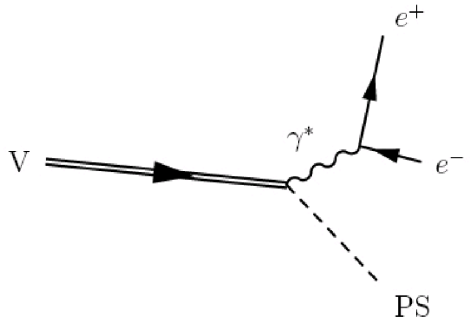

Figure 1.3: Decay of a vector meson (V) into a Pseudo Scalar (PS) meson and a lepton pair (l^+l^-) via a virtual photon (γ^*). *E.g.*: $\omega \rightarrow \pi^0 e^+e^-$.

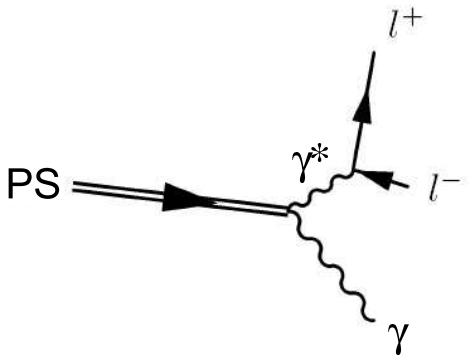

Figure 1.4: Decay of a Pseudo Scalar (PS) meson into a γ and a lepton pair (l^+l^-) via a virtual photon (γ^*). *E.g.*: $\pi^0, \eta \rightarrow \gamma e^+e^-$.

There is also the double Dalitz decay. For example: the η meson: $\eta \rightarrow \gamma^*\gamma^* \rightarrow e^+e^+e^-e^-$. However its branching ratio is very small and it is difficult to identify.

The e^+e^- decays of pseudoscalar mesons are strongly suppressed by the helicity conservation condition [52], whereas $\mu^+\mu^-$ have observable properties.

Among the excited states of the proton and neutron, the $\Delta(1232)$ is a nucleon resonance which exists in four different states (Δ^{++}, Δ^+, Δ^0 and Δ^-) with

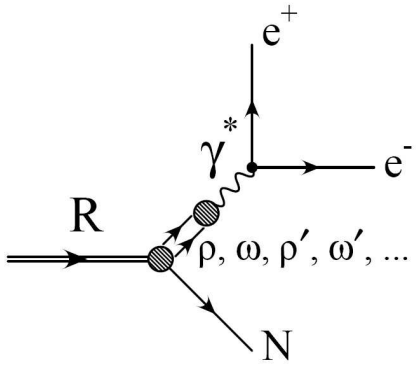

Figure 1.5: In the Vector Dominance Model (VDM) picture the Resonance (R) decays into a Nucleon (N) and a virtual vector-meson, which couples via a γ^* to a leptons pair (e^+e^-).

similar masses. Its lifetime is very short ($\tau_\Delta \simeq 1.8\ fm/c$) with $J^P = 3/2^+$ spin-parity[7]. Intermediate baryon resonances play an important role in dielectron production in NN. The Δ resonance decays predominantly in $N\pi$ (BR$\sim$ 100%) or in Ne^+e^- (BR=4.4·10^{-5}).

Tab. 1.2 summarizes the decays described in this section.

1.2.2 Virtual Bremsstrahlung

A special category of dilepton sources are the NN bremsstrahlung processes. Bremsstrahlung is normally called an electromagnetic radiation produced by the acceleration of a charged particle, such as an electron, when deflected by another charged particle, such as an atomic nucleus. Dielectron production in scattering processes of hadrons at low energies can be described essentially as bremsstrahlung from incoming and outgoing charged particles [54]. The involved processes are: $np \to npe^+e^-$ and $pp \to ppe^+e^-$.

Already the DLS collaboration noticed that there is a large difference between the dielectron productions in the p + p and p + d systems. They mea-

[7]The Δ resonances have been known since the 1950s. They are considered spin excitations of the nucleon ground state of three u or d quarks in the total spin state $J^P = 3/2^+$. Hence three quarks have parallel spins, therefore the spin wave function is symmetric with the exchange of two quarks. In the ground state, the spatial wave function must be symmetric too. Considering the state made of three u quarks (uuu), it is clear that the flavor wave function is symmetric. In order to fulfill the Pauli principle, in 1964 Greenberger assumed that there exists a new quantum number, exactly conserved by all interactions, called color quantum number. In order to have an antisymmetric total wave function, the uuu baryon must have a color wave function which is antisymmetric.

	Meson	Decay Channel	Branching Ratio
Three Body Decay	π^0	$e^+e^-\gamma$	$(1.19 \pm 0.03) \cdot 10^{-2}$
	η	$e^+e^-\gamma$	$(6.8 \pm 0.80) \cdot 10^{-3}$
	ω	$\pi^0 e^+e^-$	$(7.7 \pm 0.90) \cdot 10^{-4}$
	ϕ	$\pi^0 e^+e^-$	$(1.12 \pm 0.28) \cdot 10^{-5}$
Double Dalitz decay	π^0	$e^+e^+e^-e^-$	$(3.14 \pm 0.3) \cdot 10^{-5}$
	η	$e^+e^+e^-e^-$	$< 6.9 \cdot 10^{-5}$
Direct Decay	π^0	e^+e^-	$(6.46 \pm 0.33) \cdot 10^{-8}$
	η	e^+e^-	$< 7.7 \cdot 10^{-5}$
	ρ	e^+e^-	$(4.7 \pm 0.051) \cdot 10^{-5}$
	ω	e^+e^-	$(7.16 \pm 0.12) \cdot 10^{-5}$
	ϕ	e^+e^-	$(2.97 \pm 0.004) \cdot 10^{-4}$

Table 1.2: Summary of the dilepton decays of low mass mesons. Data has been taken from [2].

sured dielectrons in p + p and p + d collisions at different beam energies from 1.04 to 4.88 GeV. They noticed that the shape of the dilepton invariant-mass spectra change dramatically as the beam energy increases. Also, at 1.04 GeV, the p + d cross section has a different mass dependence and is nearly an order of magnitude greater than the p + p cross section. As the beam energy increases, the shape difference disappears and the p + d cross section becomes approximately twice the p + p cross section at all masses [44].

Theoretically, the pd/pp mass dependence of e^+e^- pair production, at the lower beam energies, can be explained with charged pion exchange and as the interference between the bremsstrahlung and the Δ isobar decay [54].

In a recent analysis [43], the HADES collaboration has observed a large enhancement of dielectron production in n + p relative to p + p reactions in the mass region above the π^0 Dalitz decay with beam kinetic energy of 1.25 GeV. In addition, a strong difference between the shapes of the n + p and p + p mass spectra is apparent. The drop of the p + p mass spectrum is much steeper than the n + p one, which can be partially explained by the smaller available energy in the proton-proton system. The contribution of NN bremsstrahlung is being investigated by comparison of the dielectron yields observed in p + p

and n + p reactions with theoretical calculations [49]. This production process is especially important at low energies where other production channels play a minor role or are not allowed (sub-threshold processes).

1.3 Spectroscopy with the HADES Spectrometer

1.3.1 Di-electron Spectroscopy

The High Acceptance Di-Electron Spectrometer (HADES) [22] is a detector system for dielectron spectroscopy built up in 1996-2002 at GSI (Darmstadt) by a European collaboration involving groups from 19 institutions in 9 countries.

The experimental program of HADES [23] aims at a systematic study of e^+e^- pair production in heavy-ion collisions, in hadron-induced nuclear collisions (p + A, π + A) and in elementary reactions (π + p, p + p, p + d). With the range of energies available at GSI (protons up to 4.5 GeV, ions of 1-2 $AGeV$ and the possibility to use secondary pion beams), the interest is focused on the invariant mass region up to 1 GeV/c^2.

The HADES program combines systematic studies of dielectron production in elementary reactions, in Sec. 1.3.2, with dielectron spectroscopy in heavy-ion collisions, with special interest on the vector meson properties in nuclear matter. Measurements have started with an investigation of dielectron production in ^{12}C+^{12}C collisions in 2002. Data on ^{12}C+^{12}C collisions at 1 $AGeV$ has been presented in [16, 17, 18, 19], corroborating the measurements of the former DLS Collaboration [19] at BEVALAC. Currently, a significant theoretical effort is underway to understand these observations.

Ar+KCl collisions were measured in 2005 at 1.756 $AGeV$ beam kinetic energy. For the first time high-resolution spectroscopy of the vector-meson region at SIS energies was performed [20]. The investigation of the medium-heavy Ar+KCl system also allows to study the dependence of the pair excess, already observed in the previously mentioned C+C reactions, on the system size and centrality of the collision. In the Ar+KCl reaction, the production of strangeness has been studied as well. Particles containing strange quarks produced in this energy regime are mainly the K mesons, the Λ and Σ hyperons, as well as the ϕ meson. Recent results can be found in [21].

1.3.2 Elementary Reactions

Experiments on the production of vector mesons form an integral and important part of the HADES experimental program.

The particular features of these "elementary" reactions is that the particles are produced in vacuum, *i.e.* without complications of medium effects. While in relativistic heavy-ion collisions the physics interpretation is complicated, because the reaction occurs in a non-equilibrium state before proceeding to equi-

librium[8], in elementary reaction the system is under control and the nucleus is always at $T = 0$ and at constant baryon density ρ_0. These allow to establish the line shape of the vector mesons and provide the constraints for the simulation.

The medium modifications of the mesons are predicted [10] to be large enough to be observed in reactions with hadron and photon beams on nuclear targets.

Dilepton invariant-mass spectra in elementary collisions were explored by several experiments at BEVALAC energies. A brief overview of these results is given in Sec. 1.4.

The proton-induced experiments, which have been done with the HADES spectrometer, are listed below:

- p + p and d + p at $E_{kin} = 1.25\ GeV$. These reactions have been studied for a better understanding of the contribution of Δ-Dalitz decays and NN bremsstrahlung processes to dielectron production in heavy-ion collisions. The p + n system has been studied using d + p collisions with forward tagging of the proton spectator, hence allowing for unique selection of the p + n reaction channel.

- p + p at $E_{kin} = 2.2\ GeV$. The reaction $pp \to pp\eta$ has been studied via an exclusive reconstruction of the hadronic and the dielectron decay channels [13, 14]. An inclusive measurement has been done in order to compare the dielectron spectra with ^{12}C+^{12}C at 2.0 GeV [15].

- p + p at $E_{kin} = 3.5\ GeV$. The analysis of the ω-meson provides a reference for the line shape measurement in p + A and π + A reactions which ultimately aims at establishing medium effects of light vector-meson embedded in nuclei. Indeed, with the knowledge of the inclusive experiment the sources of the invariant-mass spectrum can be studied and a model for the future p + A or A+A reactions can be stated.

  In order to reconstruct the exclusive ω production cross section, the decay channel $pp \to pp\omega \to pp e^+e^-$, with one proton being reconstructed with the missing mass technique, has been studied as well.

- p + Nb at $E_{kin} = 3.5\ GeV$. Production of vector mesons in p + Nb reaction has been measured in year 2008. Preliminary spectra from this run already show a prominent ω peak [82, 83, 84]. The analysis of these data is currently ongoing.

[8] At higher energies both the temperature and the baryon density vary during the collision dynamics.

Furthermore it is planned to measure the reaction π^- + p at $E_{kin} = 1.1\ GeV$ as a reference for future π^- + A experiments and several A+A runs scheduled in 2010-2013 [23, 24].

1.4 Light Vector Meson Spectroscopy in Hadron-Induced and in Elementary Reactions

A number of experiments have attempted to measure properties of light vector mesons in elementary reactions under various conditions. This chapter reports a brief summary of their results. However, it is not meant to be complete. A more complete overview can be found in [36, 37].

Experimentally, in order to observe in-medium modification of light vector mesons, the following conditions have to be fulfilled [36]:

- The lifetime of the meson has to be sufficiently short and the recoil velocity from the production reaction on a nuclear target has to be small enough such that the meson has a significant probability to decay within the nucleus[9].
- The momenta of the decay products should not be distorted by final-state interactions with the nuclear medium. Thus, decay products which interact only electromagnetically, like leptons or photons, are the preferred probes.

As an example of calculations, the in-medium modification of the vector meson spectral function, in Fig. 1.6, has been predicted by the Vector Meson Dominance (VMD) model[10].

The interaction with nucleons causes a strong broadening of the ρ meson down to the pion mass while the ω and ϕ mesons maintain approximately their line shape: the ω drops by about 100 MeV at normal nuclear matter density and its width increases by a factor of about 5, while the ϕ remains close to its vacuum value and its width increases by about a factor 9.

[9] The ρ meson has the advantage that it is a short-lived particle and has a large probability to decay inside the nucleus. A disadvantage consists in disentangling the ρ yield from the ω one. The ϕ meson has opposite properties: it is a narrow and isolated resonance with a low probability to decay inside the nucleus.

[10] In the VDM, the structure and decays of ρ, ω and ϕ mesons are based on a chiral $SU(3)$ Lagrangian approach [39].

The photon spectral function enters the dilepton rate (differential pair production rate):

$$\frac{d\mathcal{N}}{d^4x d^4q} = \frac{\alpha^2}{12\pi^4} \frac{\mathcal{R}(q,T)}{e^{4\beta q^0} - 1} \tag{1.12}$$

where q is the four-momentum of the time-like virtual photon, which decays into a dilepton pair, $\alpha = e^2/4\ \pi$, $\beta = 1/T$ and the lepton masses are neglected. $R(q,T)$ is the averaged photon spectral function [39, 40].

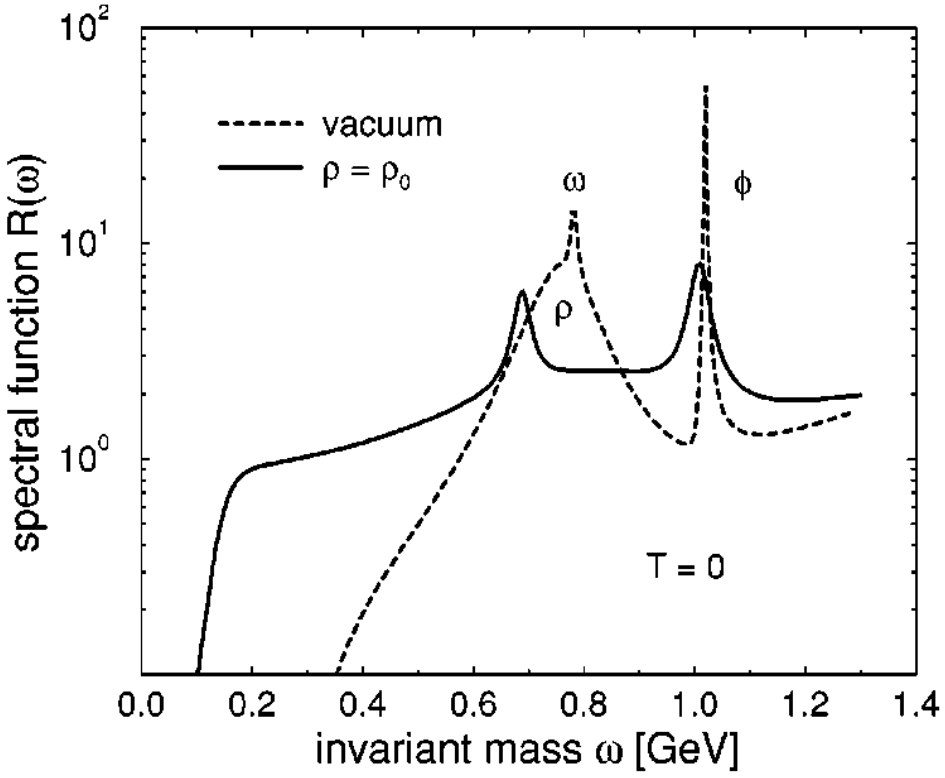

Figure 1.6: The vector meson spectral function at $T = 0$ and normal nuclear matter density $\rho_B = \rho_0 = 0.17\ fm^{-3}$. The picture has been taken from [40].

The CERES Experiment at CERN, first gave evidence for a spread of the in-medium ρ mass term in the yield of positron-electron pairs [42]. The observation was done at ultra-relativistic energies in heavy-ion collisions. However the mentioned experimental conditions are complicated since in heavy-ion collisions a complex system is created out of two nuclei which evolves in space and time. As vector meson spectral functions are subject to environmental changes in baryon density as well as in temperature, the complete reaction dynamics complicates the interpretation of the data.

For selectively investigating the dependence on baryon density, vector meson production off nuclei with hadronic or photon beams is a promising approach [36]. In these conditions, the conditions of the system are controlled since the nucleus stays always at temperature $T = 0$ and at constant baryon density ρ_0.

A number of recent experimental results obtained by various experiments dedicated to the study of light vector meson properties are reported here, while

the next chapter summarizes their results. This summary shows that there is still need for new and better data in order to have a consistent picture of the physics case.

1.4.1 The KEK Experiment (E325)

The KEK experiment (E325) measured the invariant-mass spectra of electron-positron pairs produced by a proton beam of 12 GeV energy on different targets. They observed a significant difference in the mass spectra below the ω meson between the light target (C) and the heavy target (Cu).

This difference indicates that the spectral shape of mesons is modified at normal nuclear matter density. However to confirm the results published in [25], it has been suggested to improve the statistics[11].

The results with higher statistic reported again a significant excess of e^+e^- pairs in the low-mass side of the ω meson [26]. The combinatorial background shape was determined using an event mixing technique. However due to the difficulty to treat the combinatorial background, this method is still a source of discussion in the physics community[12].

The result of this experiment, shown in Fig. 1.7 and in Fig. 1.8, agrees with a model inspired by the Brown-Rho scaling, which assumes a linear decrease of the vector meson masses. The mass decreases linearly as a function of the density ρ, following the relation [26]: $m(\rho)/m(0) \simeq 1 - k(\rho/\rho_0)$. The best fit of the data gives $k = 0.092$, meaning a dropping mass scenario for the ρ and ω meson by 9.2%.

A more recent publication, from the KEK collaboration [27], corroborated the previous observations in [25] and [26] for the ϕ meson too. The mass modification of the ϕ mesons was investigated by studying the e^+e^- invariant-mass distributions obtained in p + A reaction, with an incident beam kinetic energy

[11] Considering the high ω recoil velocity, induced by a 12 GeV proton beam on the target, the finite vector meson formation time of the order of 1 fm/c, and the collisional broadening, about 90% of the ω decays and 55% of the ρ decays will occur outside the nuclear medium and thus are not sensitive to in-medium modifications. Indeed high statistics experiments allow the selection of low momentum vector mesons, thereby enhancing the fraction of in-medium decays [36].

[12] The combinatorial background shape has been determined using an event mixing technique. Since the like-sign spectrum ($N_{e^-}N_{e^-}$ and $N_{e^+}N_{e^+}$) was not taken into account during the experiment, the quality of the mixed event technique could not be absolutely demonstrated. In Section 3, it is shown that the like-sign pairs provide a natural normalization of the uncorrelated background. This is possible if the detector measures lepton pairs of any charge combination, such that the data contains both like-sign and opposite-sign-pairs. Without the like-sign spectrum the background cannot be normalized easily and correctly subtracted.

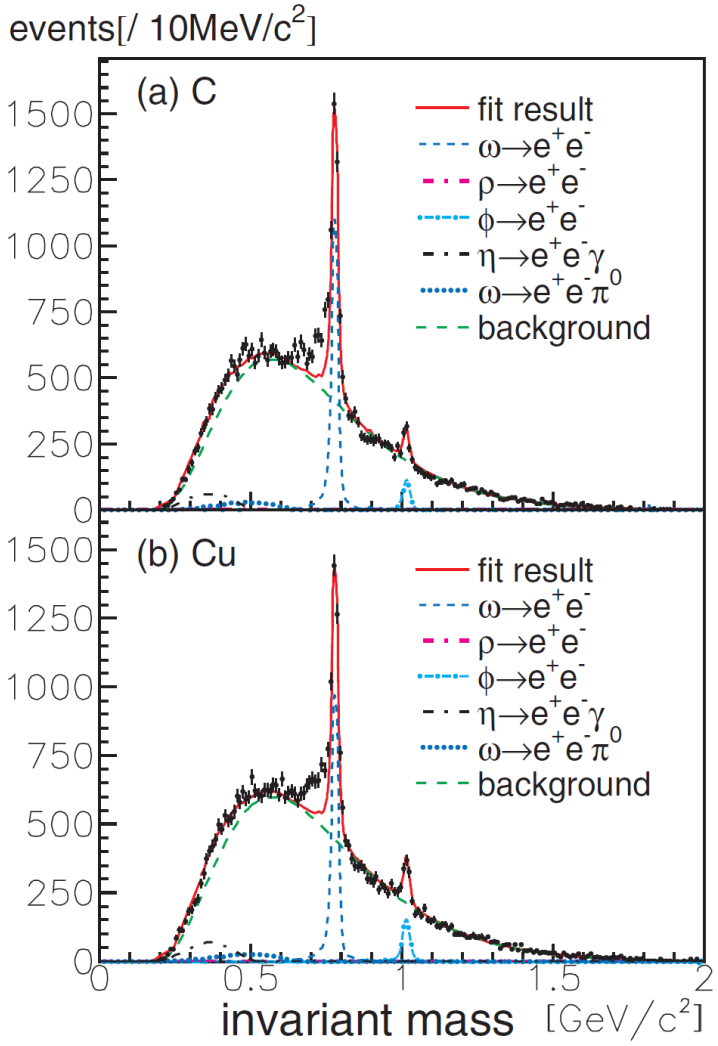

Figure 1.7: KEK experiment (E325): invariant-mass spectra of e^+e^- for C (upper most plot) and for Cu (lower most picture) targets plotted with the known hadronic sources and with the background. The picture has been taken from [26].

of 12 GeV. The data obtained with a Cu target shows a significant excess on the low-mass side of the ϕ meson peak in a certain p_T bin, with a parameter $k = 0.034$ and an increased width Γ_ϕ^{ee}[13]. This observation is consistent with the

[13]Since the ϕ meson lifetime is $\sim 46\ fm$ (much longer than the ρ meson $\sim 1.3\ fm$), its decay length is much bigger than the typical C or Cu nucleus size. Selecting these ϕ mesons

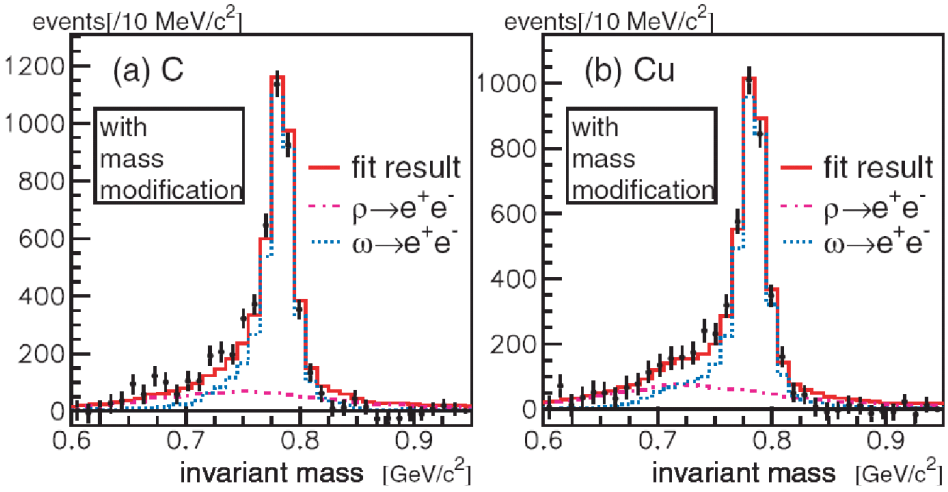

Figure 1.8: KEK experiment E325: e^+e^- invariant-mass spectra obtained with C and Cu targets with 12 GeV incident proton beam. The combinatorial background (obtained with mixed event technique) and the physical background given by $\eta \to e^+e^-\gamma$, $\omega \to e^+e^-\pi^0$ were subtracted. This results in the in-medium modification of $\rho \to e^+e^-$ and $\omega \to e^+e^-$ (a) and (b) plotted with the known hadronic sources and with the background. The $\omega \to e^+e^-$ (blue dotted line) and the $\rho \to e^+e^-$ (magenta dash-dotted line) are simulated adopting the formula $m(\rho)/m(0) \simeq 1 - k(\rho/\rho_0)$ with $k = 0.092$, given from the best data fit. The picture has been taken from [26].

picture of the ϕ modification in the nucleus.

1.4.2 The CLAS experiment

The CLAS experiment[14] observed dileptons in the final state, which were induced with a photon beam on various nuclear targets. Particular attention has been paid to the ρ meson spectral function in γ + A reactions on different targets (^2H, C, Fe and Ti). It was compared to liquid deuterium target, relatively free of nuclear effects [32]. An energy scan has been done in the range $0.6-3.8\ GeV$. In contrast to the KEK experiment, no significant ρ meson mass shift has been

which decay inside the nucleus is mandatory. The nuclear radius R can be approximated by the following formula $R = r_0 A^{1/3}$, where A is the mass number of the nucleus and $r_0 = 1.25\ fm$. Approximately $R_C = 2.6\ fm$ and $R_{Cu} = 4\ fm$.

[14]The experiment was conducted with the $CEBAF$ Large Acceptance Spectrometer (CLAS) at the Thomas Jefferson National Accelerator Facility.

observed ($k = 2 \pm 2\%$). However, broadening of the width of the ρ meson has been observed: with the ρ natural width being $\Gamma_0 = 149.4 \pm 1.0\ MeV$ [2], the measured one in Fe and Ti targets was $\Gamma_\rho = 217.7 \pm 14.5\ MeV$.

Fig. 1.9 has been taken from a recent publication [31], where the results shown in a previous publication [32] are described in great detail. Here two prominent peaks (ω mesons peak on top of the ρ meson one) are visible.

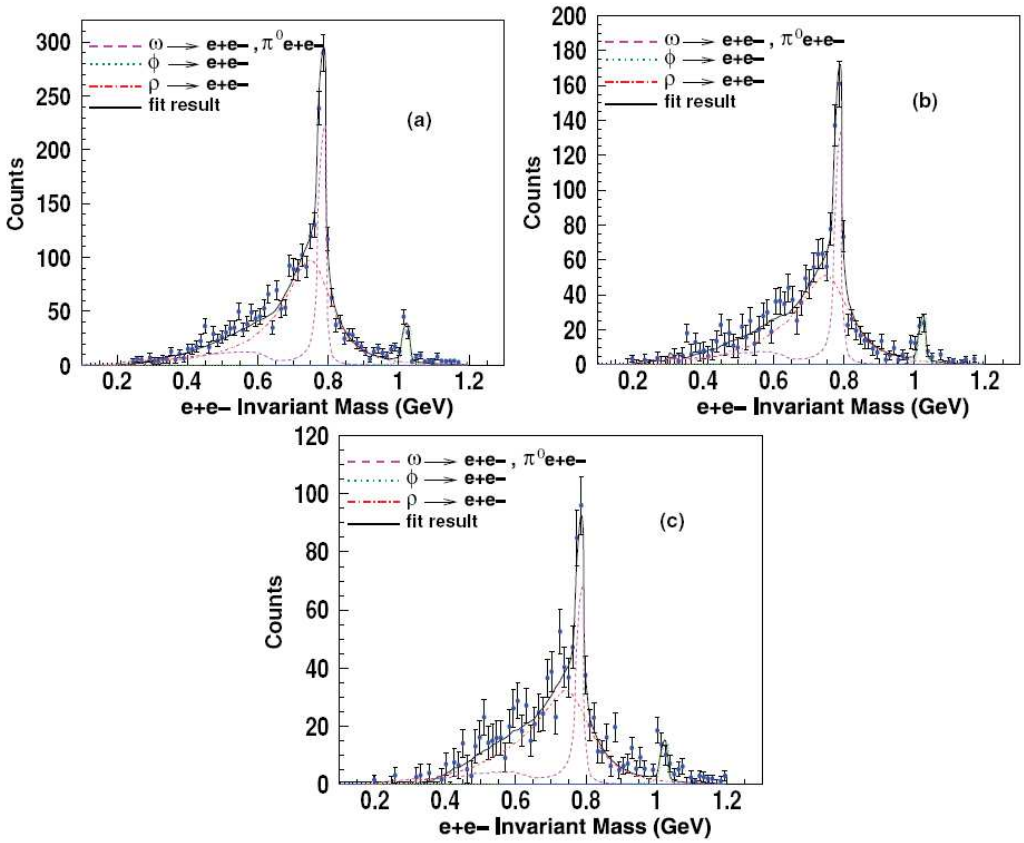

Figure 1.9: Fit of the e^+e^- invariant mass spectrum for ^2H (a), C (b) and $Fe-Ti$ (c) targets. The curves are the theoretical model employed for various vector meson decay channels. Data has been collected by the CLAS collaboration.

These results are hence in contrast with the one claimed by the KEK collaboration.

1.4.3 The CBELSA/TAPS experiment

Results similar to the one obtained by the KEK experiment have been reported by the $CBELSA/TAPS$ experiment. The ω meson has also been produced by γ on Nb and LH_2 targets, but identified through the $\pi^0\gamma$ decay channel [29]. The three γ rays produced were detected in an almost 4π photon detector (1290 Cs(Tl) and 580 BaF_2 modules). An advantage of this decay mode is the large BR of almost 9%, 3 orders of magnitude larger than the decay into dileptons. However, the disadvantage is a possible re-scattering of the π^0 within the nuclear medium, which would distort the deduced ω invariant-mass distribution.

The reconstructed ω peak is shown in Fig. 1.10 after subtraction of the combinatorial background. Only those ω mesons with low momentum contribute to the peak yield. A clear excess is visible in the low-mass side of the ω meson for the Nb case, while at high ω momenta no in medium effect is visible. In this second case the line shapes are identical for the Nb and LH_2 targets. The structure on the low mass side of the ω signal is attributed by the authors to in-medium decays of ω mesons of reduced mass [37].

The ω mass drops following $m(\rho)/m(0) \simeq 1 - k(\rho/\rho_0)$, with $k \simeq 0.16$. This result implies an in-medium drop of the ω mass by about 60 MeV, while the width is governed by the experimental resolution of $\Gamma_\omega = 55\ MeV/c^2$ (FWHM). As for the KEK experiment, the $CBELSA/TAPS$ results are sensitive to the background subtraction. The $CBELSA/TAPS$ results published in [29], claiming a a dropping ω meson mass could not be reproduced in a re-analysis of the data; rather a broadening of the ω meson has been observed in elementary nuclear reactions [30, 38], which is in line with a depletion of the ω yield at low momenta observed in ultra-relativistic heavy-ion reactions. This result is in conflict with the KEK result.

A lot of effort has already been invested but further measurements are needed to clarify the physics case. The HADES experiments aim at contributing to this understanding, thanks to its high electron pair acceptance and high momentum resolution. With an 85% azimuthal coverage over a polar angle interval from 18° to 85°, a single electron efficiency of 50% and a vector meson mass resolution of 2.5%, HADES is expected to give an important contribution to the understanding of the light vector meson. Equipped with much larger solid angle and improved resolution, HADES has the capability to complete the physics program which was pioneered by the DLS spectrometer at the BEVALAC [44, 46].

With high statistic runs, HADES will reconstruct dielectron invariant-mass spectra with high quality, enough to allow systematic studies as a function of centrality and electron pair momenta.

Dielectron production in elementary reactions at beam energies in the range

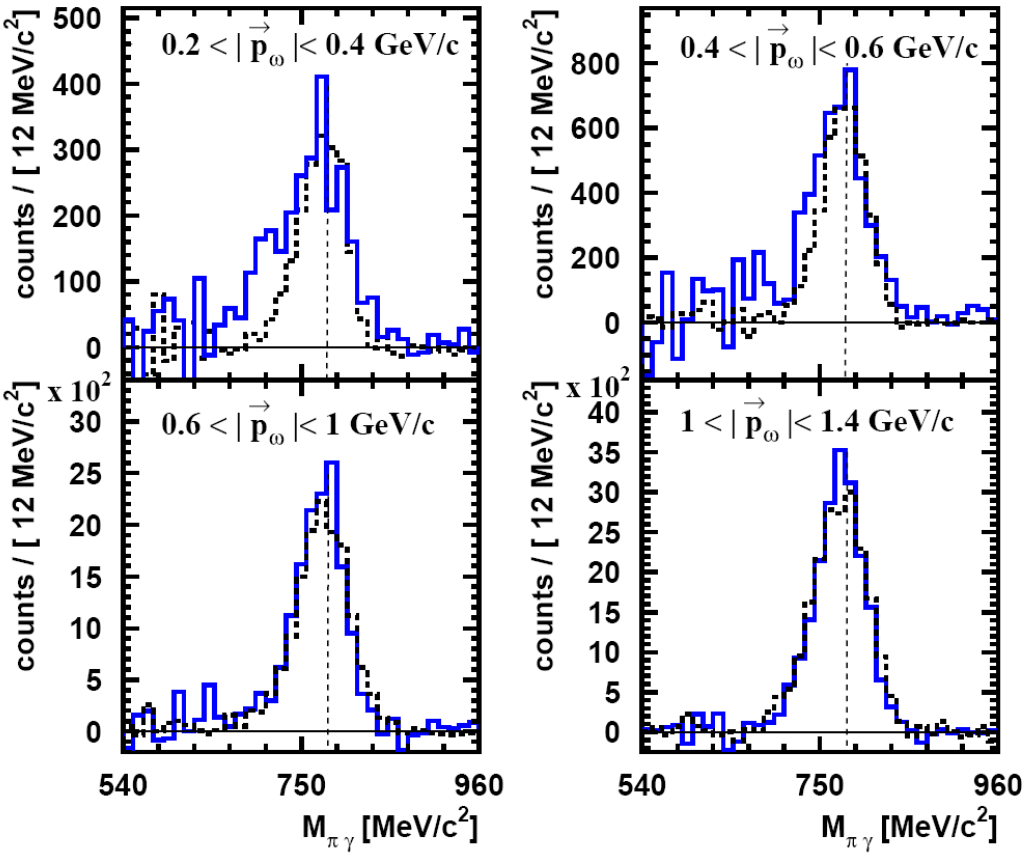

Figure 1.10: $\pi^0\gamma$ invariant-mass distributions after background subtraction measured for Nb target (solid histogram) and for LH_2 target (dashed histogram), for different ω momentum bins. The picture has been taken from [29].

1-5 GeV region are known only from inclusive measurements. A better understanding of the various processes, contributing to the dielectron production in heavy-ion collisions, is essential for a better control of in-medium effects on the dielectron production.

HADES already measured the vector meson decays in p + p reactions at $E = 3.5$ GeV, beam kinetic energy and the present thesis shows the analysis results of the inclusive and exclusive reactions: $pp \to Xe^+e^-$ and $pp \to ppe^+e^-$, respectively. From these spectra the production cross section for the ω meson has been computed in Sec. 3. The choice of this energy was made to optimize the vector meson production rate by balancing cross section and pair acceptance. The analysis of the omega in elementary p + p interactions provides a reference

	KEK-PS E325	**JLAB CLAS**	**CBELSA TAPS**
Reaction	$p + A$	$\gamma + A$	$\gamma + A$
Energy	12 GeV	$0.6 - 3.8$ GeV	$0.7 - 2.5$ GeV
Momentum	$p > 0.5$ GeV/c	$p > 0.8$ GeV/c	$p > 0$ GeV/c
Probe	$\rho, \omega, \phi \to e^+e^-$ $\phi \to e^+e^-$	$\rho, \omega, \phi \to e^+e^-$	$\omega \to \pi^0\gamma \to \gamma\gamma\gamma$
ρ	$\frac{\Delta_m}{m} = -9\%$ no broadening	$\frac{\Delta_m}{m} \simeq 0$ some broadening	
ω	$\frac{\Delta_m}{m} = -9\%$ no broadening		$\frac{\Delta_m}{m} = -14\%$ | $\frac{\Delta_m}{m} = ?$ $\frac{\Gamma(\rho_0)}{\Gamma} = 0$ | $\frac{\Gamma(\rho_0)}{\Gamma} \simeq 2.3$
ϕ	$\frac{\Delta_m}{m} = -3.4\%$ $\frac{\Gamma(\rho_0)}{\Gamma} = 3.6$		
Ref.	[25], [26], [27]	[28], [32], [31]	[29] | [30]

Table 1.3: Main experiments dedicated to the light vector mesons studies and their results.

for the line shape measurement in p + A and π + A reactions which ultimately aim at establishing medium effects of light vector-meson embedded in nuclei. This spectrum will be compared to the measurement of the p + Nb reaction at 3.5 GeV which is currently being analyzed.

It is important to remember that the HADES program focuses on vector mesons decaying via electromagnetic probes. These channels are not subject to strong final state interaction and thus provide an undistorted signal of the matter phase. The goal of the HADES experiments is to measure the spectral properties of the vector mesons such as their in-medium masses and widths with high precision, in order to identify, even small, in-medium effects.

1.4.4 Summary of the Vector Meson Experiments Presented

A list of recent results is given in Table 1.3. It includes measurements of light vector mesons through their e^+e^- decay channel which allow clean spectroscopic studies not distorted by final state interactions and a measurement where the vector mesons are identified through their hadronic decay modes. The table lists the reactions, the beam kinetic energies, the momentum ranges and results for the light vector mesons obtained in the reviewed experiments. A full understanding is not yet obvious: for the ρ meson, KEK observed a mass shift, while this is not the case for the CLAS experiment. A broadening of the ω meson has been observed in elementary nuclear reactions but it is again in conflict with the KEK-E325 result.

For the ϕ meson an in-medium mass shift and a broadening has been reported by KEK.

It should be remembered that all detectors have different acceptances. This is particularly important when comparing properties of low momenta mesons. Just for these low momenta particles the strongest medium modifications are expected and some detectors might have small or no acceptance at low momenta.

To clarify the situation further experiments are needed. Corresponding experiments are planned at GSI: HADES and CBM[15] at FAIR[16], and PHENIX[17] at RHIC[18].

1.4.5 The DLS Experiment: Pioneering Dilepton Measurements in p+p and p+d Interactions

The DLS (Di-Lepton Spectrometer) experiment was operational at Lawrence Berkeley National Laboratory Bevatron between 1986 and 1993. It has been designed and constructed to investigate the production of e^+e^- pairs with low invariant-mass in p + A, N+N and A+A collisions for incident-beam kinetic energies less than 5 $AGeV$. At that time, all transport models failed to reproduce the DLS data for heavy-ion collisions. The measured dilepton yields showed a strong excess over predictions of all transport models in the invariant-mass region 0.3 - 0.6 GeV [47, 48]. Similar disagreement was experienced by the CERES experiment [41]. The reason was due to some unknown dilepton sources which were not treated properly. For this reason the HADES collaboration has intended to repeat some of the DLS measurements with improved mass

[15]The Compressed Baryonic Matter (CBM).
[16]International Facility for Antiproton and Ion Research (FAIR).
[17]Pioneering High Energy Nuclear Interaction eXperiment (PHENIX).
[18]Relativistic Heavy Ion Collider (RHIC).

resolution. Recent papers published by the HADES collaboration corroborate the DSL data [17, 18, 19] and theory models have been developed to reproduce both data sets.

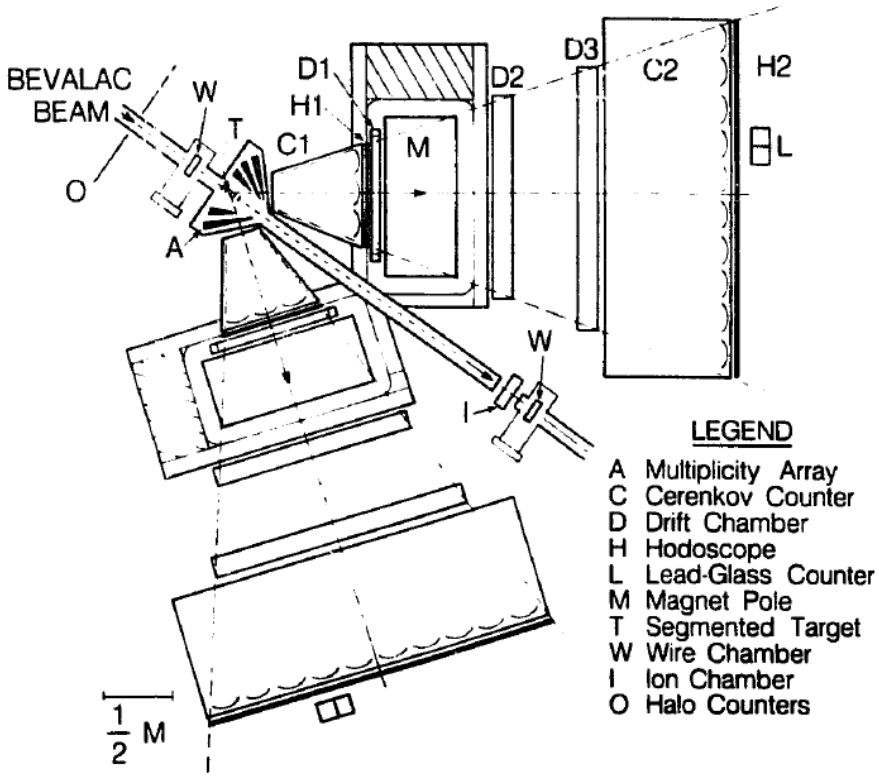

Figure 1.11: Layout of the DLS detector, top view. The picture has been adapted from [45].

Fig. 1.11 shows a top view of the DLS system. It was designed as a magnetic spectrometer combining two identical detector-arms. Each arm of the spectrometer was equipped with a large dipole magnet, a pair of segmented gas Cherenkov arrays, two hodoscopes, three drift chambers and a movable array of lead-glass blocks [45]. A segmented target was contained in a specially designed scattering chamber. Multiwire proportional chambers were used to monitor the beam alignment and a calibrated ionization chamber measures the beam intensity. Halo counters upstream of the target gave further information on the beam profile. An exhaustive description of the apparatus can be found in [45].

1.4.5.1 DLS Results in Elementary Reactions

Important measurements of dielectron production in p + p and p + d collisions with beam kinetic energies from 1.04 GeV to 4.88 GeV have been done by DLS in the late 80's and early 90's. Proton beams were provided by the Bevatron accelerator with kinetic energies equal to 1.04, 1.27, 1.61, 1.85, 2.09, and 4.88 GeV.

The results of these experiments are reported in Fig. 1.12: for six different beam energies the invariant-mass spectra are plotted. The combinatorial background has been subtracted and the resulting spectra have been corrected by detector acceptance and normalized by elastic scattering cross section.

The shape of these invariant-mass spectra changes dramatically as the beam energy is increased. In the first energy bin (1.04 GeV), the p + d cross section has a different mass dependence and it is nearly an order of magnitude greater than the p + p cross section. As the beam energy increases, the shape difference disappears and the p + d cross section becomes approximately twice the p + p cross section at all masses [44].

However, for invariant-mass values $> 0.8\ GeV/c^2$, the mass resolution of the DLS spectrometer is still not sufficient to distinguish between the contributions of the ρ and ω mesons [44] and to drive conclusions on the line shape of the ω meson.

Recently HADES measured the same system, p + p and d + p at a similar incident proton kinetic energy of 1.25 GeV/u. These results confirm remarkably well the DSL data presented in [44]. For the first time, the electron production was reconstructed for the n + p reaction by detecting the proton spectator from the deuteron breakup, using a forward wall detector [43]. HADES data has been compared with recent model calculations in which the production mechanism is not sufficiently well described. Since the invariant-mass spectrum measured in ^{12}C+^{12}C reactions with HADES can be explained by a superposition of elementary n + p and p + p collisions, it is unlikely that a unknown dilepton source contributes to the lepton emission in such light collision systems.

Since fundamental dielectron production is not yet well characterized at low energies, all these measurements are interesting in their own right, in addition to their importance in the interpretation of the heavy-ion studies.

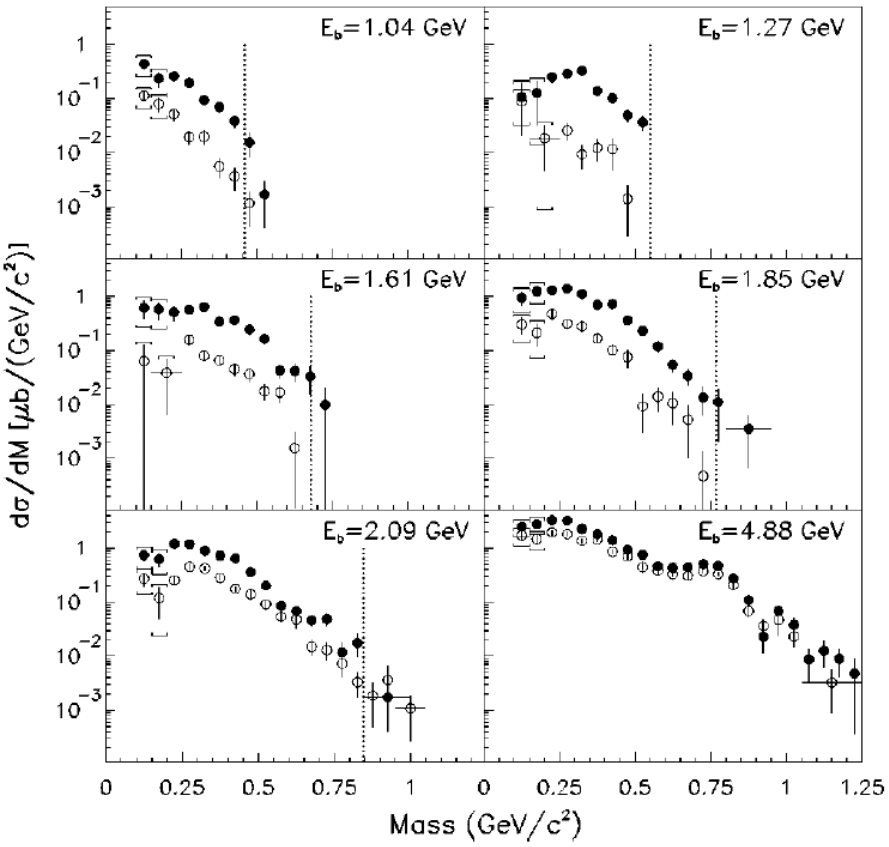

Figure 1.12: Acceptance-corrected invariant-mass spectra for the p + d (filled circles) and p + p (open circles) systems. The error bars are merely statistical. The brackets above and below the low mass data points indicate systematic uncertainties in the shape of the spectra. The dashed lines indicate the kinematical upper limit on the invariant-mass spectra in the p + p system. The bin width adopted is 50 MeV/c^2. Some of the data points have been re-binned to take the sparse statistics into account. Horizontal bars indicate the bins with enlarged widths [44].

1.5 Overview of the Present Work

This work is devoted to the study of dilepton production in p + p collisions at 3.5 GeV beam kinetic energy, using the HADES spectrometer.

The inclusive dilepton spectra presented in this work are an important bench mark for the investigation of in-medium vector meson properties in A+A colli-

sions. The spectrometer performance and lepton analysis strategy are presented as well.

This thesis is divided into the following chapters:

- The current chapter introduces the physics case and gives an overview of published related experimental results.
- The second chapter describes the HADES spectrometer and the detector performances.
- In the third chapter the dielectron analysis strategy is presented in detail. Special attention is given to the reconstruction of the dilepton pair spectra (inclusive and exclusive e^+e^- production).
- In the fourth chapter, measurement of the inclusive ω production cross section is presented. The determination of the ω production cross section is particularly important, since no data at SIS energies are available. A comparison to the ω production cross section, obtained in the exclusive dilepton channel is presented and compared with theoretical predictions.
- The fifth chapter is dedicated to the HADES upgrade. In particular the HADES Data Acquisition system (DAQ) upgrade. The upgrade of the data acquisition is currently undergoing a rebuilt of the data readout system. In order to take data in the planned measurement with heavy systems, like Au+Au up to energies of 8 $AGeV$, with a sustained trigger rate of 20 kHz and up to a factor two faster for lighter collisions systems, this upgrade is mandatory.

  This chapter focuses particularly on the upgrade of the Multi-Wire Drift Chamber (MDC) electronics started in 2006. It explores the effort done in order to improve the DAQ of the whole MDC system which consists in more than 450 hardware boards. This electronics has been designed and equipped with freely configurable FPGAs for high bandwidth data transport and easy remote software control. This chapter presents my contribution to this successful project during three years of my stay at GSI.

Chapter 2

The HADES Detector System

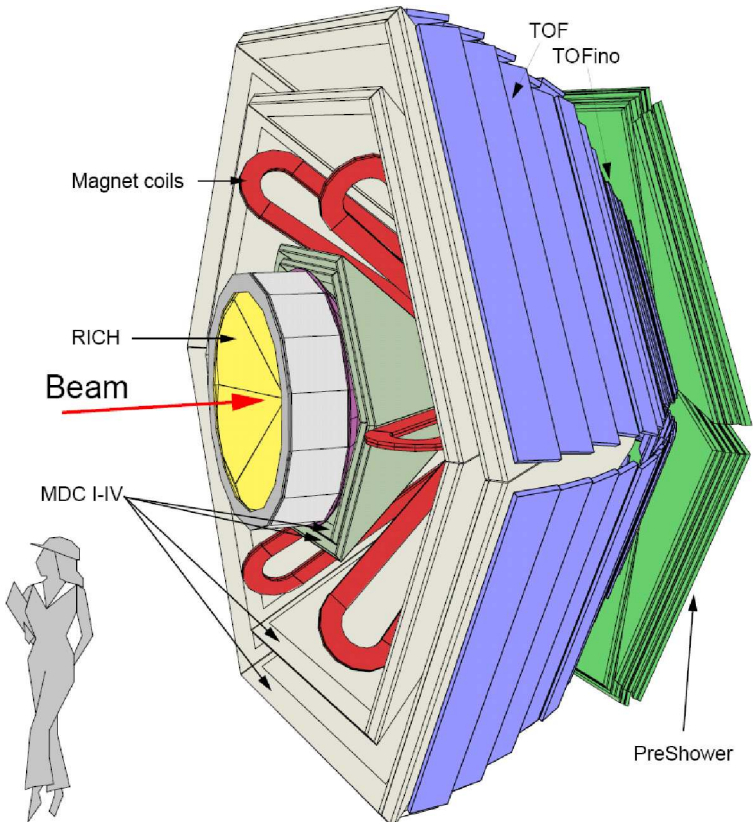

Figure 2.1: The HADES spectrometer in a 3D view.

The HADES (High Acceptance Di-Electron Spectrometer) experiment, in Fig. 2.1, is a fixed target experiment installed at the heavy-ion synchrotron

SIS-18 at GSI[1]. It was designed for the identification and invariant-mass reconstruction of electron-positron pairs (e^+e^-). The main emphasis is the study of leptonic (e^+e^-) decays of light vector mesons in elementary and in heavy-ion collisions. These decays are suppressed by a factor $\sim 10^{-5}$ compared to hadronic decay channels, thus in order to accumulate significant statistics in a reasonable amount of time, HADES has to fulfill several conditions [87]:

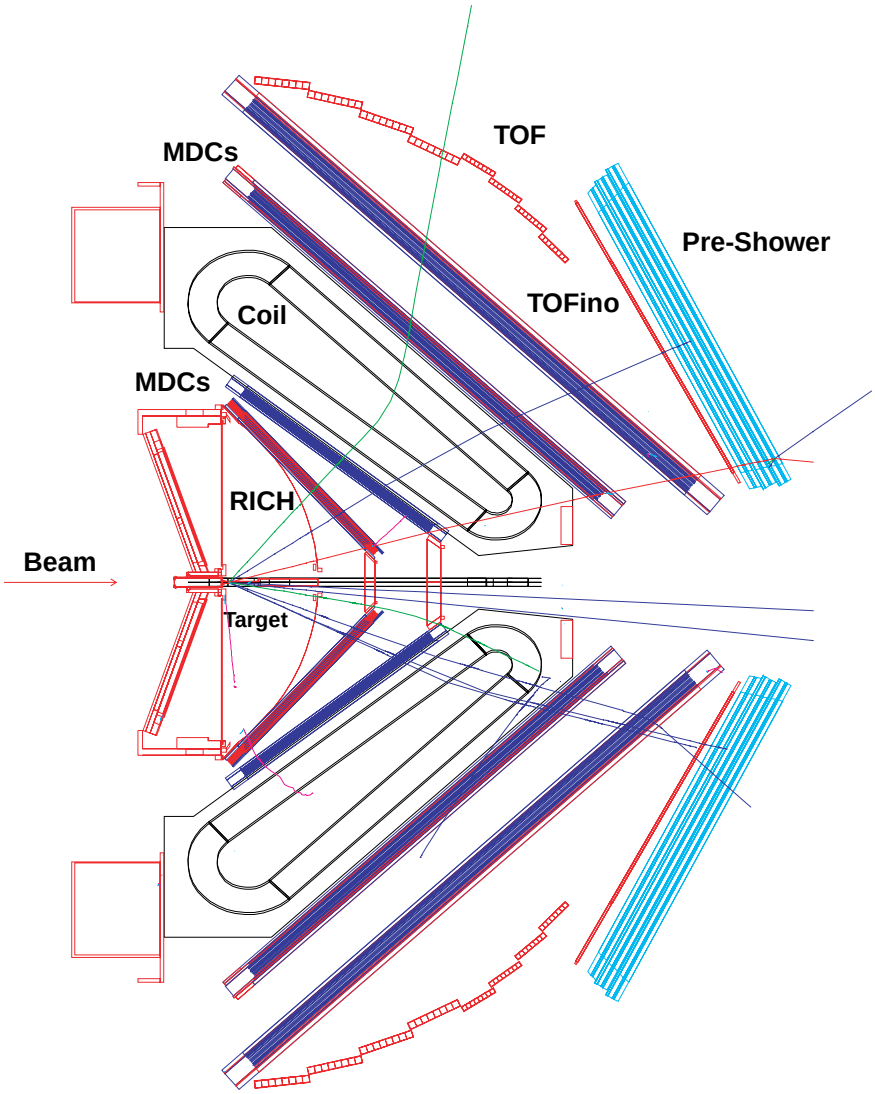

Figure 2.2: Side view of the HADES setup.

[1]Helmholtzzentrum für Schwerionenforschung in Darmstadt, Germany.

- Large geometrical acceptance: to achieve good pair detection probability.

- High rate capabilities: due to the rarity of the interesting channels, the beam intensity is 10^8 particles/s.

- Trigger system: a trigger hierarchy scheme is required to find and combine the electron signatures in the various sub-detectors and to reduce the huge background created mainly by γ conversion in the detector's material or in the target.

- High granularity: in order to deal with high particles multiplicities expected in heavy-ion collision systems.

- High lepton invariant-mass resolution: in order to detect the modification of experimentally observable properties of vector mesons such as mass and width, when embedded in a dense medium. An invariant-mass resolution for dileptons of 2-3% in the ρ and ω meson mass range is required to distinguish possible in-medium effects.

In order to fulfill the above requirements, the HADES spectrometer has several different specialized detectors.

The spectrometer, in Fig. 2.2, is characterized by a six-fold azimuthal geometry. The polar acceptance covers from 15° to 85°, while including almost the full azimuthal acceptance [87, 91, 92]. The HADES detector is divided into sub-detectors. Moving from the target to the direction of a typical particle trajectory, the detector consists of:

- Ring Imaging Cherenkov (RICH) detector.

- Two inner planes of Multi-wire Drift Chambers (MDCs).

- Toroidal magnetic field generated by six superconducting coils.

- Two outer planes of MDCs.

- Multiplicity Electron Trigger Array (META); it consists of two Time-of-Flight walls (TOF/TOFino), the first with high granularity and the second with low granularity and the Pre-Shower detector, which is placed behind the TOFino at small polar angles.

2.1 Beams and Targets

The HADES physics program requires the use of different beams and targets. The beam is obtained selecting an appropriate source and accelerating it to defined kinetic energies.

The GSI accelerator system consists of four structures: a linear accelerator (UNILAC) injecting ions into a 60 m diameter Synchrotron (SIS). From there, the beam can be extracted to the Fragment Separator (FRS) to the Electron Storage Rings (ESR) or to the experimental areas.

The target can be either composed of thin foils or a liquid element in an appropriate vessel. In the heavy ion experiments foils were used as target: a single graphite foil, 5 mm thick, 2.15 g/cm^3 dense with an interaction length of 5% was used, for example, in November 2002 for the C+C runs, at 1-2 $AGeV$ incident kinetic energies.

Figure 2.3: LH_2 target used to study elementary processes. The picture has been taken from [87].

For elementary interactions a liquid hydrogen (LH_2) target was used. It has been developed at IPN[2] (see Fig. 2.3). The liquid hydrogen is contained inside a cylindrical vessel (inner-vessel), 5 cm long with a diameter of 2.50 cm, covered by an aluminized Mylar foil (6 μm thick). An outer-vessel provides low interaction probabilities due to its low atomic number (Z) and provides

[2]Institut de Physique Nucleaire (IPN) d'Orsay.

thermal isolation to the inner-vessel, which operates at a temperature of 20 K at atmospheric pressure. The forward end cap of this cylindrical carbon fiber cylinder is also made out of a 100 μm thick Mylar foil. The system operates in vacuum. The interaction probability between beam and with the window material is of the order of $\approx 0.05\%$ while the probability of interaction with the LH_2 is around 0.7% [87]. The cooling down from room temperature takes 12 hours. The cryogenic operation is controlled by a dedicated software interface.

2.2 START and Proton-Beam Detector

With heavy-ion beams, in order to select reactions which occur inside the target, START and VETO detectors, based on poli-crystalline Chemical Vapor Deposition (CVD) diamond strip counters, are placed 75 cm upstream and downstream of the target position. They provide the start signal for the time-of-flight measurement between target and the Time of Flight (TOF) detectors. In addition the VETO detector is used to reject all particles which do not react with the target. With proton beams, this kind of detector can not be used since the energy deposited by the proton beam is below the detector-threshold.

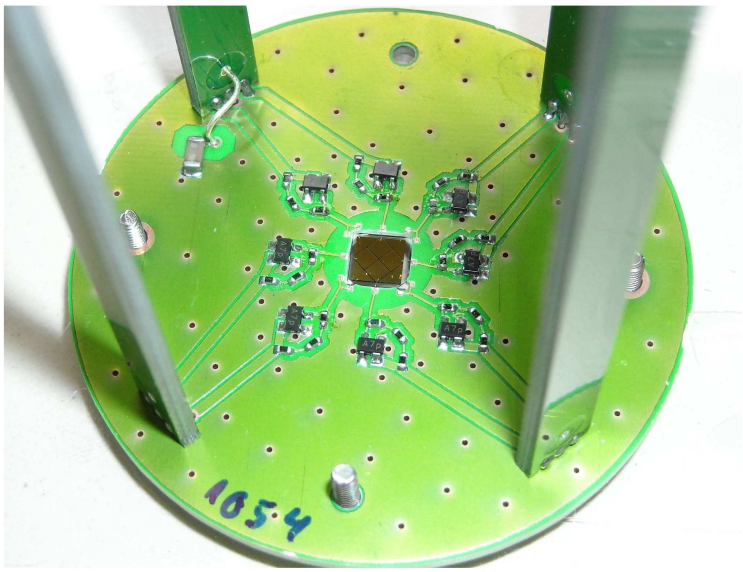

Figure 2.4: CVD mono-crystalline diamond START detector mounted on a Printed Circuit Board (PCB)(with thickness ϕ = 50 mm) with the diamond (4.7×4.7 mm^2) in the center. The diamond detectors are surrounded by 8 amplifiers [86].

For high intensity proton beams, a new radiation hard diamond detector (mono-crystalline CVD detector) has been developed: it is used as beam monitor detector or as START detector. Fig. 2.4 shows in the center mono-crystalline diamonds with two different detector sizes of 3.5×3.5 mm^2 (4 segments) and 4.7×4.7 mm^2 (8 segments) with thickness of 300 μm and 500 μm, respectively. The detectors are mounted on a thin Printed Circuit Board (PCB) with thickness of 50 mm. High sensitive operational amplifiers are closely attached to the diamond sensor [86].

2.3 The Ring Imaging Cherenkov (RICH) detector

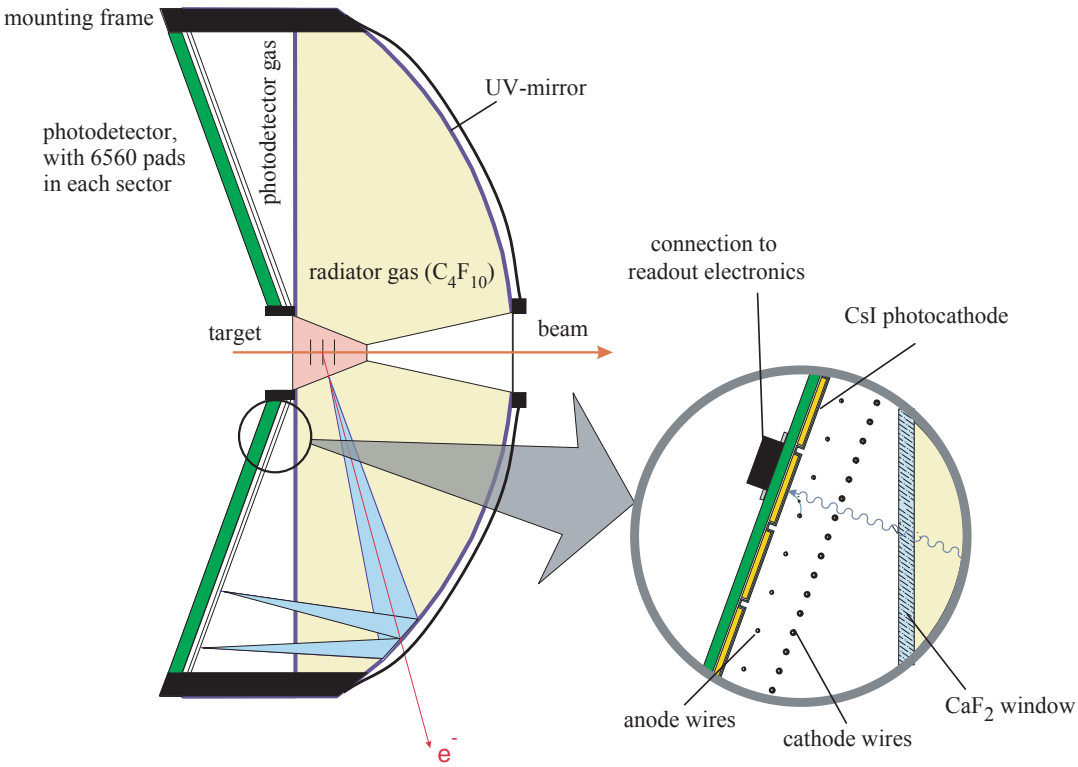

Figure 2.5: Setup of the HADES RICH detector [96].

The Ring Imaging Cherenkov detector (RICH), in Fig. 2.5, is the innermost detector and surrounds the target region. It has been designed to identify electrons and positrons with momenta in the range 0.1 $GeV/c <$ p $< 1.5\ GeV/c$. It covers the polar angle between 18° and 85° and the full azimuthal angle [94].

When a charged particle passes through a medium with refraction index n, and its velocity β is larger than the speed of light in the medium (c/n), then Cherenkov light is emitted at a constant opening angle of ϑ_c with respect to the particle trajectory:

$$\vartheta_c = \arccos \frac{1}{\beta n} \tag{2.1}$$

where β is the velocity of the particle. Hence, the particle is identified if $\beta \geq \frac{c}{n}$.

$$\gamma_{thr} = \frac{1}{\sqrt{1-\beta_{thr}^2}} = \frac{1}{\sqrt{1-(\frac{1}{n})^2}}. \tag{2.2}$$

The radiator gas (C_4F_{10}) has a refraction index of $n = 1.00151$, which corresponds to a threshold of $\gamma_{thr} \approx 18.3$. Therefore, only particles with velocity $\beta > 0.9985$ produce Cherenkov light, ensuring the hadron blindness of the detector. The minimum particle energies needed to emit Cherenkov light are $E_{thr}^p \simeq 17.8\ GeV$ for protons, $E_{thr}^\pi \simeq 2.6\ GeV$ for pions and for electron $E_{thr}^e \simeq 9.3\ MeV$, which is quite below the energy of interest. Hence, only electrons can be detected in the energy of interest of the HADES physics. Electrons and positrons have a β value close to 1, and the light cone is generated along their track in the radiator. At the energies available with the SIS accelerator, the hadrons reach a γ_{max} of about 10. The estimated γ_{thr} implies the hadron blindness of the detector.

The produced Cherenkov light cone is reflected by a spherical carbon fiber mirror [95] to a Photon Detector, which is separated by a 5 $mm\ CaF_2$ window from the radiator volume. The window should endure the pressure difference between the two gases and should have a high transparency in the Vacuum Ultra Violet (VUV) range.

The photon detector, in Fig. 2.6 is made of Multi Wire Proportional Chambers (MWPC) with a CsI segmented photocathode (cathodic plane), filled with CH_4 gas. When a Cherenkov photon reaches the photocathode, electrons are emitted by photoelectric effect (photo-electrons). The emitted photo-electrons drift from the cathodic pad-plane to the anodic wires and generate avalanches. The produced ions drift back to the cathodic plane and induce a mirror charge on the cathode. Each pad is connected to a pre-amplifier that registers the pulse height of the charge de-

posited on it. The amount of charge depends on the total charge produced in the avalanche and on the multiplicity of pads that have been fired. The photon-detector has to provide a sufficient position resolution and multi hit capability to allow ring identification. Depending on the path length of the particle in the gas radiator, the number of photons emitted by each particle varies. In the RICH detector this length varies from 38 to 68 *cm* depending on the polar angle of the track. A more detailed description of the RICH detector can be found in [87].

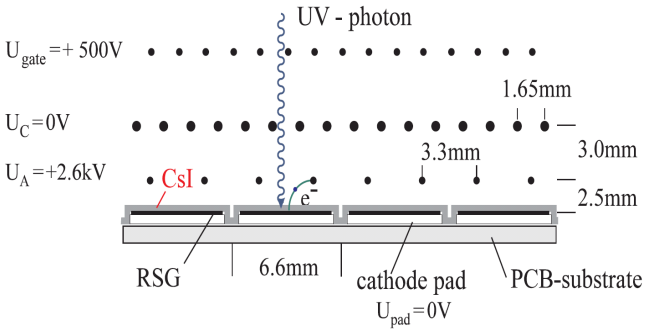

Figure 2.6: Schematic view of the RICH padplane [96].

2.4 The Multi-wire Drift Chambers

The invention of the Multi Wire Proportional chamber (MWPC) was one of the milestones in the history of particle detectors (Bouclier et al. 1974, Charpak 1978 and Sauli 1978).

When a charged particle passes through a gas, it interacts electromagnetically with the atomic electrons of the gas. This results in a creation of electron/ion pairs along the particle's track. The number of such primary pairs created depends on the energy loss of the particle, consequently on the gas type and its pressure.

If an electric field is applied, the electrons will drift towards the positive electrode (anode), undergo repeated collisions with the gas molecules. If the electric field near the anode is strong enough, an electron can acquire energy to knock additional electrons from the gas molecules. In this way an avalanche is formed in which the number of electrons increases exponentially. When this avalanche is close to the anode wire, it gives rise to a measurable fast electrical signal[3]. The amplitude of this signal is proportional to the original number of ions created.

The electrons drift with a constant velocity over most of the distance to the anode. Hence, one can measure the time which the electrons need to drift to the

[3]It is a negative analog signal of few hundreds mV. In general this signal presents a tail which is produced by slower charges.

anode and convert it into a distance between the original source particle track (distance of closest approach) and the anode wire. In general, this detector is called drift chamber and is commonly used to provide an accurate measurement of the position of a charge particle passing through it.

Stacking several layers of drift chambers allows to resolve the track left by the particle by interpolating the point identified by the chambers.

In HADES the dielectron decay channel defines the decisive design and performance constraints on the Multi-wire Drift Chambers (MDCs). They consist of 24 trapezoidal planar MDCs, symmetrically arranged in six identical sectors. They provide a polar angle coverage between 18° and 85° around the beam axis, forming four tracking planes (I-IV) of increasing size. In each sector, two modules (planes I and II) are located in front of and two (planes III and IV) behind the toroidal magnetic field, in order to determine the direction of the particle track before and after the deflection in the magnetic field and thus the momentum, as shown in Fig. 2.7. The chambers provide active areas from 0.35 m^2 up to 3.2 m^2 and cover the same solid angle per sector.

The main feature of the design and the operation parameters of the chambers is the implementation of the low-mass concept and the position of the active detector area between the six coils of the magnet. These requirements are met by: (i) cathode and field wires made of annealed aluminum (planes I-III: bare, IV: Gold-plated) with 80 μm and 100 μm diameter, (ii) a Helium-based counting gas (Helium:Isobutane = 60:40) and (iii) entrance windows made of 12 μm aluminized Mylar [87].

The MDCs [89, 90, 119] are used for the tracking of charged particles and the determination of their momenta, which depend upon their deflection in the magnetic field.

To cope with ambiguities[4] (left and right ambiguities), in the track reconstruction in a high multiplicity environment of a heavy ion reaction, all chambers are composed of six sense/field wire layers oriented in five different stereo angles, ±0°, ±20°, ±40°. This is sketched in Fig. 2.8.

The essential information which the HADES spectrometer delivers is the invariant mass of dilepton pairs. The tracking system has been optimized for high electron momentum resolution [97]. In order to resolve the various vector mesons, a dilepton invariant-mass resolution of the order of the natural meson's width is required (*e.g.* $\delta M_\omega / M_\omega = 2 - 3$ %). It corresponds to a single particle momentum resolution of $\delta p/p = 1.5$ %.

The field and cathode wires are made of bare aluminum, with diameters of 100 μm and 80 μm, respectively. The sense wires are made of gold plated tungsten with a diameter of 20 μm. All four chamber types contain about 1100

[4]Here it is meant "ambiguity" in the reconstruction of space points from fired wires.

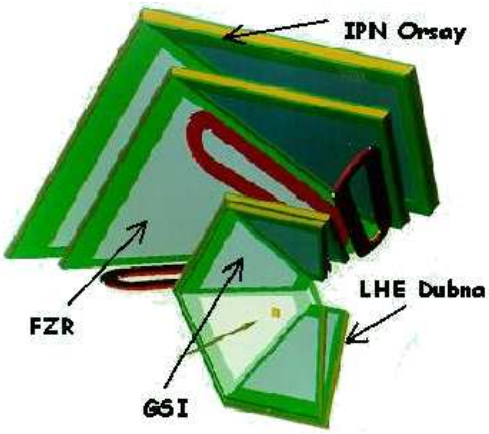

Figure 2.7: Schematic view of the position of the four MDC modules respect the magnet coils. The name of the laboratory where the chambers were produced are indicated.

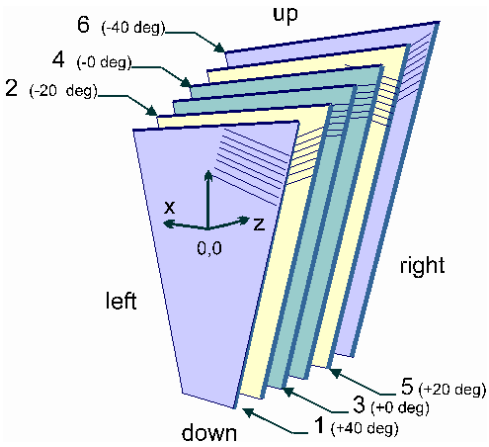

Figure 2.8: Arrangements of the sense wires in different layers in one MDC module. The layers are oriented with $\pm 0°$, $\pm 20°$ and $\pm 40°$ with respect to the symmetry axis of the module.

drift cells each, with increasing size, from 5×5 mm^2 (plane I) to 14×10 mm^2 (plane IV), in order to maintain the granularity and, therefore, the double hit resolution in the four detector planes, per solid angle.

The chambers are filled with a Helium-Isobutane mixture. Since multiple scattering is dominant at low dilepton invariant-mass ($< 0.4\ GeV/c^2$), the use of a mixture of Helium as counting gas is mandatory to keep the contribution of the multiple scattering at tolerable level. This is done because its radiation length is almost 50 times longer than for Argon gas. The lack of total primary ionization of Helium is compensated by using Isobutane as quencher. Several different concentrations of Isobutane in Helium have been tested [87, 89]. From these investigations, it was concluded that the mixture containing 30-40% of Isobutane is the optimal choice for HADES. This mixture provides enough primary ionization statistics under stable operation at moderate gains. In addition, the electric field is high enough to saturate the drift velocity at about 4.3 $cm/\mu s$, over practically the entire drift path [89].

Fig. 2.9 exhibits a particle passing through a drift cell. It ionizes the counting gas. The ionization is statistically distributed along the track. Electron clouds drift towards the sense wires and trigger the signal picked up by a fast amplifier connected to the wire. The signal, which is picked up by the analog electronic, starts a time measurement. The stop-signal is deduced from an external detector, *i.e.* a delayed trigger of the START or META detector. The

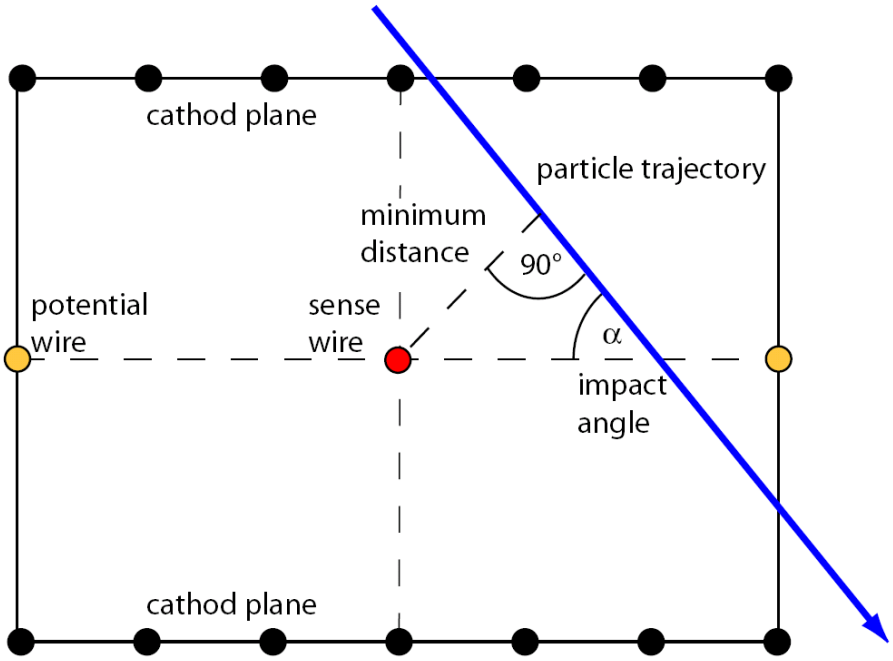

Figure 2.9: Schematic view of one MDC drift cell. It is geometrically defined by cathode wires and potential wires in the middle of the cell. In the picture, it is shown the parametrization of the track: the minimum distance to the sense wire and impact angle α. The total number of drift cells for all MDCs is approximately 27,000.

resulting arrival time of the electrons, after time offset subtraction and calibration of the TDC slope, is converted into a distance from the sense wire to the point of closest approach of the trajectory.

In order to achieve a mass resolution better than 2-3% in ω and ρ mass regions, the drift cells have to provide an intrinsic position resolution of better than 150 μm [89].

The drift chamber signals are read-out and digitized by dedicated and customized boards, which are mounted on the chamber frames, not extending into the active area [90].

In this work, particular attention is payed to the MDC data acquisition. In the next section, Sec. 2.4.1, the MDC data acquisition is presented as it was used up to the year 2009, while in Sec. 5 the upgrade of this electronics is explained in detail.

2.4.1 The Multi-wire Drift Chambers (MDC) Data Acquisition

In this section, the MDC readout concept is explained. It is based mainly on the following components:

- Front end Electronics (FEE): motherboards and daughterboards.
- VME-boards as main DAQ boards.
- Parallel copper buses for data transport between FEE and VME-boards.

This readout has been used successfully for several HADES experiments, between years 2000 to 2008.

In order to increase high data-readout rate and to improve the data quality, a new digital readout has been designed and developed. In order to eliminate the crosstalk between the copper cables and the input of the very sensitive FEE amplifiers, the upgrade of the electronics is based on high speed optical links for data transport and fast programmable devices. This innovative readout is presented in detail in Sec. 5.

Part of the MDC readout electronic is mounted on the drift chambers frames: Flexible Printed Cables (FPCs), connected to the anode wires, transport the analog signals to the Front End Electronic (FEE): 4 or 6 daughterboards equipped with the 8-channel ASD8 (Amplifier Shaper Discriminator) [120] chips are mounted on the front end daughterboard. The ASD8 chip amplifies, shapes and discriminates the analog signal produced by the detector.

Each channel of the ASD8 chip is connected to one Time To Digital Converter (TDC[5]) channel. Short motherboards (equipped with 8 TDCs [121]) with a total number of 64 channels, and long motherboards (equipped with 12 TDCs) with a total number of 96 channels are the basic constituents of the MDC FEE. The TDCs are self triggered: they continuously perform a measurement whenever the start signal is given by the TDC input and the stop signal is delivered by an external timing signal called Common Stop Signal (CMS). The time measurement of all channels is stopped simultaneously through the CMS, which has a fixed correlation with the instant of the reaction. The CMS must reach the TDCs within a predefined time range of 1 μs. If the signal is not delivered by the trigger detector within this fixed time, the TDC will be resetted and ready for a new measurement.

Digitized data is transmitted to VME-based Read-Out Controllers (ROC) via parallel bus, realized with flat copper cables. Each bit is transmitted as a

[5] A TDC is an chip, which converts pulses into a digital representation of their time indices. In other words, a TDC measures the time between a start and a stop pulses. Many experiments require a TDC to have a resolution well below 1 ns.

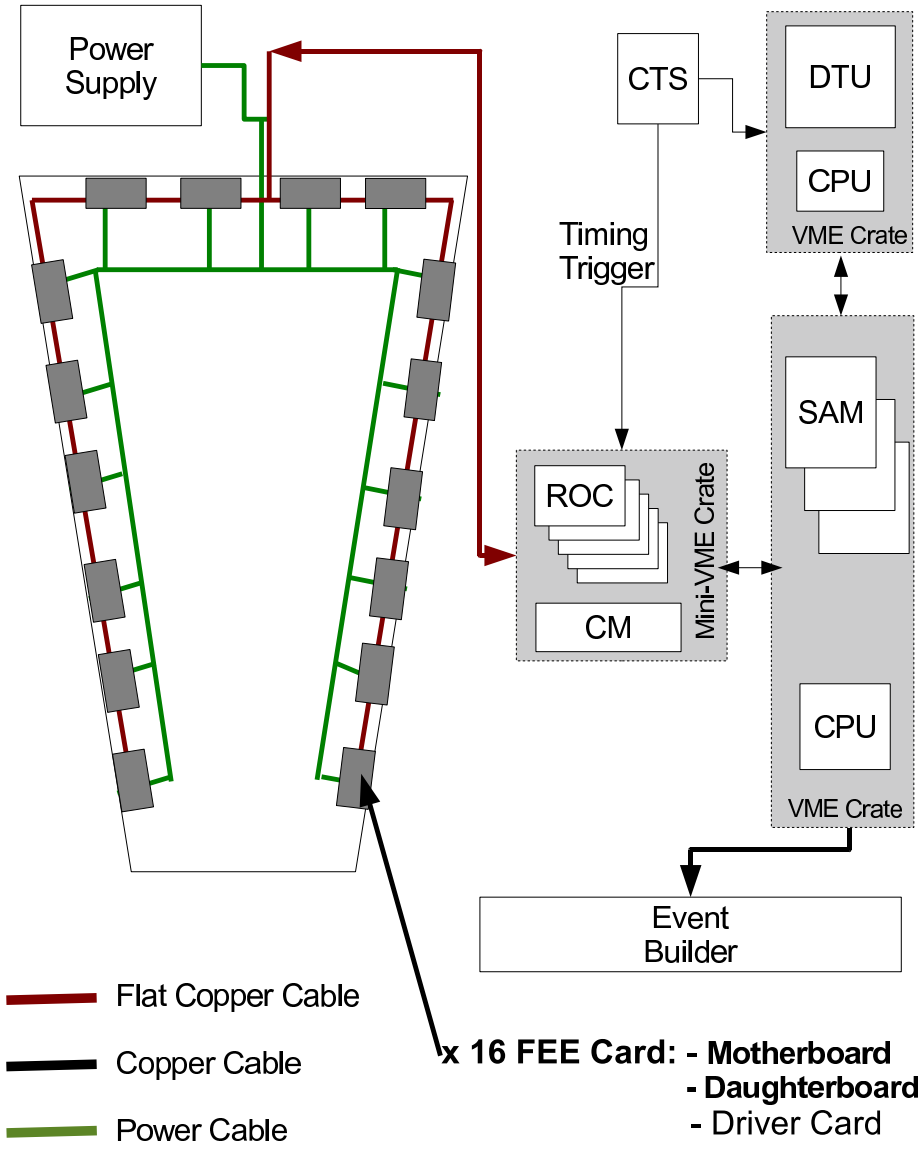

Figure 2.10: The data acquisition scheme of the drift chambers used up to 2009. Analog information is digitized on the daughter/motherboards mounted onto the MDC-chamber, and raw data is transmitted via a pluggable PCB Driver Card (DC). Then the data is received by the ROCs and forwarded via the concentrators to the SAM and finally to a VME-CPU.

differential signal. The signal conversion (to differential signals) is done by so-called Driver Cards (DCs). Each DC is a small hardware board which is plugged on the motherboard and equipped with two differential Transistor Transistor

Logic (TTL) transceivers. In the ROC data is first buffered and then transmitted to the VME-based SAM (Steuerungs- und Auslesemodul) module passing through the Concentrator Module (CM).

The CM is the hardware interface between the ROC modules and SAM. The SAM builds sub-events gathering all information of one chamber, using the information provided by the TDCs and sends them to the central event-builder of the data acquisition. The event-builder builds events from the information provided by all sub-detector systems. A schematic view of the readout concept is depicted in Fig. 2.10.

In the present work, in Chapter 5.3, the upgrade of the present digital electronic readout system, will be presented. The hardware modules shown in Fig. 2.10: DC, ROC, CM and SAM modules will be replaced with new multipurpose hardware boards: the Optical End Point Boards (OEPBs). One OEPB logic has large resources, which allows for the storage of several events close-to-front-end. With this new hardware concept, two MDC chambers can be read out in parallel at high speed through optical fibers, improving the readout bandwidth. The electrical signals which transport data from the FEE downstream to the Event Builder will be reduced; this will reduce the electrical noise which is induced by fast electrical signals running on long copper cables around the detectors.

2.5 The Superconducting Magnet

The superconducting magnet ILSE (Iron-Less Superconducting Electron magnet) in Fig. 2.11, consists of six superconducting coils, surrounding the beam axis. It generates a toroidal magnetic field. The magnet should fulfill these requirements:

- It deflects charged particles, in order to measure their momenta with sufficient resolution.
- The magnetic field should not be extended up to the neighbor detectors (RICH and MDC).

The magnetic field can reach a maximum intensity of 3.7 T on the coil's surface, but not more than 0.7 T in the HADES acceptance and it is higher at smaller polar angles [87, 98].

The magnet geometry has been chosen in order to obtain the toroidal field which deflects the particles only in the polar direction ϑ. This results in a particle momentum kick of the order of $p_T = 50\ MeV/c$ at large polar angles and $p_T = 100\ MeV/c$ at smaller polar angles.

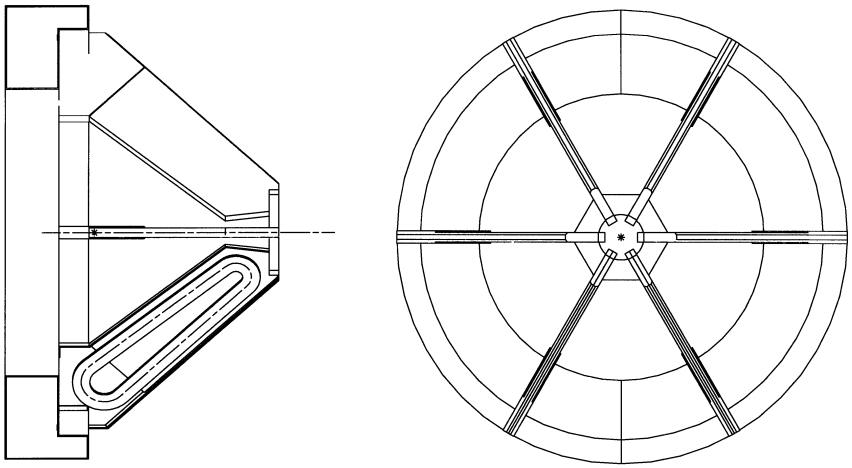

Figure 2.11: Left: side view of the magnet. One coil shows a cut at its central plane. Right: front view cut. The picture has been taken from [87].

2.6 Multiplicity Electron Trigger Array

The Multiplicity Electron Trigger Array (META) is positioned behind the outer MDCs. It is used for fast charged particle determination via the time-of-flight between the target and the TOF wall, of each detected particle, performing particle identification: electrons, positrons and hadrons (π, K, p). Since it is a fast detector, it is used for triggering.

The META consists of two Time Of Flight detectors (TOF and TOFino) and a Pre-Shower detector covering forward polar angles (18°-45°).

2.6.1 Time-Of-Flight Detectors: TOF and TOFino

The Time-Of-Flight (TOF) wall was designed to have the following features:

- Charged particle multiplicity determination in each event, thus providing a first level trigger decision (see Sec. 2.8) and selecting the centrality of the events.
- It provides position information of charged particles.
- Measurement of the time-of-flight of each hitting charged particle in order to distinguish between leptons, protons, pions and kaons.
- Measurement of particle energy loss, which can be used for particle identification.

The TOF detector follows the HADES hexagonal geometry. It covers the polar angular region between 44° and 88°. It consists of six sectors: each sector is divided in eight modules of eight scintillator rods (64 bars for each sector), connected from both sides to photo-multipliers tubes [13]. In total 384 scintillator rods are connected on both sides to photomultipliers. When a particle hits the detector, light is generated into the scintillator, which is then collected by photo-multipliers. An electric signal is generated and processed by a Constant Fraction Discriminator (CFD) and a Time to Digital Converter (TDC). From this information the time-of-flight and hit position of the particle can be extracted [99]. The TOF wall has been used stably throughout several runs. The time resolution for the C+C run at incident kinetic energy of 2 $AGeV$ was 150 ps.

The average position resolution can be determined in correlation with the MDC tracking system by taking data without magnetic field. Given a straight track, which has been generated in the target and crosses the four MDC planes and TOF wall, by projecting the segment reconstructed by the MDC on the TOF system, it is possible to calculate the position of the projected point, and its distance from the hit as measured by the scintillator rod. The distribution of the difference between the two positions $x_{TOF} - x_{MDC}$ can be fitted rod by rod by a Gaussian function. The average resolutions along the rod σ_x are between 25 mm and 27 mm [87].

In all p + p experiments no START detector has been used, since the high-intensity proton beams, interacting with the START detector and the surrounding material, prevented a stable RICH operation. As a consequence there is no common start time reference for all tracks. However, instead of the real time-of-flight of each particle, the differences in time-of-flight with respect to the fastest particle can be considered [13]. With this method an average time resolution σ_{tof}= 340 ps has been obtained, with an efficiency of about 92 % for events containing at least one lepton. A resolution of σ_{tof}= 440 ps and an efficiency of about 93 % is obtained for events with a negative pion [87].

The TOFino detector provides time-of-flight measurements in the polar angular region between 18° and 44°. It is shown in Fig. 2.12 (left). It consists of 24 scintillator rods (6 sectors × 4 modules). The rods are readout only at one end cap. Therefore, using only this detector, it is not possible to have hit position information. This information is rather provided by the correlation with the Pre-Shower detector (see Sec.2.6.2). This detector is useful for low multiplicity experiments like in p + p or C+C reactions. The time resolution of TOFino is about σ_{tofino}= 420 ps, which is determined mainly by the geometry of light collection system.

For the future experiments such as Au+Au, the multi-hit capability of this detector is too small, leading to multiple hits on the same TOFino paddle. The

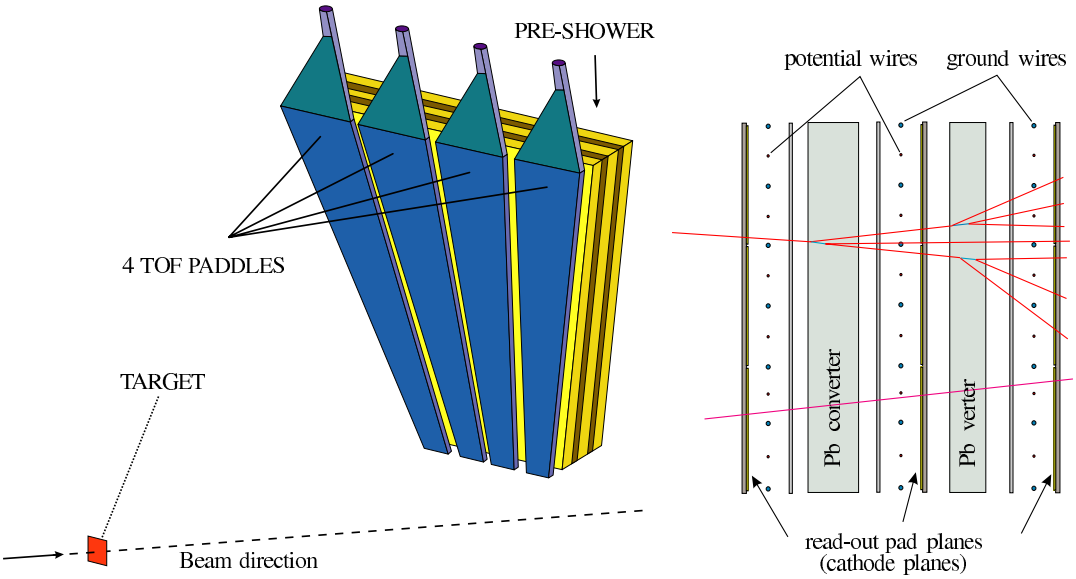

Figure 2.12: Pre-Shower and TOFino detectors. On the left side, the schematic view of Pre-Shower and the TOFino paddles are shown. On the right side, the layers which compose the Pre-Shower detector are drawn.

replacement of TOFino by a Resistive Plate Chamber (RPC) detector with fast readout is foreseen in the near future [103, 104, 105].

2.6.2 Pre-Shower Detector

Electrons and positrons induce much higher charges through the matter than hadrons. They lose energy mainly by bremsstrahlung, and if the energy of the photons emitted during this process is greater than $2m_e = 1.022\ MeV/c^2$, they can generate high energy e^+e^- pairs. The result is a cascade of electrons, positrons and photons[6].

Since the radiative energy loss per unit length ($\frac{dE}{dx}$) by photon emission, in a bremsstrahlung process, is proportional to the inverse mass squared $\frac{dE}{dx} \sim 1/m^2$, the bremsstrahlung process plays an important role mainly for light particles.

At forward polar angles, the separation of electrons from hadrons via time-of-flight measurement is more difficult than at large angles due to the higher hadron momenta and larger hits densities in the detectors. For this reason, an additional electron/hadron separation method was taken into account: an

[6]Due to the small thickness of the detector, the complete electromagnetic shower is not observed but only its first part. This is the reason for the name Pre-Shower.

electromagnetic shower measurement in the Pre-Shower detector. The Pre-Shower detector, in Fig. 2.12 (right), covers the polar angular region between 18° and 45°.

It is composed of a stack of three Multi Wire Proportional Chambers (MWPCs) layers (pre-converter, post1-converter, post2-converter). Each chamber is filled with an Ar-Isobutan gas mixture and consists of one wire (anode/cathode) plane and two flat cathode planes. A 1 *cm* thick lead layer (corresponding to 2 radiation lengths) separates the chambers.

Each cathode plane is subdivided into pads of different dimensions from which the induced charge signal is taken from. A charged particle, passing through a MWPC, ionizes the Ar-Isobutane gas producing avalanches of electrons, drifting towards the closest anode wire; the positive cloud motion induces a positive charge on the nearby cathode pads, which are connected to charge-sensitive pre-amplifiers.

By comparing the integrated charge deposited by a track in the pre-converter and post1/post2-converters, it is possible to distinguish electromagnetic showers from hadronic tracks. The last step consists in comparing the ratio of the integrated charges per layer against momentum-dependent thresholds.

2.7 The Forward Hodoscope Wall

The Forward hodoscope Wall (FW) is a detector array which consists of 287 scintillating cells with each 2.54 *cm* thickness, where each module is read out by a photomultiplier. The FW is placed 7 *m* behind the target and covers polar angles from 0.33° up to 7.17°. Charged particles are detected in the spectrometer with a momentum resolution of about 11% for protons, as described in [85].

The FW was installed in year 2007 and it was successfully used to distinguish the p + p and n + p reactions through a coincident measurement of a spectator proton in the deuteron beam experiment in May 2007.

2.8 The HADES Data Acquisition System

In order to acquire the statistics needed for the interpretation of the electron spectra, on-line data reduction and event selection are used.

A two-staged trigger system reduces the amount of purely hadronic events, thus enhancing the electron yield. The HADES trigger system is structured into several levels and implemented in different hardware modules, as shown in Fig. 2.14.

The HADES Data Acquisition (DAQ) is a distributed system. The triggers

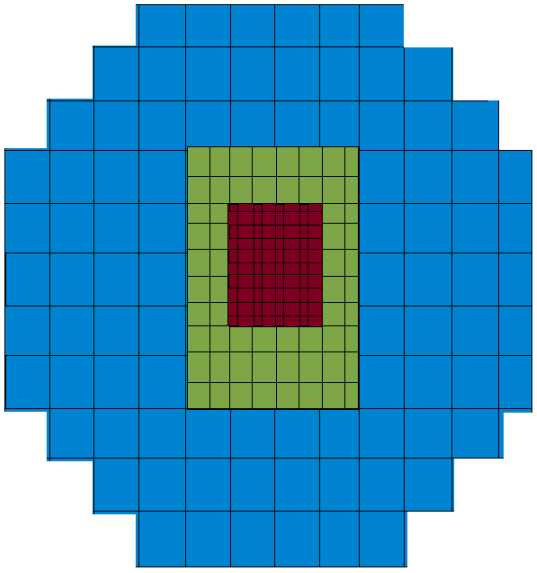

Figure 2.13: Schematic view of the arrangement of the Forward Wall detector. The detector is built with cells of different size: 160 $mm \times 160$ mm (blue color), 80 $mm \times 80$ mm (green color) and 40 $mm \times 40$ mm (red color).

are generated internally (*i.e.* calibration trigger) or as result of input signals delivered by fast detectors such as TOF and START/VETO.

A digital level-1 (LVL1) trigger[7] is generated in the Central Trigger Unit (CTU), made of a consecutive number (trigger tag) and a trigger code which contains the nature of the input signal which generated the trigger.

The triggers are transmitted to the individual subsystem via the Detector Trigger Units (DTUs) to the Front End Electronics (FEE).

After data has been read out by the detector specific DAQ, dedicated algorithms, running on the Image Processing Units (IPUs) search for electron candidates.

The hit information produced is then combined in the Matching Unit (MU) [111]. The MU generates a second level trigger (LVL2) which is forwarded to all sub-systems via the CTU. As the LVL2 trigger[8] decision is produced after a latency corresponding to several events (typically 5 to 10 events) the readout boards need to store the data in buffer or memory (LVL1 pipe) large enough to hold the data for this time. After a LVL2 trigger signal has been received the data is either copied into separate memory (LVL2 pipe) or discarded, depending on the LVL2 decision (positive or negative) [111].

[7]The LVL1 trigger is called multiplicity trigger as well. It is generated by the comparison of the number of hits in TOF and TOFino to a given settings. It is used to provide a centrality selection on the occurred reactions.

[8]This trigger can be positive or negative and it is generated by the angular correlation obtained between TOF and Pre-Shower detectors with the angular information coming from the RICH. This information is computed sector-wise.

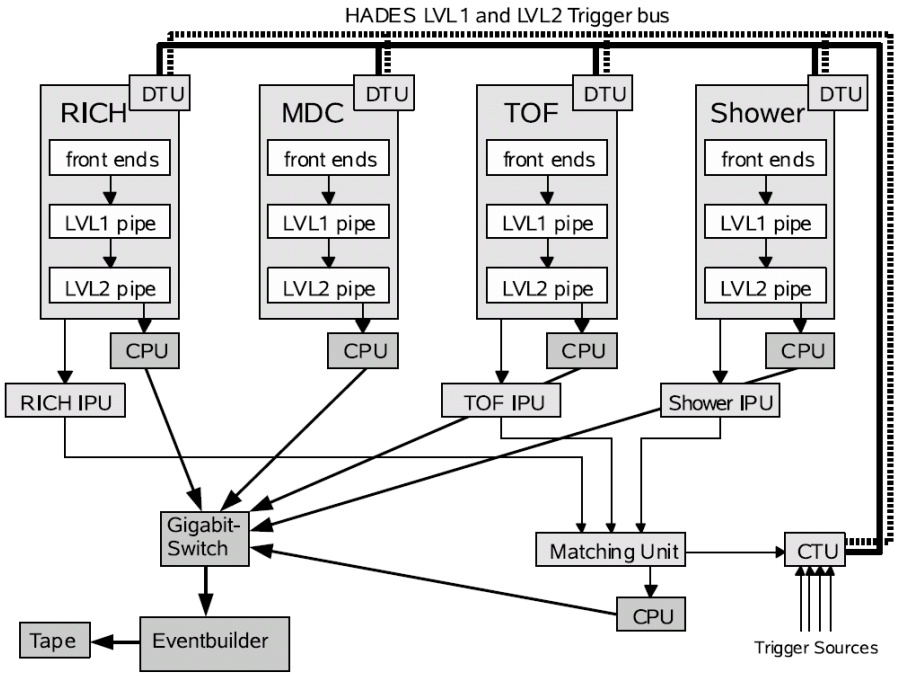

Figure 2.14: Block diagram of the trigger distribution and HADES data acquisition system. Triggers are generated by the Central Trigger Unit (CTU) and transported via the trigger bus to the Detector Trigger Units (DTUs) of each detector. In the detector specific DAQ, data is stored in a LVL1 pipe. At the same time, pattern recognition algorithms are performed in the Image Processing Units (IPUs). Finally the Matching Unit (MU) combines these results. After a positive decision (positive LVL2 trigger), the data is read out from the detector specific DAQ and sent to the Event Builder, via dedicated VME hardware modules. The picture has been taken from [87].

The stored data are then transferred to the common event-builder[9], which is responsible for the final assembling of the events.

An higher level trigger (LVL3) feasibility has been studied [113, 116] and it could significantly reduce the load on the DAQ and the off-line analysis. The main issue is the correlation between the LVL2 trigger and the tracking

[9]The event-builder is a software process, which is active on a server machine. It collects sub-events coming from different detectors and streams them in one single event. It combines the data from different asynchronous data sources into complete events and finally writes them to mass storage. This readout program runs on standardized VME-CPUs with Linux/LynxOS.

information produced by the first and second MDC planes. A third level trigger could be helpful when trying to measure heavier system, such as Au+Au, by rejecting uninteresting events already at the first stage of the acquisition process.

After the successful upgrade of the MDC DAQ, as described in Sec. 5, this correlation could be integrated in the acquisition structure.

A detailed description of the trigger system can be found in [87, 111, 113, 114, 134].

Chapter 3

Proton-Proton Data at 3.5 GeV

In this chapter, the analysis of e^+e^- pair production in elementary p + p collisions at 3.5 GeV is shown. The data have been accumulated from April to May 2007 with the HADES detector. The detector was fully operational and each sub-detector was installed in the detector setup. During this experiment, $1.036 \cdot 10^9$ events were collected.

In the analysis procedure, the inclusive reaction $pp \to \omega X \to e^+e^-X$ has been selected by making use of particle identification and a selection on the invariant-mass to identify the vector meson signals.

The number of ω mesons which have been reconstructed is 275 ± 15(stat). This number allows for the determination of the ω production cross section, which has been determined for the first time at SIS energies.

Using the same data set, the production cross section of the exclusive reactions $pp \to \omega pp \to e^+e^-pp$ has been determined as well. The result is in agreement with the production cross sections previously measured by other experiments via hadronic exclusive channel [69, 106, 107].

In order to understand the production mechanism at our energy, basic measurements such as production cross sections are indispensable. Indeed, with the knowledge of the inclusive experiment, the sources of the invariant-mass spectrum can be studied and a model for the future p + A or A+A reactions can be stated.

3.1 Detector Setup

A proton beam of $3 \cdot 10^6$ particles per second was incident on a 5 cm long liquid hydrogen target. The tracking system was fully operational. Data were taken

with a magnet current[1] of I=3.2 kA. The START detector was not used during data taking.

The data readout was started by a first level trigger (LVL1) condition, requiring at least three charged-particle hits (M3 trigger condition) in the TOF/TOFino detectors. A second level trigger (LVL2) followed, requesting at least one electron-track candidate. The M3 trigger smoothly ran at 10 kHz and the LVL2 condition reduced this rate[2] by a factor of between 3 and 4. It was investigated that the LVL2 introduced no bias on the shapes of measured pair distributions (see Sec. 3.4.1).

Data was also taken for a trigger condition requiring two charged hits, occurring in opposite sectors (M2 trigger condition). Using the M2 trigger allowed for the elastic p + p reaction selection. The p + p elastically scattered events were taken simultaneously with the main LVL1 trigger with a "down-scaling factor" of 32. The "downscaling factor" is used to combine signals coming from different detectors and sectors in order to impose different selections on the events. M2 trigger with a downscaling factor $DS = 32$ means that each 32's event is recorded[3]. Also for the M3 trigger a downscaling factor was selected[4] and was fixed to $DS = 3$.

Since the luminosity of the beam was not know during the experiment, it was mandatory to compute the proper normalization factor in order to properly normalize the spectra presented in this work (see Sec. 3.8). This normalization factor was determined by measuring the yield of a given channel relative to that of a simultaneously measured channel with known cross section. The luminosity was also calibrated using p + p elastic events and the elastic cross section (see Sec. 3.7).

3.2 Track Reconstruction and Lepton Identification

The electron track reconstruction proceeded in four steps, combining the signals of all sub-detectors [87]:

[1] The magnet current and the data of the proton beam intensity have been taken from the HADES database.

[2] This number has been taken from the HADES database and from the analysis of a selected number of data files.

[3] The downscaling factor is selected by the so called "trigger box". The trigger box is an hardware board which is programmable via a dedicated software. Via this board the downscaling factor is selected for many trigger type and this number says how many events are discarded between two accepted events.

[4] The downscaling factor for the M3 trigger was selected via the Matching Unit (see Sec. 2.8).

1. Track reconstruction and momentum determination: the track momentum was determined by a fit of an appropriate track model to the reconstructed hit positions making use of the deflection in the known magnetic field [87]. The charged tracks were reconstructed from hit positions in the drift chambers by using the Runge-Kutta fitting method. After the tracks were reconstructed, tracks corresponding to momenta between 0.1 GeV/c and 2.0 GeV/c were selected for further analysis (see Sec. 3.2.1).

2. The RICH guaranteed electron/positron detection via ring recognition. Assuming that the leptons were emitted from the target, the polar (θ) and azimuthal (ϕ) angles were calculated from the ring positions (see Sec. 3.2.2).

3. The θ and ϕ angles of lepton candidates in the RICH were correlated with the track angles reconstructed in the MDC within windows corresponding to ± 2 standard deviations (see Sec. 3.2.3).

4. Candidate tracks were then matched with those hits in the TOF or TOFino and Pre-Shower detectors fulfilling electron/positron conditions, *i.e.* the electromagnetic shower condition in the Pre-Shower and a condition on the particle velocity ($\beta = 1 \pm 3\sigma_\beta$, where σ_β is the time-of-flight resolution). (See Sec. 3.2.6 and Sec. 3.2.5).

Each of these steps is explained in detail in the following sections and the cuts chosen to identify the particles are listed with their respective losses.

Once the lepton sample has been selected, electron/positron tracks are combined into three groups of pairs: e^+e^+, e^-e^- and e^+e^- (see Sec. 3.3). The final aim of this analysis is to extract the spectral distribution of the true pairs, which is obtained by subtracting from all pairs those which are formed by combining particles originating from different sources.

3.2.1 Tracks, Momenta and Angles Reconstruction

During the p + p experimental run, the HADES detector was equipped with a complete tracking system: six MDC sectors for each plane.

The determination of a particle momentum in the HADES detector requires the knowledge of track's deflection in the magnetic field. The particle momentum is determined by various algorithms, indeed making use of the bending of its trajectory inside the magnetic field region. To determine the deflection of the particle in the magnetic field, independent inner and outer straight track segments are reconstructed from the hit information of two MDC chambers in

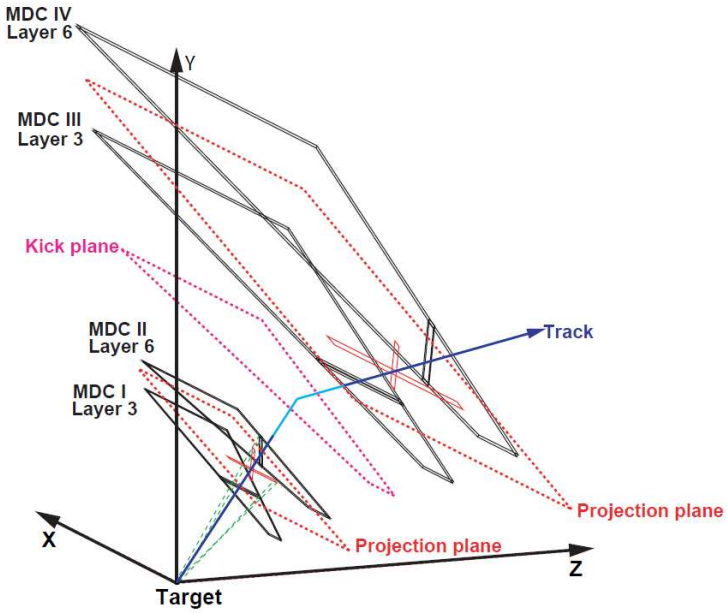

Figure 3.1: Principle of the track candidate search in the track reconstruction procedure. Here only one layer out of six for each MDC module is shown. Four MDC chambers are shown and two projection planes. In between there is the kick plane (see text for details). The picture has been adapted from [71].

front of and behind the magnetic field region. The reconstruction of the particle trajectories in the tracking system of HADES is accomplished in several steps.

First, the spatial correlation of fired drift cells in the drift chambers is performed by a "track candidate search" based on the identification of so-called "wire clusters". The "wire clusters", crossed red lines in Fig. 3.1, are calculated using only the geometrical positions[5] of the fired drift cells and define "track segments". The fired wires in both chambers (MDC-I and MDC-II) are projected from the target on a common projection plane, in Fig. 3.1, which is in the middle between the inner modules. For the inner drift chambers, the projection is performed with respect to the center of the target.

When searching for wire clusters in the outer drift chambers, the same strategy is followed as for the inner ones, except that the target position is replaced by the intersection point of an inner segment with the "kick plane", in Fig. 3.1. The "kick plane" is a virtual plane placed between MDC-II and MDC-III [72]. It is based on the assumption that the deflection can be approximated with a sharp change of the direction of trajectories on a given plane (the so called "kick-plane") and that the momentum kick suffered by the particle does not depend on the initial momentum of the particle itself, but just on its deflection in the magnetic field.

[5]The information delivered by the MDC Front End electronic (FEE) is composed of hardware addresses (TDC numbers and TDC channels) of the fired wires, which are converted via look-up tables into wire numbers. A "fired wire" is a wire which presents a signal above a certain threshold.

The particle trajectory is approximated by a straight line, *i.e.* it is assumed that this region is field free. The fit of two chambers simultaneously is performed employing a straight-line track model. The quality of the fitting procedure (χ^2 distribution) of inner and outer MDCs are used to select "track candidates". "Track candidates" are finally obtained through the matching of "track segments" in the inner and outer drift chambers of one sector.

The particle momentum is determined by a track interpolation using the Runge-Kutta algorithm. As there is no hit information between the inner and outer chambers and the kick plane method does provide an approximate momentum of the particles, a model of cubic splines for the particle trajectory is assumed. This provides a first guess of momentum and particle polarity, which are then used to start the iterative Runge-Kutta algorithm. First, the spline method obtains the particle momentum from matched reconstructed inner and outer track segments. Secondly, an higher precision momentum calculation is obtained solving the equation of motion of particles in the magnetic field. These equations can be solved using fourth order Runge-Kutta methods in recursive way [14]: this means that the new track parameter is computed with a quality parameter (χ^2). If the Runge-Kutta fit does not converge, its quality parameter (χ^2) is set to 10^6. Depending on the χ^2 value, a further step follows using the results found in the previous step. When the χ^2 converges, the fit procedure stops and the final track parameters are stored.

If the Runge-Kutta algorithm converges and the META coordinates exist, the intersection between the reconstructed outer segment with the module of the META detector is calculated. Outer segments are matched with META hits using straight lines. Using the difference between the original META hit position and the intersection point of the Runge-Kutta track on the META a quality factor is calculated. The matching window between outer MDC-META, is defined by a $\pm 3\sigma$ region around the mean value of a quality factor [14]. The quality parameter is set to the -1 value if none of the META hits is matched with a given track candidate.

For electron/positron identification, the inner track segments are matched with rings in the RICH detector. (See Sec. 3.2.2).

3.2.2 Ring Reconstruction in the RICH Detector

As mentioned in Sec. 2.3, the HADES experiment critically depends on its RICH detector. Its goal is the identification of prompt electrons by recognition of UV photons, which are reflected onto the pad plane.

Two "ring finder" algorithms have been used: one based on a Pattern Mask

(PM) and one that exploits a Hough Transform (HT) method[6]. They are used to identify the ring candidates and to determine the position of the ring center. The ring coordinates, computed by the "ring finder" algorithms, are later matched with the segment information of the inner drift chambers (see Sec. 3.2.3).

The analysis of lepton signature in the RICH starts with no information about tracks. A simplification is given by the fixed ring radius produced by leptons, which already at energies of few MeV follow the relativistic kinematics. The "ring finder" task is performed by matching the ring candidate with a pattern ring over the entire RICH "image". The mask has a circular shape, which is defined by pixels: all "on" pixels in the ring are counted, while pixel near the ring border are counted negatively ("off" pixels), as represented in Fig. 3.2.

-46	-40	-25	1	22	27	22	1	-25	-40	-46
-40	-15	27	50	47	41	47	50	27	-15	-40
-25	27	44	12	-9	-15	-9	12	44	27	-25
1	50	12	-24	-33	-35	-33	-24	12	50	1
22	47	-9	-33	-36	-36	-36	-33	-9	47	22
27	41	-15	-35	-36	-36	-36	-35	-15	41	27
22	47	-9	-33	-36	-36	-36	-33	-9	47	22
1	50	12	-24	-33	-35	-33	-24	12	50	1
-25	27	44	12	-9	-15	-9	12	44	27	-25
-40	-15	27	50	47	41	47	50	27	-15	-40
-46	-40	-25	1	22	27	22	1	-25	-40	-46

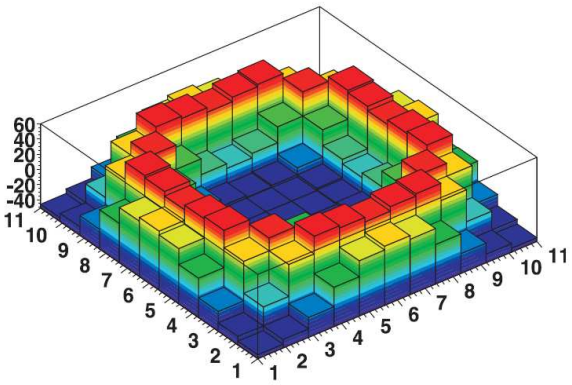

Figure 3.2: Left: a 11×11 pads pattern matrix. Each cell contains a weight reflecting the ring image. Positive values form a ring, while negative values correspond to pads which are not expected to be fired. Right: three dimensional representation of the pattern matrix. Pictures have been taken from [96].

The systematic scan of the mask over the possible ring centers with simultaneously counting positive and negative hits results in a new image and for each pad the measured charge is multiplied with a weight on the mask. For each fired pad the corresponding weight on the matrix is added to produce a quality parameter called Pattern Matrix quality (PM quality). Hence, the PM quality classifies the rings.

A second and powerful ring identification method has been adopted: the Hough transformation. For each combination of three fired pads, a ring with

[6]During the data taking the Pattern Mask was used to identify rings in the RICH detector. It was implemented already at the hardware level for on-line lepton selection [114]. The second method was used in the post-analysis (software level).

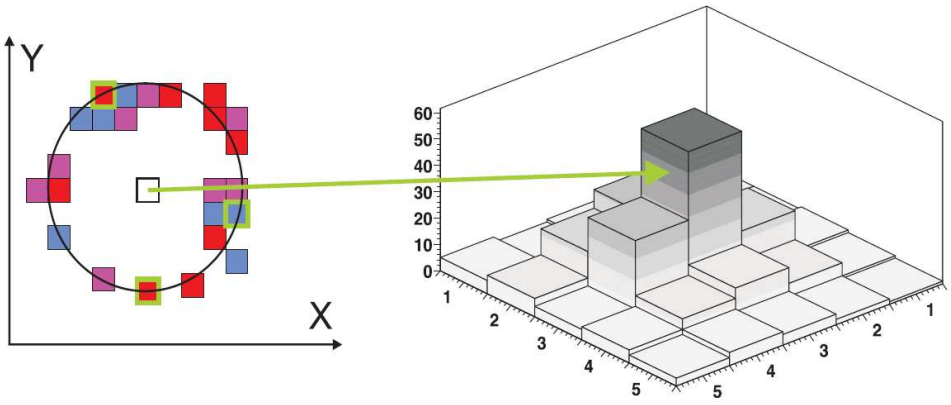

Figure 3.3: Hough transformation method. Left: a circle passes through three green pixels. Each combination of three pads defines uniquely a ring center and its radius under the constrained that all three pads lie on the ring circumference. Right: the accumulation of ring centers results in a two dimensional array. The picture has been taken from [96].

a given radius and center is associated. The center of a real Cherenkov ring is found as a local maximum in a virtual image containing pads with ring centers for all these triplets. Maxima in this virtual image (Hough transform of original rings [74]) correspond to found rings. The height of these maxima defines a quality parameter called Hough Transform quality.

Since the LVL2 trigger relies on the ring information in the RICH and has to be provided as fast as possible, the Pattern Matrix algorithm has been successfully parallelized and implemented in Field Programmable Gate Array (FPGA) technology [114]. The Hough transformation algorithm needs more computing time than the Patter Mask. This algorithm was used only in the off-line analysis, where a coincidence between the two "ring finder" algorithms defines a found ring. The "ring finder" algorithms provide the following information on the ring quality:

- Number of fired Pads (NP) forming a ring.
- Ring Centrality (RC) quality: distance between the position of the gravity center of a ring (deduced by the charge deposited in the pads) and its fitted geometrical center has to be smaller than a certain threshold.
- Pattern Matrix (PM) quality.
- Average Charge (AC): sum over the charges collected by each pad composing a ring.

Fig. 3.4 and Fig. 3.5 show the distribution of these quantities and the vertical lines indicate the cuts used in the present analysis work. Due to the charge conservation in p + p reactions the number of positively charged particles is higher compared to the negatively charged one. This difference is evident in Fig. 3.4 and Fig. 3.5, where more positively charged particles populate the distribution. In addition the geometrical acceptance for the positively charged tracks is higher than for the negative charged once; this effect enhances the probability for positively charged tracks to be misidentified as positrons. The cuts were chosen to be not restrictive: most lepton rings fulfilled them and the suppression due to these cuts was about 8-10% only. Moreover the cut on the ring centroid is applied at large values; this avoids the suppression of possible true rings (rings produced by leptons) which might be not well defined.

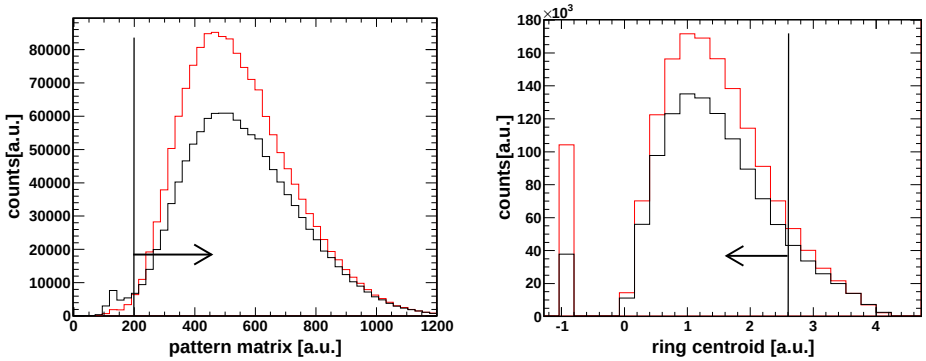

(a) Pattern matrix quality (b) Ring centroid

Figure 3.4: Ring quality distributions for lepton candidates: positrons (red color) and electrons (black color) are shown. Vertical lines and arrows indicate the cuts on the quality distributions and the accepted region. In both distributions there are more positrons than electrons. This is due to protons which are misidentified as positrons (see text for the description).

Summarizing a ring is accepted if the following conditions on the ring quality parameters are satisfied:

- The Pattern Matrix (PM) quality parameter is larger than 200.
- The Ring Centroid (RC) is smaller than 2.6.
- The Number of Pads (NP) which builds up a ring is larger than 6.
- The integrated charge (AC) on one pad in the ring is larger than 6 ADC channels/pad.

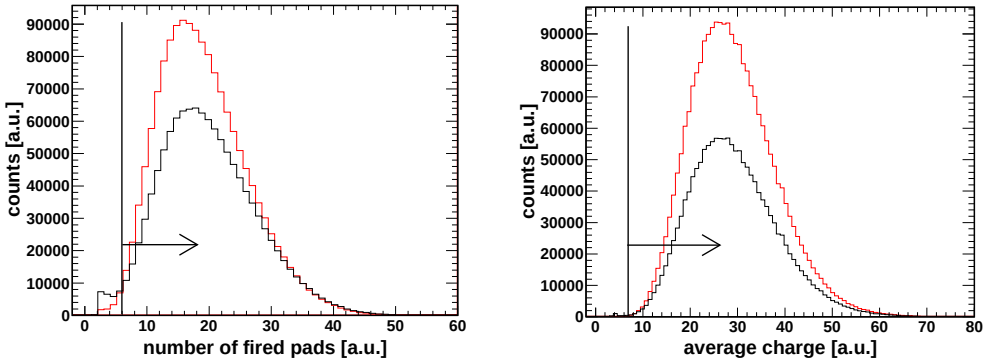

(a) Number of pads forming a ring

(b) Average charge

Figure 3.5: Ring quality distributions for lepton candidates: positrons (red color) and electrons (black color) are shown. Vertical lines and arrows indicate the cuts on the quality distributions and the accepted region. In both distributions there are more positrons than electrons. This is due to protons which are misidentified as positrons (see text for the description).

3.2.3 Angular Correlation between RICH Ring and MDC Segments

The polar and azimuthal angles of the reconstructed segments in the two inner chambers of the MDC detector must be matched with the polar and the azimuthal angles of ring candidates. In order to quantify the correlation of the ring position and the track segment position between the two detectors, the residuals, given by the Eqns. 3.1 and 3.2, are computed:

$$\Delta\theta = \theta_{RICH} - \theta_{MDC} \tag{3.1}$$

$$\Delta\phi \cdot sin(\theta_{MDC}) = (\phi_{RICH} - \phi_{MDC}) \cdot sin(\theta_{MDC}) \tag{3.2}$$

θ_{RICH} and ϕ_{RICH} are the polar and azimuthal angles of a ring in the RICH detector in the laboratory frame[7] θ_{MDC} and ϕ_{MDC} are the angular coordinates

[7]The laboratory frame is defined as three mutually perpendicular axes (xyz). The z-axis is parallel to the beam and its direction coincides with the direction of the incoming beam. In respect to this reference system the polar (θ) and the azimuth (ϕ) angles are defined. The vector from the origin of the frame ($x = 0, y = 0, z = 0$) to a point of interest (x, y, z) is projected perpendicularly onto the xy-plane ($x, y, 0$): the angle between the projected vector and the reference vectors on the xy-plane is called azimuth angle (ϕ). For a given vector, which has its origin in ($x = 0, y = 0, z = 0$) and defines a point in space (x, y, z),

of a segment found in the two inner planes of the tracking system. θ_{MDC} and ϕ_{MDC} are computed in the laboratory frame as well. The difference in the azimuthal angle between the hits is multiplied by a $\sin(\theta)$ factor to keep the solid angle spanned constant [96].

In the first analysis step, very broad windows are applied and each ring is matched with MDC segments within these windows: $\Delta\theta = \pm 10°$ and $\Delta\phi sin(\theta) = \pm 10°$.

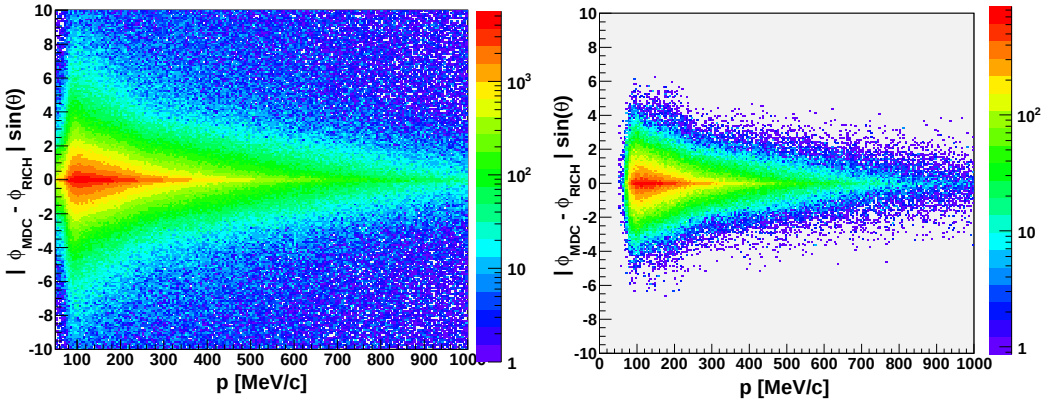

(a) No cuts are applied

(b) Matching window and low momentum cut of 80 MeV/c are applied

Figure 3.6: Ring-segment azimuthal correlation distributions. The correlation distributions are spanned by the factor $sin(\theta)$.

In the second analysis step, more narrow windows are computed as function of the momentum of the particles.

Fig. 3.7 shows these correlations as function of the momentum of a particle. They are obtained by projecting the distribution in Fig. 3.6 on the vertical axis, for different momentum slices. In order to optimize the correlation windows for a better signal to background ratio, the distributions in Fig. 3.7 are fitted with three different components:

- The signal, which has been fitted with a Gauss function (green line). Its width is mainly due to the multiple scattering in the detector's material[8].

the angle between this vector and the z-axis is called polar angle (θ).

[8]The multiple scattering contribution can be expressed by [108]:

$$\theta_0 = \frac{13.6MeV}{\beta cp} z \sqrt{\frac{x}{X_0}} [1 + 0.038 \cdot ln(\frac{x}{X_0})] \tag{3.3}$$

- The correlated background, modeled with a second broader Gauss function (blue line). This contribution is due to rings which have not been resolved (fake or unresolved double rings) and are matched with a segment in the inner MDC.

- The uncorrelated background, modeled with a linear function (red line). It is due to random matching between rings and segment coordinates. This function has been found for a given momentum bin, by fitting rings in one sector to MDC track segments in a different sector.

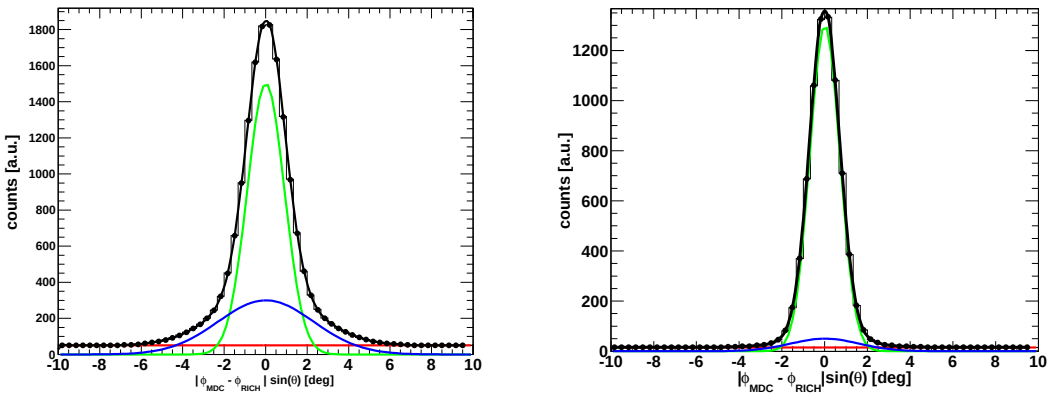

(a) Track with momenta below 200 MeV/c (b) Track in the momentum range 200 MeV/c < p < 500 MeV/c

Figure 3.7: Correlation between RICH and MDC azimuthal angles, for tracks found in two momentum bins. The modeling foresees three components (from the higher curve to the lower one): the signal (green), correlated background (blue) and uncorrelated background (red).

After the second analysis step has been done, narrower windows are required in order to better select lepton candidates. The tracks used in the analysis have been selected based on the following conditions:

$$-3\sigma_\theta(p) < \Delta\theta < 3\sigma_\theta(p) \tag{3.4}$$

where p, β, and z are the momentum, velocity, and charge number of the incident particle, and x/X_0 is the thickness of a scattering medium in radiation lengths and c is the velocity of light. *E.g.* the multiple scattering angle for a lepton of 200 MeV/c momentum in the carbon material of the RICH shell is $\theta_0 = 0.3°$. By increasing momentum the θ_0 becomes smaller and this reflects in the width of the signal in Fig. 3.7.

$$-3\sigma_\phi(p) < \Delta\phi sin(\theta_{MDC}) < 3\sigma_\phi(p) \tag{3.5}$$

where σ_ϕ(p) and σ_θ(p) are momentum dependent.

3.2.4 Electron-Positron Identification in the TOF and TOFino Detectors

Charged particles are identified using the momentum information and the time of flight measurement.

The TOF or TOFino and Pre-Shower detectors provide the particle identification by measuring the time of flight of charged particles which flight from the target to the TOF or TOFino and Pre-Shower detectors.

In Sec. 2.2 it has been mentioned that high intensity proton beams ($\simeq 10^7/s$) do not allow to use the START detector; the START detector would not have allowed the stable RICH operation, because too much background would have been created by the beam particles in the detector material (*e.g.* γ-conversion). As a consequence, there is no common start time reference for tracks in the same event. However, the difference in time of flight with respect to the fastest particle can be measured instead of the "real" time of flight (see Sec. 3.2.4.1).

3.2.4.1 Time of Flight Measurement Without START Detector

An algorithm for time calibration of TOF and TOFino detectors has been developed in [13]: electrons and positrons with energies of a few MeV travel with velocities close to the speed of light. This means that they should have the same velocity, therefore they should cover the same path length in the same amount of time. With this assumption, the time calibration of the TOF and TOFino has been calculated using leptons emitted within one event.

Dileptons were selected using the angular correlation between RICH and inner-MDCs. Their path length could be retrieved by the tracking algorithms and the sign of the charges by trajectory deflection in the magnetic field region. From all this information, all the time offsets were defined [13].

With the TOF detector the average time resolution reached is $\sigma_{tof} = 340\ ps$ and the efficiency of the algorithm is about 92% for events with a lepton. A resolution of $\sigma_{tofino} = 420\ ps$ was obtained for the TOFino/Pre-Shower system.

Fig. 3.8 shows momentum times polarity versus velocity plots after start time reconstruction for the TOF and TOFino detectors. After the start time reconstruction it is possible to use the recalculated time-of-flight in order to identify particles for inclusive and exclusive reactions.

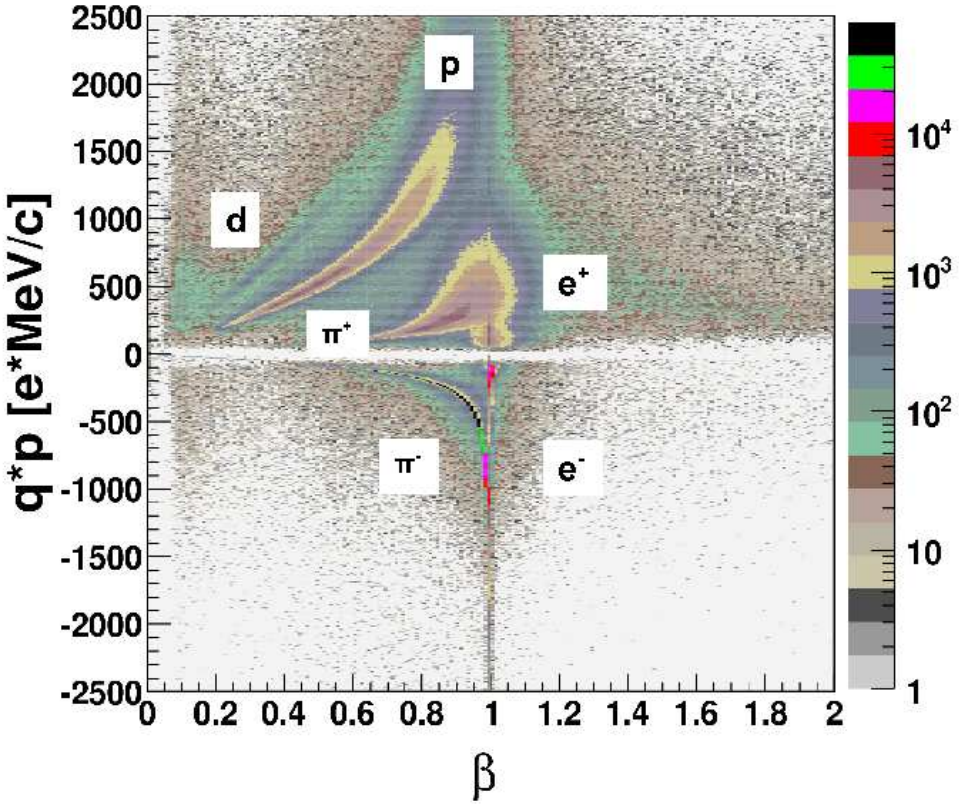

Figure 3.8: Momentum times polarity (q*p) versus velocity (β) distribution. Proton, deuterium, pions and electrons are marked with a label.

With this algorithm the particle identification was possible without the use of the START detector. This allowed to run the data acquisition at a higher rate with still a stable RICH operation.

3.2.4.2 Electron-Positron Identification

For the electron/positron candidates which remain after the ring quality cuts, additional cuts on TOF and TOFino are applied. These cuts are based on the time-of-flight information registered by the respective detectors after the start time reconstruction (see Sec. 3.2.4.1).

Fig. 3.9a and 3.9b show the time-of-flight distribution of lepton candidates. The distributions are peaked around $\beta \sim 1$, since at this energy these particles follow the relativistic kinematics.

For the TOFino detector, a lower cut on the β distribution (upper cut in the time-of-flight), is important to limit the contribution of pions and protons.

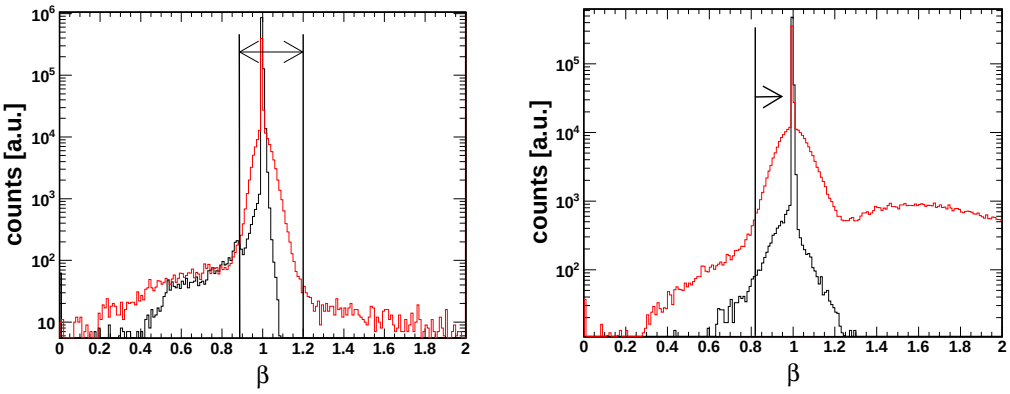

(a) TOF (b) TOFino

Figure 3.9: β distribution in TOF and TOFino detectors for those lepton candidates which passed the constraints on the RICH-inner MDC angular matching and the ring quality cuts. The red colored lines indicate positrons and the black colored lines indicate electrons. The larger yields of the positrons in both distributions show the contamination of positive charged tracks in the lepton candidate sample.

The cuts applied are defined by the following relation for TOF and TOFino detectors:

$$-3\sigma_{TOF} < \beta_{TOF} < 3\sigma_{TOF} \tag{3.6}$$

and for TOFino:

$$\beta_{TOFino} > 3\sigma_{TOFino} \tag{3.7}$$

3.2.5 Electron-Positron Identification in the Pre-Shower Detector

The Pre-Shower sub-detector is mounted directly behind the TOFino detector. It used to improve lepton identification at low polar angles and at large momenta (see Sec. 2.6.2).

Electrons and positrons passing through the two lead converter layers induce electromagnetic showers. This is schematically depicted in Fig. 3.10. The Pre-Shower detector measures the charge accumulated behind each layer. The comparison of the integrated charges in different layers is the basis of the electromagnetic shower recognition. Hadrons induce a much smaller number of

charged particles in the lead converters of the Pre-Shower detector. Hence, the charge amplification from layer to layer is smaller for hadrons than for leptons. This phenomenon helps to distinguish leptons from hadrons.

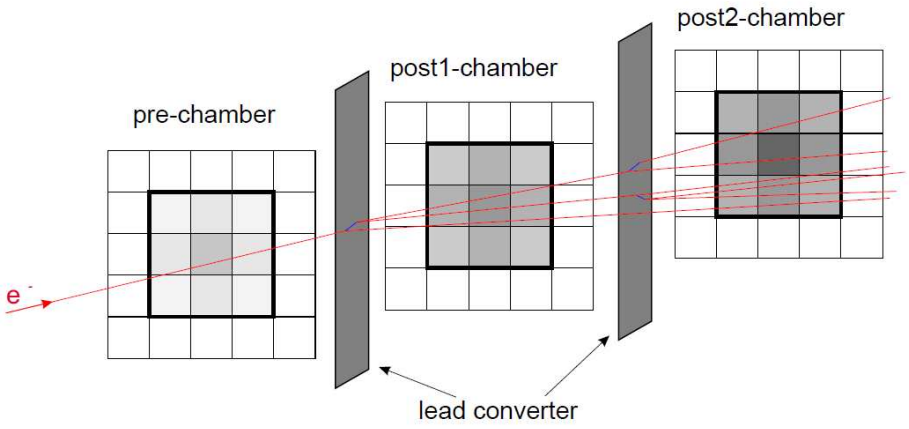

Figure 3.10: Schematic view of the electron propagation through the Pre-Shower detector. The picture has been taken from [87].

The Pre-Shower algorithm is based on the charge deposited in the three chambers: pre, post1 and post2-chambers. First the algorithm searches for local maxima of collected charge in the pre-chamber. A charge integration is performed in a 3×3 pad area in all chambers. The central pad corresponds to a local maximum and the rest of the charge is formed in the eight neighboring pads. Finally, a positive lepton signature is assigned to a particle when the following relation is satisfied:

$$Q_{post1} + Q_{post2} - Q_{pre} \geq F_{thr}(p) \tag{3.8}$$

where Q_{post1}, Q_{post2} and Q_{pre} are the integrated charges in the corresponding chambers. $F_{thr}(p)$ is the momentum dependent threshold which is parametrized as a third order polynomial:

$$F_{thr}(p) = a_0 + a_1 p + a_2 p^2 + a_3 p^3 \tag{3.9}$$

Fig. 3.11 shows the $Q_{post1} + Q_{post2} - Q_{pre}$ distribution as a function of the momentum. The function defined in Eqn. 3.9 is indicated in the plot and the condition in Eqn. 3.8 is indicated with an arrow. The constant parameters a_i

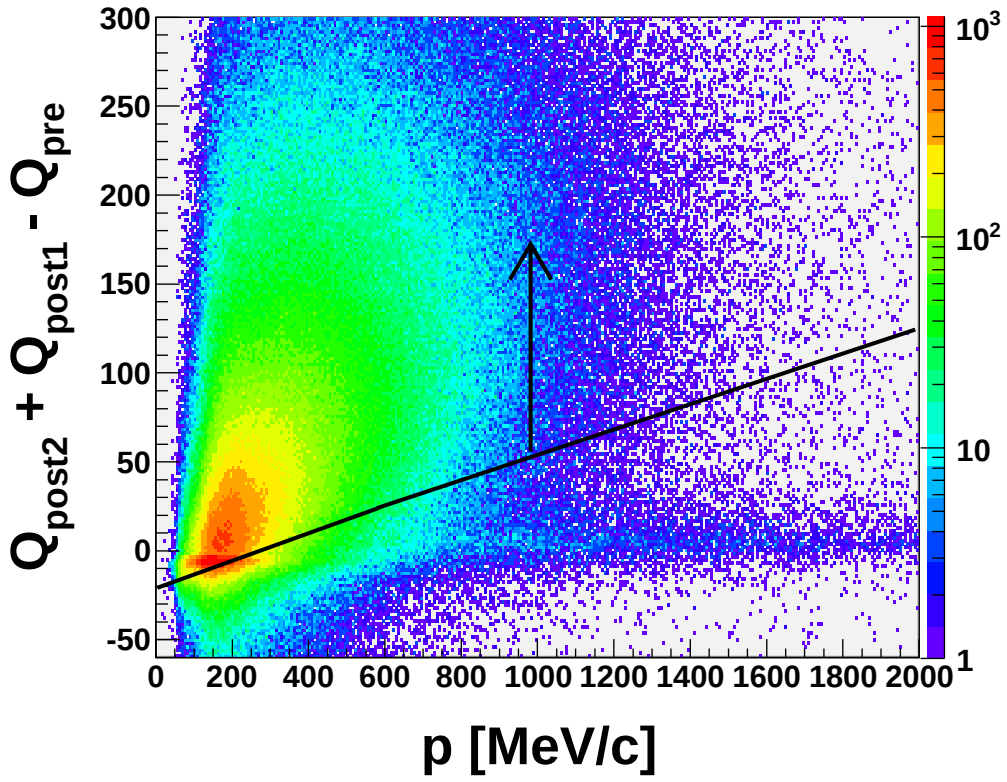

Figure 3.11: Lepton identification in the Pre-Shower detector. The figure shows the distribution of $Q_{post1}+Q_{post2}-Q_{pre}$ versus the momentum of the lepton candidates (positive and negative charged particles contribute in the distribution). The black line represents the momentum dependent function $F_{thr} = F_{thr}(p)$ and the arrow indicates the cut applied to the distribution for a better lepton selection. The horizontal line along the momentum axis is due to hadrons which have been misidentified as leptons.

$(i = 0, ..., 3)$ have been tuned based on simulation such that 70-80% of the electrons/positrons pass the shower cut.

3.2.6 Lepton Candidate Identification: Summary

In this chapter, the selection of lepton candidates has been described. Based on this data sample, the pair analysis followed and it is presented in the next chapter (see Sec. 3.3).

Fig. 3.12 shows the charge times momentum distribution for lepton candi-

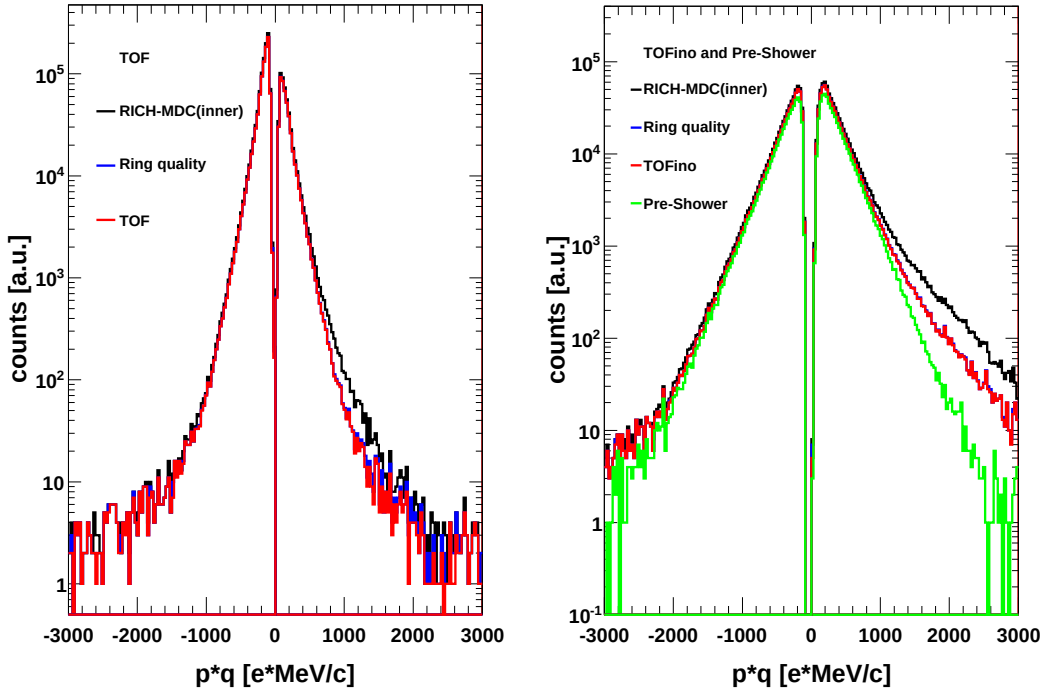

(a) TOF (b) TOFino

Figure 3.12: Momentum distribution of lepton candidates in TOF and TOFino detectors. The pictures show the effect of successive hard cuts on the lepton candidate sample.

dates separately for TOF and TOFino detectors. The distributions change when the cuts are applied consecutively (*e.g.* for the TOFino detector in Fig. 3.12b, from the larger yield to the lowest one: first the ring quality cuts then β-cut in TOFino and finally the Pre-Shower cuts are applied). In the TOFino detector, the distributions become gradually symmetric after each cut is applied. This indicates that the contamination due to positive charged particles (*e.g.* protons or pions) are suppressed by the cuts imposed. The β-cuts in both TOF and TOFino detectors are chosen not restrictive. More constraints are given by the Pre-Shower cuts in the TOFino region.

The cuts applied for lepton identification are summarized in Tab. 3.1 in the order they are applied. The table shows the relative reduction of the positive and negative lepton yields as a function of the cut applied. Each line in the table has the following meaning:

1. Reference sample: electron/positron candidates are selected by the angu-

Lepton Candidates: Cut Summary

Cut Applied	e^+	e^-
RICH-inner MDC Correlation	100%	100%
RICH: Ring Quality Cuts	90%	92%
TOF: β-Cut	89%	91%
Pre-Shower-TOFino: β-Cut and Charge-Cut	81%	87%

Table 3.1: Inefficiency of the cuts applied to select lepton candidate sample. The first line indicates the sample used as reference: with respect to this sample the effects of the hard cuts (applied in the sequence indicated) are shown.

lar correlation between RICH and the inner MDC.

2. RICH: ring quality cuts: all ring quality parameters are satisfied.
3. TOF and TOFino: β-cut (see Sec. 3.2.4.2).
4. Pre-Shower: charge-cut (see Sec. 3.2.5).

The starting point (reference sample) was the total number of the tracks which had matching between a RICH ring and an inner MDC track segment (first line in the Tab. 3.1). In the next lines in the table, it follows the relative reduction of the initial number of lepton candidates, which is defined as the ratio of lepton candidates after the identification cut to lepton candidates before any cut has been applied. There is a larger relative reduction in the positron

sample than in the electron sample. The positron sample was significantly contaminated by positive charged particles. Due to the polarity of the magnetic field, positively charged particles are bent towards the beam axis (z axis in the laboratory frame) and negatively charged particles are curved away from this axis. As results electrons hit preferentially the TOF region, while positrons hit more likely the TOFino region, where they have to satisfy much restrictive cuts: β-cut (TOFino) and charge-cut (Pre-Shower). This effect was already shown in previous HADES lepton analysis in different colliding systems and energies [16, 17].

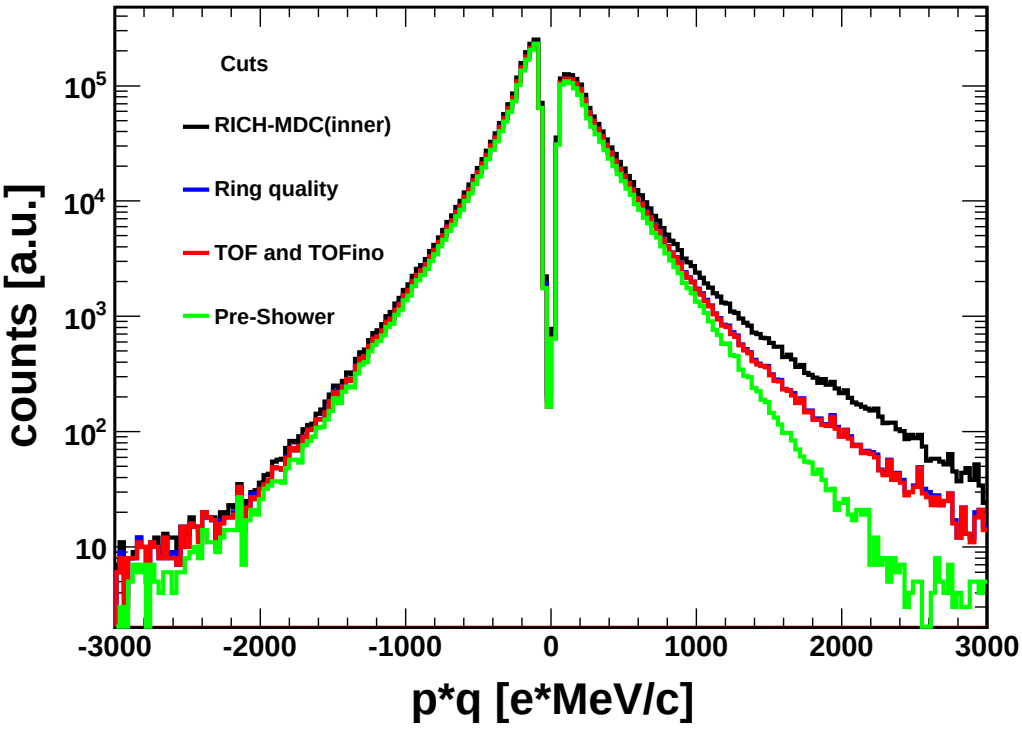

Figure 3.13: Momentum distribution of electrons and positrons candidates. The distributions show the effects of the cuts which are applied. Largest yields correspond to the initial distributions: the total number of the tracks which had matching between a RICH ring and an inner MDC track segment (black color). The distributions obtained after the ring quality cuts were applied (blue color) almost coincides with the distribution obtained imposing the β-cuts in TOF and TOFino (red color). This cuts are chosen to be not restrictive. The lowest distributions correspond to the last cut applied: the Pre-Shower condition.

Fig. 3.13 shows the momentum distribution of the leptons selected before and after all cuts have been applied in all detectors (RICH, TOF, TOFino and Pre-Shower). The amount of positive particles with the momenta above 900 MeV/c

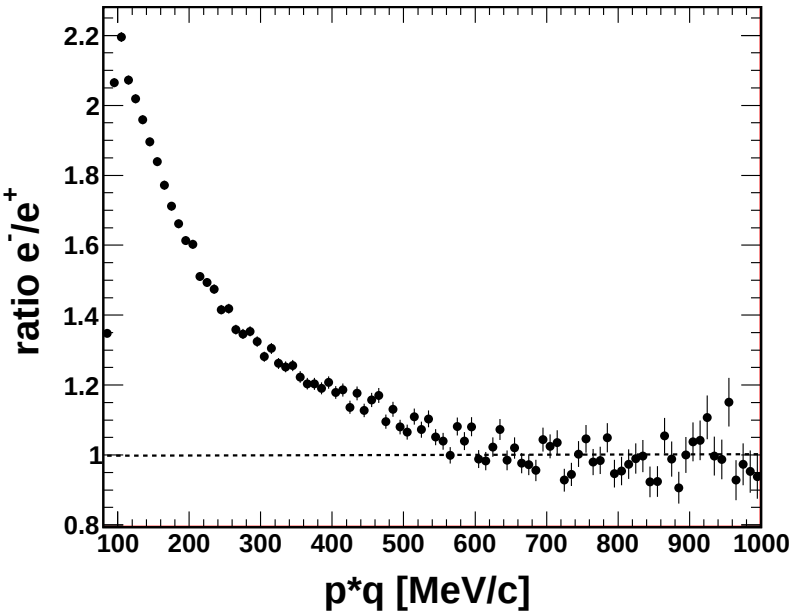

Figure 3.14: Ratio between e^- and e^+ yield after all cuts have been applied. The contamination by protons in the lepton sample is very small. The larger yield at low momenta is due to the fact that positrons are bent inwards and are out of the HADES acceptance.

shows a contamination of positively charged particles. This difference changes after all cuts have been applied.

In Fig. 3.14, the ratio between negative and positive particles is plotted as function of particle momentum after all cuts have been applied. This shows that after all cuts have been applied, the contamination of positive charged particles (*e.g.* protons with momenta > 900 MeV/c) in the lepton sample is small. The larger yield at the low momenta is due to the fact that the positrons are bent inwards and out of the HADES acceptance.

Further suppression of residual hadron contamination was done in the next analysis steps: the lepton pair analysis (see Sec. 3.3). In this chapter, the identified single electron tracks were next combined into opposite-sign pairs in order to reconstruct the signal and the combinatorial background of the invariant-mass spectrum.

3.3 Dilepton Analysis

After electrons and positrons have been selected separately (see Sec. 3.2), they are combined into pairs. Pairing electron and positron tracks is done by building up all possible combinations of electron and positron tracks which are generated in the same event; this process is done by an algorithm process called "pairing procedure". Part of these pairs represent combinatorial background and have to be identified and suppressed (see Sec. 3.3.1).

The two dominant sources of lepton pairs detected with HADES are the electromagnetic decay of hadrons and the photon conversion in the target region:

- External conversion, *i.e.* pair production: $\pi^0 \longrightarrow \gamma\ (\gamma \rightarrow e^+\ e^-)$
- Dalitz decay of the π^0 meson: $\pi^0 \rightarrow \gamma\ e^+\ e^-$

Mainly, the photon conversion takes place in the target or in the material of the RICH detector.

The decays of interest in the intermediate mass region come from the following non-trivial sources:

- η Dalitz: $\eta \rightarrow \gamma\ e^+\ e^-$
- Δ and ω Dalitz: $\Delta \rightarrow Ne^+e^-$ and $\omega \rightarrow \pi^0 e^+e^-$
- ρ, ω, and ϕ vector mesons: $\rho \rightarrow e^+e^-$, $\omega \rightarrow e^+e^-$ and $\phi \rightarrow e^+e^-$

The following sections are dedicated to the description of each analysis step, which are implemented in order to suppress combinatorial background and to obtain a clean signal of true pairs.

Since the mesons of interest (ρ, ω and ϕ mesons) are short-lived, it is only possible to actually detect their decay products. The short-lived states can, however, be reconstructed by the invariant-mass method. E_i and p_i are the total energies and the momentum vectors of the two leptons ($i = 1, 2$) measured in the laboratory frame, c is the velocity of light. p_X is the four momentum and M_X the mass of the decaying particle:

$$M_X^2 c^4 = \left(p_X c\right)^2 = \left(\sum_i E_i\right)^2 - \left(\sum_i p_i c\right)^2 \tag{3.10}$$

In case of two leptons, which are generated by one mother particle X with energies $E_i >> m_{e^+}$, and momenta p_{e^+}, p_{e^-}, Eq. 3.10 can be written as:

$$M_X c^2 = 2c \cdot \sqrt{p_{e^+} p_{e^-}} \cdot sin(\frac{\alpha_{e^+e^-}}{2}) \tag{3.11}$$

where $\alpha_{e^+e^-}$ is the opening angle formed by the momentum vectors of the electron and positron (p_{e^-}, p_{e^+}).

One can study a large number of scattering reactions and accumulate the invariant-mass spectrum given by Eqn. 3.11. Short-lived resonances, which have decayed into these particles, reveal themselves as peaks in the invariant-mass distribution.

However, many of the obtained e^+e^- pairs (obtained by the "pairing procedure") represent Combinatorial Background (CB) which has to be subtracted from the total yield (see Sec. 3.3.2); it is not possible to distinguish whether the reconstructed e^+e^- pair originates from the same source or whether it is an accidental combination of leptons from two separate processes. By definition, background pairs result from the combination of one electron and one positron produced by different sources. Mainly these sources consist in the following processes: γ-conversion, π^0 Dalitz decay and hadrons misidentification (see Sec. 3.3.1).

One problem of the pair analysis is the growth of the combinatorial background with the number of electrons and positrons in one event.

The trivial sources increase the combinatorial background, smearing the shape of invariant-mass spectrum. Therefore it is important to reduce their contribution. The γ-conversion process can generate e^+e^- pair with small opening angles and often produce partially overlapping tracks in the MDCs. This source can be removed from the data sample applying a condition on the angle formed by the momentum vectors of two leptons ($\theta_{e^+e^-} < 9°$) and the fit quality cut of the reconstructed track χ^2 (see Sec. 3.2.1), removing 95% of the conversion pairs. e^+e^- pairs generated by a trivial source such as γ-conversion are removed "recursively": this means that the pair is removed from the lepton sample and also all pairs which contain one of the two removed tracks (see Sec. 3.3.2.3).

In the next sections, the CB strategy is presented and the strategy adopted to compute the CB is explained in detail.

3.3.1 Background Study

After electron and positron identification, these lepton candidate tracks have been accumulated into pair categories: e^+e^+, e^-e^- and e^+e^-. The aim of this analysis consist in obtaining the distribution of true pairs (e^+e^-) by subtracting from all pairs those which are formed by combining tracks originating from different sources. This is done by creating all possible combination of electron and positron tracks originated in the same event. With this procedure two data samples are created: each contains like-sign (e^+e^+ or e^-e^-) and unlike-sign (e^+e^-) pairs. With these two pair samples (like-sign and unlike-sign pair), it is possible to build up from the total spectrum of unlike-sign pair, which is

composed by pairs of interest and background pairs (uncorrelated pairs), the real physics signal (see Sec. 3.3.2).

The pairs contributing to the background can be classified into the following two groups:

- Electron-positron background pairs:
  - **Uncorrelated pairs**: these pairs are formed combining dileptons coming from different mother particles, in Fig. 3.15.
  - **Correlated pairs**: these pairs are formed combining dileptons coming from the same mother particle, but not from the same intermediate (virtual) photon, in Fig. 3.16.
- Fake pairs, *i.e.* pairs which contain one or two misidentified hadrons.

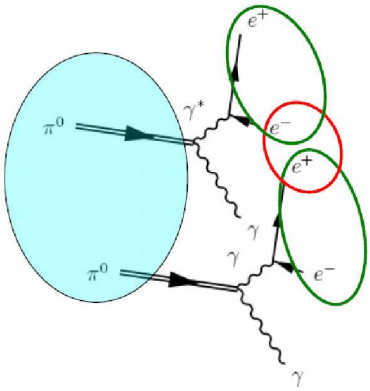

Figure 3.15: With a red circle an example of combinatorial background source is indicated. Dilepton pairs are formed combining dilepton coming from different mother-particle in the same event. This is the source of uncorrelated pairs.

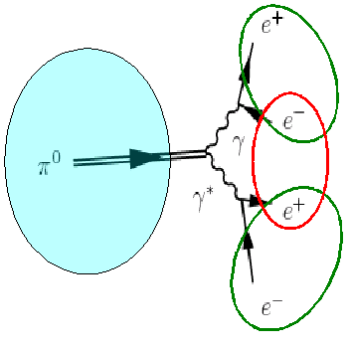

Figure 3.16: Example of correlated combinatorial pair created by a single π^0 Dalitz decay. Green circles represent the true pairs, the red one shows a correlated background pair.

Those like-sign pairs, which originate from the same source (*e.g.* $\eta \to e^+e^-e^+e^-$), have small branching ratio (*i.e.* $BR < 6 \cdot 10^{-5}$) and are rare, therefore like-sign pairs are created mostly by combining leptons from different decay vertices. Due to random combination of like-sign pairs, their invariant-mass distribution should not have any structure, but be rather smooth. However, these kind of pairs could eventually produce a correlation.

3.3.2 Background Rejection

As it was mentioned in Sec. 3.3.1, background pairs result from the combination of two leptons produced mainly by two processes: γ-conversion and π^0 Dalitz decay. The uncorrelated pairs are created by combining leptons originating from independent sources. The correlated pairs are formed by combining dileptons coming from the same source, but not from the same intermediate (virtual) photon. The invariant-mass distribution of these pairs forms a peak structure below the pion mass.

A statistical procedure has to be used in order to determine the combinatorial background. The distribution of the real physics signal ($S_{e^+e^-}$) is obtained by subtracting the distribution of uncorrelated pairs ($CB_{e^+e^-}$) from the unlike-sign distribution ($N_{e^+e^-}$). It holds the following relation:

$$S_{e^+e^-}(M_{e^+e^-}) = N_{e^+e^-}(M_{e^+e^-}) - CB_{e^+e^-}(M_{e^+e^-}) \tag{3.12}$$

where $M_{e^+e^-}$ indicates the invariant-mass of the e^+e^- pair.

The reconstruction of the combinatorial background can be established by two methods:

- Like-sign same-event combinatorial background (see Sec. 3.3.2.1).
- Mixed event technique (see Sec. 3.3.2.2).

In the next sections both methods are presented. However in the present data analysis, the like-sign method has been used to estimate the background.

In the mixed event technique, the pairs of the unlike-sign background are created by combining particles produced in different events. By construction, the mixed event technique is produced with uncorrelated leptons. The advantage of the mixed event technique is that a very high statistical precision can be reached. This method could be used to reproduce the uncorrelated background in the intermediate and high invariant-mass region ($> 0.15\ GeV/c^2$). The disadvantage consists in the possibility to create systematical errors due to its construction method itself and the impossibility to reproduce possible correlation.

3.3.2.1 Like-Sign Pair Same Event Technique

This method is based on the observation that the same-event combinatorial like-sign background is a good approximation for the combinatorial unlike-sign background. If there are no correlated like-sign pairs from physics origin and supposing that the acceptance and efficiency for electrons and positrons are the

same, the invariant-mass distribution of the like-sign pairs is smooth. However, at low invariant-mass ($M_{ee} < 0.150\ GeV/c^2$) there is correlated background (see Fig. 3.16) which appears as a bump-like structure in the like-sign invariant-mass distribution, in Fig. 3.17.

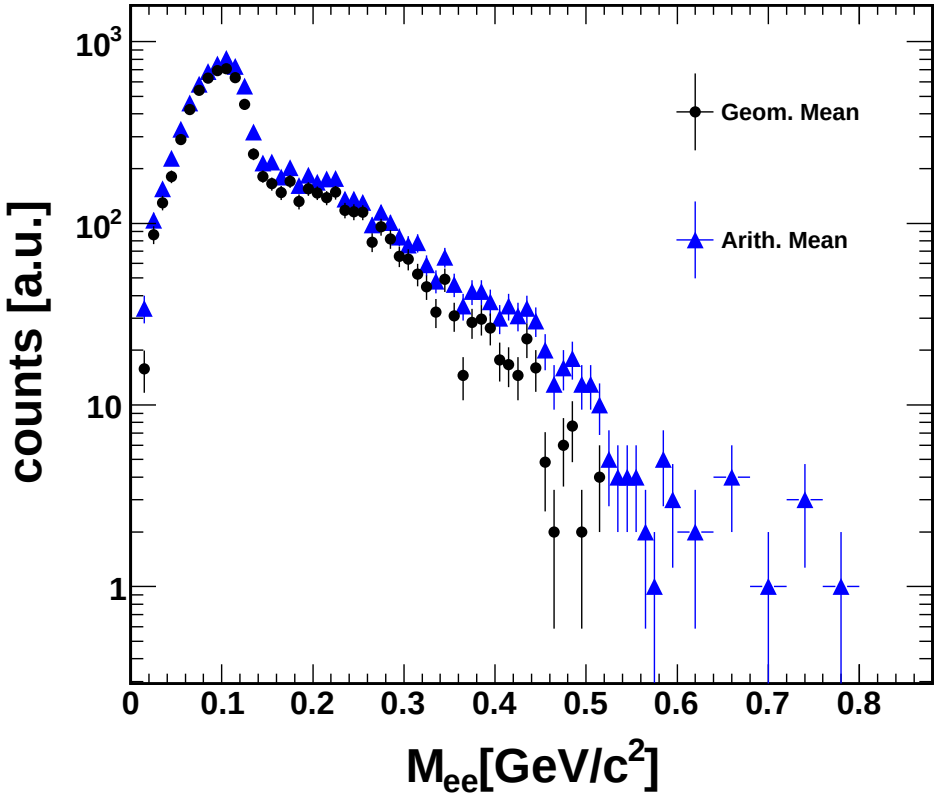

Figure 3.17: Like-sign invariant-mass spectrum. The last five points of the arithmetical mean (blue points, upper curve) at high invariant-mass are re-binned (20 MeV/c^2) instead of 10 MeV/c^2.

However, this technique has the disadvantage that the statistics in the background spectrum is limited to the number of available events. The combinatorial background can be described by the simple formula [55]:

$$CB_{e^+e^-}(M_{e^+e^-}) = 2 \cdot \sqrt{N_{e^+e^+}(M_{e^+e^+}) \cdot N_{e^-e^-}(M_{e^-e^-})} \tag{3.13}$$

or

$$CB_{e^+e^-}(M_{e^+e^-}) = N_{e^+e^+}(M_{e^+e^+}) + N_{e^-e^-}(M_{e^-e^-}) \tag{3.14}$$

where Eqn. 3.13 is the geometrical mean and Eqn. 3.14 the arithmetical mean of like-sign pair distributions ($N_{e^+e^+}$ and $N_{e^-e^-}$). Fig. 3.17 shows the invariant-mass distribution for like-sign pairs obtained with arithmetical and geometrical means.

The distributions in Fig. 3.17 are almost identical, however they differ for invariant-mass larger than 0.4 GeV/c^2. This difference could be due to the fact that the $N_{e^+e^+}$ and $N_{e^-e^-}$ distributions are not identical. Already in Sec. 3.2.6 has been shown an asymmetry in the single lepton sample as function of the lepton momentum (see Fig. 3.13). It is clear from the definition of Eqns. 3.13 and 3.14 that the geometrical mean suffers more than the arithmetical mean for lower statistics in Fig. 3.17. However, if this difference was larger, then $CB_{e^+e^-}$ evaluated with Eqn. 3.14, could be overestimated and therefore the signal underestimated.

Since the present work focuses on the study of high invariant-mass region ($0.6\ GeV/c^2 < M_{ee} < 0.8\ GeV/c^2$) the same-event like-sign (arithmetical mean) is used to estimate the combinatorial background.

3.3.2.2 Mixed-Event Technique

The possibility to use the event mixing method to estimate the background has been considered in the present work but it was not used in the analysis of this data set.

In the mixed event technique [55] unlike-sign pairs from different events (uncorrelated tracks) are combined to yield the combinatorial unlike-sign background. By construction, this strategy leads to uncorrelated pairs. Compared to the same event like-sign method, this method offers a much better statistical precision, specially since one can mix the tracks of each event with the tracks of many other events. Given a data sample of N_{event}, "mixing the events" consist of pairing one lepton in the sample with leptons generated in different events, therefore different sources are considered. The leptons are paired with different polarity.

This method was used in [16, 17] in order to describe the combinatorial background in the invariant-mass region $M_{ee} > 0.15\ GeV/c^2$, while the like-sign same event method was used for invariant-masses $M_{ee} < 0.15\ GeV/c^2$. The opposite sign mixed event strategy was used to compensate for the decreasing statistics at high invariant masses.

3.3.2.3 Angular Cuts

The aim of the pair analysis is the suppression of background pairs, in order to reach a good signal to background ratio. Therefore the background rejection is

an important point of the whole dilepton analysis.

In the background rejection strategy angular cuts are used to reduce the sources of background. This includes two cuts:

- Single lepton cut: this cut removes single tracks whose partner was not properly reconstructed (*e.g.* one of the two tracks has a missing hit in one or more detectors).

- Pair cut or opening angle cut[9] : this cut rejects the main source of combinatorial background which is due to photon conversion processes.

These cuts are applied "recursively": this means that this cut does not reject only the pair from the sample on which it acts on, but also all other pairs which include one of the two tracks of the pair which have been removed by the cut. The reason of the "recursive" cut are the following: a pair, which has been cut by a condition on opening angle, is most likely a pair produced by γ conversions. This pairs should not be used in the "pairing procedure" as already mentioned in the introduction of Sec. 3.3. Moreover, if a pair is formed by two tracks which share one or more hits in any detector, most likely one of the two tracks is a fake or a misidentified particle. These kind of pairs (both legs) are removed from the lepton sample and are not considered in the "pairing procedure" as well.

Single Lepton Cut: This cut removes from the lepton sample single tracks. It can happen that a track, which builds up a pair, is not resolved in all detectors. *I.e.* if one of the leg of a γ conversion pair has a small momentum ($p < 50\ MeV/c$), the magnetic field removes these particles. If this happens, the double track piece before the field is matched with a single META (see Sec. 2.6.1) hit of the accepted lepton. In this case the well-defined lepton track could be used in the "pairing procedure". In order to exclude this track, the cut called "cut on angle with the closest non-fitted lepton" is applied. This cut requires that the opening angle between each leg of a pair is greater than 9 *deg*. This cut removes from the lepton sample only single tracks which have non-fitted leptons closer than 9 *deg* (see Fig. 3.18b).

Pair Cut: 9 *deg* is the minimum angle which is formed between two legs of a lepton pair in order to be accepted in the analysis. It has been shown already

[9]The angle formed by two 3-momentum vectors (one positron and one electron momentum) is called opening angle of the lepton pair.

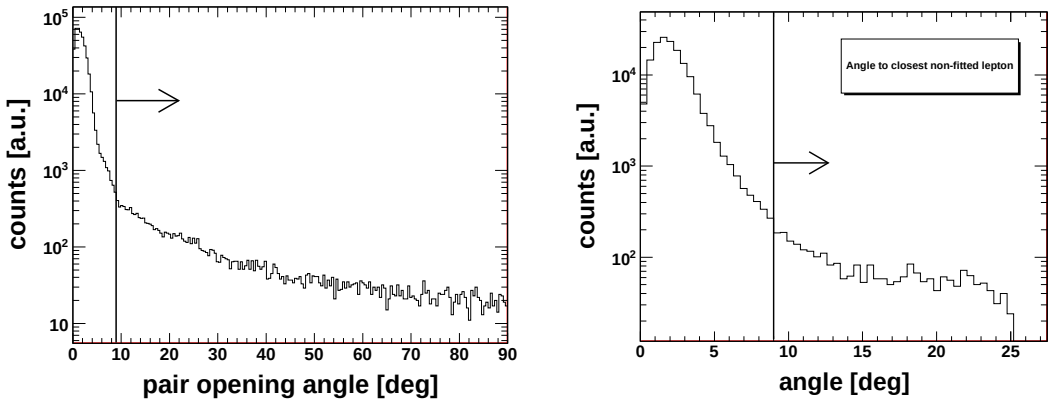

(a) (b)

Figure 3.18: Left: distribution of the opening angle of e^+e^- pairs and the cut applied: only those pairs with on opening angle larger then 9 *deg* are considered in the analysis. Right: angle to the closest non-fitted lepton distribution. The vertical lines at 9 *deg* and arrows represent the cuts applied.

in previous analysis, based on PLUTO[10] simulation [16, 17], that the opening angle condition $\theta_{e^+e^-} > 9^\circ$ removes the γ conversion pairs (see Fig. 3.18a). Unfortunately, it also removes partially contributions from π^0 Dalitz and η Dalitz decays. If a pair does not pass the 9 *deg* opening angle cut, then both legs which build up the pair are removed from the lepton sample.

3.4 Efficiency Correction Procedure

Before comparing the invariant-mass spectra with theory models, the data recorded with HADES have to be corrected for detector and reconstruction inefficiencies.

There is no attempt to extrapolate the measured dielectron yields to the full solid angle, therefore HADES data is not corrected for the geometrical

[10]The PLUTO package is based on ROOT [63] and it is written with the C++ programming language. PLUTO is a software tool to simulate particle emission from hadronic reactions. It is able to emit mesons and baryonic resonances without a collision and without considering energy and momentum conservation, by a special particle. This means that first the particles are created and sub-sequentially decay in the PLUTO framework [59]. The parameters of the reactions after the freeze-out point (meson multiplicities, angular distribution and temperature parameters) are taken or estimated from the known experimental data. Dileptons are produced from decays of hadrons with the corresponding branching ratio and angular distribution.

acceptance. The concept of acceptance, which is mentioned in this section, refers to the probability for a particle to travel through the active area of the detector. The effect of the polarity of the magnetic field is taken into account in the simulation. The acceptance is defined as the ratio between the number of test particles which pass through the detector to the total number of test particles which have been generated via simulation. The acceptance is defined for electrons and positrons separately in phase space bins defined by momentum (p) and emission angles (θ and ϕ):

$$Acceptance_i(p,\theta,\phi) = \frac{N_{accepted}(p,\theta,\phi)}{N_{4\pi}(p,\theta,\phi)} \tag{3.15}$$

where index i (1,2) defines the polarity of the test particles. In the determination of $Acceptance_i(p,\theta,\phi)$ the inefficiencies of the cut applied in the analysis are not included as well as the single detector inefficiencies.

The efficiency is then determined as the ratio of the number of correctly reconstructed test particles to the number of all test particles which were in the geometrical acceptance. The efficiency is calculated for each bin defined by (p,θ,ϕ).

$$Efficiency_i(p,\theta,\phi) = \frac{N_{reconstructed}(p,\theta,\phi)}{N_{accepted}(p,\theta,\phi)} \tag{3.16}$$

The probability to observe a produced dilepton entering the HADES acceptance

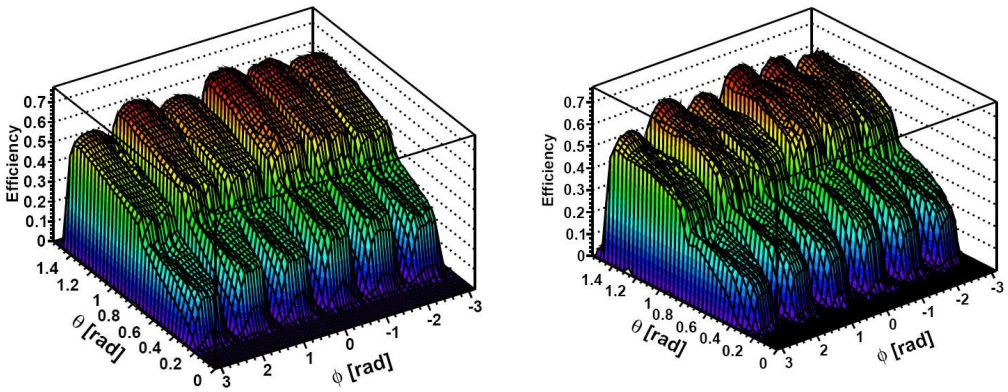

Figure 3.19: Efficiency matrices as function of polar angle (θ) and azimuthal angle (ϕ). The matrices have been averaged over electron (left) and positron (right) momenta (p) in the range 0.08 $GeV/c < p <$ 2.0 GeV/c.

is reduced by the HADES detection efficiency and by the track reconstruction efficiency. The pair efficiency can be factorized[11] into single-track efficiencies for positron (ϵ_+) and electron (ϵ_-):

$$\epsilon_{pair}(p, \theta, \phi) = \epsilon_+ \cdot \epsilon_- \tag{3.17}$$

The pair reconstruction efficiency can be expressed in terms of the single-track parameters by a 3-dimensional matrix as function of polar angle (θ), azimuthal angle (ϕ) and particle momentum (p) computed in the laboratory system.

The efficiency response of the detector is computed through the "track embedding" method and is determined following different analysis steps:

- **Event Generation**: "white" single leptons distributions[12] are generated by the PLUTO [56, 57, 58] event generator. These events are generated taking into account the vertex coordinates (three coordinates) and the sequential number of the real event, which are stored in the output files as well. The output files produced in this step are used as input files in the next step.

- **Event Simulation**: the simulated events are propagated through the spectrometer simulation (GEANT [60]), which determines and applies the spectrometer acceptance. The purpose of GEANT is the simulation of the detector response of the HADES spectrometer to the passage of charged particles. The simulated events which are propagated through the spectrometer have the same vertex coordinates as the real one. The output data has the same structure as the real one, therefore it is used as input for the reconstruction programs in the same way as for the real data.

- **Event Digitization**: the resulting events were digitized and processed in order to take into account the detector and electronics response (*e.g.* electronics noise). The digitizers are part of the HYDRA framework and give the response of each sub-detectors. All parameters needed by the digitizers are retrieved from the ORACLE database in order to be consistent with the analysis of the real events.

- **Event Embedding**: the simulated events produced in the previous analysis steps are embedded into real data events. This is a technique to

[11] There are no reasons for a correlation of reconstruction losses of tracks generated by e^+ and e^- in the same event. This is an important assumption and has been checked in our simulations and proven to be valid within 15% for pairs with opening angles $\theta_{e^+e^-} > 9°$ [87].

[12] The adjective "white" means that electron and positron were generated randomly with a uniform distributions in p, $cos\theta$ and ϕ with momentum range $0\ GeV/c < p < 2.0\ GeV/c$ and angle range $0\ ° < \theta < 90°$ and $0° < \phi < 360°$.

find out about the reconstruction efficiency under "realistic" conditions. "Realistic" means that background of the simulated tracks is as close as possible to the real one. The sequential number of the events is used to synchronize the embedded events with the real events.

- **Event Reconstruction**: the full events are reconstructed and the same cuts applied in the real data are considered in this stage.

The single-electron efficiencies, ϵ_+ and ϵ_- were calculated as a function of charge, momentum (p), polar angle (θ), and azimuthal (ϕ) emission angles. The efficiency matrices have been computed with 20 bins in θ, 40 bins in ϕ and 80 bins in p.

Fig. 3.19 shows the efficiency matrices for electron (left) and for positrons (right), averaged over all momenta. On average, for low θ angles ($\theta < 50°$) the efficiency is between 30 % and 40 % and for high θ it is around 60 %-70 %. Fig. 3.20 shows the efficiency matrices projected on θ and p axis.

The data has been corrected on a pair-by-pair basis with the weighting factor $1/\epsilon_{pair}(p, \theta, \phi)$, for given electron/positron momentum and emission angles (p, θ, ϕ).

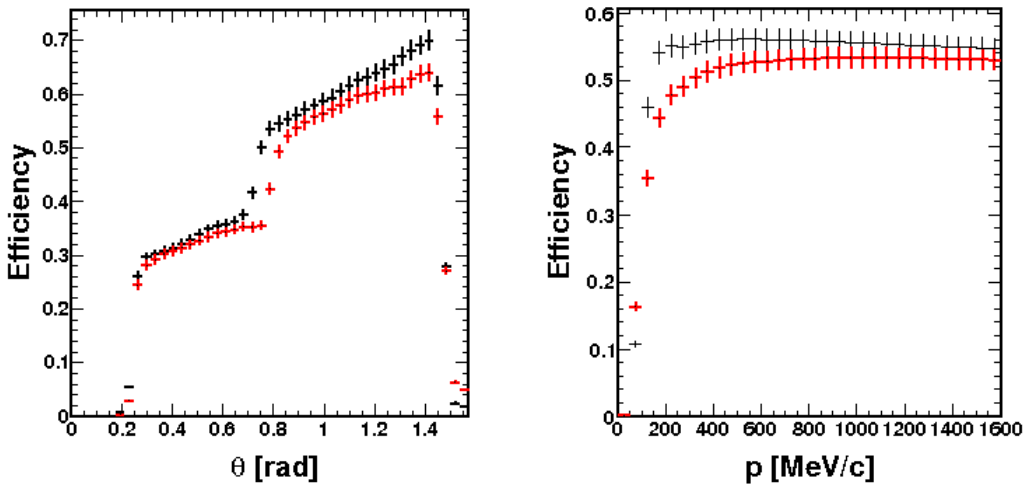

Figure 3.20: Projection of the efficiency matrices as function of polar angle (θ) and momenta (p). The black color refers to e^- (upper curve), while the red color refers to e^+ (lower curve).

Only dileptons passing through the "fiducial region"[13] of each detector were

[13]The "fiducial region" consists of the active area within each sectors. *I.e.* 4° cuts have been

considered in the matrix calculation.

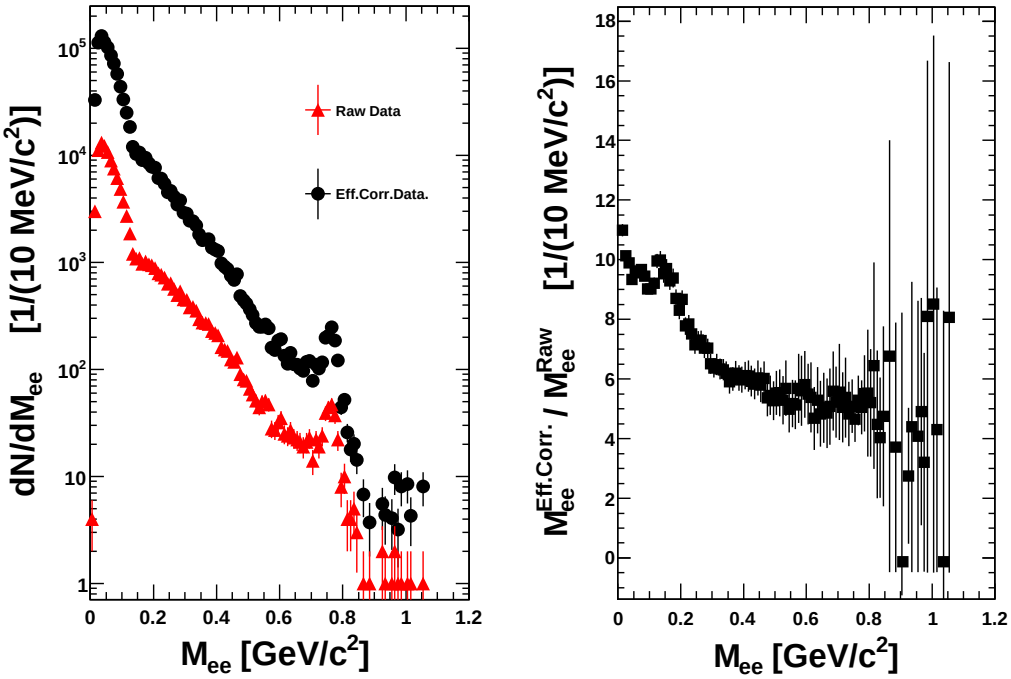

Figure 3.21: Left: invariant-mass spectra non corrected for efficiency (red triangle, lower curve) and efficiency-corrected (black circle points, upper curve). Right: ratio between raw and corrected spectra.

The effect of the efficiency correction can be seen in Fig. 3.21. Here the uncorrected and corrected experimental invariant-mass distributions and the ratio of the two distributions are plotted. A correction factor of ~ 9.5 in the low mass region is applied ($M_{e^+e^-} < 0.1\ GeV/c^2$). In the higher invariant-mass region ($M_{e^+e^-} > 0.4\ GeV/c^2$) the correction factor remains constant between 4 and 6.

With the same procedure, the CB was treated and subtracted from the opposite-sign sample. In Fig. 3.22, on the left hand side, the like-sign combinatorial background, before and after efficiency correction, is plotted. On the right side the ratio between the two spectra is plotted.

applied in ϕ angle on the left and on the right of each sector's side. These cuts avoid the creation of large fluctuations on the border of each sector.

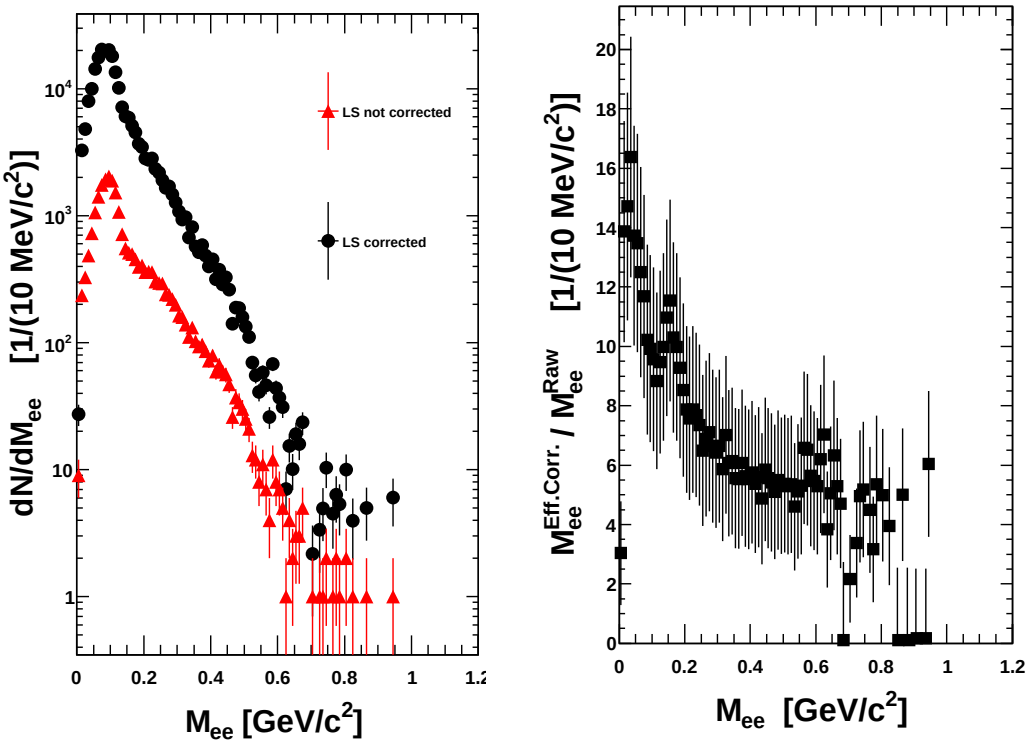

Figure 3.22: Left: Like-sign combinatorial background. The plots show the raw (red triangle, lower curve) and the efficiency-corrected spectra (black circle points, upper curve). Right: Ratio of the efficiency-corrected and raw data.

3.4.1 The LVL2 Trigger Efficiency Study

The beam intensity for HADES operation is about 10^7 particles per second, which is reduced to 10^5 collision events per second, due to the target interaction length of 1%. The number of events per unit time is too high to be stored, therefore a second level trigger (LVL2) is used to select events containing at least one lepton. With this trigger architecture, already presented in Sec. 2.8, the dileptons were selected on-line with dedicated hardware modules.

In order to understand possible biases due to the event selection procedures on the physical quantities of interest, the LVL2 efficiency has been studied. The LVL2 efficiencies are defined as:

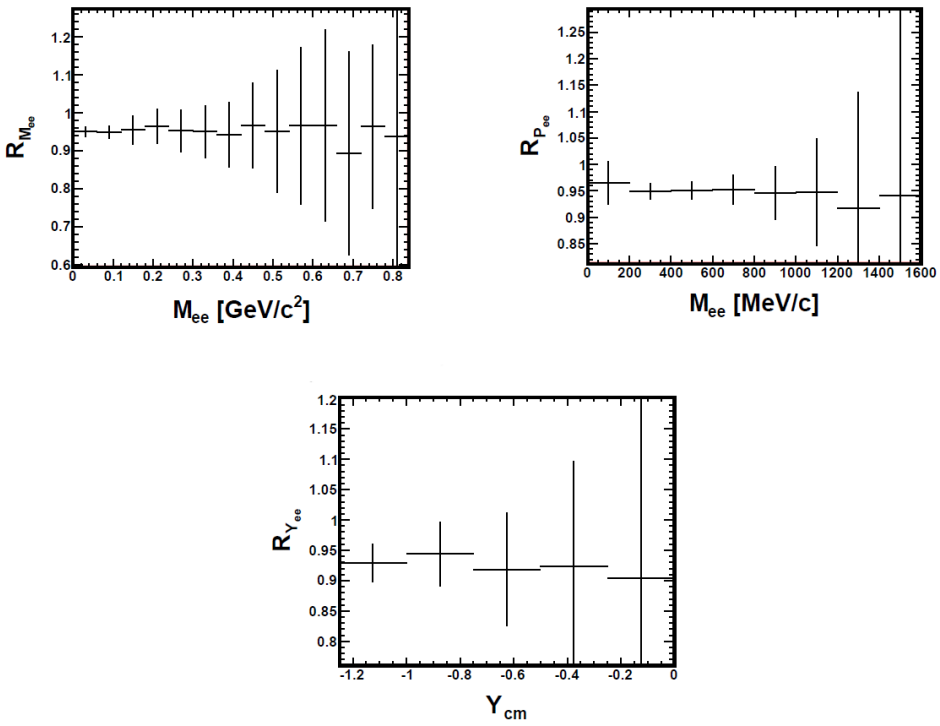

Figure 3.23: LVL2 efficiencies as a function of invariant-mass, transverse momentum and rapidity of the unlike-sign pairs.

$$R_{M_{ee}} = \frac{M_{ee}^{LVL2}}{M_{ee}^{LVL1}} \quad , \qquad R_{p_{ee}} = \frac{p_{ee}^{LVL2}}{p_{ee}^{LVL1}} \quad , \qquad R_{Y_{ee}} = \frac{Y_{ee}^{LVL2}}{Y_{ee}^{LVL1}} \tag{3.18}$$

The above equations represent the ratio between the number of dileptons found in one LVL2 event with respect to the number of dileptons found in the corresponding LVL1 event per invariant-mass (M_{ee}), momentum (p_{ee}) and rapidity (Y_{ee}) bin. Eqns. 3.18 are plotted in Fig. 3.23 after all dilepton cuts have been applied. These relative efficiencies turn out to be independent of invariant-mass, momenta and rapidity of the pairs. The average efficiency in the second-level trigger, entering in the final invariant-mass spectrum, has been computed to be $\epsilon_{LVL2} = 0.945 \pm 0.011$ in the full invariant-mass region ($0\ GeV/c^2 < M_{ee} < 0.85\ GeV/c^2$).

3.5 Estimation of the Systematic Errors

All measurements are prone to systematic errors. Systematic errors are "biases" in measurements which lead to the situation where the mean of many separate measurements differs significantly from the actual value of the measured attribute. By contrast to the statistical error, systematical errors act in the "same direction" and may be due to imperfect calibration of measurement instruments, changes in the environment which interfere with the measurement processes or to imperfect knowledge of the experimental conditions.

In the case of the analysis here presented, the main contributions to the systematical uncertainties are:

- The normalization of the dilepton yield to the elastic scattering cross section $\sigma_{ppelastic} = \pm 20\%$ [80]. (See Sec. 3.6).
- Uncertainties due to the efficiency correction. Correcting the dielectron spectrum by detector efficiency introduces a systematical error of $\sigma_{eff} = \pm 35\%$.

The systematical uncertainties come from independent measurements, hence they can be added quadratically: $\sigma_{sys} = \sqrt{(\sigma_{eff})^2 + (\sigma_{ppelastic})^2} = 40.3\%$ and can be applied to the whole invariant-mass dielectron spectrum.

3.6 Selection of Elastic p + p Scattering Events

During the experiment run in year 2007, p + p elastic scattering events were selected by triggering on at least two charged particles in opposite sectors of the time-of-flight detectors. The elastic p + p events have been used to derive the absolute normalization of the invariant-mass spectrum presented in this work. These events are also useful in order to investigate the dependence of the momentum resolution on particle momentum as well.

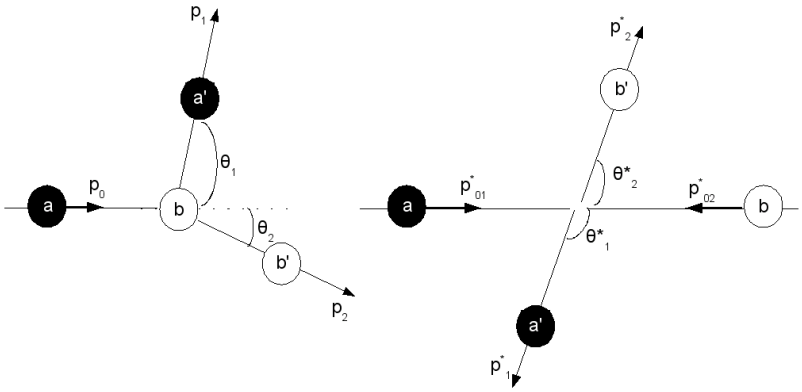

Figure 3.24: Left: p + p elastic event in the laboratory frame. Right: the same event viewed in the center-of-mass system of the two protons. The apostrophe indicates that the particles in the initial state and in the final state are identical, except to momenta and energies.

In an elastic process such as:

$$a + b \rightarrow a' + b' \tag{3.19}$$

the same particles are present both before and after the scattering process. The target particle (b) remains in its ground state, absorbing the recoil momentum and hence changing its kinetic energy. a represents the incoming beam particle. Fig. 3.24 shows a sketch of the elastic process in two reference frames: the laboratory frame and the center-of-mass frame.

The following relations are used to select the elastic events. Scattering angles, energy of particle a' and energy of particle b' are correlated as shown in the equation:

$$tan\theta_1 \cdot tan\theta_2 = \frac{1}{\gamma_{cm}^2} \tag{3.20}$$

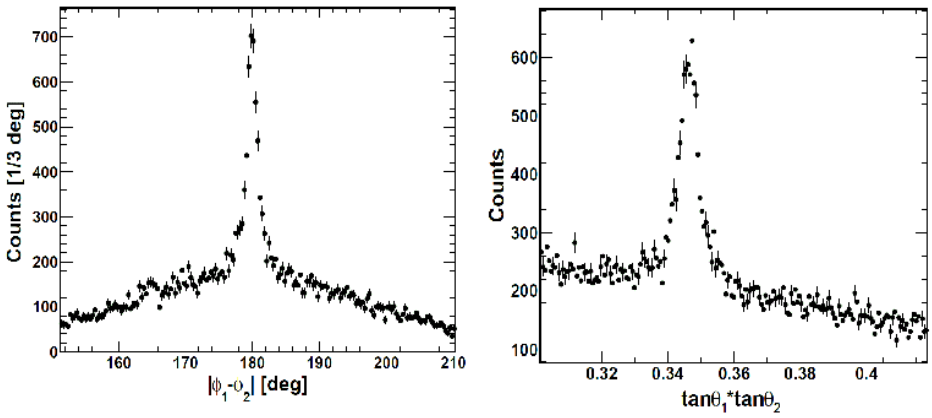

Figure 3.25: Left: coplanarity distribution for azimuthal angles ϕ_1 and ϕ_2. The peak is centered at mean $180.019° \pm 1.316°$. Right: angular distribution between polar angles (θ_1 and θ_2), here the peak is centered at 0.346 ± 0.004.

where γ_{cm}^2 is the Lorentz factor of the pp center-of-mass system in the laboratory frame. This factor can be computed using the relation:

$$\gamma_{cm} = \sqrt{\frac{E_0 + m}{2m}} = \sqrt{\frac{\gamma_0 + 1}{2}} \tag{3.21}$$

E_0 is the total energy of the proton beam, m is the proton rest mass. At 3.5 GeV beam kinetic energy, $\gamma_{cm}^{-2} = 0.349$. Hence, elastic events were selected by imposing momentum conservation, $|\phi_1 - \phi_2| = 180°$ and the relation between polar angles θ_1 and θ_2, (Eqn. 3.20).

Fig. 3.25 shows the correlation relations between the scattering angles. The peaks indicate the elastic p + p events.

Data from p + p elastic events have been also used to investigate the dependence of the momentum resolution on the particle momentum. The momentum of the outgoing proton can be expressed as a function of its polar angle:

$$p_{a'}(\theta_{a'}) = \frac{p_{a'}}{cos(\theta_{a'})\ [1 + tan^2(\theta_{a'})\gamma_{cm}^2]} \tag{3.22}$$

and comparing the reconstructed momenta using only the polar angle with the measured momenta, the resolution is estimated as $\sigma_p/p \simeq 3 - 4\%$ for proton momenta in the range of 1.0-3.0 GeV/c [87].

3.7 Cross Section Determination

Due to the high intensity proton beam the START and VETO detectors were not used in the experiment presented in this thesis (see Sec. 2.2), therefore it was not possible to directly monitor the incoming beam particles.

The cross section was determined by measuring the yield of a given channel relative to that of a simultaneously measured channel with known cross section. The reference channel is the reaction pp→pp, for which a large amount of data exist. By definition the cross section for a given channel (i) is defined by:

$$\sigma_i = \frac{N_i}{\Phi_a \cdot N_b} \quad [barn] \tag{3.23}$$

where N_i is the reaction rate (number of reactions per unit time). The denominator of Eqn. 3.23 is called luminosity ($L = \Phi_a \cdot N_b$) and it is the product of the number of incoming beam particles per unit time (Φ_a) and the number of scattering centers per unit area in the target (N_b). Like the flux, it has the dimensions of $[(area \times time)^{-1}]$[14].

Considering the reaction rate for the production of ω mesons (N_ω) and for the elastic scattering reaction ($N_{elastic}$), their respective cross sections are defined as:

$$\sigma_\omega = \frac{N_\omega}{\Phi_a \cdot N_b} \ [barn] \qquad \text{and} \qquad \sigma_{elastic} = \frac{N_{elastic}}{\Phi_a \cdot N_b} \ [barn] \tag{3.25}$$

By taking the ratio, the cross section of the ω meson is expressed in terms of $\sigma_{elastic}$ in the HADES detector acceptance and the normalization factor used as reference for the dielectron yield is N, given by:

$$\sigma_\omega = \frac{N_\omega}{N_{elastic}} \cdot \sigma_{elastic} \quad [barn] \qquad \text{and} \qquad N = \frac{N_{elastic}}{\sigma_{elastic}} \quad [barn^{-1}] \tag{3.26}$$

In Eqn. 3.26, N is the ratio between the total number of elastic scattering events produced in the HADES acceptance ($N_{elastic}$) and $\sigma_{elastic}$ is the elastic p + p cross section computed in the HADES acceptance ($\sigma_{elastic} = 0.16\ mb$ and

[14]The cross section is a physical quantity with dimension of [area]. A commonly used unit is the *barn*, which is defined as:

$$1\ barn = 1\ b = 10^{-28}\ m^2 \tag{3.24}$$

$N_{elastic}/\sigma_{elastic} = 1.75 \cdot 10^7$ $[mb^{-1}]$). "Computing $\sigma_{elastic}$ in the HADES acceptance" means calculating the value of $\sigma_{elastic}$ from the elastic p + p cross section that was determined with a different apparatus at wider acceptance (namely different polar angles). $\sigma_{elastic}$ has been computed in the HADES detector acceptance ($55° < \theta_{lab} < 155°$) using data published in [62]. The computation of $\sigma_{elastic}$ is the main source of systematic uncertainties, since $\sigma_{elastic}$ has been measured with a different apparatus acceptance at energies close to the beam energy of 3.5 GeV[15]. The final differential dielectron production cross section is given by:

$$\frac{d\sigma}{dM_{ee}} = \frac{1}{N \cdot \epsilon_{LVL2} \cdot \epsilon_{pair}(p,\theta,\phi)} \cdot \frac{dN_{ee}}{dM_{ee}} \quad [mb\ MeV^{-1}c^2] \tag{3.27}$$

where:

- dN_{ee}/dM_{ee}: number of e^+e^- measured per invariant-mass bin of 10 MeV/c^2 width.
- ϵ_{LVL2}: efficiency in the second level trigger (LVL2) selection process. The description can be found in Sec. 3.4.1.
- $\epsilon_{pair}(p,\theta,\phi)$: reconstruction efficiency factor, explained in detail in Sec. 3.4.

[15] More precisely the cross sections published in [62] which were considered here in order to compute $\sigma_{elastic}$ in the HADES acceptance were computed at two incident beam kinetic energies, one below and one above the energy of interest (3.5 GeV): 2.35 GeV and 3.83 GeV respectively.

3.8 Identification of the Inclusive Reaction Channel $pp \to X\omega$

3.8.1 Invariant Mass Spectra

The analysis of the measurement of inclusive e^+e^- pair production yields a striking signal at the ω pole mass in the invariant mass distribution, in Fig. 3.26. More than $6.5{\cdot}10^6$ pairs have been obtained in the full mass range; in the π^0 region ($M_{ee} < 0.2\ GeV/c^2$) $5.2{\cdot}10^6$ pairs and 350 pairs in the ω meson region ($0.6\ GeV/c^2 < M_{ee} < 0.8\ GeV/c^2$).

The peak was fitted with a Gaussian to which a polynomial curve was added to approximate the physical background. The reconstructed ω meson signal has a width of $\sigma_{Gauss} = (18.65 \pm 0.98)\ MeV/c^2$ (or in terms of Full Width at Half Maximum (FWHM): $\Gamma_{Gauss} = 2 \cdot \sqrt{2 \cdot ln2} \cdot \sigma_{Gauss} \backsimeq 2.35 \cdot \sigma_{Gauss} = 43.82\ MeV/c^2$). The inset of Fig. 3.26 shows the ω meson peak on a linear scale.

The natural width of the ω meson reported in PDG [2] is $\Gamma_{PDG} = 8.49 \pm 0.12\ MeV/c^2$, which is smaller than the value extracted from the HADES measurement ($\Gamma_{Gauss} = 43.82\ MeV/c^2$). This difference is due to the finite resolution of the HADES detector. The width obtained from the data can not be explained by the quadratic sum of the natural width of the ω meson and the contribution of the detector resolution.

In order to better understand the resolution of the detector, the ω peak is fitted with a Voigt function, which is given by the convolution of the Lorentz function and a Gauss function. The shape of the vector meson is modeled by the first function, while the gaussian models the detector resolution. The relation between the two FWHM is expressed by: $\Gamma_{Voigt} = \Gamma_{Gauss} \oplus \Gamma_{Lorentz}$. Imposing $\Gamma_{Lorentz} = \Gamma_\omega = 8.49\ MeV/c^2$, the resolution of the detector is estimated to be $\sigma_{Gauss} = 16.4\ MeV/c^2$. If in future HADES experiments, in the same experimental conditions, the ω meson was produced in heavy ion collision and it increased its width then the measured width would be larger. Tab. 3.2 reports the results of this exercise: the expected ω meson width are calculated in the hypothesis that the ω meson could increase its natural width by a factor 2, 3 or 4 due to possible medium effects.

The ω peak position at $m_\omega = (761.82 \pm 1.21)\ MeV/c^2$ is shifted by $-20\ MeV/c^2$ with respect to the low side of the nominal position ($m_{PDG} = (782.65 \pm 0.12)\ MeV/c^2$) reported in the PDG [2]. However, taking into account the energy loss of leptons (electrons and positrons) in the detector, the position of the peak agrees with the expected value within $10\ MeV/c^2$. The remaining $-10\ MeV/c^2$ can not be explained by the lepton energy loss in the

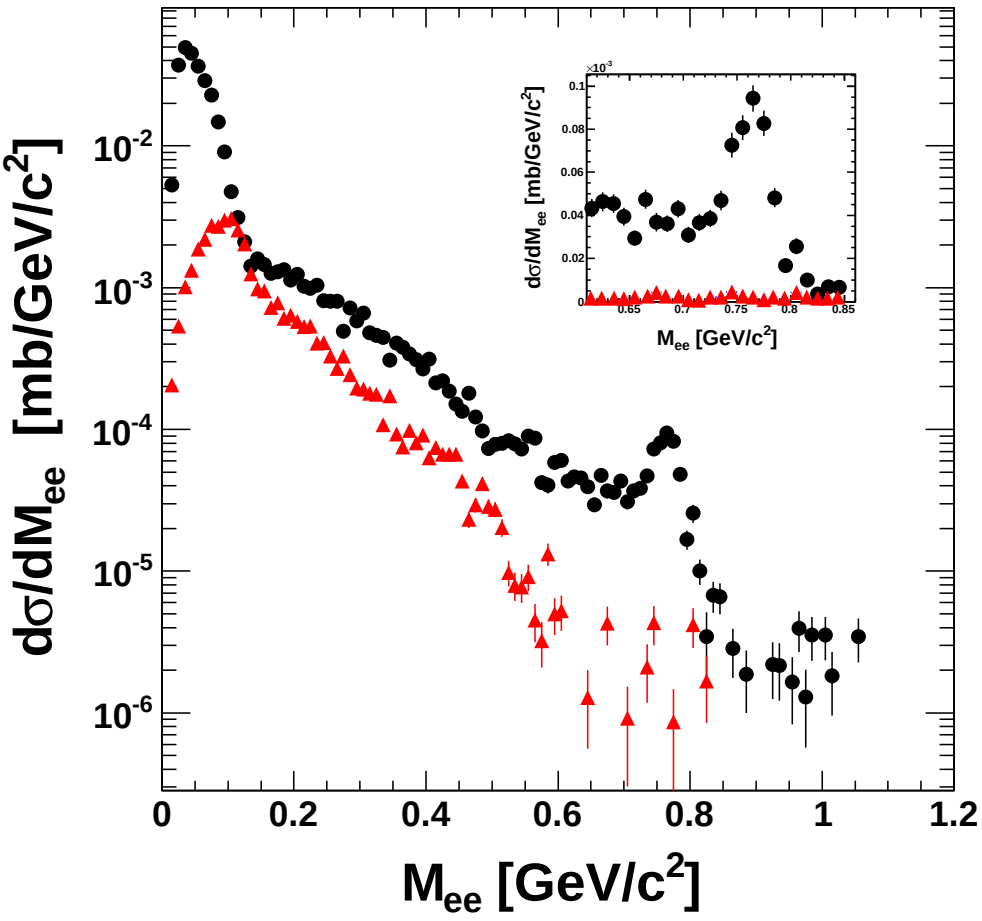

Figure 3.26: e^+e^- invariant-mass spectrum: signal (black colored circles) and background (red colored triangles). The spectrum is corrected for detector inefficiencies and normalized by proton-proton elastic cross section. The inset shows the ω meson signal and the combinatorial background in linear scale.

detector material. Since the momenta of the leptons coming from meson decays is about 200-600 MeV/c, there would have to be to much material in the active detector area to explain the remaining shift. Moreover, if the energy loss were not correctly considered, the shift in invariant-mass should apply to all meson sources in the spectrum, leading to a "global" shift of the whole dilepton spectrum to the left side. It is possible only to speculate about the reason of this shift, however more studies are ongoing. A possible explanation can be addressed to a not perfect knowledge of the magnetic field mapping or a systematic error in the current measurement of the magnetic field, which, even if

Γ_{Voigt} $[MeV/c^2]$	Γ_{Gauss} $[MeV/c^2]$ ($\sigma_{Gauss} = 16.4$ MeV/c^2)	Γ_ω $[MeV/c^2]$
41.11	38.54	$\Gamma_\omega = 8.49$
49.70	38.54	$\Gamma_\omega \times 2 = 16.98$
53.92	38.54	$\Gamma_\omega \times 3 = 25.47$
61.67	38.54	$\Gamma_\omega \times 4 = 33.96$

Table 3.2: The first line is the results of the fit of the distribution in Fig. 3.26 with a Voigt function. The second, third and fourth lines report the width of the ω which could be measured in the hypothesis its natural width increased by a factor 2, 3 or 4.

small, might affect the computation of each particle's momentum, leading to reduced lepton momenta.

The invariant-mass spectrum has been obtained with data collected in 20 days of experiment. In Tab. 3.3, the statistics of the experiment presented here is summarized. It is striking to see the huge number of LVL1 events which are needed to reconstruct the final pair signal. The LVL1 events which are reported in the table (both M3 and M2 triggers) are all events which have been recorded by HADES and written on the tape. This means these are events with a positive downscaling flag[16] and LVL2 are events with a positive second level trigger decision (at least one lepton candidate in the event). It is also important to remind that the LVL2 triggers are always written on the tape[17]. The events which are marked (M3-trigger) are events which have been recorded with at least three charged particles in the Multiplicity and Electron Trigger Array (META) detectors, consisting of time-of-flight scintillator walls (TOF/TOFino) and electromagnetic shower detectors (Pre-Shower).

[16]The downscaling factor for the M3 trigger was $DS = 3$ and for the M2 trigger $DS = 32$ (see Sec. 3.1). In order to obtain the total number of trigger "seen" by HADES during the acquisition time, one has to multiply the number of M3 trigger by a factor of 3 and the M2 trigger by a factor of 32.

[17]There is no downscaling factor for the second level trigger.

	Number of Events
LVL1 (M3-trigger)	$1.013 \cdot 10^9$
LVL1 (M2-trigger)	$4.854 \cdot 10^8$
LVL2	$2.822 \cdot 10^8$
LVL2 (M3-trigger)	$2.785 \cdot 10^8$
Number of pairs in the invariant-mass signal distribution	10^5
Observed ω mesons in the inclusive channel ($pp \rightarrow X\omega \rightarrow Xe^+e^-$)	275.4 ± 14.8
Observed ω mesons in the exclusive channel ($pp \rightarrow pp\omega \rightarrow ppe^+e^-$)	127.0 ± 31.1

Table 3.3: Summary of the statistics recorded by HADES during the experiment p + p at 3.5 GeV incident kinetic energy. The events recorded and the number of ω mesons reconstructed via the inclusive and exclusive decay channels are reported. The number of the ω mesons have been obtained by integrating the corresponding peaks in the region $0.65\ GeV/c^2 < M_{ee} < 0.82\ GeV/c^2$.

3.8.2 ω Meson: Spectral Shape and Integrated Production Cross Section in the Inclusive Dilepton Channel

In this section, special attention is placed on the spectral line shape of the ω meson and its inclusive production cross section, which is not known at SIS-18

energies.

Due to the large and flat acceptance of the HADES spectrometer for the e^+e^- invariant-mass above 0.2 GeV/c^2 and for transverse momentum of the pair $P_t < 1$ GeV/c, the acceptance correction can be considered model independent (see App. A). Again, the acceptance correction does not affect the spectral shape of the ω meson. This allows us to extract for the first time the ω meson production cross sections at these energies.

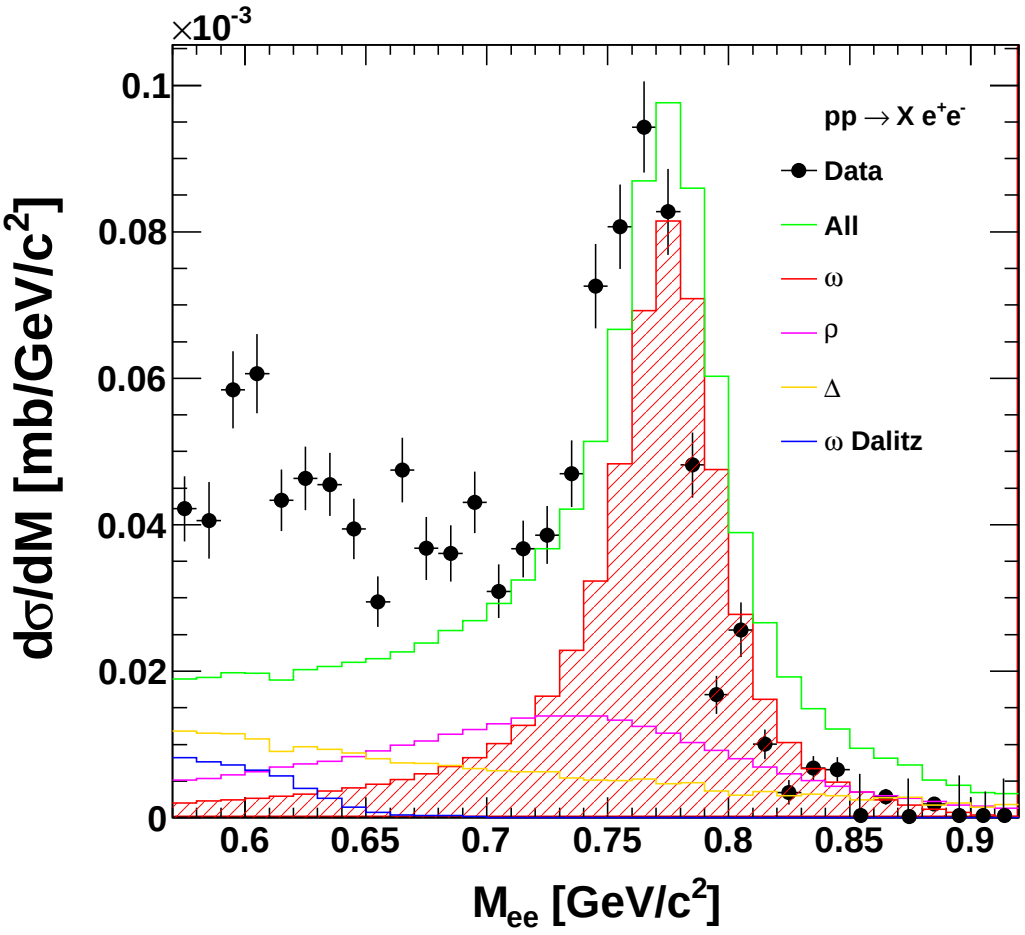

Figure 3.27: HADES data-points compared with the PLUTO cocktail, filtered through the HADES acceptance.

The spectrum already shown in Fig. 3.26 is plotted in Fig. 3.27 together with the PLUTO cocktail. Data is corrected for detector inefficiency (see Sec. 3.4) and normalized for the p + p elastic cross section (see Sec. 3.7). In order to understand the invariant-mass region around the ω peak (0.620 GeV/c^2 <

$M_{ee} < 0.900\ GeV/c^2$), three components in the cocktail have been chosen: ω and ρ mesons and the Δ resonance. The PLUTO cocktail has been generated with the input parameters listed in Tab. 3.4.

The overall normalization uncertainties are not shown in Fig. 3.27 since they do not affect the shape of the distributions. The bin width is 10 MeV/c^2. In

Reaction	Cross Section (mb)	Decay Mode	Branching Ratio
$pp \to pp\Delta$	22.0	$\Delta \to e^+e^-\gamma$	$4.0{\cdot}10^{-5}$
$pp \to pp\omega$	0.255	$\omega \to \pi^0 e^+e^-$	$7.7{\cdot}10^{-4}$
$pp \to pp\omega$	0.255	$\omega \to e^+e^-$	$7.2{\cdot}10^{-5}$
$pp \to pp\rho$	0.220	$\rho \to e^+e^-$	$4.7{\cdot}10^{-5}$

Table 3.4: Parameters entered into the PLUTO event generator in order to simulate p + p reactions at 3.5 GeV incident kinetic energy. These parameters have been chosen to match the experimental results.

Fig. 3.27, the ρ meson contributes to the peak yield only by a small fraction ($< 10\%$) and the Δ resonance by even less ($< 5\%$). It is important to quantify the yield of the ω meson in its spectral components: the peak and the tails. The total yield is shown with the red dashed area in Fig. 3.27. In order to estimate the cross section and the statistical error, the ω peak is integrated by a side band method. Accounting for the detector acceptance for lepton pairs[18], this value is:

$$\sigma_{pp\to X\omega} = 0.190\ \pm\ 0.010\ (Stat)\ mb \tag{3.28}$$

[18]For the considered reaction the pair acceptance has been estimated to be 30%.

However, taking into account the energy loss of electron/positron in the material, based on PLUTO model and GEANT calculations, the yield of the ω meson in the tails in the invariant-mass distribution is estimated to be $\sim 34\%$ of the total yield. After correcting for this factor, the inclusive production cross section becomes:

$$\sigma_{pp\to X\omega} = 0.2550 \pm 0.0140\ (Stat)\ ^{+0.0565}_{-0.0466}\ (Sys1) \pm 0.0797\ (Sys2)\ mb \quad (3.29)$$

The systematical uncertainties (Sys1) are estimated by changing the shape of the physical background under the ω meson peak and computing the corresponding variation in the ω meson yield, while the systematical uncertainties (Sys2) are due to the efficiency correction and the normalization procedure.

3.9 Identification of the Exclusive Reaction Channel $pp \to pp\omega$

In order to better understand the production mechanism of the ω meson, a dedicated analysis of the exclusive reaction $pp \to pp\omega \to ppe^+e^-$ is required. The quality of the data, already presented in this thesis and used to reconstruct the inclusive dilepton invariant-mass spectrum, allows to reconstruct the ω meson via its "exclusive dilepton channel". In the present chapter "exclusive ω production" stands for the exclusive reaction $pp \to pp\omega$.

This was possible by combining the invariant-mass and the missing-mass techniques, where one non-detected particle, namely one proton, was identified with the help of energy and momentum conservation laws. The acceptance of the detector was taken into account via a PLUTO simulation and the lepton reconstruction efficiencies were considered as well.

3.9.1 Analysis Strategy

The reaction $pp \to pp\omega \to ppe^+e^-$ can be selected by considering one unmeasured particle: one of the protons in the final state. The strategy used in this analysis follows three steps:

- Selection of the events.
- Particle identification and removal of fake tracks.
- ω meson reconstruction.
- Efficiency correction.
- Comparison of the HADES data with the PLUTO cocktail: estimation of the physical background.
- Cross section for the exclusive reaction $pp \to pp\omega$.

In this analysis only one proton is required to be in the detector acceptance. The second proton in the final state is found mostly out of the HADES acceptance (see Sec. 2), namely it goes at forward polar angles ($\theta < 18°$). Requiring two protons in the final state reduces the acceptance, therefore the statistics will be pretty low. The possibility to study this reaction with two protons in the final state is discussed in Sec. 4.1.3.

3.9.1.1 Selection of the Events

A minimal selection, based on the polarity of the particles, has been performed on all events. In a second step, all necessary cuts have been applied to the data sample and every track is marked with the corresponding flag, according to the particle identification strategy described in the next step (see Sec. 3.9.1.2). Following this strategy, all necessary cuts which were needed to identify protons and leptons were applied in the next analysis steps.

At first, the events were selected using the trigger information (M3 trigger), where only events containing at least three charged particles were considered.

Based on the polarity information, it was not possible to distinguish which of the positively charged tracks corresponded to protons, pions or positrons; for this reason, a table (or array) has been created, containing in each row a sub-event. Each sub-event was taken as a candidate for the next analysis steps. Tab. 3.5 shows the case when, in one event, exactly three positive and one negative particle candidates were detected. The identification of the particles was done in a second stage of the analysis. However, in general more tracks coming from physics processes and fake tracks were considered as well. For each event, many possible combinations can be created in the respective table.

Table 3.5: Three possible combinations (three sub-events) obtained from one event. In this simple example three positive particles (assumed to be two protons and one positron) and one negative particle (assumed to be a lepton) are considered. Each row of the table contains a sub-event with the pattern based on the polarity of the particles: [+ + + -].

p	**p**	e^+	e^-
p	e^+	**p**	e^-
e^+	**p**	**p**	e^-

3.9.1.2 Particle Identification and Removal of Fake Tracks

The particle identification has been obtained by the following methods: electrons and positrons by a corresponding ring in the Cherenkov counter, protons

by using a two dimensional condition on the β versus momentum plane.

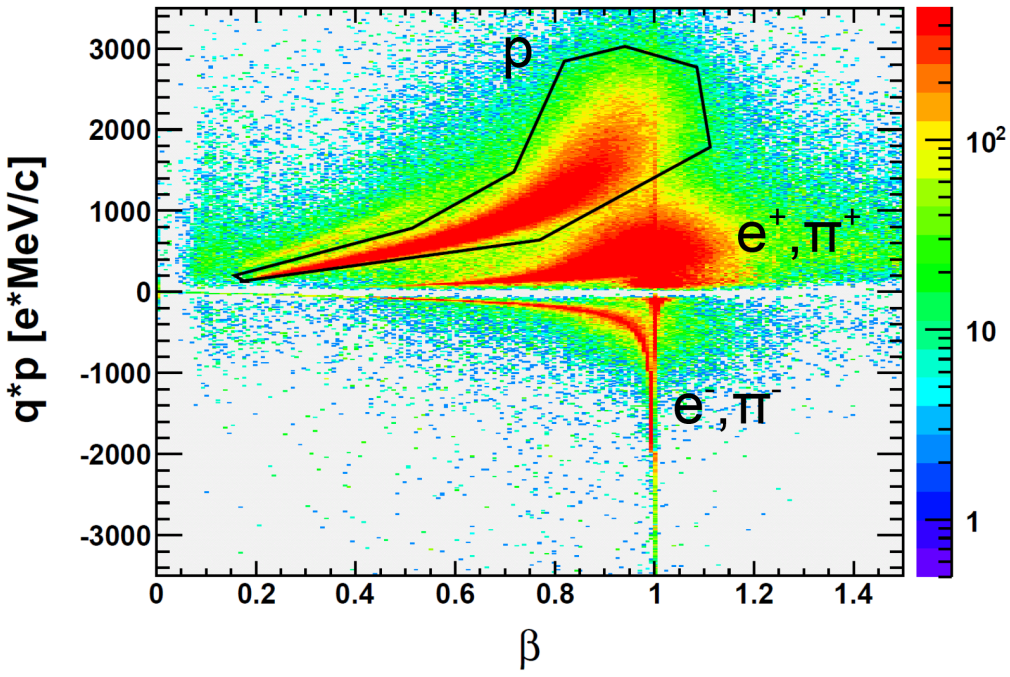

Figure 3.28: β versus momentum plane: the figure shows the graphical cut used for proton identification. However, e^+ and e^- were not selected using this method (see text for details). π^+ and π^- are visible and marked with a label as well.

In Fig. 3.28 only protons, pions and dileptons are visible. Only the protons were selected as shown by the graphical cut. The time of flight calculated for leptons was not used since the overlap between pions and electron/positron is still high. In order to not loose statistics, the lepton identification was done imposing conditions only on the existence of rings in the RICH detector. No quality cuts in the RICH detector and no quality cuts on the Pre-Shower detector were applied.

In the final state, one proton was not detected. Its properties were reconstructed using the kinematics of the reaction. Requiring two protons in the final state would reduce the interesting events and the statistics would be an important issue (see Sec. 4.1.3).

3.9.1.3 ω Meson Reconstruction

In order to detect short lived particles, one can detect their decay products. The short lived states can be selected by combining the invariant-mass (see Sec. 3.3) and the missing-mass methods.

The missing-mass method was adopted to determine the rest mass of the unobserved proton. In the laboratory reference system, the missing mass squared ($(M_{miss})^2$) is given by the formula:

$$(M_{miss})^2c^4 = (E_p + m_pc^2 - \sum_{i=1}^{n} E_i)^2 - c^2(\overrightarrow{p}_p - \sum_{i=1}^{n} \overrightarrow{p_i})^2 \qquad (3.30)$$

where the index i (1,...,n) indicates all observed particles in the final state (electron and positron), E_p is the kinetic energy of the incoming proton beam, m_p the proton mass and $\overrightarrow{p}_p$ the beam proton momentum, $\overrightarrow{p}_i$ is the electron and positron momenta in the laboratory frame and E_i their energies.

Fig. 3.29 shows the missing-mass distribution of three particles (pe^+e^-) versus the invariant-mass of two particles (e^+e^-). In the distribution the events corresponding to the ω meson are visible at missing-mass values around the proton mass (820 $MeV/c^2 < Miss_{(pe^+e^-)} < 1020\ MeV/c^2$) and invariant-mass values around the ω mass region (0.7 $GeV/c^2 < M_{ee} < 0.8\ GeV/c^2$). By adopting a cut of 2σ window around the proton peak (obtained by projecting on the horizontal axis the distributions in Fig. 3.29), the events with the missing proton can be selected.

With the constraint on the proton peak and the opening angle cut between the dilepton pairs of $\theta_{ee} > 10°$, the e^+e^- invariant-mass distribution is plotted in Fig 3.30. The opening angle cut has been applied mainly to remove conversion pairs in the low part of the invariant-mass spectrum.

Fig. 3.31 shows the polar angle correlation between the detected proton and the proton which has not been measured. On the vertical axis is plotted the polar angle of the detected proton, which reflects the acceptance of the detector (between polar angles 18° and 85°). On the horizontal axis the polar angle of the reconstructed proton is plotted. It is evident that most of the not detected protons were going into the forward direction, at low polar angles, outside the HADES acceptance (between 0° and 15°). The picture, on the right hand side, is plotted adopting the condition on the proton missing-mass (820 $MeV/c^2 < Miss_{(pe^+e^-)} < 1020\ MeV/c^2$).

3.9.1.4 Efficiency Correction

In Sec. 3.4 was already described the determination of the dilepton reconstruction efficiency. Following this procedure the single-electron efficiencies ($\epsilon_\pm$),

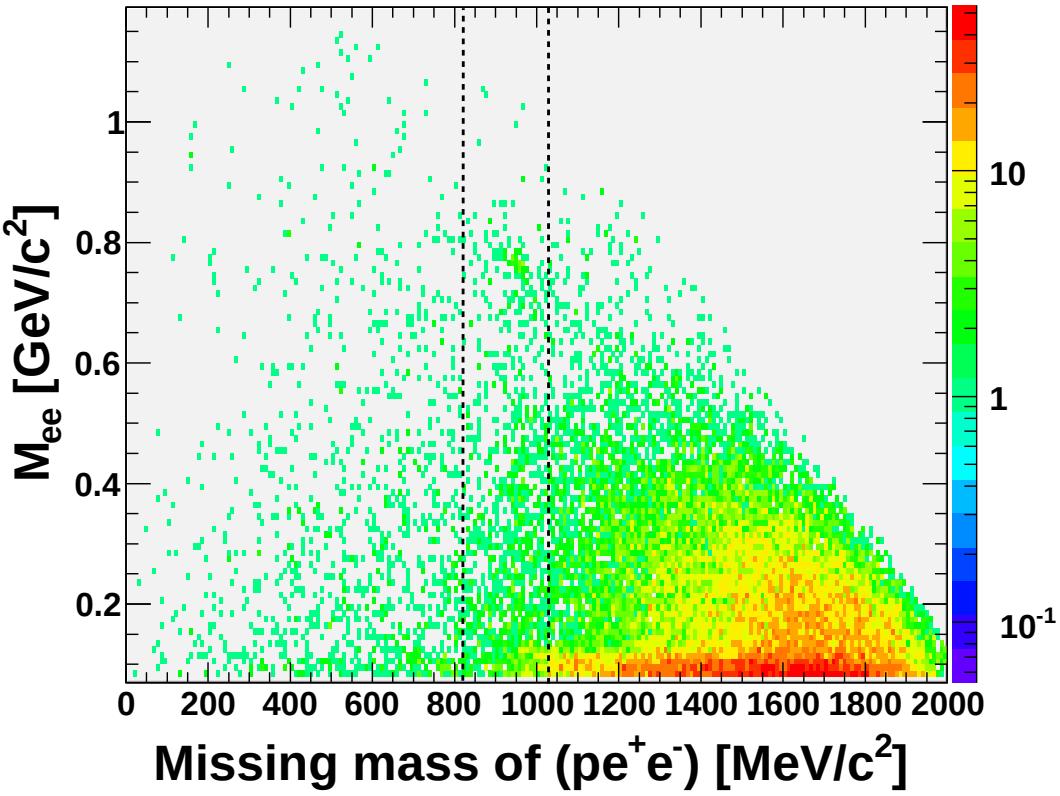

Figure 3.29: Dilepton invariant-mass versus missing mass distribution of (pe^+e^-). A cut of 2σ (vertical dashed lines) around proton mass is used in order to select those events which contribute to the ω signal in the channel $pp \to ppe^+e^-$. The suppression of conversion pairs is achieved by requiring an opening angle of the pair $\theta_{ee} > 10°$.

were calculated as a function of charge ($\pm$), momentum (p), polar (θ), and azimuthal (ϕ) emission angles by taking into account the cut applied in the context of the exclusive analysis.

In the analysis of the exclusive reaction $pp \to pp\omega \to ppe^+e^-$, three particles in the final state have been measured: one proton and two leptons of opposite charges. Since the single-lepton efficiencies ($\epsilon_\pm$) and the proton efficiency (ϵ_p) are uncorrelated, the total reconstruction efficiency can be written as:

$$\epsilon_{pe^+e^-}(p,\theta,\phi) = \epsilon_+ \cdot \epsilon_- \cdot \epsilon_p \tag{3.31}$$

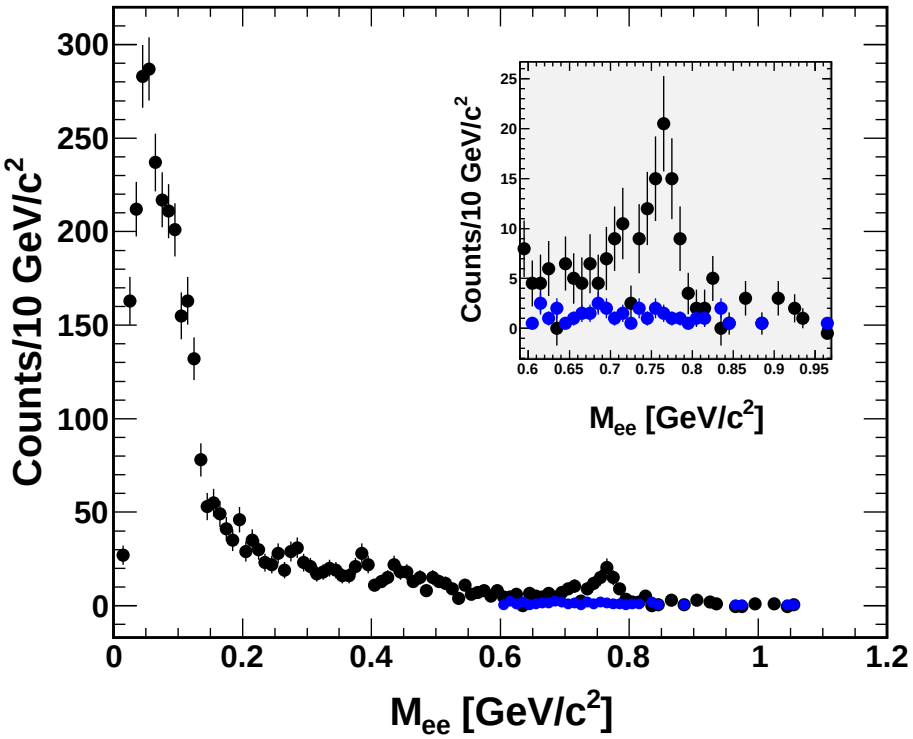

Figure 3.30: e^+e^- invariant-mass distribution. The opening angle cut ($\theta_{ee} > 10°$) and the cut on the proton missing-mass are applied. The signal (black color) and the combinatorial background (blue color) are shown. The inset shows a zoom of the invariant-mass spectrum around the ω meson peak.

Since HADES has a good efficiency reconstruction for high momenta protons ($> 90\%$) and the momentum distribution of the measured protons in the final channel is above 0.500 GeV/c, with good approximation the reconstruction efficiency of the proton can be set to 1.

The invariant-mass spectrum and the combinatorial background presented in the previous section have been treated likewise and subtracted in order to obtain the efficiency-corrected pair signal distribution.

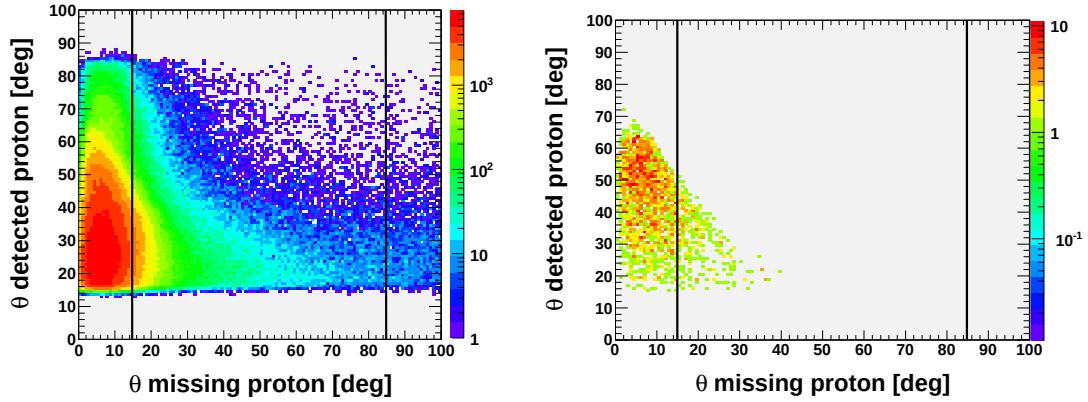

(a) (b)

Figure 3.31: Angular correlation between the detected proton and the proton which was not measured. The missing proton has been reconstructed via the kinematics of the exclusive reaction. In (a) all lepton and proton tracks which have been reconstructed are plotted. In (b) the cut on proton missing-mass ($820\ MeV/c^2 < Miss_{(pe^+e^-)} < 1020\ MeV/c^2$) has been applied. The vertical lines in $\theta = 15°$ and $\theta = 85°$ indicate the limit of the HADES acceptance. Events with two protons in the acceptance are found if θ of the missing proton and θ of the detected proton are both bigger than 15° and smaller than 85°.

3.9.1.5 Comparison of the HADES Data with the PLUTO Cocktail: Estimation of the Physical Background

In this section, it is presented the comparison between the invariant-mass distribution for the dilepton exclusive reaction and the PLUTO cocktail.

Fig. 3.32 shows the e^+e^- invariant-mass distribution for masses around the ω pole mass. The yield in each bin of the plot was obtained after subtraction of the combinatorial background under the ω peak, taking into account lepton reconstruction efficiencies (see Sec. 3.9.1.4) and the normalization factor (see Sec. 3.7). On the same plot, together with the data points, the simulation of the cocktail is shown. This simulation is based on the PLUTO event generator. The events generated with PLUTO were filtered through the HADES acceptance filter (see App. A). The parameters employed in PLUTO are listed in Tab. 3.6.

The spectrometer acceptance is applied to the simulated cocktail. The interaction of the simulated leptons with the detector material and the detector response are taken into account: the emission angles (θ and ϕ) of the simulated leptons have been smeared with momentum dependent Gauss functions, while their momenta have been subjected to the energy loss in the detector material.

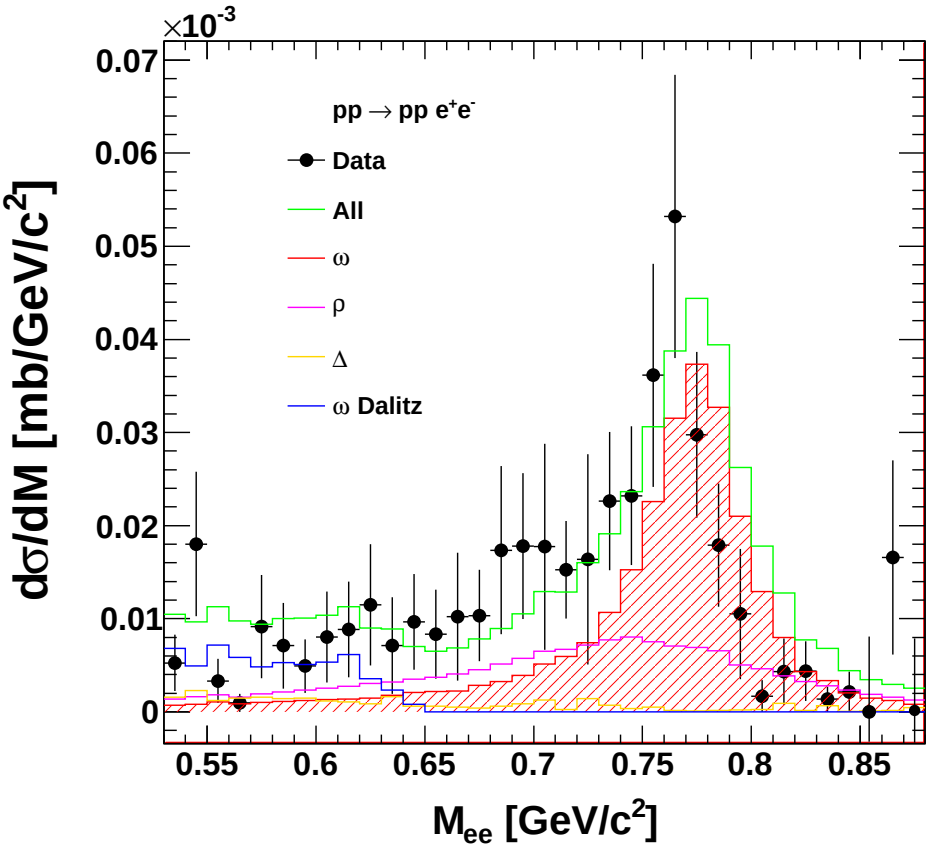

Figure 3.32: Efficiency-corrected e^+e^- invariant-mass distribution around the ω pole mass (black dots). The spectrum has been normalized with elastic cross section (see Sec. 3.6). The opening angle cut between the dilepton pairs ($\theta_{ee} > 10°$) and the cut on the proton missing-mass are applied. The simulation is shown with colored lines (from the upper to the lower curve): the ω meson signal (red color), the ρ meson contribution (magenta color), the Δ resonance (yellow color) and the ω Dalitz (blue color) are shown. With green color (uppermost curve) the sum of the four components is shown. The red colored area highlights the non symmetrical distribution of the ω meson; the tail on the left hand side is due to the electron/positron energy loss in the material of the detector.

The contribution to the peak is given by the ω, the ρ mesons and by the Δ resonance. The cocktail reproduces fairly well the data, however the data points are shifted by -10 MeV/c^2 to the low side of the invariant-mass distribution. The shift of the peak is found in the inclusive reaction as well and a possible reason to this effect is discussed in Sec. 3.8.1. The left hand side of the peak is

Reaction	Cross Section (mb)	Decay Mode	Branching Ratio
$pp \to pp\Delta$	16.0	$\Delta \to e^+e^-\gamma$	$4.0{\cdot}10^{-5}$
$pp \to pp\omega$	0.188	$\omega \to \pi^0 e^+e^-$	$7.7{\cdot}10^{-4}$
$pp \to pp\omega$	0.188	$\omega \to e^+e^-$	$7.2{\cdot}10^{-5}$
$pp \to pp\rho$	0.150	$\rho \to e^+e^-$	$4.7{\cdot}10^{-5}$

Table 3.6: Parameters entered into the PLUTO event generator in order to simulate the reaction $pp \to ppe^+e^-$ with a proton beam at 3.5 GeV incident kinetic energy.

reproduced well by the cocktail, however the right hand side of the peak falls down sharply ($\sim 0.8\ GeV/c^2$) with respect to the cocktail. It is clear, from Fig. 3.32, that the ρ meson contributes only a small fraction ($< 10\%$) to the peak yield and the Δ resonance even less ($< 5\%$).

It is crucial to point out that the energy loss of the leptons in the spectrometer leads to a distorted ω meson mass distribution. This asymmetry is highlighted with a red striped area in Fig. 3.32.

3.9.1.6 Cross Section for the Exclusive Reaction $pp \to pp\omega$

The knowledge of the reconstruction efficiency, the detector acceptance for the e^+e^- pairs, the number of measured ω mesons, the detector acceptance and the dilepton Branching Ratio (BR) of the ω meson are sufficient to deduce the cross section of the reaction: $pp \to pp\omega \to ppe^+e^-$.

From the invariant-mass distribution in Fig. 3.32, the yield of the ω meson can be extracted by taking in to account the contribution of the ρ meson and the Δ resonance.

By integrating the ω peak (data points) by a side band method, taking into account the detector acceptance for lepton pairs[19] and the ω decaying Branching Ratio into dileptons ($BR_{\omega\to e^+e^-} = 7.14 \cdot 10^{-5}$), the cross section is estimated to be:

$$\sigma_{pp\to pp\omega} = 0.1455\ mb \tag{3.32}$$

However, taking into account the consideration given above, based on the PLUTO model and GEANT calculations, this cross section must be corrected for those ω mesons which contribute to the tails of its invariant-mass distribution. This correction ($\sim 20\%$) leads to the production cross section:

$$\sigma_{pp\to pp\omega} = 0.1880\ \pm\ 0.0472\ (Stat)\ ^{+0.0669}_{-0.0240}\ (Sys1)\ \pm\ 0.0797\ (Sys2)\ mb \tag{3.33}$$

The statistical uncertainty is about 25%. The systematical uncertainties (Sys1) is due to the background under the ω meson peak, while the systematical uncertainties (Sys2) are due to the efficiency correction and the normalization procedure. These are estimated as:

- $\sigma_{background} = 25\%$
- $\sigma_{eff} = 35\%$
- $\sigma_{ppelastic} = 20\%$

Since these errors are obtained by independent analysis procedures, they were assumed independent, hence they can be added quadratically:

$$\sigma_{sys} = \sqrt{(\sigma_{eff})^2 + (\sigma_{ppelastic})^2 + (\sigma_{background})^2} = 47.4\% \tag{3.34}$$

and be applied to the whole invariant-mass dielectron spectrum.

[19]For the considered reaction the pair acceptance has been estimated to be 12%.

Chapter 4

Discussion of the Results

4.1 Dilepton Analysis

The knowledge of the ω meson in elementary p + p interactions can provide the reference for the line shape measurement in p + A and π + A collisions which aims at establishing medium effects in light vector meson production.

As shown in Sec. 3.3.2, data for Like-Sign (LS) pairs and Opposite-Sign (OS) pairs were acquired simultaneously. The signal pairs (*i.e.* e^+e^- pairs generated by a single electromagnetic vertex) form a data subset of the OS sample. The remaining OS pairs constitutes the opposite-sign background which was reconstructed and subtracted from the OS sample (see Sec. 3.3.2.1).

In this chapter the signal-pair spectrum is compared to simulations. In addition the invariant-mass spectra are corrected to the detector inefficiencies (see Sec. 3.4) and normalized by p + p elastic cross section (see Sec. 3.7).

The ω production cross section has been extracted from the signal of the invariant-mass spectrum of the reaction $pp \rightarrow X\omega \rightarrow Xe^+e^-$. The obtained cross section is compared with the corresponding parametrization used in the transport model HSD [51, 76, 77, 78]. This is the first cross section measurement which was measured at SIS energies with good statistics. For center-of-mass energies of few GeV above the ω production threshold this is the first measurement.

Using the same data set, the reconstruction of the ω meson in the exclusive channel ($pp \rightarrow pp\omega \rightarrow ppe^+e^-$) allows the calculation of the corresponding production cross section of the exclusive reaction . This second measurement agrees within the experimental error with the already available data [69, 106, 107].

4.1.1 Comparison of HADES Data with HSD Model

A big effort has been devoted by theoretical groups to describe elementary reactions, needed for an in depth understanding of the in-medium properties of the vector mesons based on transport models (*e.g.* HSD [51, 67, 76, 77, 78], UrQMD [65, 66]). In this chapter, a comparison between HADES data and HSD is presented.

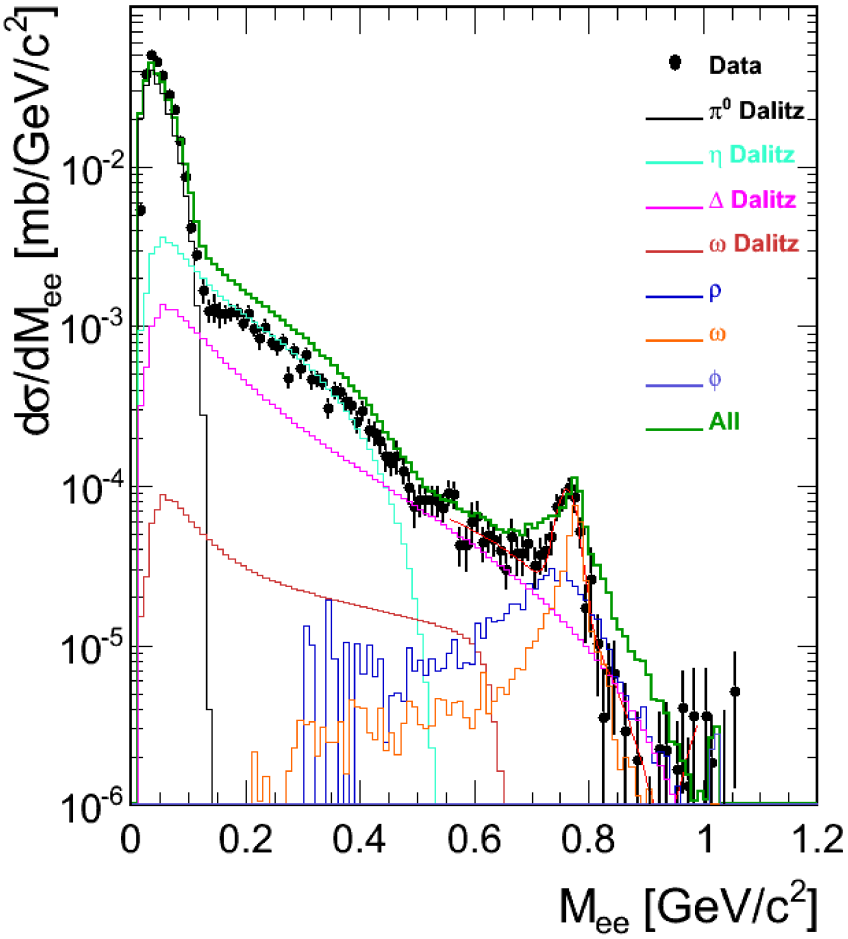

Figure 4.1: HADES data-points compared with the HSD model [76, 77, 78].

In order to perform a proper comparison between model and HADES data, the HSD simulation has been filtered with the HADES acceptance filter, and the invariant-mass spectrum normalized to the respective p + p elastic cross section (see Sec. 3.6).

The HADES filter is a 3D matrix, defined by three coordinates: invariant-

mass (M_{ee}), transverse momentum (P_t^{ee}) and rapidity (Y_{ee}) of the lepton pairs. The theory must also be smeared according to the HADES momentum resolution. This smearing is included in the HADES filter code. The HADES acceptance affects mainly the shape of the mass spectrum below 0.15 GeV/c^2. For invariant-mass values larger than 0.15 GeV/c^2 the acceptance is flat in all three variables. The technique employed to correct for the geometrical acceptance of the spectrometer is given in App. A.

In Fig. 4.1 the full invariant-mass spectrum measured by HADES is compared to the HSD model. The agreement for the π^0 Dalitz region between HSD and the data is good. For the invariant-mass region 0.15 $GeV/c^2 < M_{ee} <$ 0.4 GeV/c^2 the yield is overestimated by a factor of two. While the ω meson peak overlaps with the data, the tails of the peak are not quantitatively described.

4.1.2 ω Meson: Production Cross Sections in the Inclusive and Exclusive Dilepton Channels

In Sec. 3 the study of the reaction $pp \to X\omega$ has been described. The invariant-mass spectrum and the combinatorial background have been treated likewise and subtracted. After efficiency correction and normalization of the spectrum (see Sec. 3.4 and Sec. 3.7) the invariant-mass spectrum has been presented and the comparison with the PLUTO cocktail has been discussed (see Sec. 3.8). Via the integration of the signal peak and via the comparison of the spectrum with the simulation it was possible to estimate the production cross section of the reaction $pp \to X\omega$ (see Sec. 3.8.2).

Fig. 4.2 shows the results obtained in Sec. 3.8.2: the invariant-mass distribution is shown with the PLUTO cocktail, in Fig. 4.5a, in the invariant-mass region 0.55 $GeV/c^2 < M_{ee} <$ 0.90 GeV/c^2. The difference in the peak position between data and PLUTO cocktail has been discussed in Sec. 3.9.1.5 and it is taken in to account. The peak generated with the PLUTO cocktail is shifted by -10 MeV/c^2 in Fig. 4.5a. Fig. 4.5b shows the ratio between the HADES data and the PLUTO cocktail in the same invariant-mass region. In the ω meson mass region (0.65 $GeV/c^2 < M_{ee} <$ 0.80 GeV/c^2) the PLUTO cocktail describes well the HADES data. However, the cocktail overestimates the right side of the peak. In the region below the ω peak (0.55 $GeV/c^2 < M_{ee} <$ 0.65 GeV/c^2) the PLUTO underestimates the data by a factor of 2-3. The reason of this can be addressed to barion resonances which couple to the ρ meson [109, 110] enhancing the invariant-mass yield in this region and which are not taken in to account in the PLUTO simulation.

With a different and more selective analysis the identification of the reac-

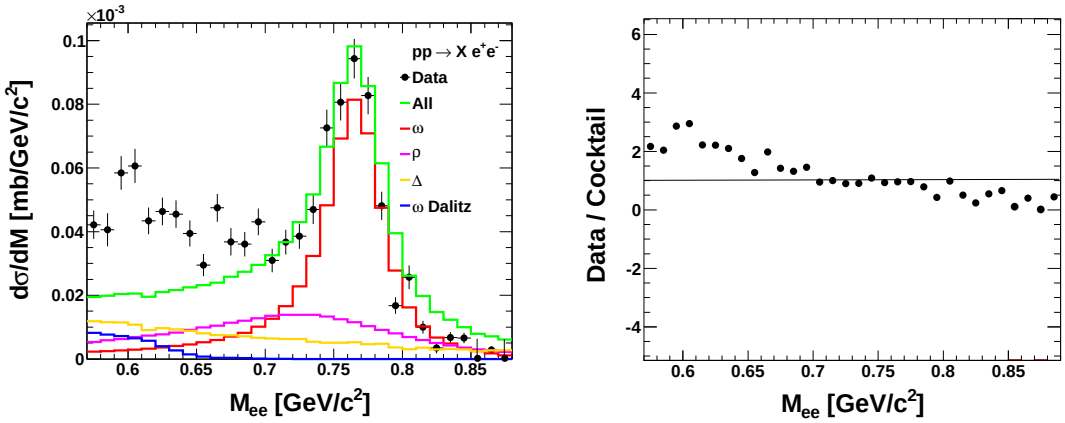

(a) (b)

Figure 4.2: Left: efficiency-corrected e^+e^- invariant-mass distribution around the ω pole mass (black dots). The spectrum has been normalized with p + p elastic cross section. The simulation is shown with colored lines. From the upper curve to the lower: the ω meson signal (red color), the ρ meson contribution (magenta color), the Δ resonance (yellow color) and the ω Dalitz (blue color) are shown. With green color the sum of the four components is shown. Right: the ratio between the HADES data points and the PLUTO cocktail is shown. The statistical errors of the bins in Fig. 4.5b are dominated by the experimental error (4-7%).

tion $pp \to pp\omega$ has been described is Sec. 3.9. While for the reaction $pp \to X\omega$ it is important to estimate the combinatorial background, for the exclusive reaction channel this contribution was not an issue, since the request of one particular channel reduced the contribution of the background. Moreover the technique employed to study the reaction $pp \to pp\omega$ was not based on the "pairing procedure" (see Sec. 3.3.1) which addressed the issue of the combinatorial background. Instead the selection of the exclusive channel was based on the β and momentum cut for proton identification, on the RICH signature for leptons and on the combination of the missing-mass and invariant-mass techniques (see Sec. 3.9).

After efficiency correction and normalization of the invariant-mass spectrum, a comparison with the PLUTO cocktail has been presented in Sec. 3.9.1.5. Fig. 4.3 shows the result obtained: the HADES data are compared to the PLUTO cocktail in Fig. 4.3a and the ratio between them is shown in Fig. 4.3b. The ratio between HADES data and the cocktail shows a good agreement, however the cocktail underestimates the right side of the peak ($0.76\ GeV/c^2 <$

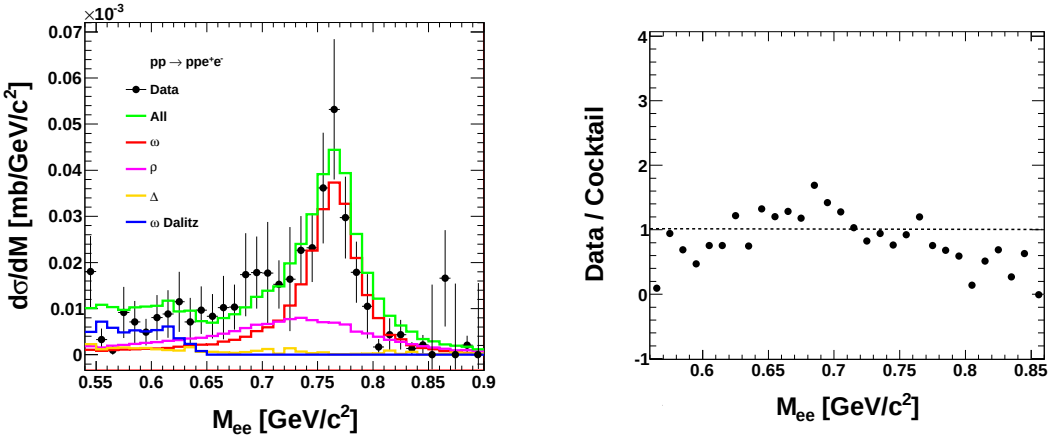

(a) (b)

Figure 4.3: Left: efficiency-corrected e^+e^- invariant-mass distribution around the ω pole mass (black dots). The spectrum has been normalized with p + p elastic cross section, which has been computed in the HADES acceptance. The simulation is shown with colored lines. From the upper curve to the lower: the ω meson signal (red color), the ρ meson contribution (magenta color), the Δ resonance (yellow color) and the ω Dalitz (blue color) are shown. With green color the sum of the four components of the cocktail is shown. Left: the ratio between the HADES data points and the PLUTO cocktail is shown. The statistical errors of the bins in Fig. 4.5b are dominated by the experimental error (25-30%).

$M_{ee} < 0.85\ GeV/c^2$) as in the inclusive reaction channel by a factor 0.5.

The production cross sections of the reactions $pp \to X\omega$ and $pp \to pp\omega$ with the respective errors (statistical and systematical) are estimated to be:

$$\sigma_{pp\to X\omega} = 0.2550 \pm 0.0140\ (Stat)\ ^{+0.0565}_{-0.0466}\ (Sys1) \pm 0.0797\ (Sys2)\ mb \quad (4.1)$$

and

$$\sigma_{pp\to pp\omega} = 0.1880 \pm 0.0472\ (Stat)\ ^{+0.0669}_{-0.0240}\ (Sys1) \pm 0.0797\ (Sys2)\ mb \quad (4.2)$$

These results are represented by star symbols in Fig. 4.4. These data are compared to model calculations (Fig. 4.4b) and model predictions (Fig. 4.4a). Previously measured experimental results are presented as crosses, triangles and squares [68, 69, 70, 106, 107] in Fig. 4.4b and exist only for the exclusive reaction channel ($pp \to pp\omega$). Fig. 4.4 shows the inclusive and exclusive ω production cross sections as function of the center-of-mass energies.

The results obtained in this work are drawn (red colored star symbols) at $\sqrt{s} = 3.18\ GeV$ (corresponding to proton beam with kinetic energy of 3.5 GeV off a proton target). The result computed for the reaction $pp \to X\omega$ is extremely important, because it will provide a constraint of the parametrization of the "inclusive curve" adopted in HSD. The errors in this cross section consist of a statistical part (Stat) together with a systematic part (Sys1 and Sys2). The larger uncertainty comes from two kinds of systematic uncertainties: the first one is due to the uncertainties in the background subtraction (Sys1), while the second (Sys2) is due to the normalization to the elastic p + p cross section and the efficiency correction procedure.

Here it worth pointing out that this is the first cross section measurement of the reaction $pp \to X\omega$, which was measured close to the ω production threshold and at energies below 100 GeV with good statistics. The HSD parametrization overestimates the inclusive ω production cross section by 6.3 standard deviation (standard deviation of the statistical errors) (at $\sqrt{s} = 3.18\ GeV$, $\sigma^{HSD}_{pp\to X\omega} = 0.485\ mb$).

4.1.3 ω Meson Exclusive Reaction: Remarks and Outlook for Future Analysis

In Sec. 3.9.1.6, the reconstruction of the exclusive reaction $pp \to pp\omega \to (p)pe^-e^+$ has been shown. This analysis was based on the observation of one proton in the final state, while the second proton was not detected. However, the second proton has been reconstructed via the missing-mass technique.

If there were a possibility to detect the two protons and the two leptons in the final state in the exclusive reaction considered, two more exclusive reactions could be accessed via such a four prongs analysis. Both additional exclusive reactions involve pion production in addition to the ω meson:

$$pp \to pp\omega\pi^0 \to pp e^+e^-\pi^0 \tag{4.3}$$

$$pp \to pn\omega\pi^+ \to pn e^+e^-\pi^+ \tag{4.4}$$

Via the reconstruction the missing π^0 in Eqn. 4.3 and the missing neutron in Eqn. 4.4, the study of these reactions could be addressed.

The knowledge of all possible exclusive reactions will help to understand the production channels making up the difference between the inclusive ($pp \to \omega X \to e^+e^-X$) and the exclusive ($pp \to pp\omega \to pp e^+e^-$) channels.

If it were possible to quantify the difference between the production cross sections of Eqns. 4.3 and 4.4, a better understanding of the ω production mechanism could be stated. Moreover, this could explain the inclusive ω production cross section and be a relevant result for all model calculations.

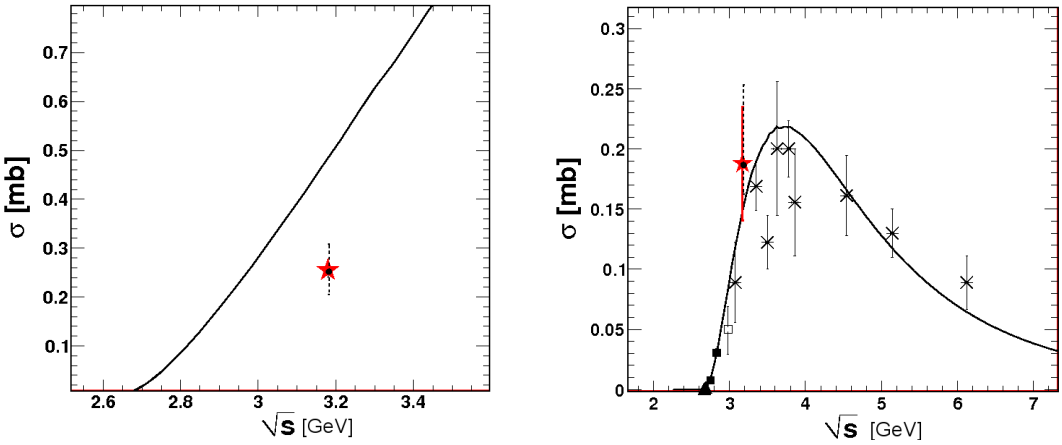

(a) $pp \to X\omega$ (b) $pp \to pp\omega$

Figure 4.4: Inclusive (4.4a) and exclusive (4.4b) production cross sections for the ω vector meson compared to the HSD predictions [76, 77, 78] (solid line in 4.4a) and OBE calculation (solid line in 4.4b). The red stars represent the cross section values presented in this work in the inclusive (4.4a) and in the exclusive (4.4b) dilepton channels: the asymmetrical systematical uncertainties are represented by dashed lines, while the statistical uncertainties are represented by a red line on top of the data point. Left: the statistical uncertainties are small ($\sim$ 6%) and are represented by the size of the symbol used. Right: the black data points are taken from [68, 69, 70, 106, 107].

Fig. 4.5 shows the angular correlation between polar angles of the detected proton and the proton which has been reconstructed in data and simulation. The vertical/horizontal lines at $\theta = 18°$ and $\theta = 85°$ indicate the limit of the detector acceptance (see Sec. 2). In this figure, most of the missing protons in the reaction $pp \to pp\omega \to (p)pe^-e^+$ go outside the HADES acceptance, namely to forward polar angles ($\theta > 0°$ and $\theta < 18°$). Only 5-8% of the events can be studied by detecting simultaneously four particles in the final state (both protons in the HADES acceptance).

However, even with only the 5-8% of the full statistics available, the study of Eqns. 4.3 and 4.4 can in principle be done. In order to include more events, the Forward hodoscope Wall (FW) detector (see Sec. 2.7) can be included in the analysis procedure and the momenta of protons at low polar angles ($0.33° < \theta < 7.17°$) could be measured. However, this additional analysis procedure is not trivial: the information provided by the FW is the time-of-flight of charge particles and their positions in the detector wall. The time resolution of the

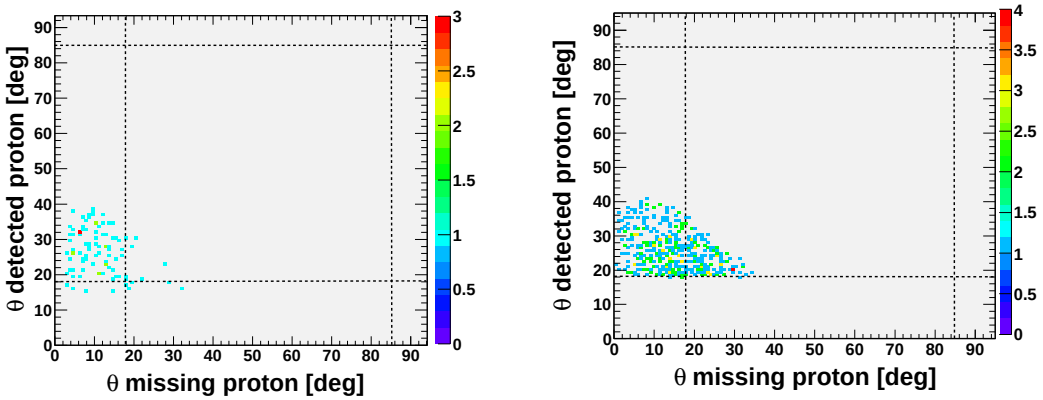

(a) Experimental data (b) Simulation

Figure 4.5: Polar angular correlation between the detected proton and the proton which was not measured. The missing proton has been reconstructed via the kinematics of the exclusive reaction $pp \to pp\omega \to (p)pe^-e^+$. In (a) all lepton and proton tracks which have been reconstructed experimentally are plotted; two cuts are applied in order to select the region around the ω meson mass: the proton missing-mass cut ($820\ MeV/c^2 < Miss_{(pe^+e^-)} < 1020\ MeV/c^2$) and the e^+e^- invariant-mass cut ($0.700\ GeV/c^2 < M_{ee} < 0.850\ GeV/c^2$). The vertical/horizontal lines in $\theta = 15°$ and $\theta = 85°$ indicate the limits of the HADES acceptance in polar coordinate.

FW does not allow to distinguish protons and pions. This ambiguity must be resolved in a dedicated analysis algorithm.

This analysis goes far beyond the intent of this work, however, it is remarkable to drive the attention to the feasibility of the study of two more exclusive reactions, which might be distinguished with 25% of the statistics used in the analysis presented here.

4.2 Summary

One goal of the High-Acceptance Di-Electron Spectrometer (HADES) at GSI is the study of in-medium modifications of ρ and ω vector mesons in hot and/or dense baryonic matter.

Dilepton probes provide the most direct information on the hadronic matter, hence HADES has been built to provide complementary results to the one obtained at higher energies (SPS, RHIC). In addition, with HADES it is foreseen to study medium effects at normal density with pion or proton beams.

The HADES experiments explore the 1-2 $AGeV$ energy regime, where moderate temperatures ($T < 100\ MeV$) and baryonic densities up to three times normal nuclear matter density can be achieved. Already in this energy regime sizable modifications of ρ and ω meson spectral functions are expected. Contrary to reactions at ultra-relativistic energies, the multiplicity of produced pions per participant is smaller; this is an advantage since the main source of combinatorial background comes from the reactions: $\pi^0 \to \gamma\gamma$ (followed by γ conversion) or $\pi^0 \to e^+e^-\gamma$.

The results obtained in this work are summarized in the following items:

- the e^+e^- invariant-mass spectrum in the inclusive dilepton channel: $pp \to \omega X \to e^+e^-X$;

- the computation of two cross sections for the reactions $pp \to X\omega$ and $pp \to pp\omega$.

The first result has been described in Sec. 3: the analysis of the p + p reaction at 3.5 GeV incident kinetic energy has been described and lepton candidates were selected using different criteria, checking the track and ring qualities, as well as the identification of the electron and positron in the RICH, MDC and META detectors.

In Sec. 3.3.2 the combinatorial background, which arises mainly from the conversion process, was obtained as the arithmetic mean of Like Sign (LS) (e^+e^+ and e^-e^-) pairs and was subtracted from the Opposite Sign (OS) (e^+e^-) sample. The correlated pairs from photon conversion were also removed, using the opening angle cut (opening angle between the e^+e^- tracks: $\theta_{ee} < 9°$) on the pair sample.

Detection and efficiency corrections are described in Sec. 3.4. The final spectra were normalized using the p + p elastic scattering computed in the HADES acceptance (see Sec. 3.7). The relevant ω meson signal arises at $M_{ee} = 0.761 \pm 0.0121\ GeV/c^2$ with $\sigma_{M_{ee}} = 18.65 \pm 0.98\ MeV/c^2$, which is comparable with the mass resolution given by the design value of 2-3%. The peak is shifted

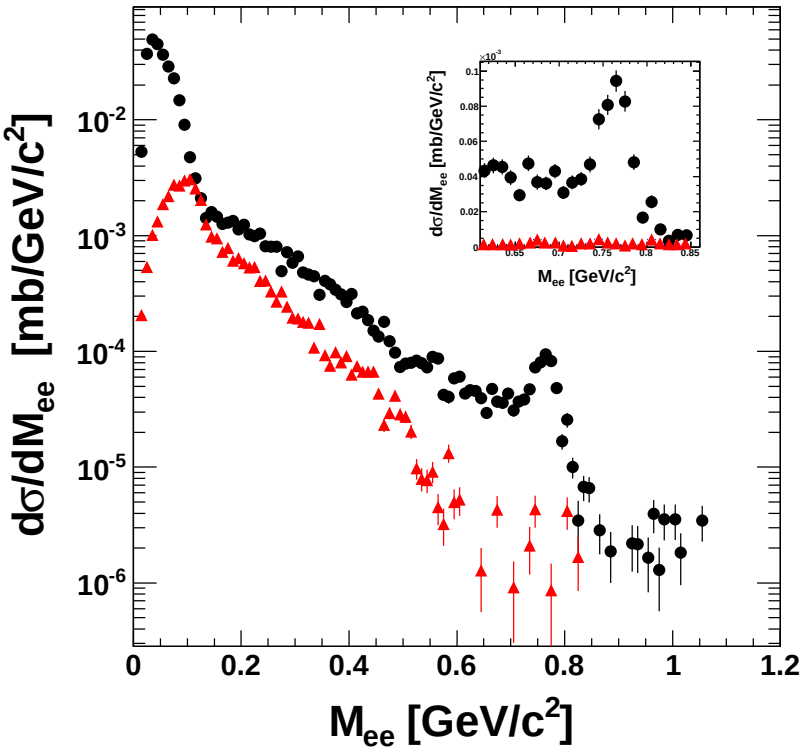

Figure 4.6: e^+e^- invariant-mass spectrum: signal (black colored circles, upper curve) and background (red colored triangles). The spectrum is corrected for detector inefficiencies and normalized by p + p elastic cross section. The inset shows the ω meson signal and the combinatorial background in linear scale.

of $-20\ MeV/c^2$ with respect to the low side of the nominal position reported in the PDG [2] have been discussed as well.

It is important to remember that a basic requirement for the interpretation of dilepton spectra in terms of medium effects is a careful description of the vector meson production in elementary p + p reaction. Concerning the ω vector meson, this means the knowledge of the peak position, its width and amplitude. The analysis of the ω vector meson will provide an important reference for the line shape measurement in p + A and π + A reactions which ultimately aim at establishing medium effects of light vector mesons embedded in nuclei.

The second result which is exposed in this work consists in the computation of two cross sections: for the reactions $pp \rightarrow X\omega$ and $pp \rightarrow pp\omega$. With two

different analysis techniques the ω meson peak has been obtained. By comparing it with the PLUTO cocktail, the contribution of the tails to the invariant-mass distributions have been taken in to account in the cross section determination. The results obtained are:

$$\sigma_{pp\to X\omega} = 0.2550 \ \pm \ 0.0140 \ (Stat) \ ^{+0.0565}_{-0.0466} \ (Sys1) \ \pm \ 0.0797 \ (Sys2) \ mb \quad (4.5)$$

and

$$\sigma_{\omega\to pp\omega} = 0.1880 \ \pm \ 0.0472 \ (Stat) \ ^{+0.0669}_{-0.0240} \ (Sys1) \ \pm \ 0.0797 \ (Sys2) \ mb \quad (4.6)$$

The former result (Eqn. 4.5) represents the only cross section measurement available in the dilepton channel in the energy range close to the ω production threshold and it is an important constraint for transport calculations.

Tab. 4.1 summarizes the main results obtained in this work for the inclusive and for the exclusive reactions. The reduction of the number of the reconstructed ω mesons from the inclusive channel to the exclusive is due to the condition on one additional particle (one proton) in the HADES acceptance. The request of one additional proton in the exclusive reaction decreases the acceptance of the detector down to 12%. This number must be compared with the e^+e^- acceptance in the inclusive reaction which has been computed to be 30%. It must be noticed that even with a big reduction in the acceptance the reconstruction of the exclusive reaction was successfully performed. The pole mass and the width of the meson are equal in the two channels and are shifted by $-20 \ MeV/c^2$ with respect to the low side of the nominal position reported in the PDG [2].

HADES is currently being upgraded in order to handle efficiently the higher multiplicities in heavier systems like Au+Au. In future HADES experiments, planned in 2010-2013, the ability to extract information from the dielectron continuum in heavy-ion reactions depends upon the ability to isolate the contributions of the various sources in elementary nucleon-nucleon collisions.

	Inclusive Reaction: $pp \to \omega X$	**Exclusive Reaction:** $pp \to pp\omega$
M_ω	0.763 GeV/c^2	0.760 GeV/c^2
σ_ω	16.2 MeV/c^2	17.1 MeV/c^2
N_ω	275.4 ± 14.8	127.0 ± 31.1
S/B	~ 10	~ 12
$Efficiency$	$\sim 20\%$	$\sim 20\%$
Acc	$\sim 30\%$	$\sim 12\%$
σ	0.255 ± 0.0140 mb	0.1880 ± 0.0472 mb

Table 4.1: Parameters obtained in analysis of inclusive and exclusive reactions. The values are obtained in the ω invariant-mass region. Only statistical errors are shown. N_ω was calculated from the raw spectra.

Chapter 5

The MDC Data Acquisition Upgrade

HADES will complete its physics program at the heavy-ion synchrotron SIS-18 and then move to the upcoming International Facility for Antiproton and Ion Research (FAIR) [124].

As already mentioned in Sec. 1.3.2 HADES will continue its experimental program at kinetic beam energies up to 8 $AGeV$. In this energy regime, the expected event size and rates from experiments with heavy ion systems such as Au+Au require bandwidths which can not be achieved by the current data acquisition system.

This chapter is organized as follows: first the motivations of the upgrade of the Data Acquisition System (DAQ) are given in Sec. 5.1. In the following section (Sec. 5.2) an overview and the concept of the whole DAQ is explained. The following sections focus on the upgrade of the MDC electronics: the first stage of the upgrade is summarized in Sec. 5.3 while the second stage, which is based on optical technology, is written in detail in the sequent sections: the concept is described in Sec. 5.4.1 and its realization in hardware and software in Sec. 5.4.2.

5.1 The Upgrade of the Data Acquisition System in HADES: Motivations

With a planned Au+Au run at 1.5 $AGeV$ incident kinetic energy, the particle multiplicity increases by a factor of 10 compared to previous HADES runs (*e.g.* Ar+KCl at 1.756 $AGeV$). This corresponds to an average particle density of 220 charged particles per event. Fig. 5.1 shows the charged particle multiplicity for each MDC module type, in the local MDC reference frame, expected for such

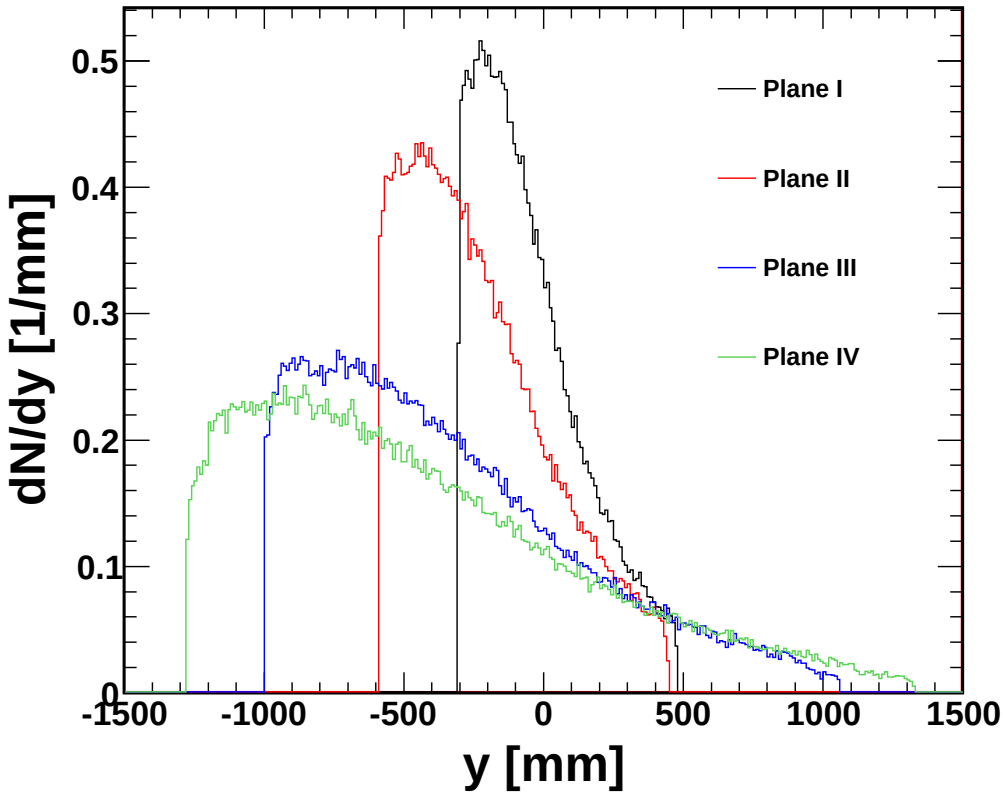

Figure 5.1: Simulation of the particle multiplicity expected for Au+Au central collisions at 1.5 $AGeV$. The events have been generated via the transport code UrQMD [65, 66] and the particles have been propagated through the HADES detector using the GEANT software package. Each color corresponds to the particle occupancy for each MDC module; the average particle multiplicity in each module is $\sim$ 36 charged particles (*i.e.* this means that 220 particles hit the plane I, since a plane consists of six layers). All particles (primary and secondaries) are considered in the simulation. The horizontal axis refers to the local MDC reference frame (see Fig. 5.2).

a reaction. The local MDC reference frame, in Fig. 5.2, is defined on a central plane in the middle of each chamber by the intersection between a perpendicular axis to this central plane, passing through the target position T($x = 0$, $y = 0$, $z = 0$).

The particle multiplicities are averaged over six sectors in order to show the

Current DAQ System			
Reaction	Particles/Event	LVL1 Trigger Rate	Data Rate
p+p	5	10 kHz	10 $MBytes/s$
^{12}C + ^{12}C	10-20	5 kHz	10 $MBytes/s$
Ar+KCl	20	3.5 kHz	10 $MBytes/s$
Upgraded DAQ System			
Reaction	Particles/Event	LVL1 Trigger Rate	Data Rate
p+p	5	100 kHz	100 $MBytes/s$
Au+Au	220	20 kHz	300 $MBytes/s$

Table 5.1: The table shows the number of charged particles per event, the LVL1 trigger rate and the data rate for different reactions. Upper table: value obtained in HADES experiments already performed (p + p, C+C and Ar+KCl at 3.5 GeV, 1.0 $AGeV$ and 1.756 $AGeV$ incident kinetic energy respectively). Lower table: the design values of the upgraded DAQ system are reported for two reactions: p + p at incident kinetic energy of the projectiles of 3.5 GeV and Au+Au at 1.5 $AGeV$.

average particle density for each HADES chamber for a given plane. Due to

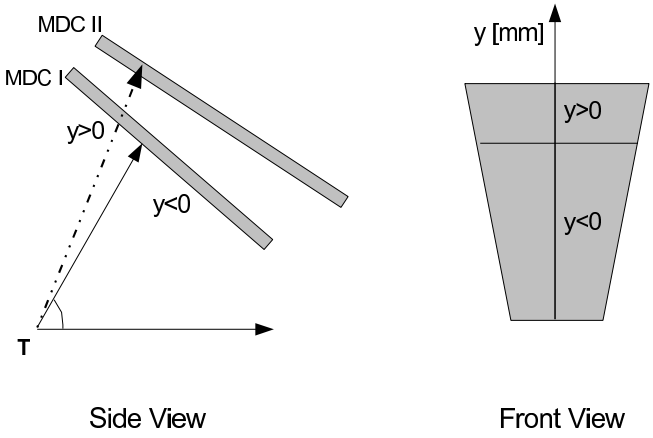

Figure 5.2: MDC local reference frame for two chambers: one chamber in plane I and one chamber in plane II. By definition the center of the MDC local reference frame is in a different position on each chamber for different planes.

higher rate and occupancy with respect to the already performed HADES runs, the detector has to be able to acquire data at higher rate with the possibility to store many events in memory or buffers close to the front-end-electronics (see Sec. 5.4.2.2).

Tab. 5.1 summarizes the charged particle multiplicities, the LVL1 trigger rate and the data rate registered in the already performed HADES run with the current DAQ system and the design values of the upgraded DAQ system. The table shows that the LVL1 trigger rate decreases with the number of particles per event (in equivalent words with the size of the event which has to be stored in the Front End Electronics (FEE)). This was experienced with the past HADES runs (*e.g.* p + p, C+C and Ar+KCl). Acquiring data with heavy systems such as Au+Au with the current DAQ would decrease further the LVL1 rate below 1 kHz which would require extremely long experimental runs in order to acquire enough statistics. With the upgraded DAQ system the LVL1 trigger rate has to be above 20 kHz for heavy system and about 100 kHz for lighter one[1]. This requires a fast Data Acquisition System (DAQ) for all sub-detectors.

[1]The LVL1 rate decreases with increasing the number of particles per event. If more particles per events are produced means that more data is recorded by the data acquisition and have to be transported from the FEE to the storage disks.

In the particular case of the MDC system, the simulation described above allows to estimate the size of one event in *bits* per one MDC module: if 36 charges particles hit one MDC module, then an average event of 18 *kbits* per event per chamber is recorded. The results of this simulation is important in order to design properly the software used to readout the data from the MDC FEE (see Sec. 5.4.2.2).

5.2 The Upgrade of the Data Acquisition System in HADES: Overview and Concept

The schematic overview of the HADES Trigger and Data Acquisition system is shown in Fig. 5.3. The readout chain consists of five basic elements:

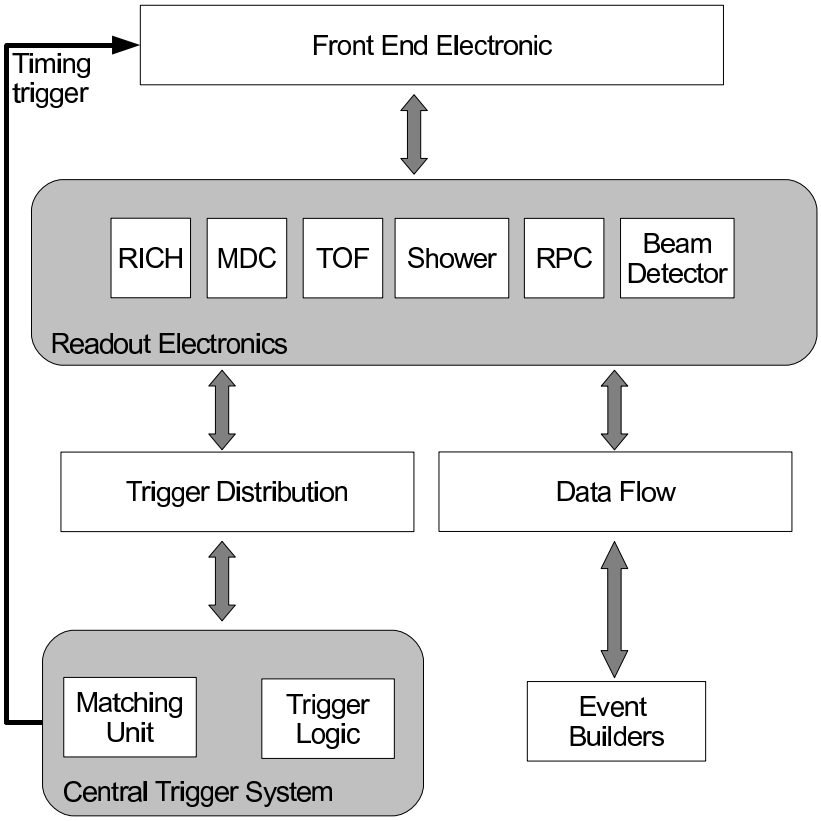

Figure 5.3: Block diagram of the HADES DAQ system: the picture shows the data and trigger flow.

- Front End Electronics (FEE) or detector specific electronics;
- Readout electronics;
- Trigger distribution;
- Central Trigger System (CTS);
- Event Building and data storage.

The Central Trigger System (CTS) consists of a first level trigger (LVL1) logic. This is implemented in one Trigger and Readout Board (TRB) [123] plus a general purpose AddOn: the LVL1 trigger[2] decision is produced by the charged particle multiplicity in an array of scintillator detectors (TOF and/or TOFino depending of the particular trigger) (see Sec. 2.6.1).

The trigger logic in the CTS generates a LVL1 trigger (LVL1 trigger word) and this induces a specific action of the readout of each individual sub-detectors. A LVL1 trigger word contains the trigger number (number of consecutive triggers) and the physics source of the trigger. This trigger word is distributed to each sub-detectors via the "Trigger Distribution path" in Fig. 5.3 via optical signals. This trigger differs from the timing trigger which is send via copper cable directly to the FEE (see Sec. 5.4.2). The LVL1 trigger word has to be distributed to each sub-detectors is not "time critical". All sub-detectors read out the events selected by this trigger.

Since the second level trigger (LVL2) comes after a latency corresponding to several events (five to ten events), the readout boards have large First In First Out (FIFO) (LVL1 FIFOs) to hold the data for this amount of time. The LVL2 decision is based on the combination of the preprocessed data from different sub-detectors. If LVL2 decision is positive, the data of each readout boards is sent to the Event Builders (EBs).

The Event Builders are software processes which combine data from asynchronous data sources to a complete event and write the events to the mass storage systems [117].

The concept of the DAQ upgrade is based on a "modular design" (in the hardware and software levels). An example of hardware "modular design" is given by the TRB. The readout electronics is based on the TRB as common readout board, therefore a specific hardware module is derived from it: *e.g.* the electronics readout of the MDC consists in one TRB and an additional board plugged onto it and a counterpart in the FEE, the Optical End Point Board (OEPB). Therefore the "modular design" of the hardware is flexible and extendable.

A major part of the DAQ upgrade is based on the general purpose Trigger and Readout Board (TRB), which serves as a platform for all subsystems. The TRB is described in the next section.

[2]The LVL1 trigger is called multiplicity trigger. It is generated by the comparison of the number of hits in TOF and TOFino to a given settings. It is used to provide the centrality selection on the occurred reactions.

5.2.1 The Trigger and Readout Board (TRB)

The upgrade project is mainly based on one hardware card: the Trigger and Readout Board (TRB) [122, 123]. It is a multi-purpose electronic device with on-board DAQ functionality.

The original motivation for the development and the construction of the TRB was the need of novel readout electronic for the HADES Resistive Plate Chamber (RPC) detector. The RPC detector is one of the main parts of the detector upgrade in HADES. It has 2232 channels and will substitute the TOFino system with a time resolution of less than 100 ps [102, 103, 104, 105], with additionally improved granularity in respect to the TOFino system.

The TRB is a Printed Circuit Board (PCB), equipped with an ETRAX-FS processor [127] for DAQ and slow-control functionality. The processor runs a standard Linux kernel and has a direct connection to 100 $Mbit/s$ Ethernet. It supports "Experimental Physics and Industrial Control System" (EPICS) to allow the integration into the HADES Slow-Control System [128].

On the back side, the TRB is equipped with two very high data-rate digital interface connectors (42 Transistor-to-Transistor (TTL) lines, 32 Low Voltage Differential Signal (LVDS) lines, 15 $Gbit/s$), which give the possibility to mount additional hardware components called add-on boards. The add-on boards are hardware cards which provide an interface to the existing electronics with additional new functionality. For example the "General Purpose" add-on (GP-AddOn) boards interfaces the existing HADES trigger bus and has the connection for many general purpose signals (like the LVL1, LVL2 trigger sources). Dedicated add-on boards have been designed to interface the existing HADES detectors Front End Electronic (FEE): RICH, TOF, Pre-Shower detectors [125].

The following chapters describe the efforts to integrate the MDC FEE into the TRB readout framework.

5.3 The Upgrade of the MDC Data Acquisition (Version I)

Two MDC-AddOn versions have been developed: the MDC-AddOn (version 1) was designed to replace the existing bus architecture by a star-like system. This is shortly described in Sec. 5.3.1.

As the general concept has been successfully tested with the MCD-AddOn (version 1), a second design has been made which contains 32 optical transceivers thus replacing the electrical connection which turned out to be a source of noise. On the front-end side, the counterpart is a small, highly integrated board: the Optical End Point Board (OEPB).

In the following sections the concept of the MDC-AddOn is explained. In Sec. 5.4.2 the new optical readout is extensively described: first the hardware is described and then the software implementation.

5.3.1 MDC AddOn Board

A first add-on board has been developed to replace the bus architecture depicted in Chapter 2.4 while keeping the electrical data transmission. This stage allows to implement ROC and SAM readout functionality, described in Sec. 2.4.1, in one single module.

The MDC-AddOn board (version 1) is the interface to the detector motherboard. However, this communication is based on a bus of copper cables (RS-485 standard, on differential bus), which are mounted along the frames of the chambers, sometimes inevitably close to the input of the pre-amplifiers of the FEE.

A FPGA (Xilinx Virtex4) is placed in the center of the MDC-AddOn. It initializes the HADES chambers FEE and performs a fast parallel data readout.

Together with the TRB, it replaces the major part of existing readout electronics chain: the ROC, the CM and the SAM (see Sec. 2.4.1).

Sub-event building is done by the ETRAX processor. One MDC-AddOn (version 1) configures and reads out 1088 Time to Digital Converter (TDC) channels in 136 TDC-ASICs which are part of the FEE, mounted on the frame of the chambers.

The functionality which have been implemented and tested on one single chamber are listed here:

- Initialization of the FEE and the following TDC working mode:
  - Initialization mode;
  - Measurement mode;
  - Configuration read-back mode;

  - Calibration mode;
  - Readout mode.

- FEE readout;
- TDC calibration readout

More information can be found in [123, 129].

5.4 The Upgrade of the MDC Data Acquisition (Version II): the Optical Readout

In the second stage of the upgrade of the MDC electronics, serial optical links replace the parallel copper buses. Optical signals reduce noise pickup and increase the data transport bandwidth. In this concept each FEE is accessible point-to-point in order to maximize the readout speed, monitor and maintain each single hardware module.

This readout scheme, via optical technology, has three ingredients:

1. A replacement of the "passive" Driver Card (DC) with an "active" board which has all the functionality already proven with the experience with the MDC-AddOn board (version 1).

2. Optical add-on board which serves 32 optical connections, since a total number of 32 FEE boards are mounted on two MDC chambers.

3. A reliable protocol which transports the data from the FEE to the Event Builders (EBs).

To better understand the transition from electrical data transmission (see Sec. 5.3.1) to optical data transmission a sketch, in Fig. 5.4, shows the readout of the MDC electronics as it is presented in Sec. 5.3.1 (MDC electronics upgrade: 1^{st} stage) and the optical readout (MDC electronics upgrade: 2^{nd} stage) which is going to be presented in this chapter. The medium between the readout system and the FEE is different: in the 1^{st} stage of the upgrade the data is transported over copper cable, while in the 2^{nd} stage the data is transported over optical fibers. The 2^{nd} stage of the electronics upgrade is also called "optical readout". It is important to explain already at the beginning of this chapter the concept of "optical readout" and its advantages compared to the readout based on electrical signals. This concept will be retrieved several times over the chapter.

In general a readout system is based on the transmission of fast signals from point A to point B (*e.g.* in Fig. 5.4 point A and point B are the OEPB and the MDC Optical AddOn respectively). In order to transport the information encoded in electrical signals, over a certain distance from point A to B, the electrical signals have to be converted to differential (which are still electrical) or to optical signals. After signal conversion the signals are transmitted over cables or through optical fibers of different length. When the signals reach the receiver (B), this has to be able to perform the inverse operation in order to recreate the original signals (differential electrical signals are converted to single-ended signals and the optical signals to electrical one).

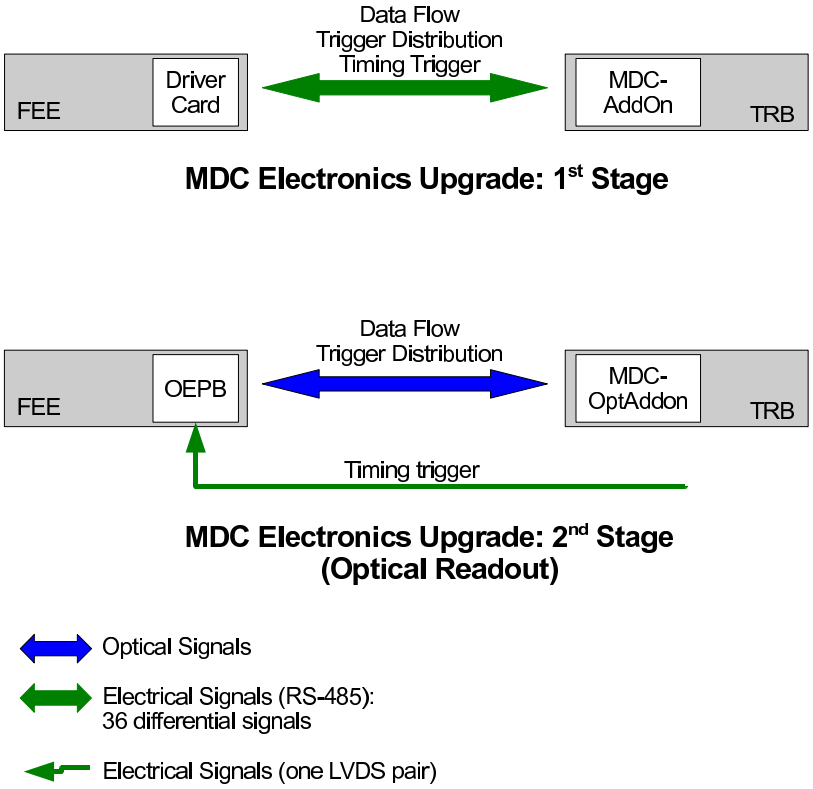

Figure 5.4: The lower figure shows data flow and the trigger distribution in the upgraded readout (2^{nd} stage of the electronics upgrade), which is based on optical transmission. This is realized by replacing the Driver Card (DC) by the Optical End Point Board (OEPB). The only electrical signal presents between the DAQ system and the FEE is the timing trigger signal, which is distributed on one single LVDS pair. It was not possible to transmit the timing trigger over optical fiber because the jitter induced by the optical transceivers is to high compared with the needed time resolution of this signal (see text for details). In the upper sketch the concept of the first readout stage is drawn, which was still based on the electrical signals.

This signal conversion is done in the so called "transceivers" which perform the conversion between signals of different types and vice versa. There are many different standards which define the type of the signals and each standard has its own features [135].

In Fig. 5.4 is clear that two different transceivers have been adopted in the two stage of the upgrade. In the first stage a standard transceiver (RS-485) has

been adopted, while in the second stage Fiber Optical Transceivers (FOT)[3].

The advantages/disadvantages of the optical readout over the readout based on electrical differential signals are explained in the following points:

- Low power consumption: the power consumption of the FOT is expressed with the electrical current the transceiver needs at its operating regime. The transmitter needs 40-55 mA and the receiver 36-45 mA [136][4]. It is important to remember that the OEPB transmits data during the acquisition process, while the receiver is seldom used (*e.g.* the receiver on the OEPB is used during the start-up process, during which the MDC Optical AddOn sends data to the OEPB. (See Sec. 5.4.2.2).

  The differential transceiver used up to year 2008 and in the upgrade stage (version 1) (see Sec. 5.3) at operating conditions needs higher current, which translates in higher temperature[5]. The average current needed by one Driver Card (DC) (one DC is equipped with two differential transceivers) has been measured 350 mA. This current include the current needed by the two devices and the current needed to transport the data through the differential lines[6]. This current must be compared with the current needed by one FOT (40-55 mA).

- Low noise: a fiber optic transport optical signal which are decouple to electrical one. For this reason fibers are immune to electrical interference,

[3] An optical transceiver converts electrical signals into optical signals and launches the optical signals into an optical fiber. A fiber optic transmitter consists of an interface circuit, a source drive circuit and an optical source. The interface circuit accepts the incoming electrical signal and processes it to make it compatible with the source drive circuit. The source drive circuit intensity modulates the optical source by varying the current through the source.

[4] In the FOT transmitter and receiver are both built in the same FOT package.

[5] The temperature is an important issue in this design. Changes in temperature change the measurement conditions of the MDC (see Sec. 2.4). Moreover the calibration of the TDC in the FEE depends of the temperature conditions.

[6] The transmitter consists of a current-mode driver, which provides few mA of current through the transmission lines of the differential pair. At the receiver, a 100 Ohm termination resistor is used to match the impedance of the transmission lines that connect the receiver to the driver. The terminator resistor reduces signal reflections that decrease signal quality. The high input impedance of the receiver causes the current coming from the driver to flow through the 100 Ohm termination resistor, resulting in a voltage difference between the receiver inputs. This current is the main source of power dissipation in the device.

As the path for the current within the driver changes from one path to another, the direction of the current flowing through the termination resistor at the receiver changes as well. The direction of the current through the resistor determines whether a positive or negative differential voltage is read. A positive differential voltage represents logic-high level (1) and a negative differential voltage represents logic-low level (0).

there is no cross-talk between signals in different fibers and no pickup of environmental noise.

- Absence of possible ground loops. This point is related to the previous one. A ground loop refers to a current in a conductor which connects two points (A and B) that are supposed to be at the same potential, but are actually at different potentials. Since there is no electrical connection ("massive electrical connection") between the readout system and the FEE, the FEE is electrically decoupled. Therefore there is no possibility to create unwanted currents. Of course the FEE (motherboard, daughterboard and OEPB) need a electrical power to work properly. This is provided by dedicated power lines which distribute all needed voltages ($+5\ V$, $+3.3\ V$, $+1.2\ V$, $+1\ V$, $\pm 3\ V$ and ground) to the FEE. This is achieved with the FanPW board in Fig. 5.5. This is the only "massive electrical connection" between FanPW and one OEPB. (See Sec. 5.4.2).

- Higher rate: with the FOT [136] it is possible to reach 250 $Mbit/s$ (up to 50 meters of optical cable), while with the differential transceiver [137] 180 $Mbit/s$ (9 differential channels which transport 20 $Mbit/s$ each).

- Low signal loss: the higher frequency, the greater the signal loss using copper cabling. With optical fiber, the signal loss is the same across frequencies, except at the very highest frequencies.

- Low weight: 6 km of optical fiber has been used to connect the all FEE boards to the respective readout. A big part of this cable is placed on the support of the chamber. The use of optical fiber decrease the weight-stress on the frame of the detector.

- Low jitter[7] accuracy: the displacement in time of a signal is an important issue when this signal is used for time measurement. Its uncertainty is directly related to the uncertainty of the spatial resolution measurement in the drift chamber (see Sec. 2.4). Therefore its precision has to be known with a given accuracy: the timing signal used to trigger the TDCs needs

[7] Jitter in technical terms used in electronics. It indicates the period frequency displacement of the signal from its ideal location. In other words, it indicates the time variation of a periodic signal. The causes of jitter in an electrical signal are:

- the limited accuracy of a transceiver;
- electromagnetic interference between devices;
- crosstalk with other signals.

The amount of tolerable jitter depends on the application.

a jitter below $\sigma_{jitter} < 1\ ns$ (σ_{jitter} refers to the standard deviation of the jitter distribution, when the jitter distribution can be represented by a Gaus function). The jitter given in the technical specification of the FOT is 1 ns [136] with a minimum of 50 cm of POF, which is too close to the minimum accuracy requested, therefore the FOT can not be used to transport "timing critical" signals.

The timing trigger is transported as differential signal (LVDS standard, on a cable of a twisted pair). The LVDS timing trigger is converted from differential to single-ended signal on the OEPB with a dedicated transceiver built in the FPGA and then distributed to the TDC on the FEE. (See Sec. 5.4.2.1).

The jitter measurement on this signal was found to be 9.5 ps with 125 MHz clock source and 7 ps with 100 MHz clock source. Therefore the jitter remains below $\sigma_{jitter} < 10\ ps$ which is acceptable for the application discussed here.

Moreover the cable used to transport this differential signal is a twisted pair cable, which reduces further the electromagnetic interference [138].

5.4.1 MDC Optical Data Acquisition System: the Concept

The optical readout, shown in Fig. 5.5, is divided into two main components:

- The OEP board.
- The MDC Optical AddOn, which gathers the FEE data belonging to one event and sends it to the central data acquisition system via a 2 $Gbit/s$ fiber optical link.

The FEE cards (64/96-channel cards, analog and digital cards)[8] are mounted on the MDC frame. They contain all the circuitry for amplification, shaping and time-to-digital conversion. The OEPBs, plugged onto the FEE cards, interface power and control signals, transmit data from the FEE to the MDC Optical AddOn which sends it to the Event Builders (EBs).

The power is supplied by the Low Voltage Switch Box to the FanPW hardware board[9]. The power distribution via the FanPW is an important concept because it avoids possible ground loops. It regulates all output voltages which

[8] Analog cards are also called daughterboards and digital cards motherboards.

[9] The FanPW is a PCB mounted close to the detector, it regulates 5 voltages needed by the FEE for a total of 35 A. It serves one HADES chamber.

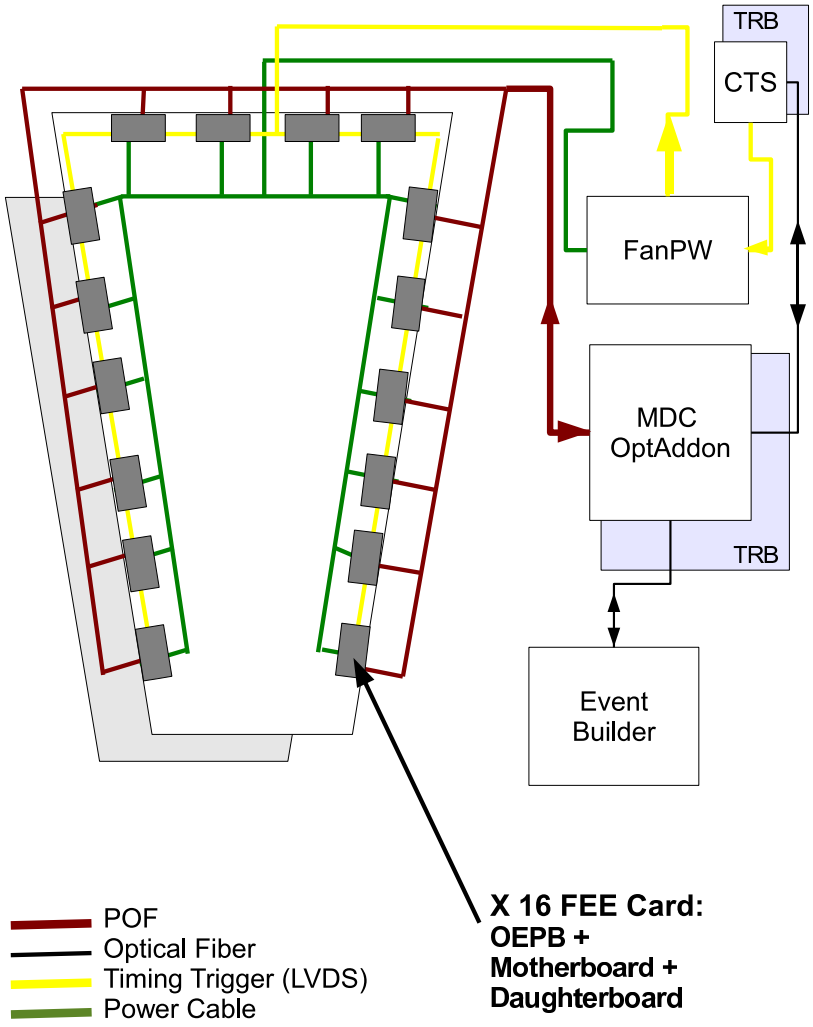

Figure 5.5: Schematic view of the readout based on optical transmission. Here, the complete digital readout chain presented in Sec. 2.4.1 is replaced, including the connection between the FEE and the readout system (realized by replacing the Driver Card (DC) by the Optical End Point Board (OEPB)). The optical readout system controls the data-flow of two MDCs via Plastic Optical Fibers (POFs). The figure shows the power distributor board (FanPW), the Central Trigger System (CTS) which delivers the timing trigger and the MDC-OptAddOn which reads out data of two MDC chambers and sends it to the Event Builders (EBs).

are distributed to 16 OEPBs. The OEPB has the features to control all voltages needed by the FEE; in order to perform a correct measurement, the TDCs

need well defined and stable voltages, as well as the electronics placed on the daughterboard.

Additionally, the FanPW board receives the timing trigger signal on a copper twisted pair cable and provides these signals to 16 OEPBs. The timing trigger signal has to be distributed to the OEPBs via a standard twisted cable (LVDS standard). As already mentioned, the transmission of this "timing critical" signal must be precise, reducing possible jitter[10].

For each timing trigger signal the CTS sends a corresponding trigger action word to the MDC Optical AddOn. When the MDC Optical AddOn receives this trigger action word, it transmits it to all OEPBs (the trigger information is encoded into this dataword) via the POF cable. This trigger action word consists in a sequence of bits. A trigger action word can initiate readout, initiate calibration readout or read events from the LVL1 event memory placed on the OEPB. The trigger uniquely identifies each event, ensuring that during event building there is no mixing of events from different triggers. The CTS generates the trigger for all detectors in HADES, initiates events, including several types of calibrations. The concept of the trigger distribution is described in Sec. 5.4.1.1.

5.4.1.1 The Trigger Distribution

In the framework of the DAQ upgrade, the trigger distribution system of HADES is replaced by a star-like distribution system, where most of the connections are based on 2 $Gbit/s$ optical links[11]. The new trigger concept uses a star-like trigger distribution via optical hubs (a hub board consists in a TRB plus a dedicated add-on, the so called Hub-AddOn), while the CTS consists of a TRB with the GP-AddOn.

Distributing a trigger to the FEE consists in a five-steps process:

- A timing trigger is sent to all front ends using a dedicated differential signal (low jitter timing trigger);
- The timing trigger signal is followed by a digital trigger which is sent over optical fibers containing information about the trigger type, the trigger

[10]The timing trigger signal, also called Common Stop (CMS) signal, is the only fast signal which is transmitted as a LVDS pair from the CTS to the FEE. Being a "fast" electrical signal, it could induce noise on the very sensitive input of the pre-amplifiers. In order to avoid possible induced noise, this cable is fixed on the frame of the chamber, far from the Flexible Printed Cables (FPCs) (see Sec. 2.4.1).

[11]The trigger distribution, which was used up to year 2008, was based on a bus-like system. It turned out that a bus-like trigger distribution system is not easy to monitor and maintain. For example, in the case of a malfunction, all the connections of the affected bus have to be checked. Furthermore, all hardware modules, besides the CTS, are in a pure slave mode and can not drive the bus without a trigger [123].

number and further control information for the readout process.

- The FEE can finish the analog-to-digital conversion or the time-to-digital-conversion and store the acquired data in internal FIFOs.
- The FEE sends to the CTS a "busy release" signal which indicates the successful trigger and the ability to accept the next trigger.
- The CTS triggers the readout process for each event by sending a request to all FEE. Finally the FEE sends data to the MDC-OptAddOn, which combines data from several FEE and sends it to the Event Builder processes. Each EB collects about 40 events and merge them into one complete event which is sent further to the data storage system.

The requirements of the protocol responsible to the trigger distribution, based on optical links, are:

- Full back pressure: if one of the readout boards becomes overloaded with detector data, it will generate and assert a trigger "busy" signal which will be forwarded to the CTS, in order to stop the generation of the LVL1 triggers.
- Short and guaranteed latency: the trigger has to be delivered not later than $1 - 2\ \mu s$ after the timing signal has arrived.
- Guarantee data integrity: the protocol should prevent any data loss by handshake software.

5.4.2 MDC Optical Data Acquisition System: the Realization

This chapter gives a description of the hardware and software used in order to integrate the MDC FEE into the TRB framework. Hardware and software are described following the path of the data flow.

The modules responsible for the MDC data acquisition are:

- The CTS board: it generates triggers.
- The OEPB: it forwards the timing trigger to the TDCs and collects FEE data. On request it transmit data to the MDC Optical AddOn.
- The MDC Optical AddOn: it gathers the data coming from 32 OEPBs.

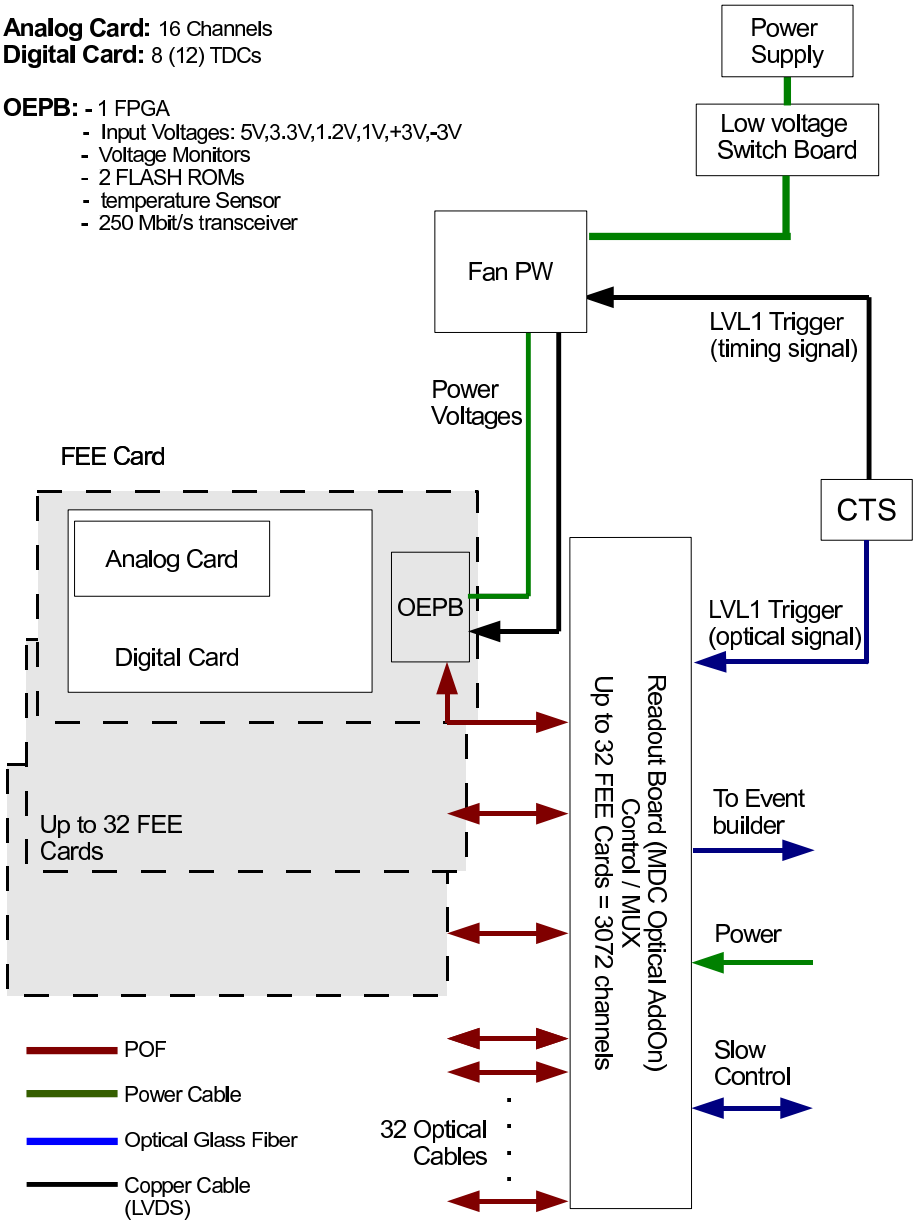

Figure 5.6: Overview of the on-detector HADES MDC readout electronics. The 64/96-channel FEE cards plug into the MDC frame, while the Optical AddOn is mounted nearby. The OEPB is placed on the FEE cards. The trigger, power and slow control cables are connected to the electronics platform.

The hardware presented in Fig. 5.6 is described in the Sec. 5.4.2.1, while in Sec. 5.4.2.2 the description of the software implemented in each module is ex-

plained following the same criteria. Particular emphasis is given to the OEP board, in its hardware and software implementations.

5.4.2.1 The Hardware

The CTS: The Central Trigger System (CTS) consists of a TRB with the GP-AddOn, providing the connections to the trigger sources and generating the digital LVL1 trigger information.

The CTS is the main module responsible for triggering and monitoring the whole DAQ system. The CTS consists of a first level trigger (LVL1) logic, implemented in one TRB plus a general purpose AddOn.

The functionality of the module is implemented in the FPGA configuration which is configured via FLASH memory or through the JTAG [139, 140] interface[12]. All signals required to generate LVL1 triggers are connected from detectors to this module.

The Optical AddOn Board: Like in the version 1, a dedicated add-on board is used to concentrate the data produced by the FEE cards. This new concept reduces the noise which was induced by fast signals in the copper bus cables into the very sensitive HADES MDC detector. The data is received by a MDC-AddOn (version 2 or MDC-OptAddOn), which is equipped with 32 optical transceivers [130]. Each transceiver transports data at a rate up to 250 $MBit/s$.

The board is equipped with two Lattice FPGAs (ECP2/M100) which receive the data and combine it to events. Upon a positive LVL2 trigger, data is transported to mass storage via 2 $Gbit/s$ optical link.

The Optical End Point Board (OEPB): On the FEE side, an OEPB has been developed and substitutes the previously used transceiver FEE card or Driver Card (DC).

The OEPB is equipped with a small but powerful Lattice FPGA (ECP2/M20) chip, which controls configuration and readout of the chamber's TDCs (see Fig. 5.8).

A Fiber Optical Transceiver (FOT)[13] is placed on the board: a resonant cavity (Light-Emitting Diode (LED) at wavelength of 650 nm) with an en-

[12] Historically, Joint Test Action Group (JTAG) was devised for testing printed circuit boards using boundary scan and is still widely used for this application. Today, the JTAG is widely used for programming Integrated Circuits (IC) chip. Many modern processors support JTAG. Embedded systems development relies on debuggers based on JTAG communication.

[13] This component is an optical transceiver which converts electrical signals into light signals. The transceiver adopted is the FDL300T built by Firecomms [130, 136].

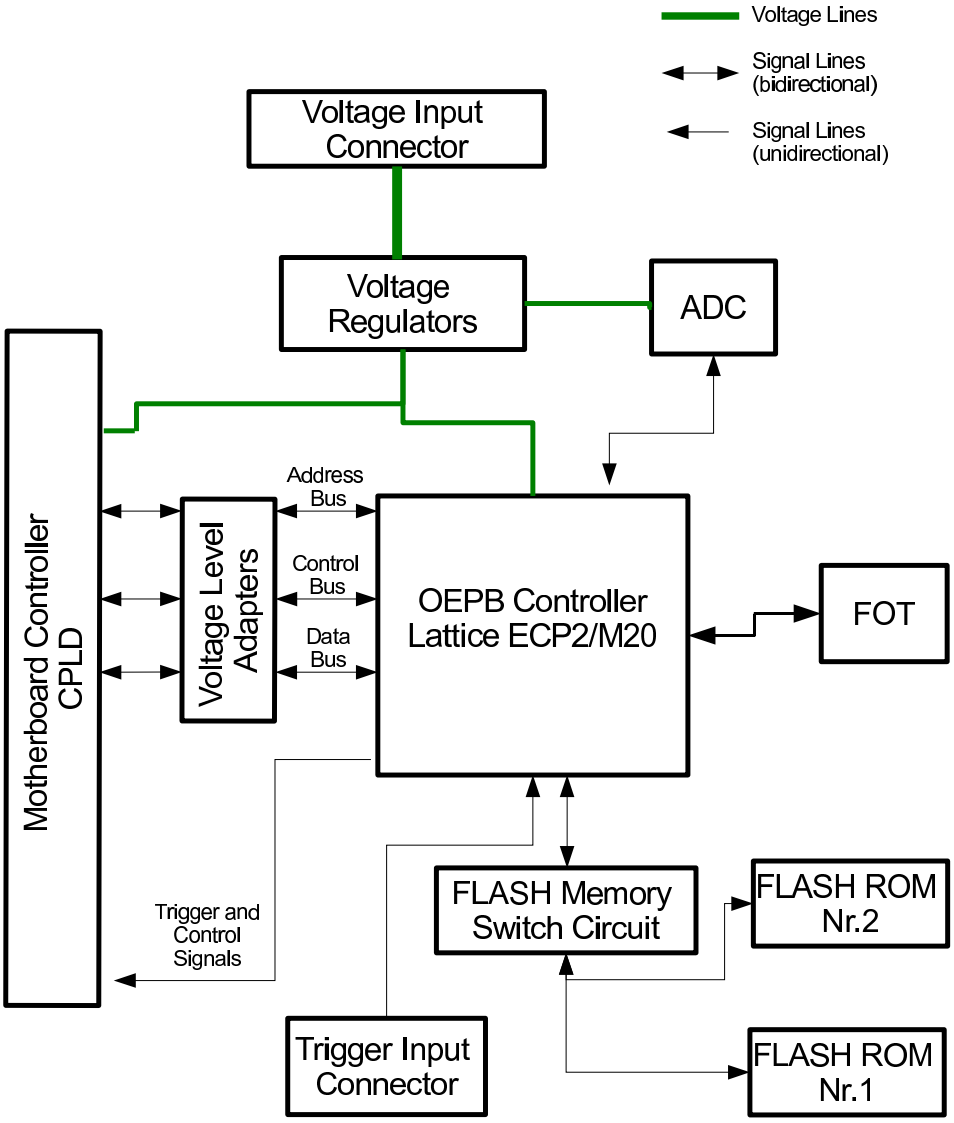

Figure 5.7: Block diagram of the hardware implementation of the Optical End Point Board (OEPB). Its main component is the Lattice FPGA (ECP2/M20), which contains the firmware dedicated to the control of the FEE. The hardware is composed by two FLASH ROMs for the FPGA firmware, the FOT, the voltage regulators and the input connector for the trigger timing signal. The software loaded into the FPGA includes TDC initialization interface, TDC calibration interface, TDC slow control interface, trigger interface and data readout interface.

capsulated driver Integrated Circuit (IC) couples electrical media signals to light [136]. Its small emission aperture is suited for many Plastic Optical Fibers (POF) packages. The POF employed has a diameter of 1.5 mm. A LVDS in-

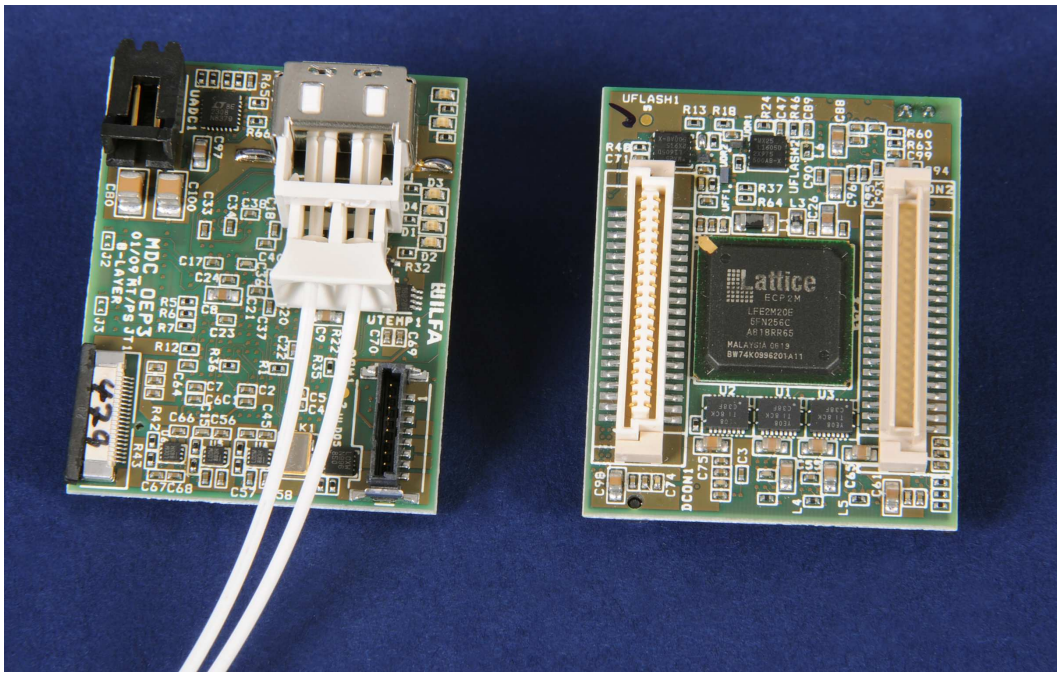

Figure 5.8: The Optical End Point Board (OEPB). Back view of the card (right hand side on the picture): the Lattice FPGA (ECP2/M20) is visible in the center of the board, it contains the data FIFOs and all the necessary logic (firmware) to configure and control the FEE. The FPGA contains dedicated hardware to detect Single Event Upsets (SEUs), described in App. B. The two parallel white connectors are used to plug the OEPBs onto the existing FEE cards. Top view of the card (left on the picture): it shows the FOT connector (white color) and two black connectors. The 8-pin black connector provides the power to the OEPB and the 2-pin one is for the timing trigger (CMS signal). The board measures 4.0×5.0 cm^2.

put/output is connected directly to the FPGA SERDES, which works down to 250 $Mbit/s$ while the FOT works up to 250 $Mbit/s$.

The advantage of the OEPB design and the use of optical fibers results in total electromagnetic immunity, amazing simplicity in handling and low power consumption. The employment of a Lattice ECP2/M20 FPGA with large resources allows for the storage of several events (up to 30 events and a few calibration events) close-to-front-end in dedicated FIFOs (see Sec. 5.4.2.2). The

software loaded into the FPGA includes the TDC initialization interface, the TDC calibration interface, the TDC slow control interface, the trigger interface and the data readout interface (see Sec. 5.4.2.2).

Since the OEPB has to be mounted on existing FEE electronics board, on the frame of the detector, the main challenge of this design was to fulfill the strict space constraints imposed by the already existing FEE boards.

Fig. 5.7 shows the block diagram of the OEPB. The main components of the board are drawn with their connection lines. The power lines are regulated and distributed to all components and to the FEE. An Analog to Digital Converter (ADC) monitors all voltages.

The connection between FEE and FPGA is made up with three different buses: address and data bus for the data flow and one control bus which is used to control the TDC operations. The voltage levels between FEE and FPGA are different: the "Motherboard Controller CPLD" uses TTL signals, while the Lattice FPGA uses LVTTL signals. Since the Lattice FPGA can not accept TTL input signals, the signals between this two devices have to be regulated by three "Voltage Level Adapters". Particular attention was placed in the test of these hardware components: indeed it is essential that the level adapters change the voltage level properly at different rate of input/output signals. The maximum expected frequency of the signals which have to be regulated is about $1.0 - 10.0\ MHz$, however the level adapters have been proven to be stable even an higher frequency $50.0\ MHz$.

Fig. 5.7 shows the input connector for the timing trigger (one LVDS pair). This differential signal is unidirectional as indicated by the direction of the arrow and it is converted from input-LVDS to output-TTL standard in the FPGA[14]. This signal is directly connected to the CPLD (Motherboard Controller) and no logic manipulates this signals in the FPGA (*i.e.* this signal is not registered in the FPGA to avoid the modification of the timing property of this signal).

Few more signals are driven directly from the FPGA to the CPLD; these are control signals which have output direction respect to the FPGA, therefore do not need any signal conversion by additional circuitry.

Two separate FLASH ROMs store two designs which can be loaded into the FPGA: one can be changed often using the slow control system, one provides a "golden image" that ensures the FPGA can be loaded again after a failure of the second FLASH ROM.

The FOT is used for the communication to the Optical AddOn Board (see Sec. 5.4.2).

[14] An advantage of using FPGA technology consists in the ability to program via software the signal type of the I/O signals. Internal FPGA transceivers can be programmed and perform the signal conversion. In this particular application the timing trigger (input respect the FPGA) is converted from input-LVDS to output-LVTTL.

The software loaded into the FPGA is described in Sec. 5.4.2.2 and includes TDC initialization interface, TDC calibration interface, TDC slow control interface, trigger and data readout interface.

5.4.2.2 The Software

The CTS: In this paragraph the basic principle of the HADES two-level trigger system software is introduced. The two-level trigger system was successfully used up to year 2008 and it was mainly implemented in VME-boards which were built more than ten years ago. Within the DAQ upgrade project it was reasonable to reconsider the whole concept and make use of new technologies in order to build a reliable TRB-based trigger system [118]. In order to explain the basic of the CTS software, a sketch is presented in Fig. 5.9 and it is based on the two-level trigger concept adopted up to year 2008.

One part of the CTS is the LVL1 trigger logic: the trigger signals are produced by a Central Trigger System (CTS) which consists of a Central Trigger Unit (CTU) and a Matching Unit (MU). The CTU generates digital trigger information, containing the trigger number and the physics source of the trigger, to induce the specific actions of the Front End Electronics (FEE) of the individual sub-detectors. The CTU can handle several types of triggers (*i.e.* different multiplicity pattern) and calibration triggers.

The Optical AddOn Board: In the framework of the HADES DAQ upgrade a media independent protocol (TRBNet) for data communication has been developed [131]. This is implemented in the MDC Optical AddOn Board as well.

The main feature of the TRBNet is the "concurrent" transmission of data/trigger and slow-control data on the same fiber; it guarantees low latency and no data loss due to the back pressure feature.

Every board is equipped with a temperature sensor each having a world-wide unique serial number that allows to identify it in the network. Based on this, a unique selectable TRBNet-address is assigned to each board during the start-up phase of the network. This allows for an individual access of all front-ends boards via the central trigger monitoring system.

The Optical End Point Board (OEPB): The Lattice FPGA is programmed with the Very High speed integrated circuit Hardware Description Language (VHDL)[15]. (See also [141, 142]).

[15] VHDL is a hardware programming language. It is a powerful and versatile language which offers numerous advantages:

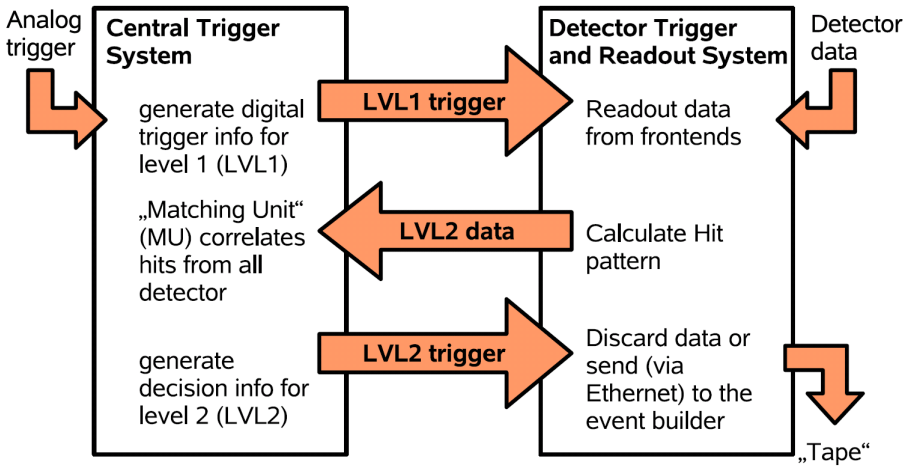

Figure 5.9: Principle of the HADES two-level trigger system: the Central Trigger System (CTS) samples the analog trigger. Trigger information is transported to the individual sub-detector trigger systems via the Detector Trigger Systems (DTS) via a LVL1 bus cable. The LVL2 trigger decision is based on hit patterns of the detectors. Only data with a positive LVL2 trigger decision are transported to the Event Builders (EBs). The picture has been taken from [123].

The FPGA Lattice programs consist of several entities or modules[16], which communicate with each other through internal programmable buses within the FPGA. Their tasks are summarized in the following points:

- *Initialization of the FPGA modules*: In this entity all registers and FIFOs are initialized to appropriate initial values. All state machines go to a defined default value.

- It is very flexible in its approach to describe hardware via "black box" named entities.
- It is technology independent: VHDL is independent of any specific technology or process. This allows to use the same code for different FPGA families or vendors.
- It is a standard language, hence it is easy to write documentation and maintain over the years.
- A large amount of packages and libraries are available. This allows common elements to be shared among members of a design group.

[16] With the word "entity" is meant a part of the VHDL code design. In general an entity module is split into two parts, each of which is called a "design unit" in VHDL jargon. The declaration of an entity represents the external interface to the design entity, input or output ports. Inside one entity, the "architecture body" represents the internal description of the design entity, its behavior or its structure.

- *FEE Initialization:* Upon an application request, the TDCs are initialized. They can be initialized to different working modes. Four of them are implemented and explained in this work:

  1. Initialization mode: the TDCs are initialized, their integrity is checked and if they are ready to perform any action the next working mode can be executed.
  2. Measurement mode: the TDCs are armed to perform a time measurement.
  3. Configuration read-back mode: the four TDC configuration registers can be read out. The read back value is written into a FIFO and they are accessible at any moment by any user application.
  4. Calibration mode: the TDCs are prepared to perform an internal calibration.

  In general, for each of the four working modes, the TDC have to be pre-initialized following a number of instructions: the TDC registers are written and upon an answer from the TDCs, the configuration registers are read back. This configuration is stored in a RAM memory and can be easily accessed via the slow control channel for the data verification[17]. After this action is completed, the TDC are armed in one of the modes mentioned above.

- *FEE data readout:* The time measurement in the TDCs starts when the signal induced on the wire arrives at the TDCs (see Sec. 2.4.1). After the initialization and after checking the TDC integrity the state machines are in idle-state, waiting for a timing trigger which will stop the measurement. After a timing trigger has been distributed to the TDCs, then the data is read out from the TDCs. The data is transferred into the LVL1 FIFO.

  A second FIFO is filled with a header word corresponding to the event collected. An acknowledgment signal is sent by the FEE when the event has been completely received. Hence, the event can be read out (consisting of one header from the LVL1 header FIFO and n-words[18] from the LVL1 data FIFO) by the IPU-channel. The IPU-channel is an entity which enables the communication between the OEPB and the MDC-OptAddOn.

[17] The slow control channel is an access point to a particular application. A typical action via the slow control channel is the temperature measurement. Data which does not require a particular timing constraints is transmitted/received via the slow control channel.

[18] In general one event consists of n-data-words, which can vary from event to event. For each event a header word is generated and stored in a dedicated FIFO.

In this entity a network protocol named TRBNet [131] is implemented. This protocol is used for sharing resources using packet-switching among the readout and control boards implemented in HADES.

TDC Configuration

For the proper operation of the TDCs, four TDC configuration registers [121] have to be loaded properly. The OEPB has a volatile programmable memory for this configuration information which have to be initialized for every start of the system (see Fig. 5.10).

External programs have to access the OEPB and write the desired TDC configuration data in a RAM memory. This is done via the Slow Control Channel programs[19]. These external programs are part of the slow control system of the HADES DAQ which access the OEPB remotely. This is done because the OEPBs are located on the detector in the high radiation area which is not accessible during HADES operation. The slow control programs run on CPU (*e.g.* on the LINUX CPU on the TRB, see Sec. 5.2.1). Launching one of this programs has a direct effect on the OEPB which is addressed.

The various configuration registers are written into the Configuration Data RAM with the help of a control program: the RAM Controller (see Fig. 5.10).

FEE Data Readout

The system is read out asynchronously, hence the FEE data has to be stored in data memory[20] until a trigger decision for that event is delivered by the MDC-OptAddOn.

Depending on the trigger decision, the data is either discarded or sent to the next FIFO or to the MDC-OptAddOn. In Fig. 5.11 the FIFOs in the OEPB are green colored. Upon a LVL1 timing trigger, the data is collected into the first LVL1 FIFO. At the same time a header for this event is generated and stored in the first LVL1 Header FIFO. When the network system requires the data, the header and the corresponding event are combined to a second FIFO and then are transmitted over the network to the MDC-OptAddOn. In Fig. 5.12 the block diagram of the implementation is shown.

As discussed earlier the first level trigger (LVL1) has to run at event rates of 100 kHz. This means that events must be read out within 10 μs, then OEPB

[19] All Slow Control programs are called "Slow Control programs" as they do not fulfill real time (fast) purposes, nevertheless they are essential for the correct operation of the whole system.

[20] Memory elements are implemented in software as First In First Out (FIFO).

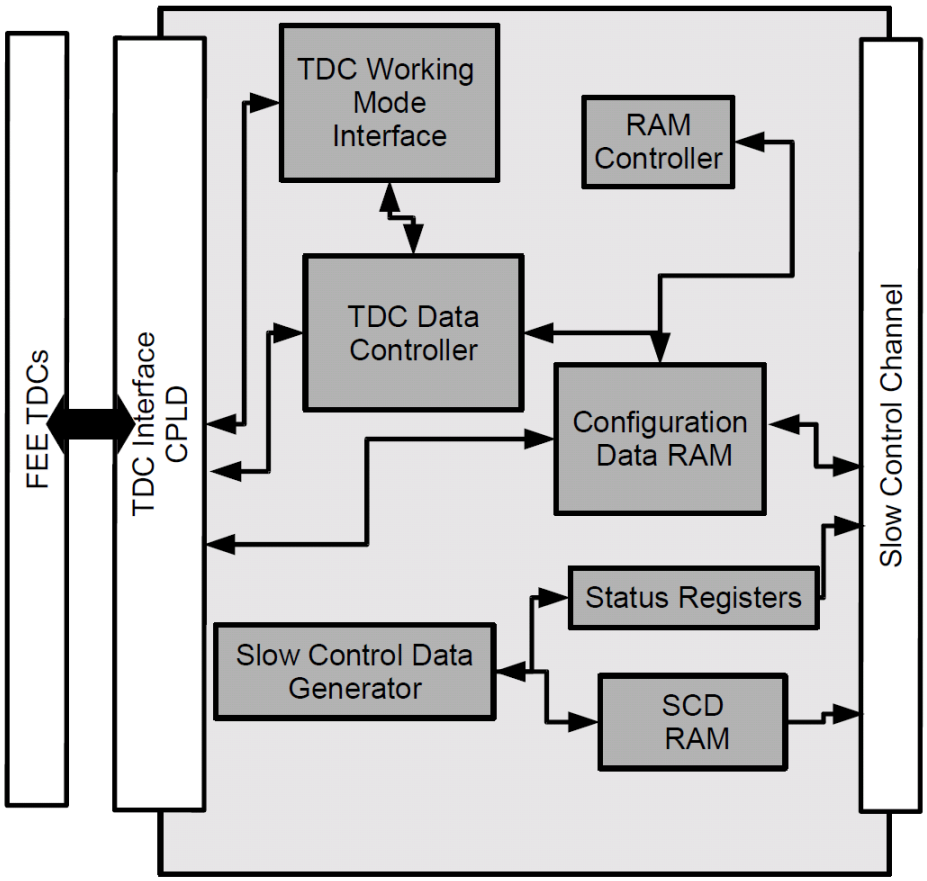

Figure 5.10: Block diagram of the software implementation of the TDC initialization modules in the OEPB. Each block represents an entity in the FPGA and the signal connection between entities is shown with arrows. The communication between external programs (slow control programs) and the OEPB is done via the Slow Control Channel. The Slow Control Data Generator (SCDG) is an entity which provides useful information (debug information) to the user via the Slow Control Channel. The SCDG generates statistics such as the number of dataword per event, the number of data request to the FEE and the relative number of answers. This data is generated and stored in the Slow Control Data (SCD) RAM. The user can access the SCD RAM and retrieve its contents via external programs.

must be able to accept the next trigger. This can be done by dividing the whole acquisition process into sufficient small steps, during which data are buffered and eventually processed. In this way, the next event can be accepted every

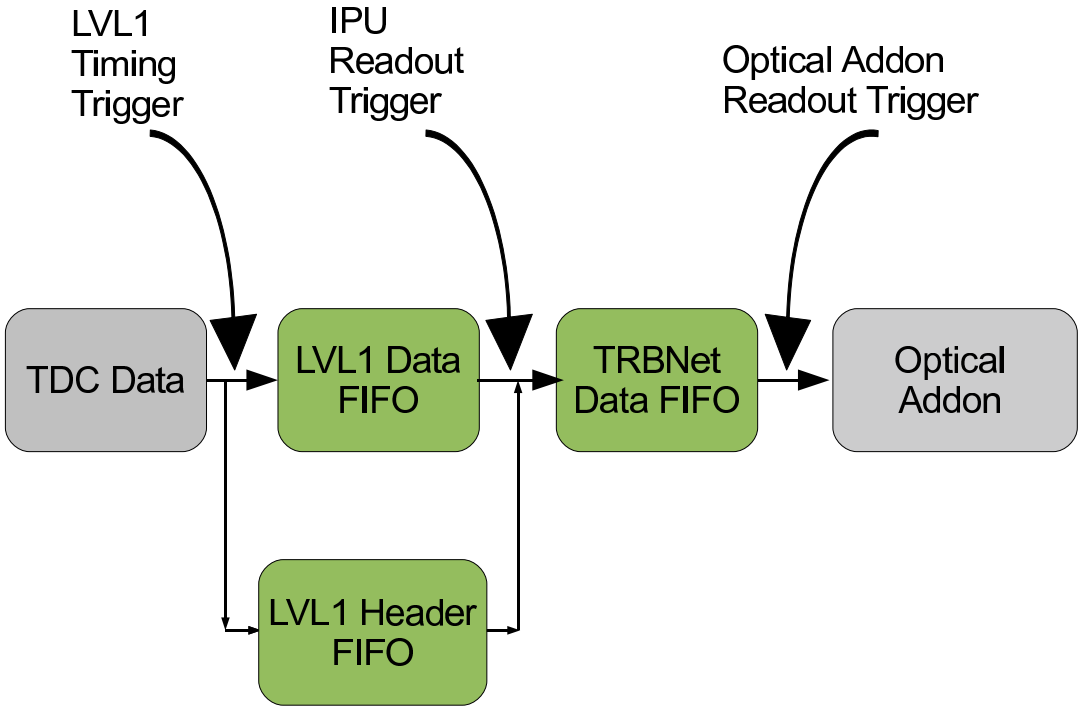

Figure 5.11: FEE data transport over the OEPB's FIFOs. The data FIFOs implemented in the OEPB are green colored. After the LVL1 Timing Trigger has been received, the TDCs generate data. The data is stored into the data FIFO. In parallel a header is generated by the logic. The header contains all information about the event collected. Upon an IPU readout request, the event (data and header) is send into the TRBNet Data FIFO and sent to the MDC-OptAddOn.

10 μs. This scheme implies a time delay between consecutive triggers, the so called latency. Moreover, the ability to store many events in the FEE gives to the data acquisition system the opportunity to handle large variations in beam intensity during the experiment.

In order to realize the readout scheme introduced above, the OEPB should accept many events before the digital trigger (IPU Readout Trigger) requests data to the OEPB (see Fig. 5.12). It is important to program the memory of the correct size to avoid possible overflow of the FIFO which collects the incoming TDC data. In the simulation shown in Sec. 5.1 the averaged event size for each chamber is estimated to be 18 $kbits$ per event per chamber. Since one chamber is equipped with 14 (16 for some particular chambers) motherboards, one OEPB collects events with an average size of 1.3 $kbits$ each. In addition to these

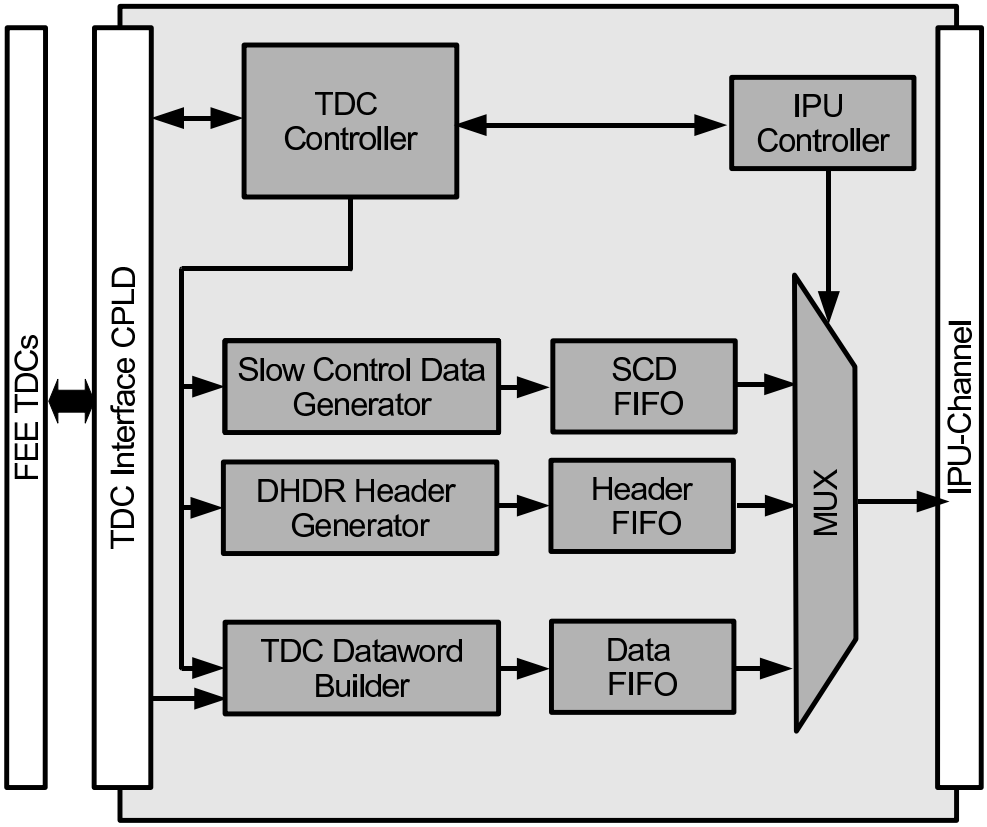

Figure 5.12: Simplified block diagram of the readout software implementation. The FEE delivers data to the OEPB. Data is stored in a FIFO and a Header Generator builds the header corresponding to the acquired event. In the header all information related to the event is stored. Upon an IPU request, data is then multiplexed into the IPU-Channel. In parallel, a Slow Control Data Generator generates additional event information (*i.e.* number of data word in each event, eventual errors, state of the readout program, and internal control statistics data) which can be read out via the same output channel.

events the calibration process of the TDCs produces event of 1.8 *kbits* for each motherboard. With this estimate the LVL1 Data FIFO has been programmed to store 100 events (180 *kbits*) and 20 calibration events ($\sim$ 360 *kbits*), for a total size of 540 *kbits*.

After the data is read out from the TDCs and stored in the LVL1 Data FIFO can be accessible via the request of the IPU Readout Trigger. The data can be read out from the OEPB and sent to the MDC-OptAddOn in two different formats:

- Verbose Mode: TDC data and additional information are transmitted;
- Compact Mode: only TDC data is transmitted and it is compressed respect to the first one in order to reduce the load over the network.

More details about the data format developed in this work can be found in App. C.

The ECP2/M20 Lattice FPGA

The most important device on the OEPB is the Lattice FPGA. Its block diagram is reproduced in Fig. 5.13. As described above, it performs all controls operations of the TDC FEE, it stores data and sends it via the optical link. The ECP2/M20 Lattice FPGA has been chosen mainly for the following reasons:

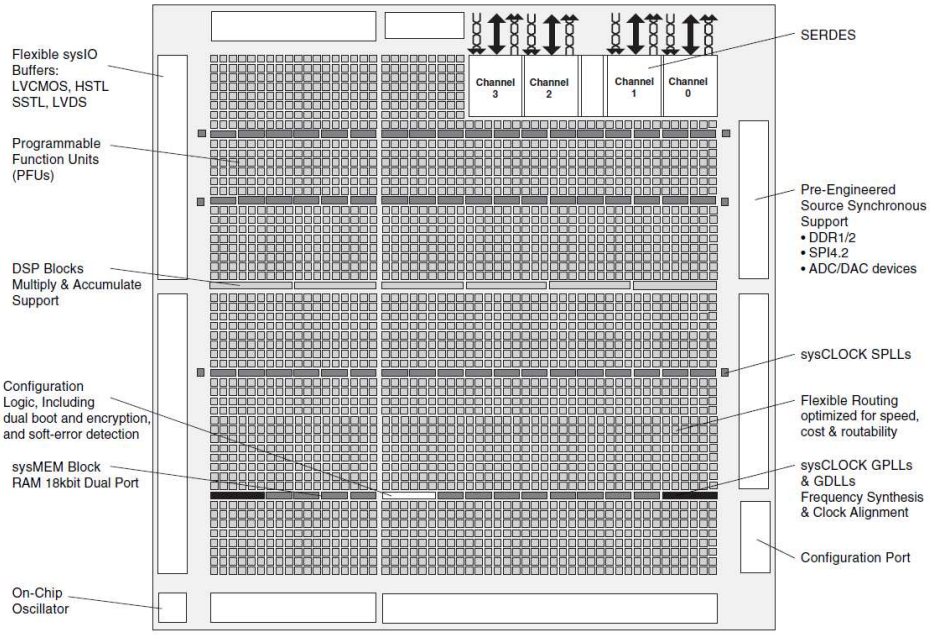

Figure 5.13: ECP2/M20 Lattice FPGA, simplified block diagram. The picture has been taken from [133].

- The Lattice FPGA has high performance features such as high speed Serializer/Deserializer channels (SERDES) and high speed source synchronous interfaces in an economical and small FPGA.

- Low power consumption. The Lattice FPGA is mounted on the OEPB which is attached to the detector's frame. The MDC detector is a gas-based detector and is extremely sensible to temperature changes as well as the TDCs. A FEE which requires low power is mandatory in the upgrade project. The current needed by the FPGA has been measured to be $\sim$200 mA.

- The Lattice ECP2/M20 devices include LUT (Look Up Table)-based logic and big memory elements (distributed or embedded memories). Each memory block can be configured in a variety of depths and widths of RAM, ROM or FIFO.

- It is equipped with Input/Output pairs (PIO) on the left and right edges. The PIO can be configured as LVDS transmit/receive pairs.

- This chip family provides Soft Error Detection (SED) capability, extremely important for the radiation environment where this chip is placed. In App. B the results of irradiation tests on the Lattice FPGA are shown.

A summary of the Lattice ECP2/M20 features is listed in Tab. 5.2. The software developed in this work is implemented using $\sim$40% of the FPGA resources.

Device	Description	Tot. Resources	Usage
LUTs (K)	programmable memory	19	42%
Embedded Memory (kbits)	basic memory elements	1217	53%
Distributed Memory (kbits)		41	19%
sysDSP Block	DSP Blocks	6	-
SERDES	Serializer/Deserializer Channel	4	25%
I/O	Input/Output pins	140	25%
SED detection		1	100%

Table 5.2: The table shows the ECP2/M20 main device features. The firmware explained in this work needs the resources listed in the last column of the table.

5.5 Conclusions and Outlook

Chapter 5 is dedicated to the hardware project namely the upgrade of the MDC readout system based on optical technology. The motivation for the detector upgrade and electronics of HADES has been introduced. The focus is placed on the MDC optical readout. Here, the main issue is the possibility to use the original MDC FEE cards (daughterboards and motherboards), reduce the noise induced by the previously used copper cables, improve the readout speed via optical fibers and the reliability of the system. The copper cables are replaced by Polymer Optical Fiber (POF) which seems to be - due to their easy handling and small drivers - a good candidate for the FEE readout of other FAIR projects as well. Due to a large number of FEE boards (nearly 372 cards) and the difficulty to access these boards while the experimental setup is operational, the idea of a small, compact and flexible (reprogrammable) board has been developed: the OEPB. Particular attention was placed in the test of the hardware components of the OEPB and in the design, simulation and implementation of the software

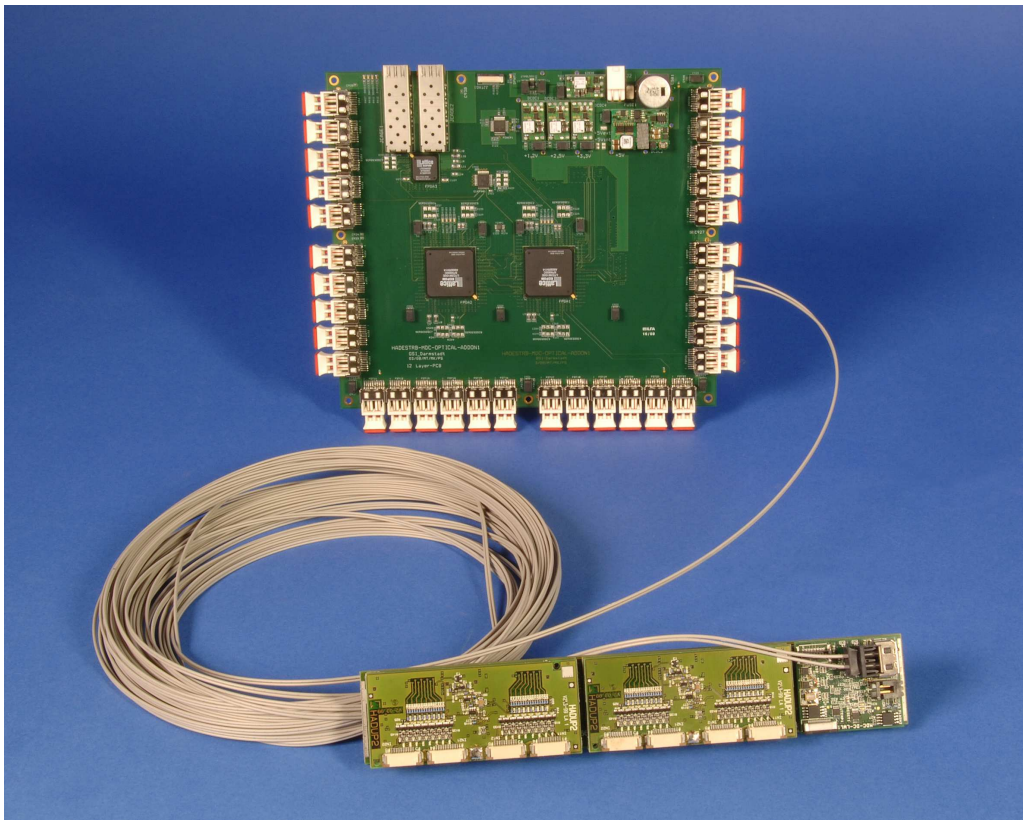

Figure 5.14: The MDC-OptAddOn (in back, size: 20.0×23.0 cm^2) together with the FEE (in front): the optical POF is connected to the OEPB (on the right side) which is plugged onto the motherboard. Here, two daughterboards are connected to the motherboard (left part). The OEPB contains all parts of the circuitry/firmware which serve to control all the working properties of the FEE card.

which is necessary for the configuration of the TDCs and their data readout.

As of the date of this thesis, all hardware modules are available. Fig. 5.14 shows a complete new readout chain for two MDC, containing the optical hub (MDC-OptAddOn). It shows the POF cable and the new driver card plugged onto a MDC motherboard. By the end of year 2009, 500 OEPBs have been produced and have been commissioned in January-March 2010.

The electronics was installed on the HADES MDC detector, and has been exercised extensively and measurements were conduced during the beginning of year 2010.

It is expected that the new developments presented fulfill the requirements

and thus the overall goal of having a new MDC data acquisition system with the techniques presented in this work.

Here, I would like to remark the following: as the upgrade of the electronics of the MDC detectors is a central part of the whole upgrade, the creation, the test and the commissioning of the system have lasted for four years and were lengthy but successful.

A huge effort of the whole HADES DAQ team [134] during the past years made these results possible. The perseverance, the cooperation and teamwork made this part of the HADES upgrade possible too.

A first paper of the results obtained in the context of this work is already available in [126] and a publication to the TNS IEEE journal will follow.

Chapter 6

Zusammenfassung

In dieser Arbeit wurde die Produktion von Elektronenpaaren in p + p Reaktionen bei einer Strahlenergie von 3.5 GeV untersucht. Die Messungen wurden mit dem HADES-Spektrometer an der GSI durchgeführt (vgl. Abschn. 6.1).

Neben der Analyse von Elektronenpaaren wurden im Rahmen dieser Arbeit einige technische Projekte zur Verbesserung mehrerer Subsysteme des Spektrometers realisiert. Zusätzlich beschäftigt sich ein Teil der Arbeit mit der Elektronik-Entwicklung für die Auslese der Multi Wire Driftkammern (MDC) (vgl. Abschn. 6.2).

6.1 Datenanalyse in HADES

6.1.1 Einführung

Das Studium der Eigenschaften von Hadronen, in Kernmaterie verschiedener Dichte und Anregungsenergie, ist von höchstem und breitem Interesse. Es wird erwartet, dass die partielle Restauration der chiralen Symmetrie der QCD bei endlichen Temperaturen oder Dichten der umgebenden Kernmaterie zu einer Reduktion der Massen von Vektormesonen führt.

Um solche Effekte zu untersuchen sind Vektormesonen bestens geeignet. Das sehr kurzlebige ρ Meson ($\tau = 1.3\ fm/c$) zerfällt meist noch im Kern bzw. innerhalb der Reaktionszone. Dies gilt teilweise auch für die langlebigeren ω ($\tau = 23\ fm/c$) und ϕ ($\tau = 44\ fm/c$) Mesonen, deren Lebensdauer in Kernmaterie verkürzt sein kann. Verktormesonen lassen sich in Photonen-, Hadronen- und Schwerionen-induzierten Reaktionen erzeugen. Da Leptonen im Ausgangskanal nicht der starken Wechselwirkung unterliegen, sind sie bestens geeignet, um den Zerfall von Teilchen in Kernmaterie zu untersuchen.

Der High Acceptance Di-Electron Spectrometer (HADES) Detektor am

Schwerionen-Synchroton (SIS) an der GSI ist ein Spekrometer der zweiten Generation.

In Anbetracht der niedrigen Wahrscheinlichkeit für die Erzeugung nichttrivialer Dileptonen waren die Hauptforderungen an den Aufbau: Trennung von Leptonen, selektives Trigger System, hohe Akzeptanz und Messung bei hohen Zählraten.

Die Rekonstruktion von Teilchenspuren im HADES-Spektrometer basiert nur auf wenigen Ortsinformationen. Daher können einzelne vollständige Spuren a priori nicht als solche gleich erkannt werden. Vielmehr werden durch verschiedene Kombinationen innerhalb derselben Mannigfaltigkeit von Positionspunkten mehr Spuren zusammengesetzt, als ursprünglich produziert wurden. Während dieser Prozedur werden Informationen gewonnen, die im weiteren Verlauf der Analyse zur Detektion von Konversions- und π^0-Dalitz-Paaren genutzt werden, die einen großen Beitrag zum kombinatorischen Untergrund darstellen.

Die identifizierten Spuren einzelner Elektronen und Positronen werden zu Paaren mit Teilchen entgegengesetzter Ladung (e^+e^-) kombiniert und aus diesen wird die invariante-Masse bestimmt.

Werden die Energie-Impuls-Vierervektoren (P_μ) der beiden Teilchen mit entgegengesetztem Vorzeichen (Elektron und Positron) rekonstruiert, kann die invariante-Masse ($M_{e^+e^-}$) wie folgt berechnet werden:

$$M_{e^+e^-} = \sqrt{P_\mu P^\mu} = \sqrt{(E_{e^-} + E_{e^+})^2 - (\overrightarrow{p}_{e^-} + \overrightarrow{p}_{e^+})^2} \tag{6.1}$$

wobei $\overrightarrow{p}_{e^-}$, $\overrightarrow{p}_{e^+}$ der Impuls und E_{e^-}, E_{e^+} die Gesamtenergie des Positrons bzw. Elektrons sind. Da die Ruhemassen der Leptonen gegenüber dem Impuls vernachlässigt werden können, vereinfacht sich Gleichung 6.1 nach Umformung zu:

$$M_{e^+e^-} = 2 \cdot \sqrt{p_{e^+} p_{e^-}} \cdot sin(\frac{\alpha_{e^+e^-}}{2}) \tag{6.2}$$

Hierbei bezeichnet $\alpha_{e^+e^-}$ den Winkel, den die beiden Teilchenspuren einschließen.

Die Herausforderung bei der Messung von Vektormesonen niedriger Masse über ihren Zerfall in ein Elektronenpaar liegt in der Unterdrückung des physikalischen Untergrundes durch Elektronenpaare von π^0 Dalitz Zerfällen und γ-Konversionen, insbesondere der hierdurch verstärkt auftretenden kombinatorischen Paare. Für eine Unterdrückung des Untergrundes braucht man weiterhin einen sehr sauber identifizierten Satz von Elektronenkandidaten.

6.1.2 Datenanalyse

Die Detektoren des HADES Detektorsystems, dessen sechs baugleiche Sektoren die Strahlachse rotationssymmetrisch umgeben, lassen sich ihrer Aufgabe nach in Gruppen einteilen:

- Der ringabbildende Cherenkov Detektor (RICH): zur Dielektronenidentifikation;
- Vier Multi Wire Driftkammer (MDC) Ebenen mit geringer Massenbelegung zur Rekonstruktion der Teilchenflugbahnen;
- Ein supraleitender Magnet mit dessen Feld sich der Impuls der Teilchen bestimmen lässt;
- Desweiteren einen im inneren Polarwinkelbereich montierten Pre-Shower-Detektor, der auch zur Identifikation von Leptonen verwendet wird;
- Das Multiplicity-Electron-Trigger Array (META), das aus der Flugzeitwand (TOF und TOFino) und für Polarwinkel $< 45°$ besteht, zur Identifikation von Elektronen und Positronen.

Die identifizierten Elektronen und Positronen werden dann zu Paare kombiniert, indem alle möglichen Kombinationen pro Ereignis berechnet werden. Viele dieser Paare tragen allerdings nur zum kombinatorischen Untergrund bei, der durch Analysebedingungen unterdrückt werden muss.

In experimentellen Daten ist es nicht möglich zu erkennen, ob die nachgewiesenen und kombinierten Leptonen ein Paar eines physikalischen Prozesses sind. Daher muss der Anteil der unphysikalischen Paare, auch kombinatorischer Untergrund (Combinatorial Background ($CB_{e^+e^-}$)) genannt, statistisch berechnet werden. Subtrahiert man den kombinatorischen Untergrund von allen rekonstruierten Paaren $N_{e^+e^-}$, so erhält man das sog. Signal $S_{e^+e^-}$, das bedeutet die Anzahl aller wahren Elektron-Positron-Paare:

$$S_{e^+e^-} = N_{e^+e^-} - CB_{e^+e^-} \tag{6.3}$$

Diese Gleichung wird jeweils verwendet, um die verschiedenen Observablen, wie invariante-Masse und Transversalimpuls, der wahren Leptonenpaare zu berechnen.

Um die gemessene Verteilung mit theoretischen Vorhersagen vergleichen zu können, müssen die Daten von Detektor-Ineffizienzen korrigiert werden. Für die Bestimmung der Rekonstruktions-Effizienz wurden in p + p Ereignisse die

mit dem PLUTO generiert wurden, Leptonen Spuren eingebettet. Die Nachweiswahrscheinlichkeit wird als Funktion der Ladung ($\epsilon_{\pm}$), des Impulses (p), des Polar (θ) und des Azimut-Winkels (ϕ) berechnet. Sie berücksichtigt die Verluste bei der Leptonen Erkennung und der Spur Rekonstruktion. Die Daten wurden für jedes einzelne Leptonenpaar mit dem Wichtungsfaktor $1/(\epsilon_+ \cdot \epsilon_-)$ korrigiert. Der kombinatorische Untergrund wurde in gleicher Weise behandelt und dann subtrahiert, um die mit der Nachweiswahrscheinlichkeit korrigierte Verteilung der Signale zu bestimmen.

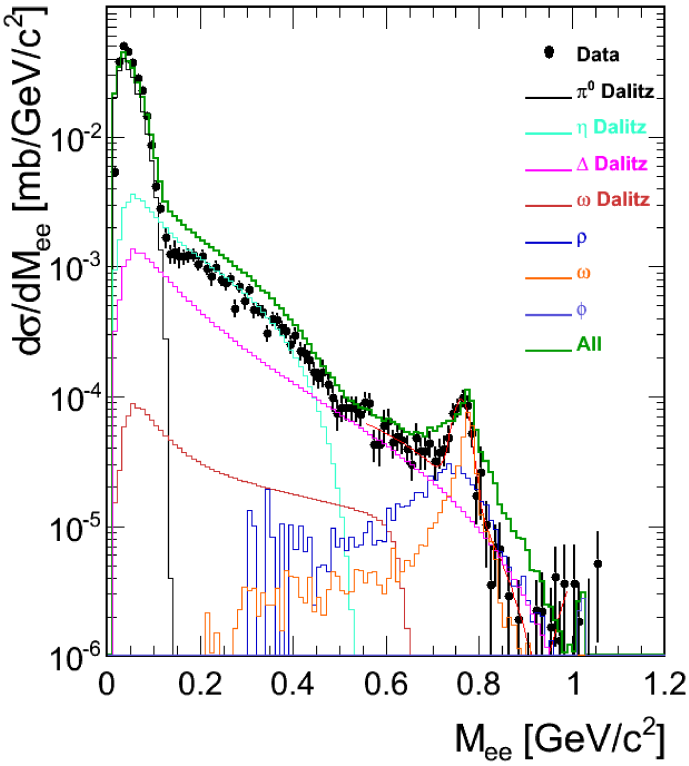

Figure 6.1: Invariante-Massenverteilung von e^+e Paare in $pp \rightarrow Xe^+e^-$. Die Abbildung zeigt HADES Datenpunkte im Vergleich mit dem HSD Modell [76, 77, 78].

Auch mögliche Nachweisbeschränkungen aufgrund des verwendeten Triggers müssen korrigiert werden. Die korrigierten Paarspektren werden anschliessend noch auf die Anzahl der elastisch gestreuten Protonen normiert.

Zur Gewährleistung einen angemessenen Vergleich zwischen Modell und HADES Daten, wurde die HSD-Simulation mit dem HADES Akzeptanz-Filter gefiltert (vgl. Abschn. 3.6). Abbildung 6.1 zeigt den Vergleich von HADES

Daten und HSD-Modell.

Die Übereinstimmung in der π^0 Dalitz Region zwischen HSD und der Daten ist gut. Für die invariante-Masse-Region $0.15\ GeV/c^2 < M_{ee} < 0.4\ GeV/c^2$ wird die Ausbeute um einen Faktor von zwei überschätzt. Während der Peak des ω-Mesons gut mit den Daten übereinstimmt, stimmen die Daten der Schwänze nicht so gut überein.

6.1.3 Ergebnisse: Inklusive und Exklusive ω Meson Produktion

In Abschnitt 3 wird die Studie der Reaktion $pp \to X\omega$ beschrieben. In Abbildung 6.2 ist die spektrale Verteilung der rekonstruierten invarianten-Masse der Elektronenpaare aus $pp \to Xe^+e^-$ dargestellt.

Das invariante-Massenspektrum und der kombinatorischen Untergrund wurden ebenfalls behandelt und abgezogen. Das invariante-Massenspektrum nach Normierung und Korrektur der Effizienz wird in Abbildung 6.2 vorgestellt und im Vergleich zu dem von PLUTO generierten Spektrum diskutiert (vgl. Abschn. 3.8). Durch die Integration des Signals im Bereich des Peaks und den Vergleich des Spektrums mit der Simulation war es möglich, den Produktionsquerschnitt der Reaktion $pp \to X\omega$ abzuschätzen (vgl. Abschn. 3.8.2).

In Abschnitt 3.9 wird die Identifizierung der Reaktion $pp \to pp\omega$ mit einer anderen selektiven Analyse beschrieben. Während bei inklusiver Reaktion die Betrachtung des kombinatorischen Hintergrunds bei der Reaktion $pp \to X\omega$ erforderlich ist, spielt sie bei exklusiver Analyse eine untergeordnete Rolle, da bei Betrachtung eines einzelnen exklusiven Kanals der Großteil der Untergrund schon abgetan ist.

Nach der Korrektur der Effizienz und nach der Normierung des invarianten-Massenspektrums wird ein Vergleich mit dem PLUTO Cocktail in Abschnitt 3.9.1.5 vorgelegt. Abbildung 6.3 zeigt das Ergebnis: Die HADES Daten werden mit den PLUTO Cocktail in Abbildung 6.3a verglichen, das Verhältnis zwischen ihnen ist in Abbildung 6.3b dargestellt. Das Verhältnis zwischen HADES Daten und der Cocktail zeigt eine gute Übereinstimmung (vgl. Abschn. 6.3b).

6.1.4 Ergebnisse: Produktionsquerschnitte für die Reaktionen $pp \to X\omega$ und $pp \to pp\omega$

Die Produktionsquerschnitte der Reaktionen $pp \to X\omega$ und $pp \to pp\omega$ mit den jeweiligen Fehlern (statistische und systematische) sind:

$$\sigma_{pp\to X\omega} = 0.2550\ \pm\ 0.0140\ (Stat)\ ^{+0.0565}_{-0.0466}\ (Sys1)\ \pm\ 0.0797\ (Sys2)\ mb \quad (6.4)$$

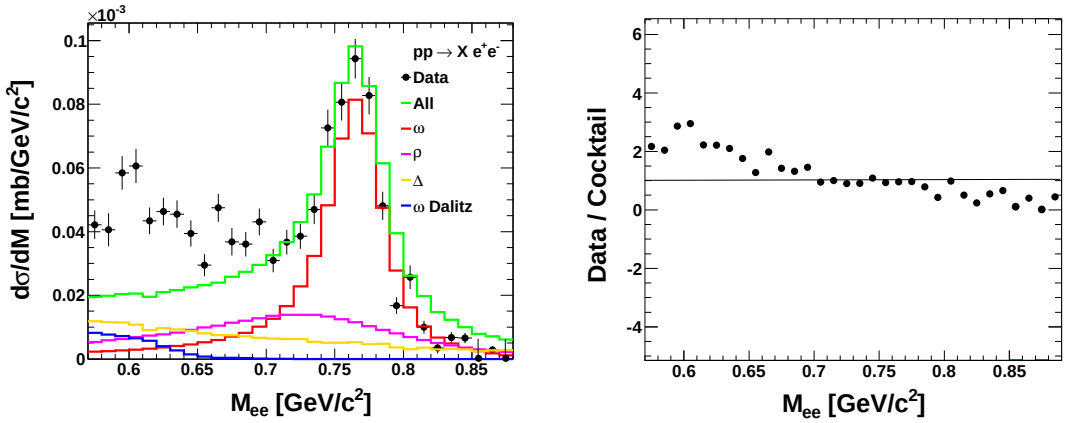

(a) (b)

Figure 6.2: Links: invariante-Massenverteilung von e^+e^- Paare in $pp \to Xe^+e^-$ aus PLUTO Cocktail. Statistische Fehler sind als vertikale Striche dargestellt. Von der oberen zur unteren Kurve werden angezeigt: das ω Meson Signal (rot), der ρ Mesons Beitrag (magenta), die Δ-Resonanz (gelb) und das ω Dalitz (blau). Die Summe der vier Komponenten wird mit grüne Farbe hervorgehoben. Rechts wird das Verhältnis zwischen HADES Datenpunkte und PLUTO Cocktail gezeigt. Die statistischen Fehler der Daten in Abbildung 6.2b werden durch die systematischen Fehler (25-30%) dominiert.

und

$$\sigma_{pp\to pp\omega} = 0.1880 \ \pm \ 0.0472 \ (Stat) \ ^{+0.0669}_{-0.0240} \ (Sys1) \ \pm \ 0.0797 \ (Sys2) \ mb \quad (6.5)$$

Diese Ergebnisse werden durch Stern-Symbole in Abbildung 6.4 dargestellt. Fig. 6.4 zeigt die inklusiven und exklusiven ω Produktion Querschnitte als Funktion der Schwerpunktsenergie ($\sqrt{s}$). Diese Daten werden mit Modellrechnungen (Fig. 6.4b)und Modellprognosen verglichen (in Abbildung 6.4a). Zuvor gemessene, experimentelle Ergebnisse sind in Abbildung 6.4b als Kreuze, Dreiecke und Quadrate dargestellt [68, 69, 70, 106, 107] und existieren nur für den exklusiven Reaktion-Kanal ($pp \to pp\omega$).

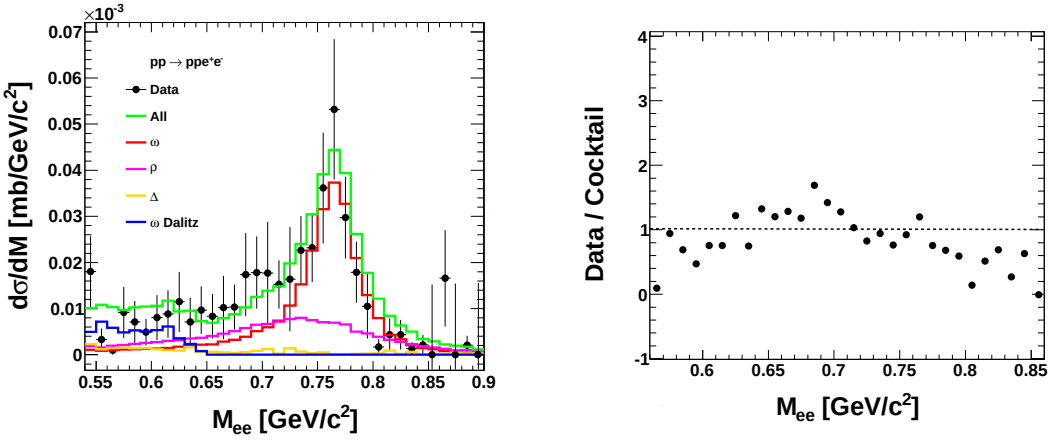

(a) (b)

Figure 6.3: Links: invariante-Massenverteilung von e^+e^- Paare in $pp \to ppe^+e^-$ mit PLUTO Cocktail. Statistische Fehler sind als vertikale Striche dargestellt. Von oben nach unten wird dargestellt: das ω Meson Signal (rot), der ρ Mesons Beitrag (magenta), die Δ-Resonanz (gelb) und das ω Dalitz (blau). Die Summe der vier Komponenten wird mit grüne Farbe hervorgehoben. Rechts wird das Verhältnis zwischen HADES Datenpunkte und PLUTO Cocktail gezeigt. Der statistische Fehler der Datenpunkte in Abbildung 6.3b werden von den systematischen Fehler (25-30%) dominiert.

6.2 Electronisches Upgrade der Multi Wire Driftkammer (MDC)

Im Rahmen dieser Arbeit wurden einige technische Projekte zur Verbesserung mehrerer Subsysteme des Spektrometers realisiert.

Wie bereits in Abschnitt 1.3.2 beschrieben, wird HADES sein experimentelles Programm mit kinetischen Strahlenergien von bis zu 8 *AGeV* weiterführen. In diesem Energie-Bereich und schweren Ionensystemen wie z.B. Au+Au werden höhere Datenströme erwartet als das aktuelle Datenerfassungssystem verarbeiten kann.

Abschnitt 5 dieser Arbeit fokussiert auf das HADES Upgrade Programm, dessen Ziel das Erreichen einer zuverlässigen und schnellen Datenerfassung der Multi Wire Driftkammer (MDC) ist.

Der Schwerpunkt liegt auf der optischen Auslese der MDCs. Hier sind die wichtigsten Fragen die Möglichkeit der Wiederverwendung der ursprünglichen MDC Front End Electronics (FEE) Cards (Zusatzplatinen und "Motherboards"), die Reduktion des Lärms verursacht durch das zuvor verwendete dif-

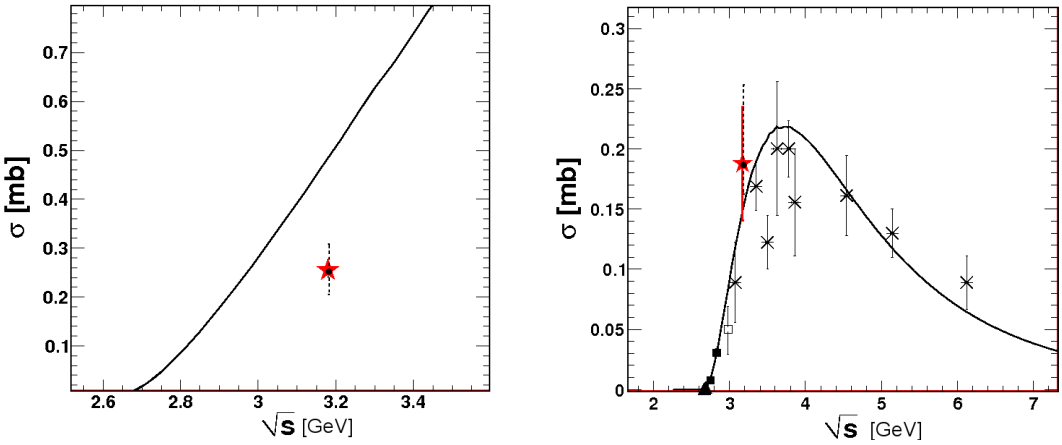

(a) $pp \to X\omega$ (b) $pp \to pp\omega$

Figure 6.4: Inklusive (in Abbildung 6.4a) und exklusive (in Abbildung 6.4b) Produktionsquerschnitte für die ω Vektormesonen verglichen mit den HSD Vorhersagen [76, 77, 78] (durchgezogene Linie in 6.4a) und OBE Berechnungn (durchgezogene Linie in Abbildung 6.4b). Die roten Sterne repräsentieren die Produktionsquerschnitte wie sie in dieser Arbeit im inklusiven (in Abbildung 6.4a) und im exklusiven (in Abbildung 6.4b) dilepton Kanäle erarbeitet wurden. Produktionsquerschnitte Werte in dieser Arbeit gezeigten in der inklusive (in Abbildung 6.4a) und in der exklusive (in Abbildung 6.4b) dilepton Kanäle: die asymmetrische systematische Fehler sind durch gestrichelte Linien dargestellt, während die statistische Fehler durch eine rote Linie auf dem Datenpunkt dargestellt werden. Links: die statistischen Fehler sind klein($\sim 6\%$) und werden durch die Dimension des Symbols dargestellt. Rechts: die schwarzen Datenpunkte sind aus [68, 69, 70, 106, 107] entnommen.

ferentielle parallele Kupferkabel, die Verbesserung der Auslesegeschwindigkeit über optische Fasern und die Zuverlässigkeit des Systems.

Aufgrund einer grossen Anzahl von FEE-Boards (fast 372 Karten) und der Schwierigkeit, auf diese Karten im laufenden Betrieb zuzugreifen, kam die Idee eines kleinen, kompakten und flexiblen (programmierbaren) "Boards": das Optical End Point Board (OEPB).

Die Kupferkabel werden durch Polymer Optical Fiber (POF) ersetzt. Dies scheint - aufgrund ihrer einfachen Handhabung und kleinen Treibern - eine bessere Alternative für die FEE Auslesen zu sein. Die wichtigsten Vorteile dieses Projektes sind:

- Geringer Stromverbrauch;

- Großer Störabstand;
- Vermeidung von möglichen "ground loops";
- Höhere Rate;
- Gute Zeitauflösung des "Timing Trigger-Signal" ("Low Jitter").

Dabei handelte es sich im Wesentlichen um die Entwicklung von Software basierend auf der Lattice Field Programmable Gate Array (FPGA) Plattform, geschrieben in Very High speed integrated circuit Hardware Description Language (VHDL). Kapitel 5 präsentiert meiner Beitrag zu diesen erfolgreichen Projekt während der drei Jahre meine Anwesenheit an der GSI.

List of Figures

List of Tables

Appendix A

The HADES Geometrical Acceptance

The acceptance of a detector is defined as a probability that a particle, emitted in the target, crosses the "fiducial volumes" of the detectors.

The computation of the detector acceptance is based on the simulation procedure described in Sec. 3.4. In analogy to the pair efficiency it is defined as the product of two single electron, positron acceptances ($A_{e^+}(p,\theta,\phi)$ and $A_{e^-}(p,\theta,\phi)$). The factor $A_{e^\pm}(p,\theta,\phi)$ is determined by the detector geometry and by the deflection of charged particles in the magnetic field as a function of the particle charge Z, momentum (p) and the emission angles θ and ϕ.

The HADES geometry results in a smooth dielectron acceptance, shown in Fig. A.1 as a function of invariant-mass (M_{ee}), transverse momentum (P_t^{ee}) and averaged over the rapidity (Y_{ee}) of the dilepton pair. As one can see in Fig. A.1, the edges of the acceptance are not sharp in the three dimensional space. The pair acceptance is rather flat and reflects the losses due to finite solid angle coverage of the detector.

The HSD theory model which is compared with the HADES data in Sec. 4.1.1 has been filtered using this matrix: the term "filtering" means keeping the pairs which lie within the detector acceptance region and rejecting those that lie outside the acceptance.

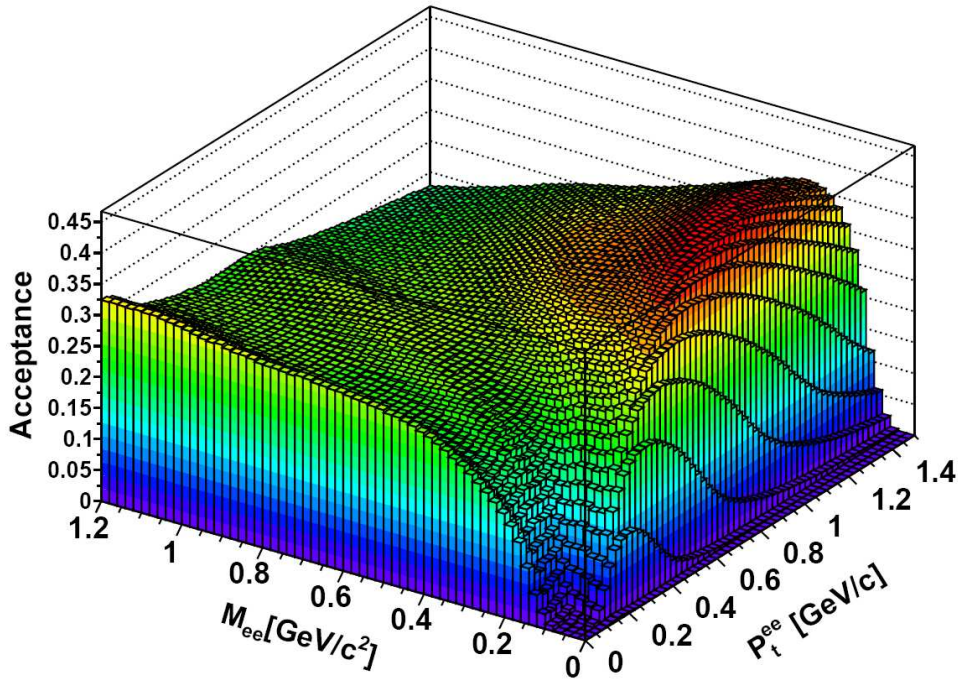

Figure A.1: Acceptance matrix of the HADES spectrometer for e^+e^- pairs with laboratory opening angle cut $\theta_{e^+e^-} > 9°$ as a function of their invariant mass (M_{ee}) and transverse momentum (P_t^{ee}). The acceptance has been averaged over the HADES rapidity covered by the detector ($0 < Y_{ee} < 2$).

Appendix B

Single Event Upset (SEU) detection with Lattice FPGA ECP2/M20

Given the remarkable success of reprogrammable logic, the interest in their front-end use has become more important in the last years. As described in Sec. 5.4.2.2, such devices have many advantages, but they are susceptible to bit upsets induced by radiation: so called Single Event Upsets (SEUs). The source of bit upset is the radiation to which an FPGA is often exposed in high energy physics experiments.

SEU are called "soft errors". They occur when charged particles alter the stored charge in a memory cell in an electronic circuit. As geometries of FPGAs have continued to shrink, the probability that soft errors appear has become significant for some devices. Designers are using a variety of approaches to minimize the effects of soft errors on system behavior [132].

In order to verify if SEUs are an issue for the application described in Chapter 5, an irradiation test, on a Lattice ECP2/M20 FPGA adopted in the upgrade project of the MDC electronics, has been performed at GSI. In year 2008, during the HADES beam time when a proton beam of 3.5 GeV kinetic energy hit a Nb target, an Optical End Point (OEP) board was placed for four weeks near the beam line at a distance of approximately 12 m from the target point. The ECP2/M20 FPGA die was exposed to different reaction products (protons, neutrons, pions, heavier particles and fragments produced in the mentioned reaction) at very different energies. The particle flux was varied by changing the distance of the FPGA from the beam line.

Dedicated Lattice ECP2/M20 Single Even Detection (SED) hardware, in Fig B.1, has been used to detect SEUs. A dedicated software firmware has been loaded in the FPGA and on the FLASH memory on board. If case a

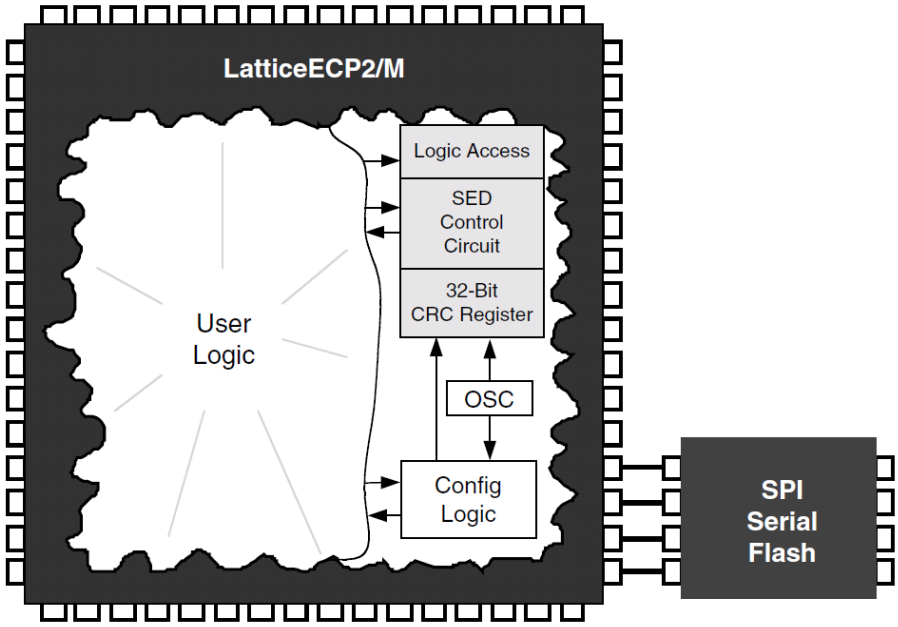

Figure B.1: The Single Event Detection (SED) hardware of the Lattice ECP2/M20 FPGA: it consists of an access point to FPGA configuration memory, a controller circuit, and a 32-bit register to store the CRC for a given bit-stream. The SED hardware reads serial data from the FPGAs configuration memory and calculates a Cyclic Redundancy Check (CRC). The CRC is recalculated every 3-6 seconds then it is compared with the expected CRC that was stored at the beginning of the process in the 32-bit register. If the two CRC values match then the matching indicates that there has been no configuration memory corruption, but if the values are different an error signal is generated. The picture has been adapted from [132].

configuration memory corruption was detected, an error signal was generated and driven to the Manual Reset Pin of the power manager chip on board. Hence in case of SEU the board was automatically rebooted and a new configuration was loaded into the chip.

The amount of time needed to perform a SED check of the whole FPGA depends on the device type and the frequency of the primary clock used in the SED entity.

An approximation of the time required can be computed using the following equation:

$$Time_{FCS} = \frac{BitSteam}{CLK} \tag{B.1}$$

where $Time_{FCS}$ is the estimated time for a full memory chip scan, $BitSteam$ is the average number of bits in the configuration FPGA bit-stream (typically $5-6$ $Mbits$) and CLK is the clock frequency (2.5 MHz) used by the SED entity. The average scan time takes 3-6 seconds for the configuration used in this experiment.

An average of 2 SEUs per hour have been recorded. The rate of the particles which passed through the FPGA was about 10^4-10^5 $particles/s*cm^2$. At each SEU the FPGA was successfully reconfigured by the circuit described before.

The FPGA was exposed at a particle rate higher compared with the particle rate expected in a future experiment such as Au+Au at incident kinetic energy of 1.5 $AGeV$. In this case the particle flux expected is about few hundreds $particles/s*cm^2$ supposing a LVL1 trigger rate of 20 kHz. This rate should not affect the Front End Electronics (FEE) operation. However the SED software will be included in each FPGA and the Slow Control software will monitor the correct operation of each single Lattice ECP2/M20 FPGA in the system.

Appendix C

Data Format

C.1 MDC Sub-Event Data Format

C.1.1 Overview

Network Header (DHDR)
First OEPB Dataword
OEPB Debug Data (at Request)
MDC Data (Verbose Mode or Compact Mode)
Padding Datawords

This document describes the data format of the event which is built in the Optical End Point Board (OEPB). Tab. C.1.1 consists of blocks of datawords. Each dataword is composed by 32 *bits*. Each block and the meaning of each bit are explained in the next sections. The **First OEPB Dataword** (see Sec. C.1.3) follows the **Network Header (DHDR)** (see Sec. C.1.2) and it is always present. The **First OEPB Dataword** is a single $32 - bit$ dataword and indicates if debug data will follow. These **OEPB Debug Data** are debug datawords and come before the **MDC data** (real dataword). The debug datawords contain all information regarding the status of the OEPB.

The **MDC Data** (see Sec. C.1.5) consists of **Verbose Mode** or **Compact Mode** datawords. The first one contains one hit of one TDC channel and eventually some debug information. The second one is thought to reduce the

load on the network. Here only the important data are transported. One can switch between the two mode writing in one configuration register.

Each event is terminated by a $32-bit$ dataword: the **Padding Datawords**.

C.1.2 Network Header (DHDR)

The first and the third DHDR are built in the OEPB. The second one by the last hub level.

The **first DHDR** word contains the trigger bus information belonging to this data sample, namely:

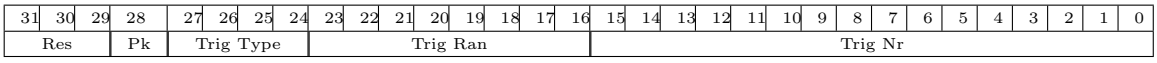

- **Res** reserved bits
- **Pk** Pack bit ('0'pack,'1' don't pack)
- **Trig Type** Trigger type
- **Trig Ran** Trigger random
- **Trigger Nr** Trigger number

The **second DHDR** word contains the length of the data packet (+1) and the HUB address.

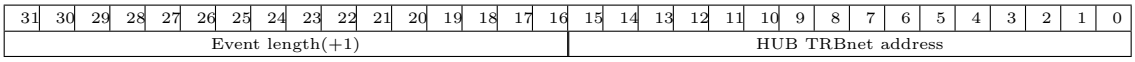

The **third DHDR** word contains the length of the data packet following, as well as the TRBnet address of the module (OEPB) the data originates from:

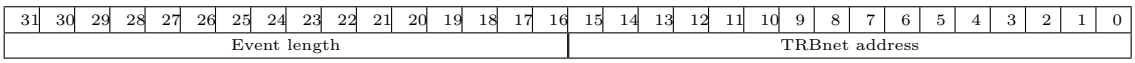

C.1.3 First OEPB Dataword

The **First OEPB Dataword** contains the length of the debug information which follows. This data can be requested at request by the user application and comes before the MDC Data.

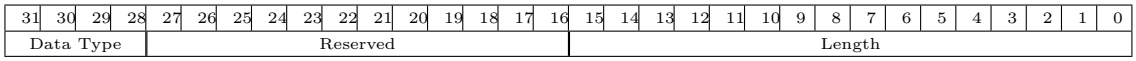

- **Data Type**
  - **x"0"** OEPB status data disabled. No debug datawords will be transported
  - **x"1"** Debug information enabled. A number of datawords defined in **Length** field will follow. Here all OEPB information will be encoded.
  - **x"2" to x"F"** for future use
- **Reserved** for future use.
- **Length** number of datawords which follow

C.1.4 MDC Data (Verbose Mode)

Each dataword contains one hit. This format is the same for normal and for calibration trigger.

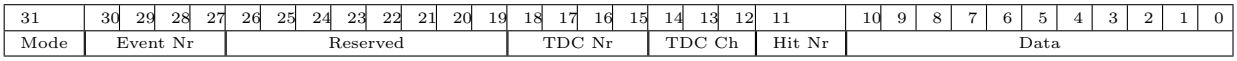

- **Mode**
  - **'0'** Verbose Mode selected
- **Event Nr** Increasing number of event
- **Reserved** for future use.
- **TDC Nr** TDC Number (1,...,12)
- **TDC Ch** TDC Channel (0,...,7)
- **Hit Nr** Number of hit '1' first hit, '0' second hit
- **Data** TDC data

C.1.5 MDC Data (Compact Mode)

With the **Compact Mode** all single hit data words are discarded; only "good data" is transmitted (two hits per measurement), in order to see the debug (noise measurement) one Motherboard (MB) the mode has to be switched to **Verbose Mode**.

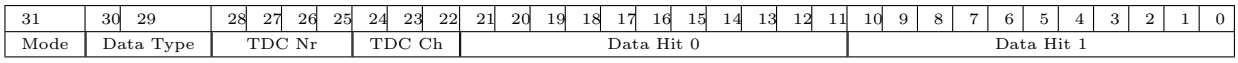

- **Mode**
  - **'1'** Compact Mode selected
- **Data Type**
  - **"00"** TDC measurement data
  - **"01"** TDC calibration data. Three datawords per TDC channel are foreseen (3 dataword x 2hit/dataword).
  - **"10"** TDC measurement data with ERROR, reserved for token not retrieved
  - **"11"** TDC calibration data with ERROR, reserved for token not retrieved
- **TDC Nr** TDC Number (1,...,12)
- **TDC Ch** TDC Channel (0,...,7)
- **Data Hit 0** TDC data
- **Data Hit 1** TDC data

In case of calibration event, one TDC channel data is packed as follows:

31	30	29	28	27	26	25	24	23	22	21	20	19	18	17	16	15	14	13	12	11	10	9	8	7	6	5	4	3	2	1	0
1	0	1	TDC Nr				TDC Ch			Data2 (Hit 0)											Data1 (Hit 1)										

31	30	29	28	27	26	25	24	23	22	21	20	19	18	17	16	15	14	13	12	11	10	9	8	7	6	5	4	3	2	1	0
1	0	1	TDC Nr				TDC Ch			Data4 (Hit 0)											Data3 (Hit 1)										

31	30	29	28	27	26	25	24	23	22	21	20	19	18	17	16	15	14	13	12	11	10	9	8	7	6	5	4	3	2	1	0
1	0	1	TDC Nr				TDC Ch			Data6 (Hit 0)											Data5 (Hit 1)										

Nomenclature

CFD	Constant Fraction Discriminator
CMS	Common Stop Signal
CPLD	Complex Programmable Logic Device
CRC	Cyclic Redundancy Check
CTS	Central Trigger System
CTU	Central Trigger Unit
DAQ	Data Acquisition System
DC	Driver Card
DSP	Digital System Processing
DTU	Detector Trigger Unit
EPICS	Experimental Physics and Industrial Control System
FAIR	Facility for Antiproton and Ion Research
FEE	Front End Electronic
FIFO	First In First Out
FOT	Fiber Optical Transceiver
FPC	Flexible Printed Circuit
FPGA	Field Programmable Gate Array
FWHM	Full Width at Half Maximum
GSI	Helmholtzzentrum für Schwerionenforschung
HADES	High Acceptance Di-Electron Spectrometer
HT	Hough Transform
HYDRA	HADES System for Data Reduction and Analysis
IC	Integrated Circuit
IPU	Image Processing Unit
JTAG	Joint Test Action Group
LVDS	Low Voltage Differential Signaling
LVL1	first level trigger
LVL2	second level trigger
MDC	Multi-Wire Drift Chamber
OBE	One Boson Exchange
OEPB	Optical End Point Board
PCB	Printed Circuit Board
PIO	Input/Output Pairs
PM	Pattern Mask
POF	Polymer Optical Fiber
QCD	Quantum Chromo Dynamics
QED	Quantum Electro Dynamics
RAM	Random Access Memory
ROC	Readout Controller
ROM	Read Only Memory
RPC	Resistive Plate Chamber
SAM	Steurung und Auslese Modul
SED	Single Event Upset
SERDES	Serializer/Deserializer
TDC	Time to Digital Converter
TOF	Time of Flight
TRB	Trigger and Readout Board
TTL	Transistor-to-Transistor Logic
UrQmd	Ultra Relativistic Quantum Molecular Dynamics model
VHDL	Very High speed integrated circuit Hardware Description Language
VUV	Vacuum Ultra Violet

References

[1] M. Schmelling, *Status of the strong coupling constant*, hep-ex/9701002, 1996.

[2] *Particle Data Group, Particle Physics Booklet*, Elsevier (2008).

[3] S. Klimt, M. Lutz, and W. Weise, *Chiral phase transition in the SU(3) Nambu and Jona- Lasinio model*, Phys. Lett. B249, 386 (1990).

[4] U. Mosel, *Symmetryes, and Quarks*, McGraw Hill (1989).

[5] V. Koch, *Aspects of Chiral Symmetry*, LBNL Report 39463 (2002).

[6] A. Hosaka, H. Toki, *Quarks, Barions and Chiral Symmetry*, World Scientific (2001).

[7] M. Gell-Mann, R. J. Oakes, B. Renner, Phys. Rev. 175 (1968) 2195.

[8] S. Leupold, V. Metag, U. Mosel, *HADRONS IN STRONGLY INTERACTING MATTER*, International Journal of Modern Physics E, July 14, 2009.

[9] M. Lutz, S. Klimt, and W. Weise, Nucl. Phys. A542, 621 (1992).

[10] G. E. Brown and M. Rho, *Scaling effective lagrangians in a dense medium*, Phys. Rev. Lett. 66, 2720 (1991).

[11] R. Rapp and J. Wambach, *Chiral Symmetry Restoration and Dileptons in Relativistic Heavy-Ion Collisions*, Adv. Nucl. Phys. (Springer, New York, USA, 2000), vol. 25, ISBN 978-0-306-46440-9.

[12] Lewis H. Ryder, *QUANTUM FIELD THEORY*, second edition, Cambridge University Press.

[13] S. Spataro, *Characterization of the HADES spectrometer in pp collisions at 2.2 GeV: elastic scattering and exclusive eta reconstruction*, Ph.D. Thesis, Universitá di Catania (2006).

[14] A. Rustamov, *Exclusive η Meson Reconstruction in Proton-Proton Collisions at 2.2 GeV with the HADES Spectrometer and High Resolution Tracking*, Ph.D. Thesis, GSI Darmstadt (2006).

[15] B.Sailer, *Inklusive e^+e--Paarproduktion in pp-Reaktionen bei $E_{kin} = 2.2GeV$*, Ph.D. Thesis, GSI Darmstadt (2006).

[16] M. Sudol, *Measurement of low-mass e^+e pair production in 2 AGeV $C-C$ collisions with HADES*, Ph.D. Thesis, Frankfurt (2007).

[17] Y. C. Pachmayer, *Dielektronenproduktion in $12C + 12C$ Kollisionen bei 1 GeV pro Nukleon*, Ph.D. Thesis, Frankfurt (2008).

[18] M. Sudol et al., *Measurement of low-mass e^+e^- pair production in $1-A-GeV$ and $2-A-GeV$ $C-C$ collision with HADES*, Eur. Phys. J. C.

[19] Y. C. Pachmayer et al., *Dielectron Production in $C + C$ Collisions at 1 GeV/u and the Solution to the DLS Puzzle*, Quark Matter 2008: 20th International Conference on Ultra-Relativistic Nucleus Nucleus Collisions (QM 2008), Jaipur, India, 4-10 February 2008.

[20] F. Krizek, *Study of inclusive electron-positron pair production in collisions of $Ar + KCl$ at 1.756 AGeV*, Ph.D. Thesis, Prague (2008).

[21] G. Agakishiev et al., *ϕ decay: A relevant source for K^- production at energies available at the GSI Schwerionen-Synchrotron (SIS)?*, Phys. Rev. C 80, 025209 (2009).

[22] *http://www-hades.gsi.de*

[23] *$http://www-hades.gsi.de/central/motivation/HADES\_proposal\_S333.pdf$*

[24] *$http://www-hades.gsi.de/central/motivation/HADES\_proposal\_S333.pdf$*

[25] K. Ozawa et al., (KEK-PS E325 Collaboration), Phys. Rev. Lett. 86, 5019 (2001).

[26] M. Naruki et al., (KEK-PS E325 Collaboration), Phys. Rev. Lett. 96, 092301 (2006).

[27] R. Muto et al., (KEK-PS E325 Collaboration), Phys. Rev. Lett. 98, 042501 (2007).

[28] R. Nasseripour et al., PRL 99 (2007).

[29] D. Trnka et al., (CBELSA-TAPS Collaboration), Phys. Rev. Lett. 94, 192303 (2005).

[30] M. Kotulla et al., (CBELSA-TAPS Collaboration), Phys. Rev. Lett. 100, (2008).

[31] M. H. Wood et al., (CLAS Collaboration), Phys. Rev. C78, 015201 (2008).

[32] R. Nasseripour et al. (CLAS Collaboration), Phys. Rev. Lett. 99, 262302 (2007).

[33] G. J. Lolos et al., (TAGX Collaboration), Phys. Rev. Lett. 80, 241 (1998).

[34] G. M. Huber, G. J. Lolos and Z. Papandreu, Phys. Rev. Lett. 80, 5285 (1998).

[35] G. M. Huber et al., (TAGX Collaboration), Phys. Rev. C68, 065202 (2003).

[36] V. Metag, *The Structure of Hadrons and their Modification in the Nuclear Medium*, Progress in Particle and Nuclear Physics 50 (2003) 635-648.

[37] V. Metag, *In-medium properties of hadrons-Recent experimental results and perspectives*, Pramana Journal of Physics, Vol.66, No 5, May 2006, pp. 833-856.

[38] V. Metag, *Photons and Dileptons as Probe in the pre(non) RICH Era* RICH-AGS-users meeting, BNL, 27 May 2008.

[39] F. Klingl, N. Kaiser, and W. Weise, Z. Phys. A356 (1996) 193.

[40] T. Renk, R. A. Schneider, and W. Weise, Phys. Rev. C66 (2002) 014902.

[41] G. Adamova et al., Phys. Rev. Lett. 91 N. 4 (2003).

[42] S. Yurevich, *Electron-Pair Production in* 158 *AGeV/c Pb-Au Collisions from CERES*, Ph. D. Thesis, Heidelberg, Germany, 2006.

[43] T. Galatyuk, *Di-electron spectroscopy in HADES and CBM: from p+p and n+p collisions at GSI to Au+Au collisions at FAIR*, Ph.D. Thesis, Frankfurt (2009).

[44] W. Wilson et al., Phys. Rev. C 57, 1865 (1998).

[45] A. Yegneswaran et al., Nuclear Intruments and Methods in Physics Research A290 (1990) 61-75.

[46] *http : //macdls.lbl.gov/DLS_WWW_Files/DLS.html.*

[47] R. Porter et al., *Dielectron cross section measurements in nucleus nucleus reactions at 1.0 AGeV*, (DLS Collaboration). Phys. Rev. Lett., 79:12291232, 1997.

[48] G. Roche et al., *DIELECTRON PRODUCTION IN Ca + Ca COLLISIONS AT 1.0 AND 2.0 AGEV*, (DLS Collaboration). Phys. Rev. Lett., B226:228232, 1989.

[49] The HADES collaboration *Status of the HADES physics program*, GSI SCIENTIFIC REPORT 2008, NQMA-EXPERIMENTS-03, GSI JUNE 2009.

[50] R. P. Feynman, *Photon-Hadron Interactions*, Advanced Book Classic, Westview (1989).

[51] W. Cassing, E. L. Bratkovskaya, *Hadronic and electromagnetic probes of hot and dense nuclear matter*, Phys. Rep 208 (1999) 65-233.

[52] L. G. Landsberg, *Electromagnetic Decays of Light Mesons*, Phys. Rep. 128, 6:301-376 (1985).

[53] P. Braun Munzinger and J. Wambach, *Colloquium: Phase diagram of strongly interacting matter*, Reviews of modern physics, Vol. 81, July-September 2009.

[54] L. P. Kaptari and B. Kämpfer, *Di-Electron Bremsstrahlung in Intermediate-Energy pn and Dp Collisions*, Nucl. Phys. A764: 338-370, 2006, arXiv:nucl-th/0504072v2.

[55] G. Hering, *Dielectron production in heavy ions collisions at 158 GeV/c per nucleon*, Ph.D. Thesis, Fachbereich Physik, T.U. Darmstadt (2001).

[56] M. A. Kaligaris, *Pluto++*, GSI Report (2000).

[57] I. Froehlich et al., *Pluto++ A monte Carlo simulation tool for hadronic physics*, arXiv:0708.2382v2 (2007).

[58] I. Froehlich et al., *Design of the Pluto Event Generator*, 17th International Conference on Computing in High Energy and Nuclear Physics (CHEP 2009).

[59] I. Froehlich et al., arXiv:0909.5373 [nucl-ex.] (2009).

[60] http://consult.cern.ch/writeup/geant/

[61] W. Press, B. Flannery, S. Teukolsky, W. Vetterling, Numerical Recipes in C: The Art of Scientific Computing, Cambridge University Press, 1992.

[62] R. C. Kammerud et al. *Large-Angle Proton-Proton Elastic Scattering at Intermediate Momenta*, Phys. Rev. D 4,5 (1971).

[63] http://root.cern.ch/

[64] K. Teilab Ph.D. Thesis in progress.

[65] S. A. Bass et al. *Microscopic Models for Ultrarelativistic Heavy Ion Collisions*, Prog. Part. Nucl. Phys. 41 (1998) 225-370.

[66] M. Bleicher et al. *Relativistic Hadron-Hadron Collisions in the Ultra-Relativistic Quantum Molecular Dynamics Model*, J. Phys. G: Nucl. Part. Phys. 25 (1999) 1859-1896.

[67] http://th.physik.uni-frankfurt.de/ brat/hsd.html

[68] COSY-TOF Collaboration, Phys. Lett. B 522, 16 (2001).

[69] F. Balestra et al., DISTO Collaboration, Phys. Rev. C 63, 024004 (2001).

[70] V. Flaminio et al., CERN-HERA Report No. 84-10, 1984.

[71] G. Agakichiev, V. Pechenov et al., Particle and Nuclei, Letters 2 (2000) 1001.

[72] M. Sanchez et al., *Kick Plan (Beamtime Edition)*. Internal Paper, GSI, 2000.

[73] Garfield, Simulation of gaseous detectors, $http://www.cern.ch/garfield$, Online User Guide.

[74] P.V.C. Hough, *Methods and means for recognition complex patterns*, U.S. Patern 3 069 654, Dec. 1962.

[75] S. Eidelman et al. Phys. Lett., B 592(1), 2004.

[76] E. L. Bratkovskaya, W. Cassing, Nucl. Phys. A619 (1997) 413.

[77] W. Ehehalt, W. Cassing, Nucl. Phys. A 602 (1996) 449.

[78] E. L. Bratkovskaya, W. Cassing *Dilepton production and off-shell transport dynamics at SIS energies*, Nucl. Phys. A807: 214-250, 2008.

[79] B. Ramstein, et al., *Study of elementary reactions with the HADES dielectron spectrometer* MetharXiv:nucl-ex: 0912.2677.

[80] A. Rustamov, Private Communication (2009).

[81] A. Rustamov et al., HADRON 2009 Conference Proceedings (2009).

[82] M. Weber talk given at HADES Collaboration Meeting XXI, GSI, 23-26 March, 2010.

[83] M. lorenz talk given at HADES Collaboration Meeting XXI, GSI, 23-26 March, 2010.

[84] A. Dybczak talk given at HADES Collaboration Meeting XXI, GSI, 23-26 March, 2010.

[85] K. Lapidus et al., arXiv:0904.1128 [nucl-ex].

[86] W. Koenig et al., *Diamonds as timing detectors for MIPS: The HADES proton-beam monitor and start detectors*, INSTRUMENTS-METHODS-02, GSI Scientific Report 2008.

[87] G. Agakishiev et al., *The High-Acceptance Dielectron Spectrometer HADES*, Feb 2009, Eur. Phys. J. A41:243-277, 2009.

[88] F. Sauli, *Principles of operation of multiwire proportional and drift chambers*, Lectures given in the academic training programme of CERN; European Organization For Nuclear Research, Geneva, 1977.

[89] C. Garabatos et al., *Optimisation of Low-Mass Drift Chambers for HADES*, Nucl. Inst. and Meth. A 412, 38 (1998).

[90] C. Müntz et al., *The HADES tracking system*, Nucl. Instr. Meth. A535 (2004) 242, 10th Vienna Conference On Instrumentation, 16-21 Feb 2004, Vienna, Austria.

[91] HADES Collaboration, *A Proposal for a High Acceptance Di-Electron Spectrometer*, GSI, Darmstadt (1994).

[92] P. Salabura et al., *High Acceptance DiElectron Spectrometer*, Nucl. Phys. Proc. Suppl, 44:701707, 1995.

[93] E. Berdermann et al., *First Applications of CVD Diamond Detectors in Heavy-Ion Experiments*, Nuclear Physics B (Proc. Suppl.) 78, 533-539, (1999).

[94] K. Zeitelhack et al., *The HADES RICH Detector*, Nucl. Inst. and Meth. A 433, 201 (1999).

[95] J. Friese et al., *A New Carbon Based VUV Mirror of High Radiation Lenght for the HADES RICH*, Nucl. Inst. and Meth. A 502, 241-245 (2003).

[96] L. Fabbietti, *Studies of the e^+e^- pair acceptance in the dilepton spectrometer HADES.*, Phd thesis, Technische Universität München, 2003.

[97] J. Markert, *Untersuchung zum Ansprechverhalten der Vieldrathdriftkammern niedriger Massenbelegung des HADES Experimentes*, Ph.D. Thesis, Fachbereich Physik der Johann Wolfgang Goethe Universität (2005).

[98] T. Bretz, *Magnetfeldeigenschaften der Spektrometer HADES*, Ph.D. Thesis, Physik Department der Technischen Universität Muenchen (2003).

[99] C. Agodi et al., *The HADES Time-of-Flight Wall*, Nucl. Inst. and Meth. A 492, 14-25 (2002).

[100] A. Balanda et al., *The HADES Pre-Shower Detector*, Nucl. Inst. and Meth. A 531, 445-458 (2004).

[101] A. Balanda et al., *Development of a Fast Pad Readout System for the HADES Shower Detector*, Nucl. Inst. and Meth. A 417, 360 (1998).

[102] A. Blanco et al., *Single-Gap Timing RPCs with Bidimensional Position-Sensitive Readout for Very Accurate TOF Systems*, Nucl. Inst. and Meth. in Physics Research A 508, 70-74 (2003).

[103] D. Gonzalez-Diaz, *RESEARCH AND DEVELOPMENTS ON TIMING RPC'S. APPLICATION TO THE ESTRELA DETECTOR OF THE HADES EXPERIMENT AT GSI*, Ph.D. Thesis, Santaigo, Spain, 2006.

[104] D. Belveder et al., *The HADES RPC inner TOF wall*, Nuclear Instruments and Methods in Physics Research A602 (2009) 687690.

[105] A. Blanco et al., *In-beam measurement of the HADES-TOF RPC wall*, Nucl. Inst. and Meth. in Physics Research A 602 (2009) 691-695.

[106] F. Hibou et al., *Near-Threshold Production of ω Mesons in the $pp \to pp\omega$ Reaction*, Phys. Rev. Lett. Vol. 83 Nr3 July 1999.

[107] S. Abd El-Samad et al., *Production of ω mesons in proton-proton collisions*, Phys. Rev. Lett. B 522 2001.

[108] S. Eidelman et al. Phys. Lett., B 592(1), 2004.

[109] S. Vogel and M. Bleicher, *Resonance Rescattering and Absorption in Low Energy Heavy Ion Collisions*, Romanian Reports in Physics, Vol. 58, No. 1, P. 6368, 2006.

[110] K. Schmidt et al., *Production and evolution path of dileptons at energies accessible to the HADES detector*, PRC 79, 064908 (2009).

[111] M. Traxler, *Real-Time Dilepton Selection for the HADES Spectrometer*, Ph. D. Thesis, Justus-Liebig-Universität Giessen, 2001.

[112] A. Toia, *Performance of the HADES Spectrometer for Dilepton Identification in the Reaction C+C at 1 AGeV*, Ph.D. Thesis, II Physikalisches Institut, Justus Liebig Universität Giessen (2004).

[113] D. G. Kirschner, *Level 3 Trigger Algorithm and Hardware Platform for the HADES Experiment*, Ph.D. Thesis, II Physikalisches Institut, Justus Liebig Universität Giessen (2007).

[114] J. Lehnert, *Echtzeit-Mustererkennung zum Elektronennachweis mit einem RICH-Detektor in Relativistischen Schwerionenkollisionen*, Ph.D. Thesis, II Physikalisches Institut, Justus Liebig Universität Giessen (2000).

[115] M. Heilmann *Untersuchung zur Spurrekonstruktion des HADES-Experiments in simulierten zentralen Au+Au Schwerionenkollisionen bei 1.5 AGeV*, Diplomarbeit, Johann Wolfgang Goethe Universität Frankfurt am Main, 2007.

[116] W. Kühn *FPGA based Compute Nodes for High Level Triggering in PANDA*, International Conference on Computing in High Energy and Nuclear Physics (CHEP07), IOP Publishing Journal of Physics: Conference Series 119 (2008) 022027.

[117] S Yurevich et al., GSI thecnical report INSTRUMENTS-METHODS-06, 2008.

[118] M. Palka, Ph.D. Thesis in progress.

[119] H. Bokemeyer et al., *Development of low-mass drift chambers for the HADES Spectrometer*, Nucl. Instr. Meth. A477 (2002) 397. 5th International Conference on Position Sensitive Detectors (PSD 5), London, England, 13-17 Sep 1999.

[120] F. M. Newcomer, *A Fast Low Power, Amplifier-Shaper-Discriminator for High Rate Straw Tracking System*, IEEE Trans. Nucl. Sci.n 40, 630 (1993).

[121] Gleichmann Elektronics, *Funktioansbeschreibung für den HADES Drift Chamber TDC*, (1998).

[122] M. Traxler et al., GSI Scientific Report 2006, (GSI Report 2007-1), p. 225.

[123] I. Fröhlich, M. Kajetanowicz, K. Korcyl, W. Krzemien, M. Palka, P. Salabura, C. Schrader, P. Skott, H. Ströbele, J. Stroth, A. Tarantola, M. Traxler, R. Trebacz and S. Yurevich, *A General Purpose Trigger and Readout Board for HADES and FAIR-Experiments*, IEEE Trans. Nucl. Sci. 55, 59 (2008).

[124] *An International Accelerator Facility for Beams of Ions and Antiprotons*, FAIR conceptual design report, http://www.gsi.de/GSI-Future/cdr/.

[125] M. Palka et al., *The New Data Acquisition System for the HADES Experiment*, Nuclear Science Symposium Conference Record, 2008, NSS 08, IEEE, p. 1398-1404.

[126] A. Tarantola et al., *The Upgrade of the Multiwire Drift Chamber Readout of the HADES Experiment at GSI*, Nuclear Science Symposium Conference Record, 2008, NSS 08, IEEE, p. 2146-2149.

[127] *www.axis.com.*

[128] L. R. Dalesio et al., Nucl. Instrum. Meth. A352, 179 (1994); *http://wiki.gsi.de/cgi-bin/view/Epics.*

[129] A. Tarantola et al., Proceeding of the XLVI International Winter Meeting on Nuclear Physics, Bormio(Italy), January, 20-26 2008.

[130] *http://www.firecomms.com/products-optolock.html.*

[131] J. Michel, *Development of a Realtime Network Protocol for HADES and FAIR Experiments*, Goethe Universität Frankfurt am Main, August 2008.

[132] *LatticeECP2/M Soft Error Detection (SED)*, Usage Guide, Technical Note TN1113.

[133] *LatticeECP2/M Family Data Sheet*, DS1006 Version 0.3.5, November 2009.

[134] *http://hades-wiki.gsi.de/cgi-bin/view.*

[135] P. K. Budig, *Routledge Langenscheidt German Dictionary of Eletrical Engineering: 1* (März 1998).

[136] FOT Data Sheet, Firecomms *Industrial OptoLock, Fiber Optic Transceiver with Termination for Bare POF.*

[137] SN75976A Data Sheet, Texas Instruments, *9-Channel Differential Transceiver.*

[138] Application Report, SLLA030C, Texas Instruments, September 2000.

[139] O. Rob *Introduction to JTAG*, Embedded Systems Design, 2002.

[140] IEEE Std., 1149.1 (JTAG) Testability Primer, Texas Instruments, Semiconductor Group, 1997.

[141] P. J. Ashenden, *The Designers Guide to VHDL*, System on Silicon, (2001).

[142] Perry, *VHDL: Programming by Example*, Fourth Edition, Mc Graw Hill, 2006.

Danksagung

Als erstes danke ich meinem Doktorvater, Herrn Prof. Dr. H. Ströbele, für die Überlassung der Aufgabenstellung, die hervorragende Betreuung dieser Arbeit und die nützlichen Diskussionen. Ich bedanke mich bei ihn für die Weisheit, mit der er mir Ratschläge gegeben hat. Seine Hilfe war mir sehr wichtig für meine Ausbildung. Ich danke ihm für die sorgfältige Lektüre dieser Arbeit und die Lektionen-Fragen, die er mir gestellt hat. Herrn Prof. Dr. J. Stroth danke ich für die Unterstützung, für die nützlichen Diskussionen, und für die Gelegenheit, an seiner Arbeitsgruppe Teil zu nehmen. Ich danke Herrn Prof. Dr. H. Ströbele, Herrn Prof. Dr. J. Stroth und Herrn Prof. Dr. S. Leupold für die Teilnahme an meinem "Ph.D. Commetee" und für ihre wichtigen Empfehlungen. Herrn Prof. Dr. P. Salabura danke ich für die Unterstützung und die hilfreichen Diskussionen über das Thema meiner Arbeit.

Unsere H-QM Schule hat eine grundliche Rolle in meiner Ausbildung gespielt: Ich danke Herrn Prof. Dr. H. Appelshäuser und dem Managing Director Herrn Dr. Prof. Büsching für die Gelegenheit, die sie mir geboten haben. Die Zeit, mit den Kollegen der H-QM Schule verbracht habe, wird als eine der schönsten Erinnerungen in meine Erfahrungen bleiben.

Vor drei Jahren begann meine Arbeit in der DAQ-Elektronik-Gruppe beim GSI. Ich danke Dr. M. Traxler für seine Einführung in die Gruppe, für die nützlichen Erklärungen und für die Freiheit mir gegeben bei der Arbeit hat und bei den vielen Herausforderungen. Diese vergangene Zeit werde ich als sehr schön und intensiv erinnern.

Vielen Dank für die Einführung Dr. B. Kolb: um die Codes zu verstehen und danke für die Verbesserung dieser Arbeit.

Vielen Dank für die Einführung Dr. I. Fröhlich: danke für die Verbesserung dieser Arbeit: die Analyse sowohl der Elektronische Teil.

Ich bin Herrn J. Hoffmann sehr dankbar: ich habe viel von Ihm gelernt. Vielen Dank an den Mitarbeitern der Abteilung für Elektronik beim GSI.

Herrn Dr. C. Müntz eine großes Danke für seine vielfältigen nützlichen Informationen und für seine Unterstützung.

I thank Dr. R. Holzmann and Dr. A. Rustamov for introducing me to the data analysis and for our many and interesting discussions. Their deep knowledge, experience, help and suggestions have been fundamental for me in

order to carry out my knowledge and finally this work. Thank you for real.

Ich danke Prof. Dr. E. Bratkovskaya für die Kommentare und Diskussionen über die theoretischen Gründe meiner Arbeit. Ich hoffe, über das interessante Thema der Dileptonen weiter mit ihr diskutieren zu können.

Together with my colleague M. Palka a lot of work has been done. I thank him for these years we worked close together and for explaining me the "secret" of electronics. Thanks to R. Trebacz and Y. Wang with whom it was a pleasure to work.

I would like to acknowledge all my colleagues in the HADES Collaboration. I am especially grateful to all colleagues and friends in the HADES Group at GSI. I remember Dr. Y. Pachmayer, Dr. M. Sudol, Dr. J. Markert, Dr. W. König, Dr. J. Pietraszko, Dr. A. Schmah, Dr. Peter Zumbruch, Dr. S. Lang, M. Lorenz, Herrn E. Schwab, Dr. D. Gonzalez Diaz, Dr. I. König, Dr. C Sturm, Dr. S. Yurevich and Dr. T. Galatyuk.

Ich danke Kollegen und Freunden bei unserer Gruppe im IKF: C. Wimmer, K. Teilab, C. Schrader, J. Michel und S. Amar und Kollegen bei der CBM Gruppe in Frankfurt. Vielen Dank Samir für deine Hilfe und Geduld bei meinen Deutschen Übersetzungen. Danke an M. Frey und Herrn U. Köpf.

Voglio ringraziare la Prof. Dr. Laura Fabbietti per le utili discussioni e per i suggerimenti riguardanti questo lavoro. Ringrazio Dr. Elvira Santini per le utili discussioni.

Ringrazio il Dr. Adriano Gobbi per l'incoraggiamento e per gli utili consigli che mi ha dato in questo periodo.

Sono sicuro che se la Prof. Dr. I. Iori fosse qui sarebbe contenta di leggere questo lavoro e felice di discuterne. I suo insegnamenti e la sua guida sono stati importanti per la scelta del mio indirizzo di studi. Voglio ringraziare anche il Prof. Dr. W. Kühn che mi ha introdotto in questo campo della fisica e mi ha sempre dato suggerimenti e idee utili.

Thanks to all my colleagues in the H-QM School for their kind company during the times we spent together. Thank you very much S. Altinpinar for sharing the room with me in many occasions during trips and for the many discussions we had.

Non ultimo in ordine di importanza, voglio ringraziare Maria per tutto quello che ha fatto per favorire il mio studio, la passione per il mio lavoro in questi anni. Dedicarle questo lavoro vorrebbe dire dare troppa importanza al lavoro stesso e non sarebbe sufficiente per esprimere la gratitudine che provo per lei.